Graphene on Iridium with Aromatic Molecules and $3d$ or $4f$ Metals: Binding, Doping, Magnetism, and Organometallic Synthesis

I n a u g u r a l - D i s s e r t a t i o n
zur
Erlangung des Doktorgrades
der Mathematisch-Naturwissenschaftlichen Fakultät
der Universität zu Köln

vorgelegt von
M. Sc. Felix Huttmann
aus Köln

Köln, 2017

Erster Berichterstatter:	Prof. Dr. Thomas Michely
Zweiter Berichterstatter:	Prof. Dr. Heiko Wende
Dritter Berichterstatter:	Prof. Dr. Harold Zandvliet
Vorsitzender der Prüfungskommission:	Prof. Dr. Hans-Günther Schmalz
Tag der mündlichen Prüfung:	11.10.2017

Abstract

This work employs the surface of graphene (Gr) on Ir(111) in versatile roles as the starting point in investigations of (1) doped Gr's binding to nonpolar molecules, (2) the magnetism in monolayers of the rare-earth metal Eu and its coupling to $3d$ metal films, and (3) the on-surface synthesis and magnetism of organometallic compounds with aromatic ligands. All work is carried out under ultra-high vacuum conditions, using surface science techniques: low-energy electron diffraction (LEED), scanning tunneling microscopy (STM), thermal desorption spectroscopy (TDS), and soft-x-ray magnetic circular dichroism (XMCD). The experiments are complemented by density functional theory (DFT) calculations conducted by cooperation partners.

In project (1), we use STM to visualize and TDS to quantitatively measure that the binding of naphthalene molecules to graphene, a case of pure van der Waals interaction, strengthens with n and weakens with p doping of graphene. DFT calculations that include the van der Waals interaction in a seamless, ab initio way accurately reproduce the observed trend in binding energies. Based on a model calculation, it is proposed that the van der Waals interaction is modified by changing the spatial extent of Gr's π orbitals via doping.

In project (2), we create new interfaces of Gr with metallic and magnetic supports which leave Gr's electronic structure largely intact. This is achieved by exposing epitaxial Gr to Eu vapor at elevated temperatures, resulting in the intercalation of a Eu monolayer in between Gr and its growth substrate. Eu intercalated under Gr/Ir(111) forms different phases depending on the coverage, which are discussed more thoroughly here than before. XMCD on the $(\sqrt{3} \times \sqrt{3})\mathrm{R30}^{\circ}_{\mathrm{Gr}}$ superstructure shows ferromagnetic coupling, in one preparation with $T_C \geq 15\,\mathrm{K}$, and a dominant dipolar anisotropy. To stabilize the magnetic order to higher temperatures, we use thin films of the ferromagnets Co and Ni underneath the Eu layer to obtain hybrid $3d$-$4f$ systems. In this case, the intercalated Eu monolayer forms exclusively a $(\sqrt{3} \times \sqrt{3})\mathrm{R30}^{\circ}_{\mathrm{Gr}}$ superstructure. X-ray absorption spectroscopy confirms that Eu intercalation yields an electronic decoupling of Gr from the otherwise strongly interacting $3d$ metal substrates. XMCD is used to characterize the magnetic behavior with elemental specificity. An antiferromagnetic coupling between Eu and Co/Ni moments is found, which is so strong that a net moment of the Eu layer can be detected at room temperature.

In project (3), we use Gr as a substrate for the growth of organometallic compounds. Metal

vapor is combined with ring-like aromatic ligands in the pursuit of sandwich compounds and molecular nanowires of interest for magnetism. The rare-earth metals Eu and Tm are reacted with cyclooctatetraene (Cot) molecules, and the 3*d* metal V is combined with benzene (Bz).

The combination of Cot with Eu yields EuCot nanowires under all conditions with molecular excess. A rich and intriguing growth morphology is revealed. STM indicates that EuCot is insulating, and XMCD measurements show that it is ferromagnetic with a Curie temperature between 5 and 10 K. To achieve a single orientation of nanowires in the substrate plane, we develop Gr on Ir(110) as a growth substrate, a surface with only twofold rotational symmetry. One Gr phase is atomically flat and leads to growth of the EuCot nanowires oriented along the [001] direction of the substrate.

In contrast to EuCot, TmCot nanowires are obtained only on *n*-doped Gr, and the growth is highly sensitive to the Tm-to-Cot flux ratio. On undoped Gr, simultaneous exposure to Tm and Cot vapor instead results in the formation of two non-wire phases: A disperse "dot" phase of repulsively interacting TmCot monomers at low coverages, and an island-forming "coffee bean" herringbone phase for higher coverages. The different behavior of Eu and Tm is traced to the more favorable +3 oxidation state for the latter. The coffee bean phase is modeled as a dimer of distorted metal-ligand "riceball" structures, where each riceball consists of three Tm atoms in 5*d* covalent bonding surrounded by one ionically-bonded Cot ring each. XMCD measurements on the coffee bean phase reveal a peculiar anisotropy and saturation behavior.

For VBz, no wires could be identified, only VBz_2 molecules, interpreted to result from the covalent bonding character in this case.

Frequently used symbols and abbreviations

Bz	-	benzene
Cot	-	cyclooctatetraene
CVD	-	chemical vapor deposition
DFT	-	density functional theory
(L)DOS	-	(local) density of states
fcc	-	face centered cubic
FM	-	ferromagnetic
Gr	-	graphene
hcp	-	hexagonal close packed
hBN	-	hexagonal boron nitride
LEED	-	low-energy electron diffraction
MD	-	molecular dynamics
ML	-	monolayer
Nph	-	naphthalene
QMS	-	quadropole mass spectrometer
STS/STS	-	scanning tunneling microscopy/spectroscopy
TDS	-	thermal desorption spectroscopy
TPG	-	temperature-programmed growth
UHV	-	ultrahigh vacuum
vdW	-	van der Waals
XAS	-	x-ray absorption spectroscopy
XMCD	-	x-ray magnetic circular dichroism
XMLD	-	x-ray magnetic linear dichroism

Contents

Chapter 1

Introduction

Graphene (Gr) is an atomic monolayer of graphite, and has been the subject of an explosion of interest by the scientific community after its production by mechanical exfoliation by Geim and Novoselov [1, 2], who were awarded the 2010 Nobel Prize in Physics "for [their] groundbreaking experiments regarding the two-dimensional material graphene". The excitement has since then transferred to many other two-dimensional materials [3]. Outstanding physical properties and effects were found in diverse areas, beginning with the electric field effect [2] and continuing with room-temperature quantum hall effect [4], single-molecule detection in gas sensors [5], or monolayer-specific photoluminescence [6].

While the experiments which started the Gr rush were conducted on exfoliated samples handled in ambient conditions, Gr has also become a deep subject elsewhere, such as in the realm of surface science and related theory. This is because it turns out that the excellent structural quality with which epitaxial Gr may be grown, the ease with which it can be affected by changes in its environment, and its high structural stability, creates a rich playground for experiments in ultra-high vacuum conditions: There, the binding of Gr to its substrate can be modulated by intercalation of more strongly or weakly interacting materials [7, 8], and new properties may be obtained in Gr, such as many-body effects at high doping levels achievable via adsorption or intercalation of highly reactive atoms [9–11], as well as spin-orbit coupling from intercalation of heavy elements [12, 13]. On the other hand, Gr can be put to use, for example to create quantum wells for electronic states at a surface [14–17], to increase the magnetic hardness of intercalated transition metal layers [18], or as a substrate for the growth of other two-dimensional materials [19].

This work follows those paths, using the particularly high-quality, effectively single-crystalline epitaxial Gr on the Ir(111) surface as a starting point for a range of experiments where Gr takes the most diverse roles: tunable adsorber, oxidation protector, material for spintronic applications, exceptionally inert growth substrate, and even that of a catalyst.

Two-dimensional materials have strong chemical bonds within, but their bonding to the en-

vironment is limited to the far-weaker van der Waals (vdW) interaction. This begs the question: What influences the strength of the vdW binding, and can we possibly even intentionally control it? As part of this work, it was indeed found that, yes, we can. In chapter 5, we discuss how doping of Gr with electrons or holes strengthens or weakens the vdW interaction of Gr with the small aromatic molecules benzene and naphthalene.

Gr is capable of high electron mobility, and because it is a light element, its spin orbit coupling is weak. This means that Gr is a very good conductor for spin currents [20]. Therefore, one of Gr's many envisioned fields of application is in spintronics [21], an approach to information processing that uses the electron spin rather than its charge for the processing of information. Gr on magnetic metallic substrates, such as the extensively studied case of Ni [22–25], is of particular interest, since such an interface can be envisioned as a building block in a spin injection contact of a spintronic device [26, 27], and because it can be epitaxially grown, thus representing a highly scalable approach, especially compared to graphite exfoliation. One drawback of the Gr/Ni system, however, is the strong hybridization of the Ni $3d$ electrons with the π system of Gr, which strongly modifies the Gr band structure in a wide window around the Fermi edge [28]. In contrast, a $4f$ metal atom that does not possess a d electron, such as europium, binds mainly ionically to Gr [29], adsorbs in the center of the carbon ring, and thus largely leaves the Gr band structure intact [30]. In chapter 6, we investigate the structure and magnetism of europium monolayers intercalated in between Gr and its substrate. We use ferromagnetic thin films as substrates in addition to the non-magnetic iridium substrate to explore magnetic coupling of the europium layer within itself as well as coupling to the substrate.

Gr is highly inert, and this property can be exploited to use it as a substrate. Thereby, materials can be grown by molecular-beam methods that would be difficult to grow on other surfaces, because the surface would participate in the reaction [31–33]. Here, we are interested in materials where the magnetic moment of an element of the $3d$ or $4f$ series is combined with organic ligands. Such compounds have potential for applications in molecular spintronics, which has motivated a vast body of research [34]. A particularly peculiar class of materials, so-called sandwich molecular wires (SMWs), or simply nanowires, composed of alternating metal atoms and 5-, 6-, or 8-membered carbon rings [cyclopentadienyl (Cp=C_5H_5), benzene (Bz=C_6H_6), or cyclooctatetraene (Cot=C_8H_8)], could make a unique contribution to this field [35]. This is because they join the robust magnetic moments on $3d$ or $4f$ metal atoms by ring-shaped aromatic molecules, creating sufficient electronic hybridization between the metal atomic states via the extended π orbitals, and hence magnetic coupling along a one-dimensional chain. This should result in more stable magnetism with higher blocking temperatures than in, *e.g.*, the lanthanide-based double-decker single-molecule magnets [36]. Exciting electronic and magnetic properties and efficient spin filtering have been predicted for sandwich molecular wires, for example in EuCot (ferromagnetic and semiconducting) and VBz (ferromagnetic and half-metallic) [37–44]. However, it appears that the characterization of these compounds would greatly benefit from a

synthesis method that could yield the product in a more ordered form and experimentally accessible to a wider range of techniques. Thus in chapter 7, we investigate Gr on Ir as a substrate for the growth of sandwich molecular nanowires and other organometallic nanostructures from the metal and ligand vapors. We find that the molecular-beam growth on Gr can yield well-ordered as well as oriented, effectively single-crystalline samples of sandwich molecular wires. Due to the exposure of the clean wires to the vacuum, an excellent method of magnetic characterization becomes available. Furthermore, graphene can serve as a catalyst in the selective growth of complexes that appear to not have been previously observed in any other synthesis method.

Before discussing the results, chapters 2, 3, and 4 introduce the reader to previous research, the experimental methods used, and the setup and procedures, respectively.

Chapter 2

Fundamentals

In this chapter, selected topics of interest for this work are reviewed. Further references to literature are given in the introductions to the corresponding chapters.

2.1 Graphene

Gr is a 2D crystal made of a honeycomb lattice of carbon atoms, i.e., two equivalent carbon atoms per unit cell in a hexagonal lattice as shown in Fig. 2.1 (a). The carbon atoms are in sp^2 hybridization. With the graphene sheet in the xy plane, three σ orbitals per carbon atom are formed from the s, p_x, and p_y orbitals, and the σ bonds dominate the structural stability of the crystal. However, the electronic bands of σ character are far from the Fermi level. Thus, the electronic properties are only due to the p_z-derived π and π^* bands, which are occupied and unoccupied, respectively. The outstanding property of the graphene band structure is that the π and π^* bands are linear at the K point and touch, i.e., there is a crossing of bands without a band gap, as shown in Fig. 2.1 (b). The crossing point is called Dirac point. In undoped graphene, this is also the location of the Fermi level, i.e., the density of states at charge neutrality is zero. Graphene has therefore been called a gapless semiconductor [45].

Generally, when bands cross without a gap opening, there are two possibilities: (1) The bands are of different symmetry. This is not the case for the π and π^* bands in graphene. To give an example of what is meant by different symmetry, consider the case of the σ and π bands in graphene: If Ψ_σ and Ψ_π are wave functions of a state in the σ and π bands, then $\Psi_\sigma(x,y,-z) = \Psi_\sigma(x,y,z)$, but $\Psi_\pi(x,y,-z) = -\Psi_\pi(x,y,-z)$. Thus, the π and σ bands may cross. However, the crossing occurs far from the Fermi level and is irrelevant for the electronic properties. (2) The band crossing is associated with a particular symmetry. In graphene, the symmetry associated with the band crossing is the equivalence of the two carbon atoms in the honeycomb lattice, which is called sublattice symmetry. The two carbon atoms in the unit cell are often referred to as A and B, and thus one speaks of A and B sublattices. Whenever the

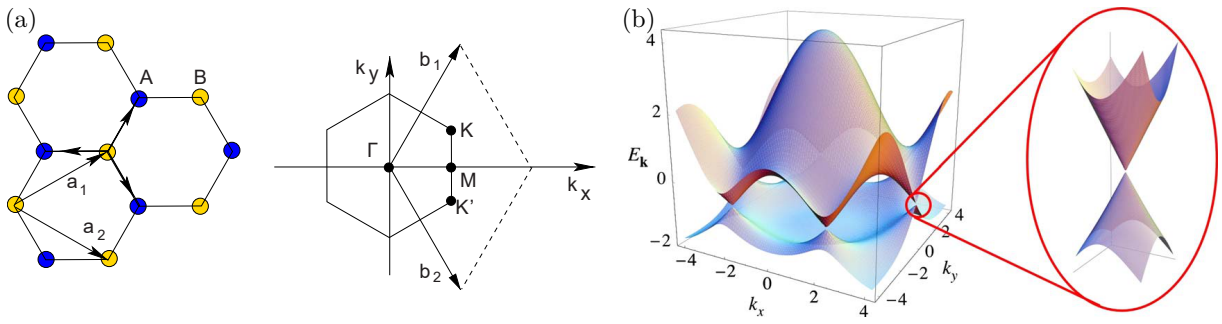

Figure 2.1: (a): Real-space structure (left) and corresponding reciprocal space Brillouin zone (right). a_1 and a_2 denote the real-space lattice vectors, while A and B denote the sublattices, b_1 and b_2 are the reciprocal-space lattice vectors, Γ, M, and K are high-symmetry points of the Brillouin zone. (b): Three-dimensional plot of the dispersion of the π and π^* bands. Zoom-in on one K point reveals the linear dispersion in this region. Both (a) and (b) are reprinted with permission from Ref. [46], © 2009 APS.

sublattice symmetry is broken, e.g., by adsorption, a gap will open at the K point.

There are further fundamental properties of the electronic structure of graphene: Related to the sublattice symmetry is a property called pseudospin, and the linear dispersion and particle-hole symmetry near charge neutrality give rise to the term massless Dirac Fermions for electrons in graphene. However, this is of no particular relevance for this thesis.

2.2 Graphene on Ni(111) and Ir(111)

2.2.1 Graphene grown on surfaces

All the fundamental experiments in the initial phase of the graphene rush that started with the electric field effect in 2004 [2] were conducted on graphene samples exfoliated from graphite. However, consensus emerged quickly that epitaxial graphene is probably the only route to scalable production [1]. The growth of graphene directly by carbon deposition [47], by precipitation of dissolved carbon from the bulk to the surface [48], or through the thermal decomposition of carbon-containing crystals such as SiC [49], where Si evaporates from the surface before C, is possible. However, the thickness control with these methods is challenging, and even with the best control, the sample surface will never be exclusively monolayer graphene, because the growth is not self-limiting. In contrast, the graphene growth from gaseous precursors on catalytically active metal surfaces, which is called chemical vapor deposition (CVD), allows to produce exclusively graphene monolayers, because the growth stops as soon as the catalytically active surface is fully covered.

2.2.2 Graphene growth on metals

For purposes nearer to devices or industrial applications, copper foil has emerged as the most commonly employed substrate [50], as it permits graphene growth close to or at ambient pressures, and because the copper foil is cheap and can be removed by etching for transfer of the graphene onto an insulating substrate [51]. In contrast, for experiments conducted in UHV, as done throughout this thesis, the preferred substrates are the dense-packed surfaces of single crystals of those transition metals which have partially open d shells. Graphene on Ni(111) [24, 52, 53] and Ir(111) [54–58] are among the best characterized systems in this category. Open-d-shell metals are more reactive, i.e., have a higher sticking probability for the precursor molecules from the gas phase, and are therefore less suitable for high-pressure CVD because the growth rate would be extremely high. On the other hand, the closed-d-shell metal Cu is unsuitable for low-pressure CVD as the growth rate is negligible [59, 60].

The sticking probability depends not only on the surface, but also on the gaseous precursor: The smallest hydrocarbon methane has the lowest sticking, because it is a fully saturated hydrocarbon, and is therefore used only in high-pressure CVD. In contrast, the smallest unsaturated hydrocarbon, ethylene (C_2H_4), has a C-C double bond, such that an additional bond to the metal surface is more easily formed. In fact, ethylene's sticking coefficient on the open-d-shell metals is near unity [58], which makes it the most used precursor for CVD in UHV, including throughout this thesis.

The elemental close-packed metal surfaces can be further categorized into cases of strong and weak interaction [61]. Here, some caution is required because the interaction strength of substrate and graphene depends also on the relative orientation of their crystal lattices, where aligned graphene generally has the strongest interaction [55, 62–64]. As the aligned phase is the "canonical" one and the one that is usually desired, a metal is referred to as weakly interacting if the aligned phase adsorbed on its close-packed surface is weakly interacting. The transition from weak to strong interaction has a continuous component (e.g., going from Au via Pt to Ir [65]), but a discontinuity has been shown to exist in the transition from a physisorbed to a chemisorbed system, with two well-separated regimes [66]. Of the open-3d-shell metals, Ni and Ir are examples for strong and weak interaction, respectively [56, 67].

2.2.3 Atomic structure of graphene on Ni(111)

Graphene on Ni and Ir have a further qualitative difference: Due to the small lattice mismatch of graphene with Ni(111) of about 1 %, a (1×1) registry is possible. In contrast, on Ir(111), the lattice mismatch is about 10 %, and a moiré lattice always forms. This might suggest that graphene on Ni(111) is the far simpler system, with one distinguished, commensurate (1×1) phase, yet the opposite is the case.

Figure 2.2 (a) shows LEED patterns of pristine Ni(111), the surface carbide phase on Ni(111),

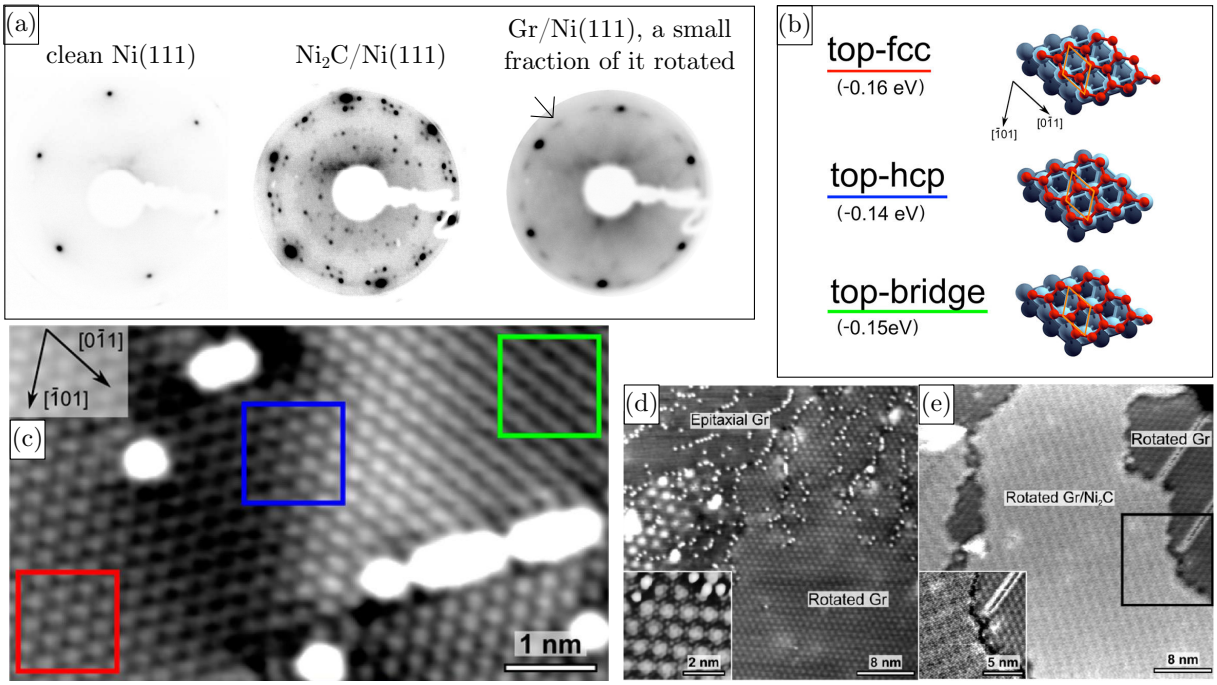

Figure 2.2: (a): LEED images of the Ni(111) surface before (left) and after growth of the nickel surface carbide phase (middle) or Gr/Ni(111) (right), arrow indicates rotated Gr. Electron energy 82 eV. (b): Different possible (1×1) domains. The given adsorption energies of the Gr sheet onto the Ni(111) surface from DFT calculations show that the configurations are very close in energy. (c)–(e): STM topographs of Gr/Ni(111). (c): The top-fcc, top-hcp, and top-bridge configurations can all occur over a length scale of a few nanometer, with smooth distortions of the Gr lattice in between, color of the squares indicates the color-underlined configurations as depicted in (b). (d): Image taken at 790 K of Gr/Ni(111) shows adjacent rotated and aligned domains. Moiré is visible on the rotated domain. (e): Same sample as (e) after cool-down shows formation of the stripe-like Ni_2C surface phase underneath rotated Gr. The subfigures are reproduced with permission from: (a) Ref. [68], Supplement; (b,c) Ref. [24]; (d,e) Ref. [69]. © 2012-2014 ACS.

and Gr/Ni(111). The formation of a metastable surface carbide phase instead of graphene occurs for growth temperatures below 500°C [69]. At higher temperatures, the (1×1) Gr phase grows. However, in addition incommensurate graphene rotated by $(17 \pm 5)°$ as indicated by the arrow in the LEED image can form and coexist with the aligned Gr [63]. The rotated phase is more favored at higher growth temperatures, above 650°C [63]. Even restricting ourselves to the (1×1), there is not one domain but rather several ones, where the two carbon atoms of one ring are in different high-symmetry positions of the Ni(111) substrate as shown in Fig. 2.2 (b). The most common domain is top-fcc, but top-hcp and top-bridge also occur. The different (1×1) domains on the sample are varyingly separated by both, smooth in-plane transitions as seen in Fig. 2.2 (c), as well as sharp boundaries, where the carbon rings are rearranged [24]. The density of point defects is generally high on the (1×1) phases. The rotated Gr domains are distinguished by a moiré pattern as seen in the STM topograph in Fig. 2.2 (d), and exhibit less

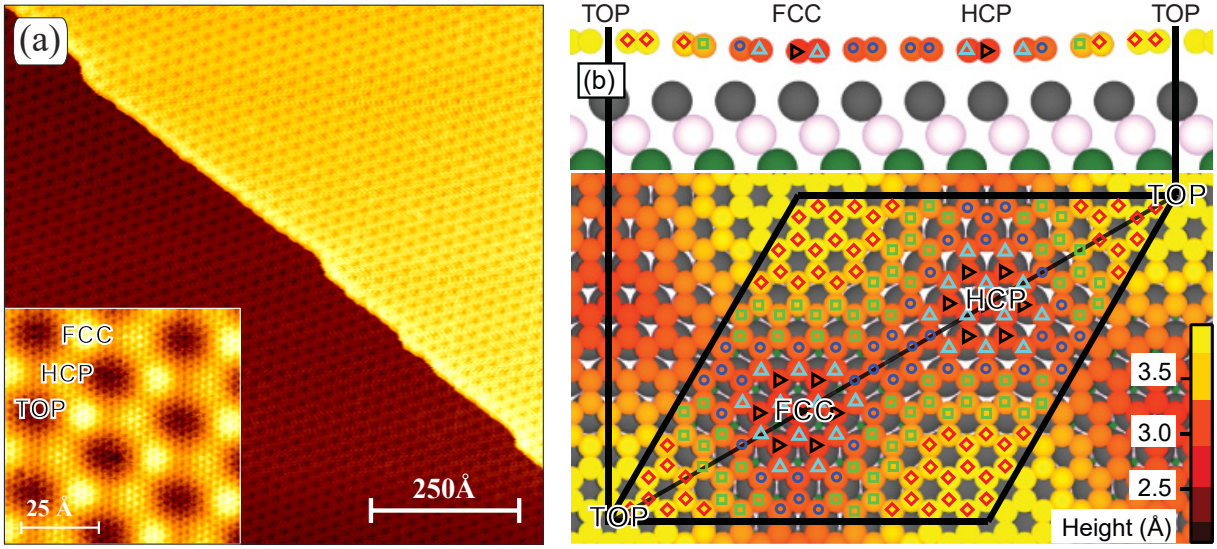

Figure 2.3: (a): STM topographs of Gr/Ir(111). The lattice in the main image is only the moiré, while the inset has atomic resolution. Both images show hcp and fcc regions to be apparently higher than top, this is called inverted moiré contrast. It is the most common contrast in STM, although other contrasts are also possible depending on the tip and tunneling conditions. Reproduced from Ref. [54], CC license. (b): Geometry as resulting from a DFT calculation on a (10×10) on (9×9) unit cell shows that the hcp and fcc regions are in fact lower than top. Lower part: Top view, rhombus indicates moiré unit cell. Upper part: Side view on a cut plane through the indicated diagonal of the rhombus in the lower part. Color of the carbon atoms encodes their height above the first Ir layer. Reproduced with permission from Ref. [71], © 2012 APS.

point defects. Another major complication of Gr on Ni is the significant solubility of C in Ni at the growth temperatures, which can give rise to precipitation of carbon to the surface to form either multilayer graphene or the surface carbide phase underneath a completed Gr sheet [63], the latter seen in the STM topograph in Fig. 2.2 (e). Thus, graphene on nickel leaves much to be desired in terms of quality, and was used in this thesis in only one project, due to nickel's ferromagnetism.

In comparison to Ni, the carbon solubility in Ir is small, and no surface carbide phase exists on the latter's close-packed surfaces. This is part of a general trend in the interaction strength of carbon with the metal in the periodic table: It decreases from left to right, and from top to bottom. Exemplarily for the first row: Ti to Fe form bulk carbides; Co(111) and Ni(111) still have high carbon solubilities and carbidic overlayer phases on their dense-packed surfaces competitive with strongly interacting aligned graphene; while for Cu, the carbon solubility is low [70], and graphene on Cu(111) is weakly interacting.

2.2.4 Atomic structure of graphene on Ir(111)

On Ir(111), rotated graphene phases can form just as in the case of Ni(111) [55]. However, using the TPG+CVD method [72], a single, aligned domain can be easily produced. The TPG (temperature-programmed growth) step refers to the adsorption of ethylene at low temperature, followed by annealing. Graphene flakes covering about 20% of a monolayer form during the heating and form compact islands consisting exclusively of the aligned domain. During the next step, the CVD, these flakes act as seeds for the further growth of fully aligned graphene into a closed film. From now on and throughout the rest of this thesis, Gr/Ir(111) refers exclusively to the aligned domain.

Gr/Ir(111) has an incommensurate superstructure with (10.32×10.32) graphene unit cells on (9.32×9.32) Ir unit cells [54]. The moiré superstructere is visible in the STM in Fig. 2.3 (a). Depending on tip and tunneling conditions, it can appear in STM in different contrasts as either high points in a low background, or low points in a high background. The latter is more common, and is referred to as inverted contrast, because it is opposite to the real height of the carbon atoms.

In first-principles calculations, a model with (10×10) Gr unit cells on (9×9) Ir is the approximation used for the incommensurate cell [56, 71, 73]. Figure 2.3 (b) shows the geometry resulting from a DFT calculation in such a model [71]. Three different regions can be distinguished, according to whether the center of the carbon ring is located above the hcp, fcc or top sites of the Ir(111) surface [54]. The overall character of the binding is physisorbed, but the smoothly varying relation of the carbon atomic positions with respect to those of the Ir(111) substrate in the moiré superstructure results in a chemical modulation of the binding [56]. Gr/Ir(111) has an average height of 3.4 Å, which is similar to what is found in bulk graphite, where the interaction is purely vdW. This contrasts with the height of the most common top-fcc domain of Gr/Ni(111) of about 2.1 Å, which is typical for a chemical bond [67].

In LEED images of Gr/Ir(111) as shown in Fig. 2.4 (a/b), the moiré superstructure results in satellite spots around the Gr and Ir ones. In Fig 2.4 (a), we show a SPA-LEED image, which permits to observe the moiré also around the zero-order reflection, where an image obtained with a conventional LEED analyzer as shown in Fig. 2.4 (b) is obscured by the electron gun.

One defect that occurs far more often in Gr/Ir(111) than in Gr/Ni(111) are wrinkles [76]. In general for graphene, wrinkles can occur as a result of a transfer process, but this is a different kind of wrinkles compared to the wrinkles in graphene resting on its growth substrate[1]. The latter kind of wrinkle results from the negligible thermal expansion of Gr compared to that of the metal substrate. When Gr is grown at high temperature and the sample then cooled down to room temperature, the differential thermal contraction causes a compressive strain in Gr. This strain is partially relieved through the formation of wrinkles, where the Gr locally

[1] Wrinkles are called ridges in Ref. [55].

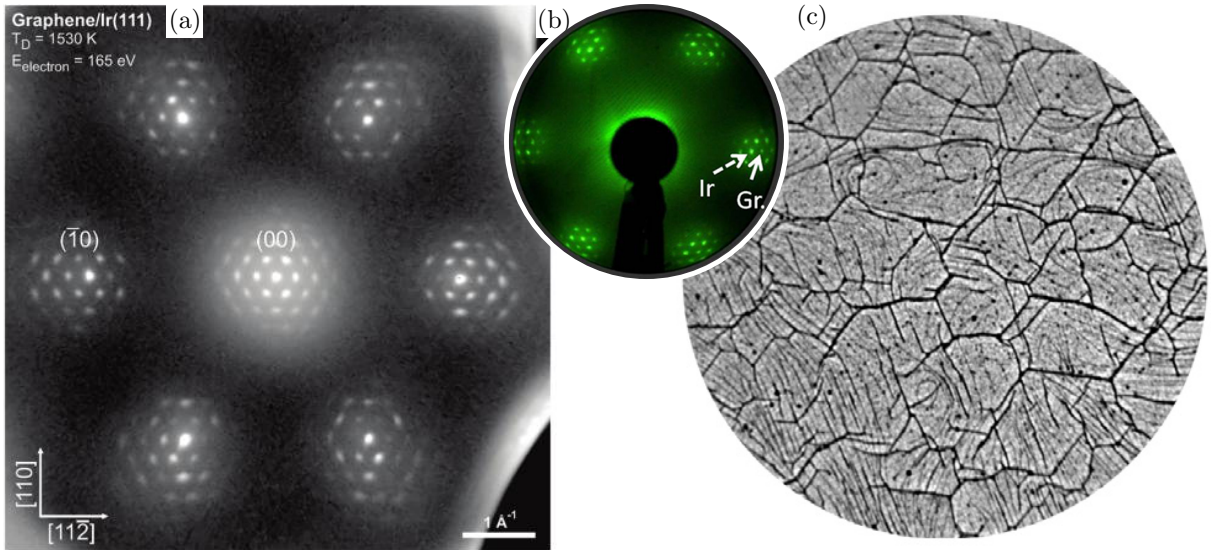

Figure 2.4: (a): SPA-LEED image of Gr/Ir(111), intensity in logarithmic scale. Moiré satellites appear around the Gr, Ir, and (00) reflexes. Compared to conventional LEED analyzers, SPA-LEED has higher resolution, higher dynamic range, and no electron gun shadow. Reprinted with permission from Ref. [74], © 2012 ACS. (b) Conventional LEED Image (primary electron energy 70 eV) of Gr/Ir(111). Reprinted with permission from Ref. [75], © 2012 AIP. (c): Low-energy electron microscopy (LEEM) image of Gr/Ir(111), field of view 9.3 µm. Thick dark lines are Gr wrinkles, thinner wavy lines are Ir steps. Reprinted with permission from Ref. [76], © 2015 Elsevier.

delaminates from the Ir(111) substrate. Figure 2.4 (c) shows a large-scale (9.3 µm) low-energy electron microscopy (LEEM) image of Gr/Ir(111). The strong dark lines are Gr wrinkles, which form a network. Compared to STM, imaging by LEEM allows a larger field of view, without which the network structure would not be revealed. The wrinkles are preferentially oriented in three different directions, which are the dense-packed rows of the Ir(111) substrate. The crossing point of three wrinkles is often located at a defect [76–78].

2.3 Electronic structure of graphene on Ni(111) and Ir(111)

Angle-resolved photoemission spectroscopy (ARPES) can be used to investigate the occupied part of the electronic band structure of surfaces. Figure 2.5 shows ARPES measurements conducted on (a) Gr/Ni(111) and (b) Gr/Ir(111). For Gr, the most interesting part is the region around the Dirac point. In Gr/Ni(111), the bands of Gr and the Ni(111) 3*d* states strongly hybridize and this destroys the Dirac cone in a wide window around the Fermi edge. In constrast, in Gr/Ir(111), the Dirac cone is clearly seen. However, also for Gr/Ir(111), the Dirac cone is not perfectly preserved: Minigaps and Dirac cone replicas occur as a result of the moiré superstructure [80]; they are not visible in Fig. 2.5 (b), but in Fig. 2.6 (c).

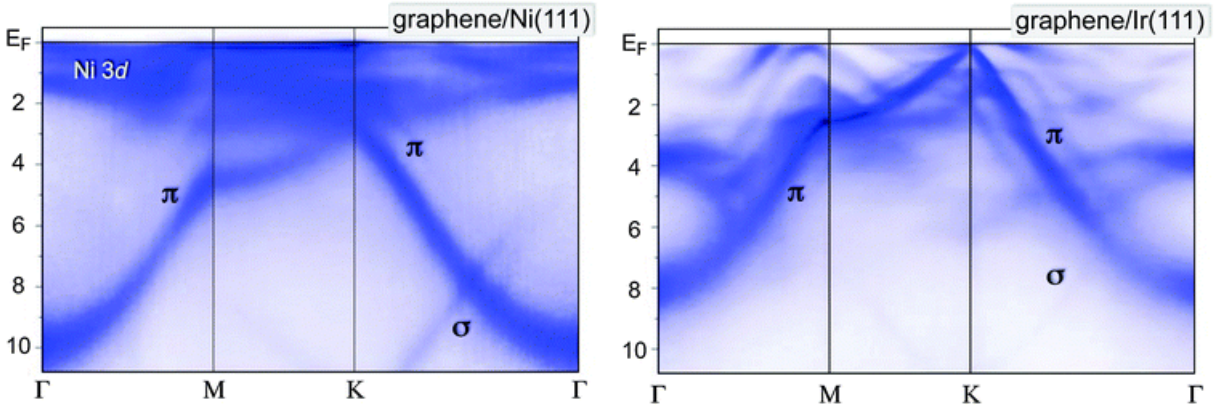

Figure 2.5: ARPES intensity maps of Gr/Ni(111) and Gr/Ir(111) on a line through the Γ-M-K-Γ high-symmetry points of the Brillouin zone. Reprinted with permission from Ref. [79], © 2012 RSC.

2.4 Intercalation of graphene on metals

It is energetically favorable for many species deposited onto graphene to intercalate in between graphene and the substrate, because the bond of the species to the substrate is stronger than the bond of graphene to the substrate, due to graphene's low reactivity. The intercalation of graphene is useful to modify graphene's properties and its interaction with the support, without changing the growth substrate and without any mechanical transfer process. For the purposes of this thesis, there are the following four applications of intercalation:

The first application is to dope graphene with electrons or holes. Doping by intercalation permits large shifts of the Fermi level on the order of ±1 V [81]. The doping of graphene results in a shift of the Dirac cone up and down relative to the Fermi level. This is directly visible in ARPES measurements: In Gr/Ir(111), the Dirac point is located very close to the Fermi level as seen in Fig. 2.6 (a) and (c). In contrast, the ARPES measurements shown in Fig. 2.6 after intercalation of (b) Cs and (d) O show that the Dirac point is shifted down (Cs) or up (O) due to n and p doping by about -1.1 eV and $+0.6$ eV, respectively.

The second application of intercalation is to "decouple" graphene from its support, where decoupling can have different meanings: It either means that (1) the electronic features of freestanding graphene, in particular a well-developed Dirac cone, are recovered, or (2) that the binding to the support is weakened, including the binding at the edges of graphene flakes, where the dangling σ bonds might bind to the substrate. Electronic decoupling of Gr/Ir(111) has been obtained by intercalation of O, Eu, Cs, Au, Ag. This, too, is well visible in the ARPES in Figure 2.6 (b) and (d), where the minigaps and Dirac cone replicas of Fig. 2.6 (a) and (c) have disappeared in both cases. Evidence for structural decoupling of Gr/Ir(111) is available for intercalation of Br [82] and Au [65], but is not relevant for this thesis.

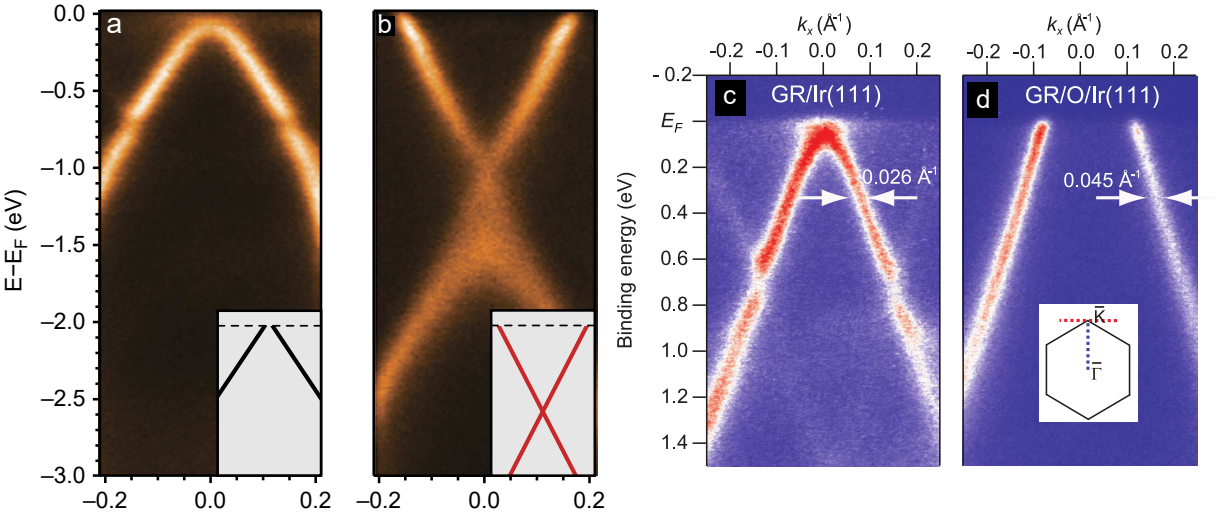

Figure 2.6: (a), (c): ARPES intensity maps of Gr/Ir(111) around the K point show the Dirac cone with minigaps at around -0.7 eV. (b), (d): After intercalation of one monolayer of Cs and O, respectively. n doping by Cs shifts the Dirac cone down relative to the Fermi level, while p doping by O shifts it up. Both Cs and O decouple Gr as seen in the disappearance of the minigaps. (a,b): Reproduced from Ref. [78], open access. (c,d): Reprinted with permission from Ref. [7], © 2012 ACS.

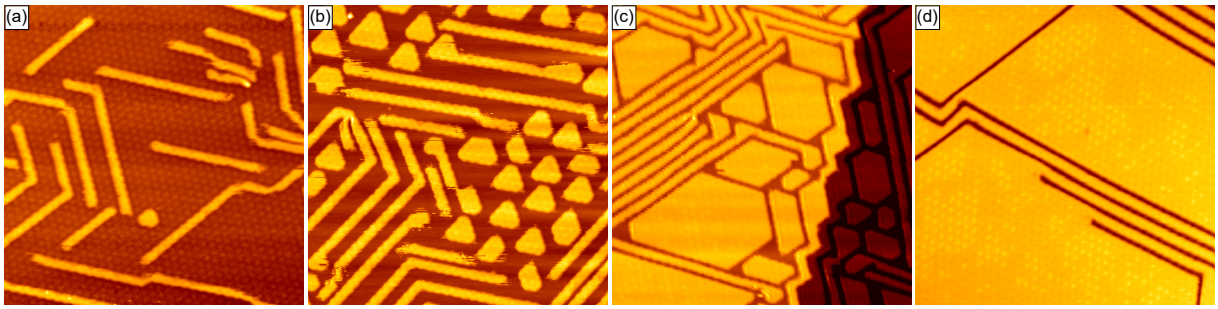

Figure 2.7: (a)–(d) STM topographs [image size $(80\,\mathrm{nm})^2$] after intercalation of Eu resulting in successively larger intercalation coverages of (a) 18% ML, (b) 39% ML, (c) 72% ML, and (d) 89% ML. Reprinted with permission from Ref. [83], ©2013 APS.

The third application of intercalation is to bring graphene into contact with a magnetic material. While graphene can be grown directly on some ferromagnetic metals as described before, the growth of Gr on Ir(111) followed by intercalation can result in very different kinds of Gr-substrate interfaces. Gr/Ir(111) intercalated with monolayer thin layers of Fe, Ni, and Co has been investigated by several researchers, who found peculiar spin textures, modified magnetic remanence, and a small induced magnetization in Gr [8, 18, 84, 85].

The fourth application is to pattern graphene in a self-organized way on a length scale of nanometer. As shown in Fig. 2.7, the intercalation of submonolayer amounts of Eu gives rise to a pattern consisting of Eu stripes, Eu islands, and Eu-free channels [83]. The pattern results

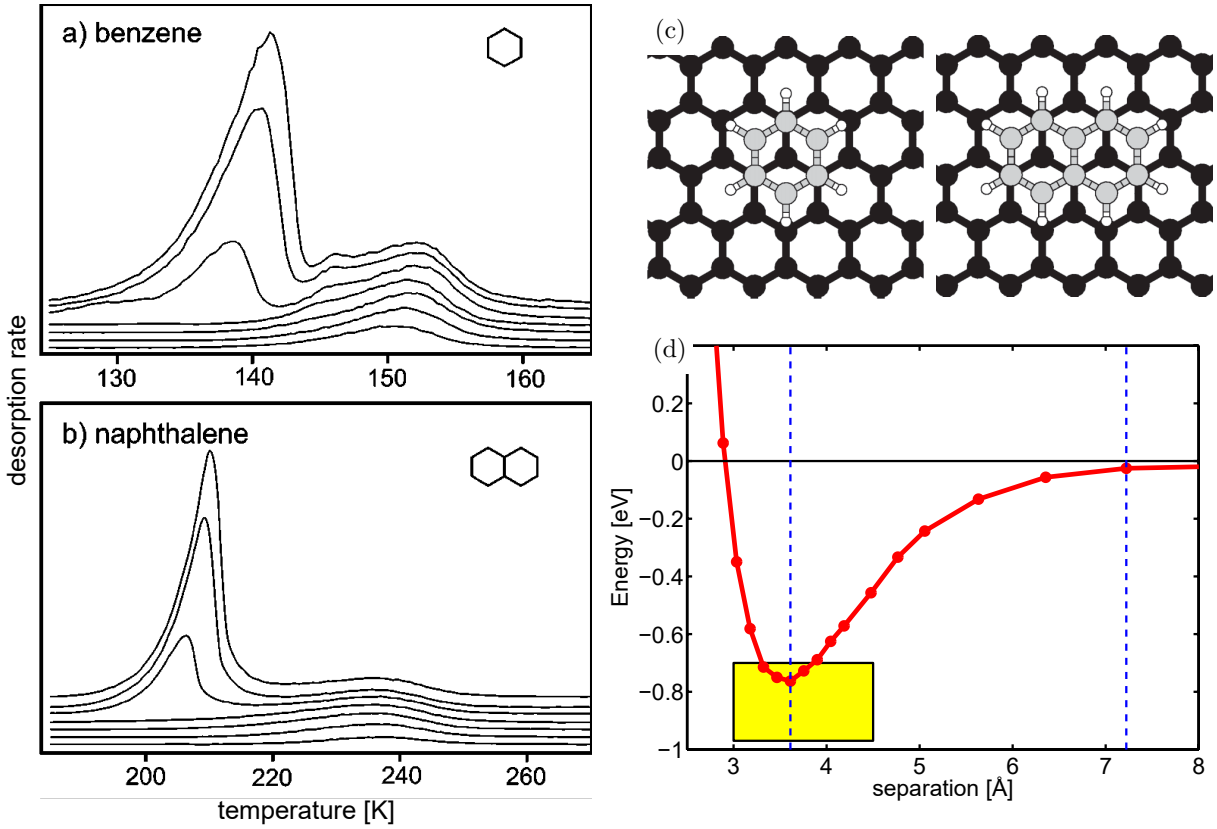

Figure 2.8: (a) and (b): Thermal desorption spectra for benzene and naphthalene from graphite for several coverages, heating rate 0.7 K/s and 1.0 K/s, respectively. Curves vertically offset for clarity. Reprinted with permission from Ref. [87] © 2004 APS. (c): Adsorption geometry of benzene and naphthalene on Gr as predicted by vdW-DFT. (d): Energy vs. adsorption height for naphthalene on Gr as calculated in vdW-DFT, yellow box gives the range of experimental values of the binding energy. (c) and (d) are reprinted with permission from Ref. [88], © 2006 APS.

from the slight inhomogeneity of the binding of Gr/Ir(111) in different moiré regions, coupled to the compressive strain in graphene due to the differential thermal expansion. The Gr is locally n doped in the Eu-intercalated regions, but only hardly doped in the non-intercalated regions [86].

2.5 Adsorption of benzene and naphthalene on graphite

As a model case of π-π interaction, the adsorption of benzene and naphthalene on graphite has been studied by several authors using LEED [89, 90], TDS [87], DFT [88], and STM [91].

In LEED, both benzene and naphthalene form well-ordered superstructures also at submonolayer coverages, implying an attractive interaction of the molecules, although the behavior for naphthalene is rather complex [90]. Also for both molecules, the superstructures in LEED disappear and reappear reversibly upon heating and cooling through a critical temperature. This suggests that the molecular islands melt before desorption and the molecules thus desorb from a

fluid on-surface phase, such that the influence of the intermolecular interaction on the desorption process is rather weak.

In thermal desorption experiments as shown in Fig. 2.8 (a) and (b), the desorption kinetics are first order for both benzene and naphthalene, although the transition between monolayer and multilayer behavior is more complex for benzene. First-order kinetics are expected for individually desorbing molecules, in line with the results from LEED.

In DFT calculations, the adsorption geometry of the molecules is found to be as shown in Fig. 2.8 (c). It is analogous to the stacking of graphene layers in graphite. Inclusion of the vdW interaction via the Langreth-Lundqvist vdW-DF method [92] yields a curve for energy vs. separation as shown in Fig. 2.8 (d), here exemplarily only for naphthalene. The benzene curve is the same except for the different energy scale. The curve implies that the barrier for the desorption process is identical to the binding energy of the molecule. By calculations using the vdW-DF method, a binding energy in good agreement with the experimental value is found.

2.6 Organometallic sandwich complexes and nanowires

The prototypical organometallic sandwich compound is ferrocene, and the discovery of its structure was a milestone of organometallic chemistry [93]. It consists of one Fe atom sandwiched between two cyclopentadienyl (Cp) rings (C_5H_5=Cp). Fischer and Wilkinson suggested ferrocene's structure and were awarded the 1973 Nobel prize in chemistry "for their pioneering work performed independently on the chemistry of the organometallic, so-called sandwich compounds."

The neutral cyclopentadienyl C_5H_5 is a radical, because the total number of valence electrons ($5 \cdot 4 + 5 \cdot 1 = 25$) is odd. However, adding one electron from a ligand, an aromatic configuration can be obtained: Each of the C atoms contributes one electron to the π system, and one from the ligand to yield 6 in total, which satisfies the Hückel rule for aromaticity (π electron number of the form $2 + 4n$). Thus, Cp acts as an anion.

For ferrocene, the high stability also rests on the number of 18 valence electrons: 5 each from the π systems of the two Cp rings, and 8 from the Fe atom. The number 18 is magic because it is of the form $2n^2$, just like the atomic numbers of the noble gas atoms. The number of 18 valence electrons can also be obtained by combining Cr with two benzene (Bz) rings, and the compound $CrBz_2$ is also very stable. In these compounds, Cr and Bz are both formally zerovalent. Substituting Cr with V yields VBz_2, a 17 electron system, which is paramagnetic with one unpaired spin [94].

It is natural to expand on the idea of sandwich compounds by alternately stacking more metal atoms and aromatic rings on top of each other. This gives a multidecker sandwich compound, and in the limiting case an organometallic sandwich molecular wire (SMW), or simply nanowire. An alkali metal can donate one electron to one Cp ring, and compounds such as CsCp indeed form

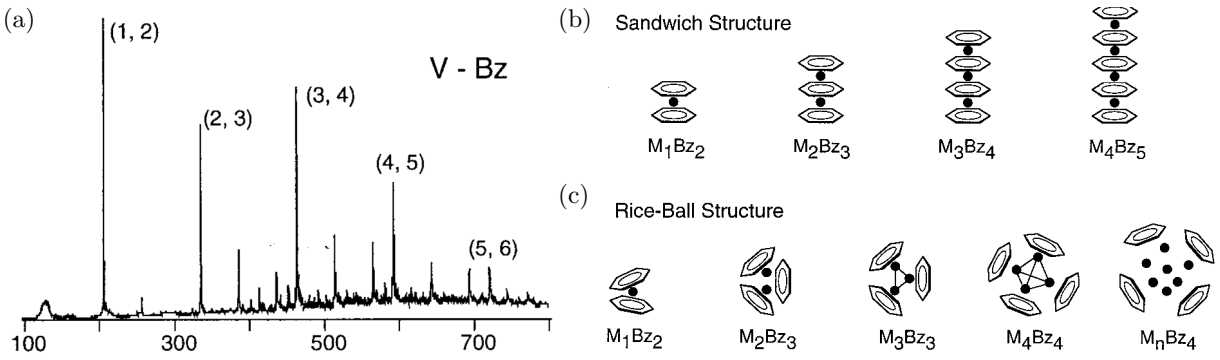

Figure 2.9: (a): Time-of-flight mass spectrum of the gas-phase reaction of V with Bz, peaks are labeled with (n,m) according to V_nBz_m. (b): Model of multidecker full-sandwich structures. (c): Model of riceball structures formed for $3d$ metals heavier than Cr. All subfigures reproduced with permission from Ref. [96] ACS 1999.

bulk crystals with a structure made of parallel SMWs [95]. However, no interesting electronic magnetic properties are expected in CsCp. In contrast, the VBz SMW has been predicted to be a ferromagnetic half-metal, i.e., metallic for one spin direction, and semiconducting for the other [37].

Some SMWs can be produced by synthesis in solution [95, 97], however, a larger number has been produced by the gas-phase reaction of laser-evaporated metal atoms with the ligands in a noble gas stream, chiefly by the group of Nakajima [96]. The complexes could be characterized by time-of-flight mass spectrometry for composition, photoemission spectroscopy for electronic structure, and Stern-Gerlach method (beam deflection by an inhomogeneous magnetic field) for the magnetic moments.

Figure 2.9 (a) shows a mass spectrum obtained from the reaction of the V with Bz. The strongest peaks are at the masses corresponding to complexes with composition V_nBz_m with $m = n + 1$, which are called full-sandwich complexes due to their termination by a Bz molecule on both sides as shown in Fig. 2.9 (b). The sandwich structure with Bz is preferred only for the lighter $3d$ metals, up to Cr, while the heavier $3d$ prefer to form so-called "riceball" structures as depicted in Fig. 2.9 (c), where a cluster of metal atoms is surrounded by Bz molecules [96].

In contrast to Cp, which requires one additional electron to become aromatic, and Bz, which requires none, the compound cyclooctatetraene (Cot = C_8H_8) requires two additional electrons to fulfill the Hückel rule with 10 electrons. Therefore, Cot can form SMWs with sufficiently electropositive, divalent metals. The rare-earth metals are magnetically interesting and give away their $6s^2$ electrons easily. While they are mostly trivalent, some of them occur divalent as well. Among the magnetically interesting divalent rare-earth ions, Eu^{2+} is by far the most stable, due to the half-filled $4f$ shell and the resulting maximum stabilization from Hund's rule energy of the parallel electron spins. The EuCot SMW was predicted to be a ferromagnetic semiconductor.

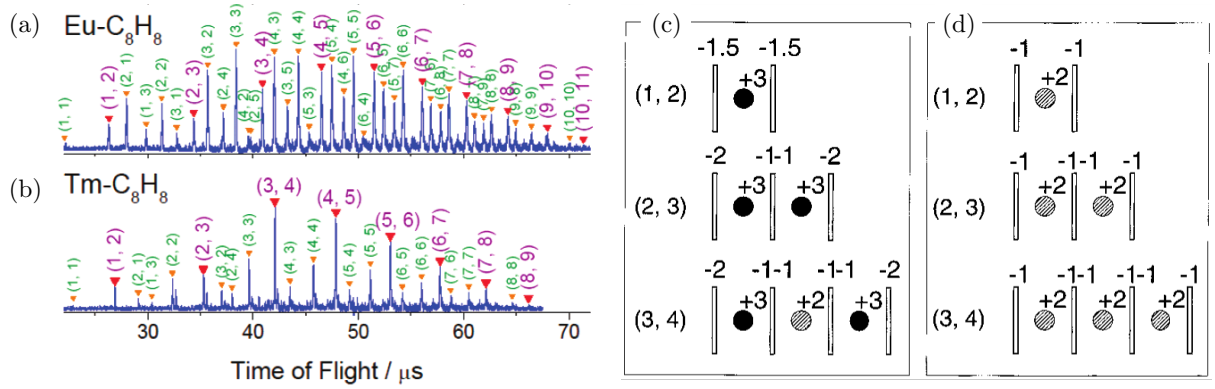

Figure 2.10: (a), (b): Time-of-flight mass spectra of products of the reaction of Cot with Eu and Tm, respectively. Peaks are labeled (m,n) corresponding to $(\mathrm{Eu, Tm})_n$, Cot_m. (c), (d): Model of the oxidation states for (c) most lanthanides (d) Eu and Yb. (a), (b): Reproduced with permission from Ref. [98], © ACS 2008. (c), (d): Reproduced with permission Ref. [96] ACS 1999.

Figure 2.10 (a) and (b) show mass spectra resulting from the reaction of Cot with Eu and Tm, respectively (the choice of Tm is motivated in section 7.3). As in the case of VBz, the main peaks can be indexed with $n = m \pm 1$. However, additional peaks in between resulted in this experiment, because the low reaction temperature facilitated the attachment of weakly-bound, physisorbed molecules on the wires. Furthermore obvious from the comparison of Fig. 2.10 (a, b) with Fig. 2.9 (a) is the higher intensity for longer wires in the former, up to $n = 10$ in this measurement, and beyond $n = 20$ elsewhere for EuCot [99].

Figure 2.10 (c) and (d) show a model of the oxidation states of the lanthanides in finite-length wires with Cot. The model has been developed based on photoemission spectroscopy, experiments with attachment of Na atoms, and electron affinities. Inside a wire, there is one Cot ring for every Ln atom, such that the oxidation state is 2+. However, at a Cot-terminated wire end, most lanthanides will be oxidized to the 3+ oxidation state, so that Cot can assume its favorable -2 state also at the wire end. Only the lanthanides Eu and Yb, which have a particularly stable $4f$ electron configuration, which is half-full and full, respectively, do not give an oxidation state higher than +2 in reaction with Cot.

Stern-Gerlach-type experiments yield magnetic moments of VBz [100] and EuCot [98] which scale linearly with the number of metal atoms in the complex, while for TmCot, the suppression of magnetic moments in larger clusters was suggested to be the result of antiferromagnetic interactions [98].

Chapter 3

Experimental methods

The experimental methods used in this thesis are scanning tunneling microscopy (STM), low-energy electron diffraction (LEED), thermal desorption spectroscopy (TDS), x-ray absorption spectroscopy (XAS), and x-ray magnetic circular dichroism (XMCD).

3.1 Scanning tunneling microscopy

Scanning tunneling microscopy is capable of resolving atoms, and the STM's developers Gerd Binnig and Heinrich Rohrer were awarded the 1986 Nobel Prize for the development of this instrument, the prize being shared with Ernst Ruska, the developer of the electron microscope, another technique that has advanced to atomic resolution. Since then, STM has become ubiquitous and has been reviewed often, see for example Ref. [101].

In an STM, an electrically conducting sample surface is imaged by a conducting tip, making use of the quantum mechanical tunneling of electrons through a vacuum gap between tip and sample. A bias voltage U is applied to obtain a net current. When the tip is held at a distance of about 1 nm above the surface, the tunneling effect leads to a current I that is exponentially dependent on the distance d between tip and sample. As the height of the tunneling barrier is given by the work functions of tip and sample, the decay length into the barrier is on the order of the wavelength of electrons with that kinetic energy. Typically, a change of the tip-sample separation 1 Å leads to an order of magnitude difference in the conductivity, giving STM a high vertical sensitivity. The height of the tip (Z) and its lateral position (X, Y) over the sample can be controlled on the sub-Å scale using piezo elements. In the most commonly employed constant-current mode, a feedback loop regulates the voltage on the Z piezo to minimize the deviation between the measured tunneling current and a current setpoint, the latter controlled by the operator. The setpoint current is typically in the range of pA to nA. The lateral position (X, Y) is scanned line-by-line while the feedback loop output Z is recorded to obtain a topographic image.

STM is generally not sensitive to the positions of the atomic nuclei, but rather to the local density of states in the energy interval between the Fermi level and the applied bias voltage. Furthermore, it is just as sensitive to the properties of the tip as it is to those of the surface. Mathematically, this is expressed as the tunneling current resulting from the convolution of the space- and energy-dependent density of states of the tip ρ_T and that of the sample ρ_S according to

$$I \sim \int_{-\infty}^{+\infty} |M|^2 \left[f(E - eU) - f(E) \right] \rho_S(E_f - eU) \rho_T(E_f)$$

where M is the tunneling matrix element, $f(E)$ is the Fermi function describing the occupation of levels at a finite temperature, and e the elementary charge.

Because STM probes the local density of states many Å away from the atoms, the observed weight of the electronic states can differ rather strongly from that inside the material, as electronic states vary in their asymptotic decay towards the vacuum. For example, states with high parallel momentum, such as those at the K points of graphene, decay faster than those near the Γ point [102], and their rapid decay often makes localized $4f$ states inaccessible to STM [103].

3.2 Low-energy electron diffraction

Low-energy electron diffraction (LEED) from a surface was the first proof of the wave nature of electrons [104]. A recent introduction to the LEED technique in surface science is given in Ref. [105].

In a nowadays typical rear-view hemispherical LEED analyzer, a beam of monochromatic low-energy electrons (tunable, typically $E = 10$ up to 1000 V) impinges on the sample surface, almost always in or close to normal incidence. Because of the small penetration depth of electrons of the order of a few Å (also depending on the energy), the method is highly surface sensitive. From the backscattered electrons, only the elastically scattered part is filtered out by a hemispherical retarding grid. The electrons are converted into visible light by acceleration with a high voltage of typically around 5 kV onto a fluorescent screen. Crystalline order in the sample plane leads to a diffraction pattern on the screen.

At the surface, the translational symmetry normal to the surface is always broken, and therefore, the electron momentum in this direction is not preserved. This relaxes the Laue condition from the three-dimensional case, and as a result, diffracted beams have non-vanishing intensity at almost all energies also on a single-crystal surface. This contrasts to x-ray diffraction, where a monochromatic x-ray beam impinging on a single crystal almost always does not give diffracted beams, and either polychromatic x-rays (Laue method), polycrystalline samples (Debye-Scherrer method), or four-circle instruments (to also control the orientation of the crystal axes with respect to the beam) are employed.

For a normally incident primary electron beam, the zero-order diffracted beam is reflected

back into the electron gun, which is mounted in the center of the screen. The other diffracted beams move toward the center of the screen with increasing energy as the electron wavelength becomes shorter and the diffraction angles smaller.

In a conventional LEED instrument, the primary electron beam current is typically of the order of a few μA. This current is sufficient to damage sensitive structures on the sample, such as weakly bound adsorbates or molecular systems. In such cases, microchannel plate (MCP) LEED instruments should be used, which feature either a single MCP or a chevron double MCP between the retarding grid and the screen to amplify the diffracted beams. This allows to reduce the primary beam current, down to a few nA for single MCP, and to below 100 pA with a double MCP. Because the MCPs can only be manufactured as flat discs, and not as hemispheres, the diffraction pattern in such instruments is geometrically distorted.

3.3 Thermal desorption spectroscopy

Thermal desorption spectroscopy is a very common method in surface science [106], and is also called temperature-programmed desorption. Typically, a sample surface with a coverage θ of adsorbates is heated at a constant ramp rate β, while a mass spectrometer above the surface measures the intensity at the mass of the adsorbate. The desorption process is described by the Wigner-Polanyi equation

$$-\frac{d\theta}{dt} = \theta^n \nu e^{-\frac{E_A}{k_B T}} \tag{3.1}$$

with n the order of the desorption process, ν the attempt frequency, and E_A the activation energy, which is equal to the binding energy for non-activated adsorption. The attempt frequency ν is of the order of the phonon frequency in simple cases. Note that T varies with time as it is ramped. Furthermore, ν and E_A may change with the coverage.

The order of the desorption process n can take various values: In case of the desorption of a thick film, the behavior is like the evaporation of a bulk sample, and it is always $n = 0$, the Wigner-Polanyi equation being equivalent to an equation for the vapor pressure. In the case of a monolayer or less of non-interacting adsorbates, which desorb individually and independently from one another, it is $n = 1$. For adsorbates that exist on the surface as monomers but have to desorb as dimers, e.g., chemisorbed oxygen atoms desorbing as O_2 molecules, it is $n = 2$. And when the rate-limiting step is the desorption of molecules from the one-dimensional edge of two-dimensional islands existing on the surface, it is $n = \frac{1}{2}$.

The equation 3.1 is a differential equation without closed form solutions for most n. For $n = 1$, the temperature $T_{\max}$ where the desorption rate peaks can be approximated with the Redhead formula:

$$E_A = k_B T_{\max} \left[\ln\left(\frac{\nu T_{\max}}{\beta} \right) - 3.64 \right] \tag{3.2}$$

3.4 X-ray absorption spectroscopy

The advent of intense, tunable, and polarized synchrotron-based x-ray sources has created entirely new experimental methods and corresponding fields of research in the last decades. In x-ray absorption spectroscopy (XAS), one looks at optically excited transitions of electrons from a core-shell into the unoccupied valence states. In a simple one-electron picture, the core state is a source of photoelectrons, which are then used to probe the valence states. Dipole-allowed transitions are the strongest and thus most commonly investigated, i.e., the difference in the angular momentum quantum number of the core and valence shell is $\Delta L = \pm 1$.

To measure the absorption, various modes are employed, such as transmission, fluorescence yield, or total electron yield (TEY). In this thesis, TEY is used exclusively, due to its high surface sensitivity. In the soft x-ray region, the decay of the core-level photo-hole proceeds predominantly via an Auger process, which leads to emission of electrons from the sample surface into the vacuum, both directly, and via generation of secondary electrons. The charge lost from the sample reaches ground via the metallic inner walls of the experimental apparatus. The sample is virtually grounded via a current amplifier, and the measured current is the signal. The method is surface sensitive because the escape path length of electrons up to the keV range is typically in the nanometer range. The penetration depth of the x-rays must be large compared to the electron escape depth, or otherwise, a saturation behavior is observed, which distorts the peak shape and leads to errors in the analysis [107, 108].

The processes dominating the line shapes in XAS are very different depending on the elements and transitions considered: In the $1s$ to $2p$ transition (K edge) of graphite, the line shape can be related to the density of states of the p-derived valence bands and their symmetry [109]. In contrast, in the $2p$ to $3d$ transitions of the first-row transition metals, the interaction of the core hole with the valence electrons additionally leads to a so-called multiplet structure, which is however generally still convoluted with the density of states in the valence band. The multiplet structure in the $2p$ to $3d$ transitions is thus less apparent in metallic films and becomes clearest for single $3d$ atoms [110]. In contrast in the rare-earth elements, because of the small bandwidth of the $4f$ level, the $3d$ to $4f$ spectral shape is generally dominated by the multiplet structure. There, the line shape depends almost exclusively on the number of $4f$ electrons in the ground state.

3.5 X-ray magnetic dichroism

Magnetic dichroism is the difference in optical properties, such as absorption, for differently polarized light in magnetic samples. Circular magnetic dichroism occurs for circularly-polarized light between helicities parallel and antiparallel to the magnetization, while magnetic linear dichroism occurs for linearly-polarized light between polarizations parallel and perpendicular to

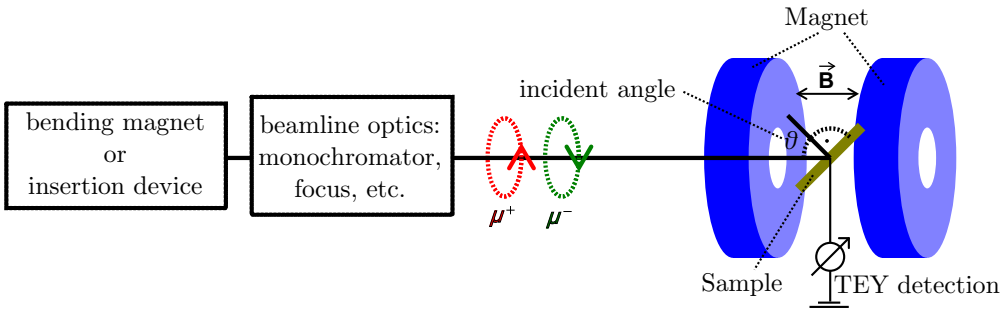

Figure 3.1: Sketch of the experimental setup for the XMCD measurement. Partially adapted from Ref. [111], © 2014 Elsevier.

magnetization. The unique capability of x-ray dichroism compared to other methods of magnetic characterization are (1) the elemental sensitivity, which arises from the characteristic core levels for every element, and (2) the ability to assess spin- and orbital moment separately. Note that in this section, we review only circular dichroism, as the linear one was strong in only one element (Tm) investigated in this thesis, and is thus discussed in the corresponding section 7.6.

The most commonly investigated elements are those of the $3d$ and $4f$ series. There, the dipole-allowed transitions are $2p$ to $3d$ for the $3d$ transition metals and $3d$ to $4f$ for the rare-earth metals. Due to spin-orbit coupling, the core level is split into $2p_{3/2}$, $2p_{1/2}$ and $3d_{5/2}$, $3d_{3/2}$, respectively. The spin-orbit interaction is so strong that the lines are generally well separated in energy. The absorption edges resulting from the $2p_{3/2}$ and $2p_{1/2}$ level are also referred to as L_3 and L_2, while those from the $3d_{5/2}$ and $3d_{3/2}$ are also referred to as M_5 and M_4. These edges lie in the soft x-ray range: In the $3d$ elements, the $L_{3,2}$ start at 399 eV (for Sc) and go up to 950 eV (for Cu), while in the $4f$ elements, the $M_{5,4}$ start at 836 eV (for La) and go up to 1576 eV (for Yb). The absorption cross-sections are high enough that a sensitivity down to 1 % of a monolayer can be obtained with TEY. In this thesis, only soft x-rays were used; hard x-rays require different measurement setups, but permit other elements, e.g., at the $L_{3,2}$ edge of Pt (around 12 keV) in FePt $L1_0$ [112].

3.5.1 X-ray magnetic circular dichroism

There are a number of reviews on x-ray magnetic circular dichroism (XMCD) [111, 114–116]. A typical measurement setup for XMCD measurements is shown in Fig. 3.1. The circularly-polarized, monochromatic x-ray beam impinges on the sample under an incident angle θ to the surface normal. Varying θ allows access to the magnetic anisotropy. The sample is located in a magnet, where the magnetic field is always parallel or antiparallel to the incoming light.

Explaining the XMCD effect is simplest in the so-called two-step model, which is sketched for the $3d$ transition metal case in Fig. 3.2 (a). The first step is the excitation of an electron from the core level. Because of the spin-orbit coupling in the core level, the excited electrons have a partial spin polarization, which depends on the helicity of the incoming light: From

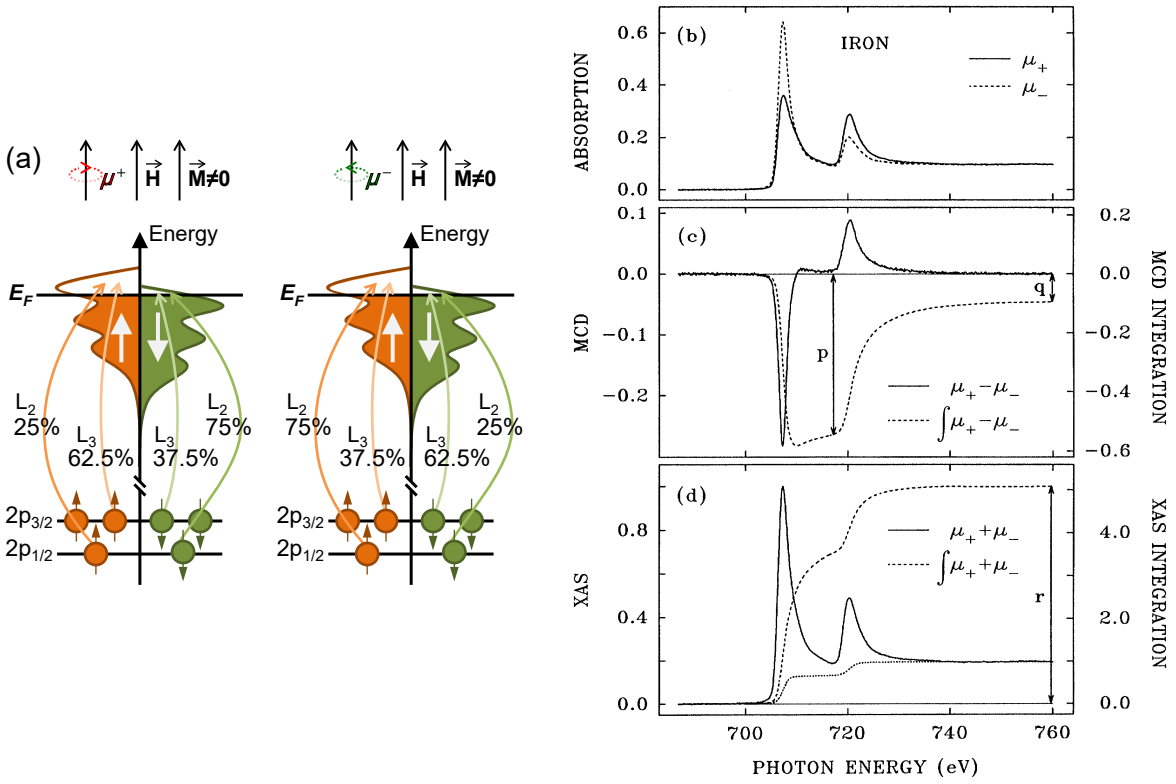

Figure 3.2: (a) Diagram of the two-step picture of XMCD, explanation see text. Reprinted with permission from Ref. [111], © 2014 Elsevier. (b) XAS at the Fe $L_{2,3}$ for right (μ^+) and left (μ^-) circular polarization. (c) Difference spectrum, the XMCD (solid line) and integrated XMCD (dotted line) to obtain p and q. (d) Polarization-averaged XAS with double step background and integral r. (b) to (d) reprinted with permission from Chen et al. [113], © 1995 APS.

the $2p_{3/2}$ level (L_3 edge), x-rays with positive helicity excite 62.5% spin up electrons and those with negative helicity excite 37.5% spin-up electrons, while from the $2p_{1/2}$ level (L_2 edge), these numbers are 25% and 75%, respectively. The second step is then for this excited electron to find a hole in the magnetic $3d$ valence shell. If the valence shell carries a spin- or orbital moment, there will be an imbalance in the number of holes for the different spin and orbital moment directions, and the absorption cross-section will change with the magnetization.

In Fig. 3.2 (b) to (d), a typical XMCD measurement is shown as obtained at the $L_{3,2}$ edges of a film of metallic Fe. The absorption spectra μ^+, μ^- are acquired for opposite helicities of the incoming light (or, equivalently, opposite magnetization directions). The XMCD is then calculated as the difference spectrum,

$$\mu^{XMCD} = \mu^+ - \mu^- \tag{3.3}$$

and exhibits opposite sign at the L_3 and L_2 edges due to the opposite predominant spin polarization of the photoelectrons excited from the two corelevels.

3.5.2 XMCD sum rules

This subsection reproduces material from the master thesis of S. Kraus [117].

The XMCD sum rules developed by Thole et al. [118] and Carra et al. [119] relate the integrated intensities at the two spin-orbit split edges to the expectation values of the spin and orbital moment.

We define the polarization-averaged XAS spectrum as

$$\mu^{average} = \frac{1}{3}(\mu^+ + \mu^- + \mu^0) \tag{3.4}$$

where μ^0 is the isotropic spectrum. μ^0 is not commonly measured and so one usually takes instead

$$\mu^0 = \frac{1}{2}(\mu^+ + \mu^-) \tag{3.5}$$

although this is only valid when linear magnetic dichroism is negligible. For analysis, the areas under the different edges have to be evaluated. We define the integral over the first absorption edge of the XMCD spectrum as

$$p = \int_{j_+} dE\,(\mu^+ - \mu^-), \tag{3.6}$$

the integral over both edges of the XMCD spectrum as

$$q = \int_{j_+ + j_-} dE\,(\mu^+ - \mu^-) \tag{3.7}$$

and the integral over both edges of the averaged XAS spectrum as

$$r = \int_{j_+ + j_-} dE\,\frac{1}{3}(\mu^+ + \mu^- + \mu^0). \tag{3.8}$$

For the $3d$ and $4f$ elements, $j_{+/-}$ correspond to $\mathrm{L}_{3/2}$ and $\mathrm{M}_{5/4}$, respectively.

In Ref. [119], Carra et al. give the sum rules in the most general case. To avoid confusion every symbol used in the formulas is listed in Table 3.1.

The expectation value of the orbital momentum operator satisfies eq. 3.9.

$$\frac{q}{3r} = \frac{1}{2}\frac{l(l+1)+2-c(c+1)}{l(l+1)(4l+2-n)} \cdot \langle L_z \rangle \tag{3.9}$$

The expectation values of the spin and magnetic dipole operator satisfy eq. 3.10.

$$\begin{aligned} \frac{p-(c+1)/c(q-p)}{3r} &= \frac{l(l+1)+2-c(c+1)}{3c(4l+2-n))} \cdot \langle S_z \rangle + \dots \\ \cdots + \frac{l(l+1)[l(l+1)+2c(c+1)+4]-3(c-1)^2(c+2)^2}{6lc(l+1)(4l+2-n)} &\cdot \langle T_z \rangle \end{aligned} \tag{3.10}$$

$\langle S_z \rangle$	Expectation value of spin momentum operator
$\langle L_z \rangle$	Expectation value of orbital momentum operator
$\langle T_z \rangle$	Expectation value of magnetic dipole operator
S	Total spin quantum number
L	Total orbital momentum quantum number
J	Total angular momentum quantum number
n	Number of electrons in magnetic shell
n_h	Number of holes in magnetic shell
l	Orbital quantum number of magnetic shell
c	Orbital quantum number of absorption shell
$\langle M \rangle$	Expectation value of the magnetic quantum number, $\lvert M \rvert \leq J$

Table 3.1: List of symbols used in the formulas for the XMCD sum rules. Reproduced from Ref. [117].

This is the most general formulation of both equations and they can be used for different absorption edges and magnetic shells. In this work, detailed spectral analysis was conducted only on the investigated $4f$ systems and more specifically Eu^{2+} ($4f^7$) and Tm^{3+} ($4f^{12}$). All relevant values for both of these systems are listed in Table 3.2.

	n	n_h	l	c	S	L	J
Eu^{2+}	7	7	3	2	$^7/_2$	0	$^7/_2$
Tm^{3+}	12	2	3	2	1	5	6

Table 3.2: Required values for Eu^{2+} and Tm^{3+}. Reproduced from Ref. [117].

With the number of holes $n_h = 2(2l+1) - n$ and the relations between expectation values and magnetic moments in eq. 3.11

$$m_l = \mu_B \langle L_z \rangle \,, \quad m_s = 2\mu_B \langle S_z \rangle \tag{3.11}$$

where μ_B is the Bohr magneton, this leaves us with eq. 3.12 and 3.13. These two equations hold in general for the $4f$ elements with the only specific parameters being n_h and $\langle T_z \rangle$.

$$\frac{q}{r} = \frac{\langle L_z \rangle}{n_h} = \frac{m_L}{n_h \mu_B} \tag{3.12}$$

$$\frac{5p - 3q}{4r} = \frac{\langle S_z \rangle}{n_h} + 3\frac{\langle T_z \rangle}{n_h} = \frac{m_s}{n_h 2\mu_B} + 3\frac{\langle T_z \rangle}{n_h} \tag{3.13}$$

According to Ref. [119], $\langle T_z \rangle$ can be calculated analytically for the rare-earth ions as

$$\langle T_z \rangle = \langle M \rangle (l - n + {}^1\!/_2) \frac{3(S-J)^2(S+J+1)^2 - L(L+1)[L(L+1) + 2S(S+1) + 2J(J+1)]}{2(2l+3)(2l-1)(2L-1)SJ(J+1)} \quad (3.14)$$

with $\langle M \rangle$ the expectation value of the magnetic quantum number, which in saturation is equal to J. As can easily be seen from eq. 3.14 the dipolar term equals zero in the case of Eu^{2+} ($L = 0$, $S = {}^7\!/_2$, $J = {}^7\!/_2$) giving direct relations between magnetic moments and measured spectra. In the case of Tm^{3+} ($L = 5$, $S = 1$, $J = 6$), we obtain the saturation value $T_z = -0.45$ from the formula. Teramura et al. [120] have calculated corrections to this value with more elaborate theory and give $T_z = -0.407$ for Tm^{3+}. According to their calculations, the deviations of formula 3.14 become large only for the left half of the rare-earth series.

Not only the spin and orbital moments m_S and m_L are of interest, but also the total magnetic moment m_{tot}. When the system is in saturation the expectation values are given by

$$\langle S_z \rangle = S; \quad \langle L_z \rangle = L \quad (3.15)$$

so that the total moment can be calculated as

$$m_{tot} = g_J \mu_B \cdot J = g_J \mu_B \cdot (S + L) = g_J \mu_B \cdot \big(\langle S_z \rangle + \langle L_z \rangle\big) = g_J \cdot \Big(\frac{m_s}{2} + m_l\Big) \quad (3.16)$$

with $g_J = {}^7\!/_6$ for $4f^{12}$, and $g_J = 2$ for $4f^7$.

3.5.3 XMCD and magnetization curves

Magnetization curves can be measured in XMCD by recording field-dependently the signal at the maximum of the XMCD and the signal in the pre-edge region for both polarizations. Measuring the field-dependent pre-edge signal is necessary because the detection efficiency in TEY strongly changes with the magnetic field, which forces the electrons in the vacuum onto spiral orbits. The magnetization curve is then calculated by (3.17)

$$M \quad \sim \quad \frac{P_+/p_+ - P_-/p_-}{(P_+/p_+ + P_-/p_-) - 2} \quad (3.17)$$

Here, we used the intensities at the main peak position P and in the pre-edge region p for positive (+) and negative (−) helicity. Note that this formula can be invalidated when $\mu^0 \neq {}^1\!/_2(\mu^+ + \mu^-)$.

Chapter 4

Experimental setups and procedures

The experimental setups used in this thesis can be divided into home labs and beamlines.

4.1 Home labs

At home, we used the UHV systems Athene and TuMA II to conduct STM, LEED, and TDS measurements. The Athene system was described by Förster [121], while the TuMA II system was described by Standop [122]. The systems are similar.

Briefly, the Ir single crystal sample is mounted by clamping between tungsten leaf springs and sapphire balls. Samples can be transferred to air without venting the chamber only in Athene. In TuMA II, the sample is fixed on the manipulator. A filament for electron beam heating is underneath the sample. Type K thermocouples (nickel-based alloys) are attached directly to the sample. The direct contact with the thermocouple allows precise temperature measurements, rapid adjustments and long-term stability by a temperature controller with feedback loop. Precision of the thermocouple suffers only at the lowest temperatures, i.e., below liquid nitrogen temperatures, where no precise knowledge of the sample temperature was required in this thesis. On the other extreme, the melting point of the thermocouple limits the highest possible temperature to $< 1600\,\mathrm{K}$. For the Ir(110) crystal, the effort to install the thermocouple was evaded by using an optical pyrometer focused onto the polished sample surface. The sample can be cooled to $20\,\mathrm{K}$ (TuMA II) or $\approx 35\,\mathrm{K}$ (Athene) with liquid helium flow cooling, but measurements were conducted at room temperature whenever possible. Both systems are single-chamber designs, i.e., from preparation to analysis no sample transfer through a gate valve is necessary. Also, both systems use beetle-type STMs with PtIr tips, where the tips are not transferable and stay in the chamber for years. For LEED, conventional Specs rear-view optics are used on both systems. On TuMA II, LEED optics were only installed after the experiments on vdW molecule adsorption, Gr on Ni films, EuCot and VBz had been concluded. TDS could be conducted only in TuMA II. A standard quadrupole mass spectrometer with mass range up to $200\,\mathrm{e/u}$ was used.

A gold-plated inverse funnel is used to guide the desorbing species into the spectrometer. To be able to measure larger molecules, a new triple quadrupole spectrometer with mass range up to 500 e/u was installed later, but was not used to acquire data for this thesis. For TDS, the temperature controller is set to a constant heating ramp rate, e.g., 1 K/s. Both the LEED optics and the new mass spectrometer at TuMA II were installed by J. Hall.

4.2 Beamlines and endstations

XAS and XMCD measurements were conducted at synchrotron beamlines. Sample preparations were always performed at the beamline endstation, and the vacuum was never broken between sample preparation and XMCD measurements. Procedures were adapted to be as in the home labs as far as possible. There were no gas inlet tubes available at the beamline endstations, so that chamber pressures during gas dosing were correspondingly increased. Thermocouples for sample temperature measurement were also either unavailable or not attached directly at the sample. Therefore, highly temperature-sensitive preparations were avoided.

Eu-intercalated Gr on Ir(111) was investigated at the ESRF's ID08 beamline in 2012 and at the ESRF's ID32 beamline in 2016. In both cases, characterization was performed by LEED only. Eu-intercalated Gr on nickel and cobalt thin films was investigated in two beamtimes at the pm3 beamline of BESSY II, using the mobile preparation and XMCD chamber of the group of H. Wende. The EuCot wires were investigated at the VEKMAG endstation attached to the pm2 beamline of BESSY II in May 2016 and at the ID32 beamtime in December 2016. At the VEKMAG endstation, samples were characterized by MCP-LEED before and after measurements. At ID32, all the EuCot samples were investigated by MCP-LEED only after the measurements to avoid beam damage from LEED. Some samples with EuCot were also characterized by STM. Furthermore measured at ID32 were the TmCot coffee beans, with the preparation quality confirmed by STM, because a LEED pattern could not be observed for this phase. No indications of sample degradation were seen except from the electron gun of the LEED.

ID08 and ID32 are undulator-based while pm2 and pm3 are bending-magnet beamlines. The endstation at ID32 is also described in Ref. [123]. ID08, ID32, and VEKMAG are equipped with superconducting magnets allowing fields of 5, 8, and 9 T, respectively, while the Wende group's chamber is equipped with a copper coil magnet where 35 mT was the maximum field used. In all measurements, the magnetic field is parallel to the incoming beam, but the angle θ between the surface normal and the beam direction is varied to gain information on the anisotropy of the system. Spectra were always taken for both polarizations of incoming light and both external field directions, to avoid non-magnetic artifacts in the XMCD, yet for brevity, we refer to X-ray helicity parallel (antiparallel) to the external magnetic field only as positive (negative) helicity or polarization. At different beamlines, the switching sequence for the magnetic field and the polarization of the light were different, depending on whether the switching of the magnet or of

the light polarization were faster. To record magnetization loops, the field was changed in small steps. For each field step, the signal at the energy of the maximum of the XMCD is recorded and then normalized to the field-dependent pre-edge value. This procedure, too, was conducted for both helicities.

4.3 Sample preparation procedures

The Ir single crystals were cleaned by sputtering with noble gas ions (Ar, Kr, or Xe) at energies in the range of 1 to 5 keV. Upon first preparation of a newly polished Ir(111) crystal, a few hundred nanometer of the surface were sputtered off in order to remove the near-surface layer, which is not well-oriented because of the polishing procedure. The sharpness of the LEED spots was used as an indicator of the surface quality at this stage. For the newly bought Ir(110) crystal, less initial sputtering seemed necessary, possibly a result of the higher mobility on the more open (110) surface. When a crystal was exposed to air, typically a few tens of nanometer were sputtered off before the first heating in vacuum. Annealing in oxygen ("oxygen firing"), typically 1×10^{-6} mbar pressure at the sample surface for 300 s at a temperature of 1100 K, was used after exposure of a crystal to air, and occasionally when carbon contaminations seemed relevant. Mostly, however, only sputtering of a few nanometers, cycled with annealing, was used to clean the crystals between preparations. Sputtering times were increased during the experiments with thicker Ni and Co films, because these elements can dissolve in the Ir crystal and might thereby contaminate it. Annealing the Ir(111) crystal to 1500 K then results in a sharp LEED pattern, and in STM, terraces with sizes of the order of 100 nm are found.

Noteworthy is that in Athene, samples exhibited in STM a pattern of craters and mounds on a µm scale [see Fig. A.5 (b)], which results from long sputtering and annealing at too low temperatures. In contrast, samples in TuMA II always had regularly spaced step edges with a well defined step-up direction on a µm scale. In Athene, sputtering is conducted in normal incidence, while in TuMA II, sputtering is under 75° to the surface normal. Sputtering in grazing incidence might result in less crater and mound formation, but different thermocouple errors (for the annealing temperature) or different sputtered amounts could also play a role.

For Gr growth on Ir(111), we used the TPG+CVD method as described in Ref. [124]: Ethylene is adsorbed to saturation onto the clean Ir(111) surface at below 400 K, the ethylene valve is closed, the sample is annealed to $T_{\mathrm{TPG}} = 1500\,\mathrm{K}$ for a few ten seconds, then the temperature can be lowered a bit to T_{CVD} somewhere between 1150 K and 1500 K, then ethylene is dosed again with p_{CVD}, then the ethylene valve is closed, and then the sample is allowed to cool.

The ethylene dose during CVD can be chosen such that the Gr film is closed, or it can be chosen such that holes remain in the Gr layer. Holes in the Gr layer were introduced to intercalate oxygen in chapter 5. For the intercalation of metals (Eu, Tm, Yb, Ni, Co, V), holes in the Gr layer are not necessary.

For the evaporation of metals, we used three different kinds of evaporators.

For Eu, Tm, and Yb, the evaporators are effusion cells of manufacturer Dr. Eberl MBE-Komponenten. The crucibles made of Al_2O_3 are heated by thermal radiation from tantalum filaments mounted around them. A thermocouple near the crucible allows temperature control for a reproducible flux.

For Ni and Co, mini e-beam evaporators were used, of manufacturers Omicron, Focus, and Oxford Applied Research. The 2 mm-diameter rods are at a high voltage of +1 or +2 keV with respect to ground. One end of the rod is mounted to the evaporator, while the other end is heated by bombardment with electrons emitted from a tungsten filament near ground potential. The evaporation rate is controlled with an ion flux monitor, which is a metal plate at ground or somewhat negative potential mounted in line of sight of the rod. A small part of the metal vapor is ionized by the electron current, and these ions are seen on the flux monitor as a positive current in the nA range.

In electron beam evaporation, the partial ionization of the evaporant vapor in combination with the positive kV potential on the rod means that some of the evaporant atoms arrive as ions on the sample with keV energies, similar to sputtering. This can lead to markedly different outcomes in some kind of experiments, e.g., nucleation of Cu on graphite [125]. Because benzene might be destroyed by ion irradiation, V was not evaporated from an e-beam evaporator in those experiments. Instead, a filament was wound from V and W wires (0.25 mm), and the filament spot-welded onto metal support rods such that a direct current can heat the filament to the evaporation temperature. Due to its lower vapor pressure, W will not evaporate during V evaporation. The W is necessary because filaments made from V alone repeatedly failed, presumably either due to local melting or poor hot strength of V.

The molecules benzene (Bz), napthalene (Nph), cylooctatetraene (Cot), and hexafluorobenzene (Hfbz) were obtained from Sigma-Aldrich. The highest available purities were chosen: Bz and Nph were "analytical standard", Hfbz was "$\geq$ 99.5%, NMR grade" and Cot was "98% with 0.1% hydroquinone as inhibitor". They were placed in glass capillaries and attached to variable leak valves with all plumbing in contact with the molecule vapor made of glass, stainless steel, or ceramic. The air over the molecules was removed with a turbo pump. For Bz and Hfbz, pumping leads to freezing of the liquid and the material evaporates quickly so that the pumping time has to be kept short. In contrast, Nph and Cot can be pumped on for minutes without visible loss of material, and no freezing was observed for Cot (Nph is already solid at room temperature). Baking had to be used sometimes to remove Nph from the plumbing, presumably because it evaporates in the glass capillary and re-condenses elsewhere, combined with its low vapor pressure at room temperature.

Chapter 5

Tuning the van der Waals interaction of graphene with molecules via doping

This chapter is published in Ref. [126] and its supplement. The contributions of the coauthors of the article are as follows: N. Atodiresei had the idea that n doping would increase the van der Waals interaction, and thus proposed to pursue this project to the experimentalists. I conducted the STM experiments, assisted A. J. Martínez-Galera with the TDS experiments, and wrote the experimental part of the manuscript with T. Michely. A. J. Martínez-Galera measured and evaluated the TDS data. The DFT calculations were conducted by the theorists N. Atodiresei and V. Caciuc of the group of S. Blügel in Jülich and they contributed that part of the manuscript. They also developed the model with the changing polarizability as a result of more extended charge distribution. S. Schumacher and S. Standop provided initial guidance in the experimental efforts. I. Hamada enabled the theoretical calculations with his revised exchange functional. T. Wehling contributed to the theoretical discussion. S. Blügel supervised the theory work. T. Michely lead the project.

In the broad realm of sparse matter, which comprises essentially all organic and biological systems, the van der Waals interaction is central to holding the constituents together [127]. The adsorption of hydrocarbons on the basal plane of graphite or graphene (Gr) is a model system for the vdW interaction, and as such, has been the subject of a large number of both experimental and theoretical studies [87, 88, 128, 129].

One of the key properties of Gr is the wide-range tunability of its Fermi level and corresponding charge carrier concentration, either by a gate electrode [2], substitutional doping [130], adsorption [9, 131], or charge transfer from a supporting material or intercalation layer [7, 30,

78, 132]. The tunability of the Fermi level through the otherwise rigid band structure results from the material being atomically thin and having a negligible density of states near the Dirac point.

In recent years, interest has arisen in using this tunability to control adsorption: For the case of ionic adsorbates, Brar *et al.* [133] demonstrated a dependence of the ionization state of a Co adatom on the Gr Fermi level position, and Schumacher *et al.* [86] found a doping-dependent binding energy E_b of ionic adsorbates to Gr, with a shift in E_b on the order of the shift in the Fermi level induced by doping. For the case of radicals and based on *ab initio* calculations, Wehling *et al.* [134] predict doping-dependent adsorbate phase transitions for hydrogenated as well as fluorinated Gr, while Huang et al. [135] find a stronger binding of isolated H radicals for larger magnitudes of doping.

For the case of van der Waals (vdW) interaction, the effect of the Gr doping level on the binding energy of adsorbates has not yet been explored. Here, we investigate this case with the help of epitaxial Gr on Ir(111), which can be doped from the backside by intercalation of highly electropositive (*e. g.*, Cs, Eu) or -negative (*e. g.*, O) elements into its interface with the substrate, while Gr's other side remains available for the adsorption experiment itself. This strategy enables us to achieve large Fermi level shifts on the order of $\pm 1\,\mathrm{eV}$ that are otherwise accessible only by ionic liquid gating. Benzene and naphthalene are chosen as test molecules, since their binding to Gr is a pure vdW case studied previously, both experimentally [87] and theoretically [88].

The chapter is organized as follows: In section 5.1, we use doping patterns to visualize the binding energy difference of vdW adsorbates by STM on samples with molecules adsorbed on dopant-patterned Gr. Section 5.2 describes the experiments on thermal desorption of van-der-Waals type adsorbates from homogeneously doped Gr, which allows to quantitatively measure the binding energy of the molecules. Section 5.3 discusses DFT calculations that reproduce the experimentally measured binding energies, and an intuitive picture is proposed to understand the effect. Section 5.4 summarizes the results and gives an outlook on possible future research.

5.1 Visualization of binding energy differences by adsorption on graphene with patterned doping

Upon intercalation of submonolayer amounts of Eu, a complex pattern of stripes and islands of Eu-intercalated Gr (high/bright) in coexistence with non-intercalated Gr (low/dark) emerges as shown in the STM topograph in Fig. 5.1(a) and discussed in Ref. [83]. Within the intercalated patches, Eu forms a p(2×2) superstructure and leads to local doping of Gr by $-1.36\,\mathrm{eV}$, while the surrounding pristine Gr areas remain hardly doped at $0.1\,\mathrm{eV}$ [86]. No Eu is left atop Gr.

After deposition of submonolayer amounts of naphthalene at $T < 50\,\mathrm{K}$ and subsequent brief annealing to $T = 150\,\mathrm{K}$, the sample is cooled down again for STM imaging. The cor-

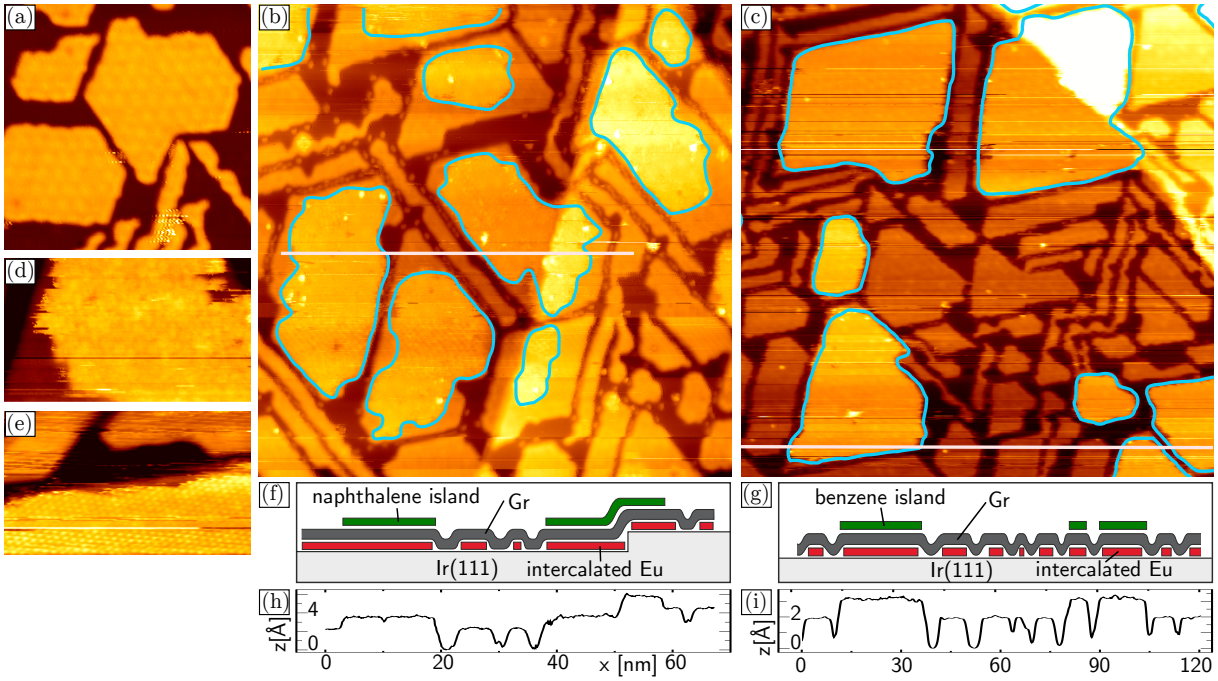

Figure 5.1: (a-e): STM topographs imaged at 35 K. (a): Gr/Ir(111) after intercalation of about half a monolayer coverage of Eu [$(39\,\mathrm{nm})^2$]. (b): Like (a), but with additional submonolayer coverage of naphthalene [$(90\,\mathrm{nm})^2$]. (c): Like (a), but with additional submonolayer coverage of benzene [$(20\,\mathrm{nm})^2$]. (d): Molecular resolution of naphthalene island [$(18 \times 11)\,\mathrm{nm}^2$]. (e): Molecular resolution of benzene island [$(20 \times 12)\,\mathrm{nm}^2$]. (f, g): Schematic cross section corresponding to profiles in (b) and (c), respectively. (h, i): Corresponding height profiles.

responding Fig. 5.1 (b) displays additional naphthalene islands (cyan encircled) only on top of Eu-intercalated patches. The profile in Fig. 5.1 (e) taken along the white line in Fig. 5.1 (b) shows that the apparent height of the Eu intercalation island itself stays unchanged at 2 Å, while the naphthalene islands have an apparent height of about 1.3 to 1.5 Å on top of the Eu-intercalated Gr. The schematic cross section of Fig. 5.1 (d) visualizes the morphology underlying the height profile. Higher-resolution imaging displayed in Fig. 5.1 (c) reveals molecular resolution of the naphthalene adsorbate layer. A $(2\sqrt{3} \times 2\sqrt{3})$R30° superstructure is formed as described for the previously studied system naphthalene on graphite [89, 91]. Our interpretation is as follows: During annealing, the molecules are highly mobile, diffusing over the surface while sensing local adsorption energy differences. As the sample is cooled down again, the arrangement is frozen and the preferential coverage of intercalated areas by molecules then directly reflects the preferential binding to these areas.

To strengthen our case for the generality of this result, we repeated the experiment exchanging naphthalene with benzene, and found qualitatively the same, as shown in Fig. 5.1 (c), (e), (g), and (i). Also here, molecular resolution in Fig. 5.1 (e) is consistent with the previously reported superstructure of benzene on graphite [$(\sqrt{7} \times \sqrt{7})$R19°, Ref. [89]]. However, in the STM

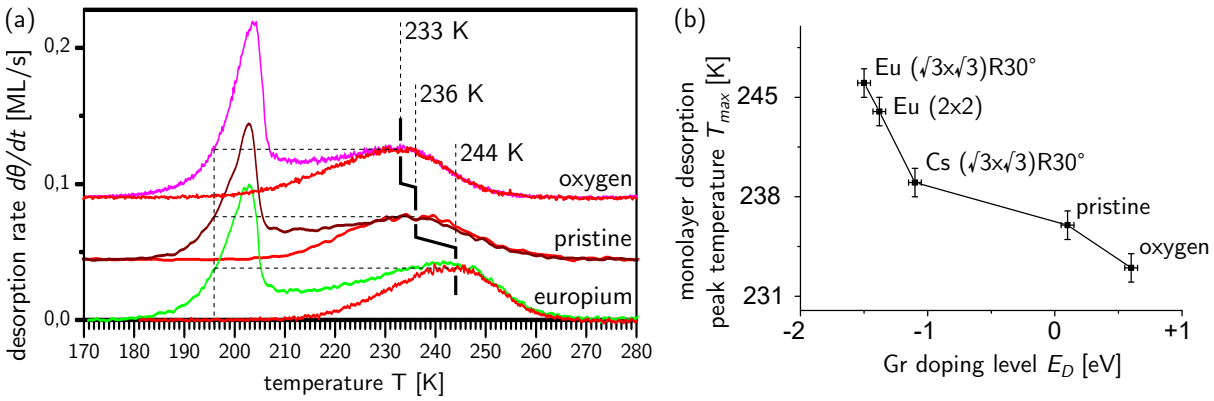

Figure 5.2: (a) Mass spectrometer signal of desorbing naphthalene ($m = 128\,\mathrm{u}$) while heating the sample with a ramp rate of 1 K/s in dependence of intercalant for the coverages of 1 ML and (2.3 ± 0.2) ML each. (b) Desorption temperature of naphthalene vs. Gr doping. Each data point corresponds to a certain intercalation structure.

topograph in Fig. 5.1 (c), another peculiarity is visible: It stands out that benzene islands fill an intercalation island always either completely or not at all. Furthermore, larger intercalation islands are predominantly covered with benzene islands (the three largest islands in the image are all covered), while smaller intercalation islands are less often and thin stripes never covered. Our interpretation is that this is a confined Ostwald ripening process: As larger islands have smaller edge-to-area ratios, they are energetically more favorable. During annealing, thermal energy is sufficient to make the molecules mobile also over non-intercalated areas. Then, larger benzene islands grow at the expense of smaller ones until the area of preferential binding on the intercalation island is completely filled.

5.2 Binding energies by thermal desorption from homogeneous substrates

To quantify the difference in E_b observed in STM, we investigated thermal desorption of naphthalene from homogeneous Gr layers, *i. e.*, which are either entirely pristine or entirely Eu p(2×2)-intercalated, rather than the partially intercalated sample employed for STM measurements of Fig. 5.1. This way, the desorption signal results from a phase-pure sample, avoiding difficulties in the interpretation of the desorption traces.

Figure 5.2 (a) shows the desorption traces for naphthalene coverages of 1 ML and (2.3 ± 0.2) ML. The low-temperature peak corresponds to desorption from the naphthalene multilayer and is zero-order as seen in the exponential leading edge followed by a sharp drop in intensity, while the high-temperature peak is almost symmetric, indicative of first-order desorption. For pristine Gr, the maximum of the monolayer peak is at $T_{\mathrm{max}} = 236\,\mathrm{K}$. These findings agree in the limits of error with those of Zacharias et al. [87] for naphthalene desorption from graphite,

	experiment			theory			
	E_D^{exp} [eV]	T_{max} [K]	E_b^{exp} [eV]	E_b^{tot}	E_b^{DFT} [eV]	E_b^{NL}	E_D^{theor}
oxygen	$+0.68$[a]	233	-0.808	-0.806	0.366	-1.172	$+0.88$
pristine Gr/Ir	$+0.10$[b]	236	-0.819	-0.852	0.556	-1.408	$+0.15$
Eu p(2×2)	-1.36[c]	244	-0.848	-0.865	0.736	-1.601	-1.21
Eu $(\sqrt{3}\times\sqrt{3})$R30°	-1.43[c]	246	-0.855				
Cs $(\sqrt{3}\times\sqrt{3})$R30°	-1.13[d]	239	-0.830				
graphite		235[e]	-0.816				0.00

[a] Ref. [17] (also Refs. [7, 137]) [b] Ref. [80] [c] Ref. [30] [d] Ref. [138] [e] Ref. [87]

Table 5.1: Doping level E_D, naphthalene desorption peak maximum T_{max} and binding energy E_b of naphthalene on pristine Gr/Ir(111), Gr with different intercalation structures, and graphite, from experiment and theory. E_b^{exp} is given assuming $\nu = 5\times10^{16}$ Hz (without error as it acts equally on all values).

a hint that the influence of the Ir substrate on the binding of naphthalene to Gr is negligible.

Upon intercalation of Eu p(2×2) (associated with a −1.36 eV Gr doping level), the monolayer peak is shifted up to 244 K, evidence for increased $|E_b|$, while the position of the multilayer peak is the same as seen in its intercept with the desorption rate at the maximum of the monolayer peak (horizontal dashed lines) at 196 K (left vertical dashed line). As the multilayer peak is not expected to shift due to the diminishing effect of the substrate with increasing molecular film thickness, its presence provides an integrated temperature calibration.

As shown in Fig. 5.2 (a), by TDS we also investigated naphthalene desorption from O-intercalated Gr, for which the monolayer T_{max} is shifted down to 233 K. This case would have been difficult to analyze by STM, as the intercalation is not regularly patterned as for the case of Eu. Also here for the thermal desorption measurements, the O intercalation of Gr was homogeneous as checked by STM (cf. Ref. [136]) both before and after the thermal desorption measurements. The 0.1 ML holes in Gr needed to intercalate O do not affect the $T_{\mathrm{max}} = 233$ K obtained, since naphthalene desorbs at significantly higher temperatures from the hole area, *i.e.*, from O-covered Ir(111).

Thermal desorption of naphthalene from two other Gr intercalation systems [Cs, Eu-$(\sqrt{3}\times\sqrt{3})$] was also measured and fits the trend. The entire TDS data set including all intercalation structures and all coverages measured is given in the appendix A.3. As all intercalation structures are associated with a different doping level (see 5.1 for references), we obtain one point for each in our plot of desorption temperature vs. doping level in Fig. 5.2 (b). While our expectation of a monotonous increase of naphthalene's desorption temperature with increasing electron transfer into Gr is confirmed, the effect seems nonlinear, regardless of whether the desorption temperature is plotted as a function of the shift of the Dirac point, or as a function of the charge transfer. Therefore, a simple functional dependence cannot be inferred from our present data.

To extract E_b from the desorption temperatures, we employed the Redhead method using the

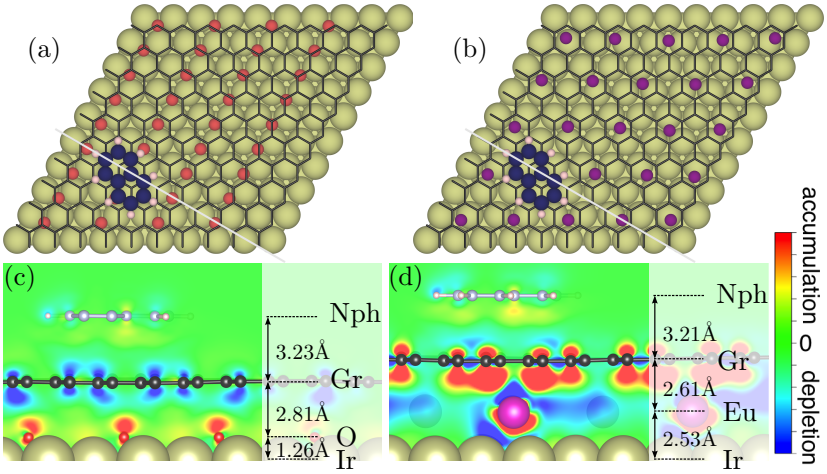

Figure 5.3: Top view of relaxed adsorption geometries of naphthalene (Nph) on (a) O-intercalated and (b) Eu-intercalated Gr on Ir(111). In (c) and (d), the corresponding plots of the charge density difference for each system are also presented. Color scale range is $\pm 5 \times 10^{-4}\,\mathrm{e/a_0^3}$ with a_0 the Bohr radius.

previously determined value of the pre-exponential factor $\nu = 5 \times 10^{16\pm2}\,\mathrm{Hz}$ [87]. The left part of Table 5.1 lists the experimentally determined E_b^{exp} alongside the doping levels E_D^{exp}, which are given in terms of the position of the Dirac cone relative to the Fermi level as determined in angle-resolved photoemission measurements. The experimental error in E_b is about 100 meV, and dominated by the error of the pre-exponential factor. However, as the pre-exponential factor acts equally in the calculation of all E_b, the errors of the differences in E_b for differently doped Gr are dominated by the reproducibility of the temperature measurement, and are therefore much smaller, only about 4 meV.

5.3 From density functional theory calculations to an intuitive picture

In order to better understand the origin of the observed change in E_b upon intercalation, cooperation partners in theory conducted DFT calculations with the naphtalene molecule on non-intercalated as well as O- and Eu-intercalated Gr. The calculations were carried out in the generalized gradient approximation [139] with a kinetic energy cut-off of 500 eV using the projector augmented wave method [140] as implemented in the VASP code [141, 142]. The ground-state geometry and the corresponding electronic structure were investigated using the non-local correlation energy functional vdW-DF2 [143] with a revised [144] Becke (B86b) exchange energy functional [145]. The unit cell comprised (10×10) Gr unit cells on 4 layers of (9×9) Ir(111), either pristine or (Eu/O)-intercalated.

Figure 5.3 (a) and (b) show the geometry of the calculations for the intercalated systems,

while the right part of Table 5.1 provides the calculated values for doping level E_D^{theor} and binding energy E_b^{tot}. The calculated doping level E_D^{theor} has been determined from the shift of Gr's Dirac point against the Fermi level and should thus be directly comparable to the value extracted from angle-resolved photoemission. Indeed, we find that the calculated doping levels E_D^{theor} are in reasonable agreement with the experimentally determined E_D^{exp}, in particular confirming n doping of Gr by Eu and p doping of Gr by O intercalation. Qualitatively, the doping is also seen in the charge density difference plots in Fig. 5.3 (c) and (d), which give a direct image of charge accumulation (for Eu) and depletion (for O) on the Gr site. These plots also visualize that charge transfer between the molecule and Gr is absent (a Bader analysis [146] yields a charge transfer of less than 0.03 electrons), which is a precondition for naphthalene adsorbed to Gr being a model for vdW interaction even when Gr is supported on a substrate and doped by intercalation.

Next, we look at the theoretical binding energy, defined as $E_b^{\mathrm{tot}} = E_{\mathrm{sys}}^{\mathrm{tot}} - (E_{\mathrm{surf}}^{\mathrm{tot}} + E_{\mathrm{molec}}^{\mathrm{tot}})$, where $E_{\mathrm{sys}}^{\mathrm{tot}}$ is the total energy of the molecule-surface system, $E_{\mathrm{surf}}^{\mathrm{tot}}$ denotes the total energy of the surface (*i. e.*, the Gr/O/Ir(111), Gr/Ir(111), and Gr/Eu/Ir(111) systems) and $E_{\mathrm{molec}}^{\mathrm{tot}}$ corresponds to the total energy of the naphthalene molecule in the gas phase. As obvious from Table 5.1, the calculations reproduce the experimentally observed increase in $|E_b|$ rather well when going from naphthalene on O-intercalated via pristine to Eu-intercalated Gr.

Yet, considering absolute numbers, two points have to be noted: Firstly, while Gr is essentially freestanding when intercalated with O or Eu [7, 30], Gr on bare Ir(111) is slightly hybridized with its substrate in specific areas of its moiré [56]. This induces a certain modulation of E_b and thus renders the non-intercalated case less reliable. Secondly, the excellent match of the absolute values (within $< 25\,\mathrm{meV}$) of the binding energies must be considered fortuitous, as E_b extracted from thermal desorption data is expected to carry a larger systematic error. Unaffected by these two caveats, however, is the *difference* in E_b between the O- and Eu-intercalated cases, which matches reasonably well being $\approx 60\,\mathrm{meV}$ in the calculation and $\approx 40\,\mathrm{meV}$ in the experiment.

To gain an insight into the role of the vdW interactions in these systems, the total binding energy E_b^{tot} was decomposed into a DFT contribution E_b^{DFT} and a non-local one E_b^{NL} as seen in Table 5.1. The data show that for all systems considered in our study, the DFT contribution E_b^{DFT} to E_b^{tot} is positive while the non-local one E_b^{NL} is negative indicating that the vdW interactions are indeed the driving force leading to a stable molecular adsorption. Furthermore, the magnitude of the attractive non-local contribution E_b^{NL} to the naphthalene binding significantly increases in the series from the O-intercalated (1.172 eV) via the pristine (1.408 eV) to the Eu-intercalated (1.601 eV) system.

To find out the reason for the modification of the vdW binding upon intercalation, calculations were conducted on a freestanding Gr sheet of (10×10) unit cells. It was doped by directly adding or removing 0.05 electrons per C atom. To keep the calculated unit cell on the whole

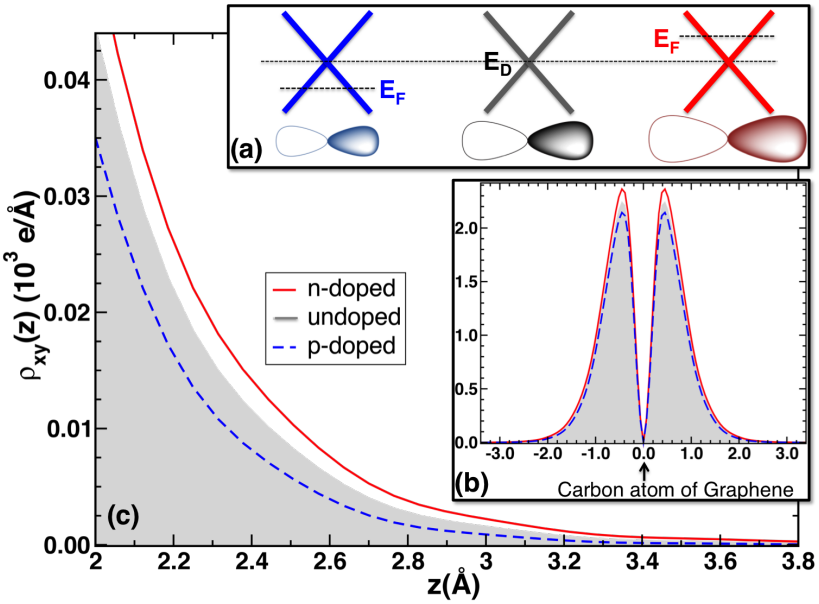

Figure 5.4: (a) Schematic band structure near the Dirac point and representation of the π orbital extension for p-, undoped and n-doped Gr. (b) In-plane xy-integrated π-state charge density for (10×10) unit cells of freestanding Gr as a function of z-direction. (c) Zoom into the low-density tail of (b).

charge-neutral, a balancing background charge had to be introduced. Figure 5.4 (b) shows the resulting xy-integrated charge density for all π orbitals corresponding to the differently doped cases. As qualitatively illustrated in Fig. 5.4 (c), the p or n doping of Gr results in a π charge density distribution that is less (p-doped) or more (n-doped) spatially extended than that of undoped Gr. A less (more) spatially extended π charge density corresponds to less (more) polarizable C atoms in the Gr layer and therefore will govern a weaker (stronger) vdW binding of the π adsorbates. This view is backed up quantitatively by a recent analysis of Berland *et al.* [147], who found for benzene on Gr, that most of the non-local energy in the vdW-DF arises from the extended regions of low charge density.

The increase in the non-local contribution with electron doping in Table 5.1 is mostly counteracted by the simultaneous increase in the repulsive DFT contribution, such that the total binding energy E_b^{tot} of the molecule to the surface is modified only slightly. Generally in a pure vdW system, the attractive interaction forces have to be balanced by a counteracting Pauli repulsion force in any stable adsorption geometry. If one approximates the vdW contribution by the non-local correlation, one might tentatively attribute the increase in the repulsive DFT term to an additional Pauli repulsion as Gr's charge density becomes more extended due to n doping.

5.4 Conclusion and outlook

In conclusion, in agreement of experiment and theory we find an increase in the vdW binding energy of naphthalene to Gr by about 5 % when changing from p to n doping in the experimentally accessible range. Based on the DFT calculations, the Gr π orbitals become spatially more extended with n doping, making the space of low electron density between Gr and the molecule more polarizable, which in turn gives rise to a stronger vdW binding.

For future investigations, I see five questions of interest:

(1) Will tuning of the Gr Fermi level through a gate electrode affect the vdW contribution of adsorbate binding in a similar way? Electrical control of molecular adsorption could be interesting from an application point of view. Muruganathan et al. [148] show electrical tunability of adsorption CO_2 molecules by a gate voltage, however, their mechanism is that of a bending of the CO_2 molecule, such that it obtains a small, static dipole moment.

(2) It would be interesting to compare different methods of including the vdW interaction in DFT, as the Langreth-Lundqvist style vdW-DF [88, 92, 127, 143] is not the only way [149]. The earlier semi-empirical approach of Grimme [150] includes the vdW contribution to the binding energy via pairwise $C_6 \cdot R^{-6}$ terms, where R is the distance of a pair of atoms and C_6 is a coefficient determined by fitting to experimental reference values. This method is expected to fail to describe the tunability of the vdW interaction by doping, because it has no way to account for the doping level. In contrast, the method of Tkatchenko and Scheffler [151] goes beyond the approach of Grimme [150] in that it includes the chemical environment in the calculation of the C_6 coefficient via the ground-state electron density. Calculations based on the Tkatchenko-Scheffler method should therefore also reproduce our experimental findings.

(3) What is the influence of the Gr support (i.e., what is underneath Gr) on the binding energy of the molecules, apart from doping of Gr? In the semi-empirical approach to vdW interaction in DFT, the influence of the support is expected to be suppressed by the $1/R^6$ factor. As the distance [(Gr support)–molecule] is about a factor of 2 larger than the distance [Gr-molecule], this could have an effect on the binding energy on the order of percent, not much less than the observed effect size. Within DFT, the effects could be separated as follows: The adsorption energy of a vdW-type adsorbate is calculated on a Gr sheet which is doped from the backside by a layer of alkali (e.g., Li) and halogen atoms (e.g., F) which are fixed laterally in the center of the carbon rings, while the distance to the Gr sheet is varied. Fixing the halogen atoms in the carbon ring center is necessary to preserve the Dirac cone of Gr, because the halogen atoms would otherwise prefer to enter into a covalent bond with an sp^3-rehybridized C atom. By varying the distance between Gr sheet and dopant atom, the doping level could be modulated, and oppositely so for alkali and halogen doping. In particular, moving an F atom further away from the Gr sheet should result in less p doping of Gr and thus a higher binding energy for the vdW-type adsorbate on the other side. This would directly contradict

System	E_D (eV)	
Gr/Al/Ni(111)	−0.64	[152]
Gr/Au/Ni(111)	0.0	[153, 154]
graphite	0.0	
Gr/Ir(111)	+0.07	[7]
Gr/Pt(111)	+0.3	[155]
Gr/O/Ir(111)	+0.68	[17]
Gr/Cl/Ir(111)	+0.7	[156]
Gr/Eu (2×2)/Ir(111)	−1.36	[30]
Gr/Eu $(\sqrt{3} \times \sqrt{3})$R30°/Ir(111)	−1.43	[30]
Gr/Cs $(\sqrt{3} \times \sqrt{3})$R30°/Ir(111)	−1.20	[78]

Table 5.2: Doping levels as gauged by the position of the Dirac cone with respect to the Fermi level E_D. Adapted from Ref. [81].

the Grimme method, which would always predict a lowering of the binding energy as the F atom is moved away from Gr, because the treatment assumes the vdW interaction is always attractive and decreasing with the atomic separation.

(4) What is the precise functional relationship between doping level and binding energy? For this purpose, the thermal desorption measurements should be conducted with a larger number of Gr support structures, each of which yields a different doping level. Table 5.2 (adapted from Ref. [81]) gives the doping levels of the supporting structures investigated here in comparison with some not yet explored. Such experiments would also contribute to answer the question (3).

(5) There has been a discussion in the literature on so-called "wetting transparency" of Gr, i.e., it was found that covering some surfaces with Gr hardly influences their contact angle with water, due to Gr's thinness [157], although the effect is not uncontroversial [158, 159]. Interestingly, the "wetting transparency" picture is directly opposite to the view adopted in this chapter, where we implicitly assumed vanishing contributions to the vdW interaction from Gr's support. Certainly, the nonlocal interactions of water will be quite different from those of naphthalene, because water molecules have a permanent dipole moment. Furthermore, water has a non-zero contact angle with Gr (i.e., it does not fully wet the surface), while for benzene and naphthalene, the formation of flat, monolayer-high islands under UHV conditions suggests that these molecules, as liquids in ambient conditions, would fully wet the Gr surface. Compared to the measurement of the contact angle under ambient conditions, our experiments in UHV are more controlled because they allow to exclude effects of atmospheric contaminants. While contact-angle measurements are not possible in UHV, Gr doped by intercalation can be stable in air and permit such experiments in ambient conditions. Indeed, two independent, recent works [160, 161] report on the water wetting behavior of chemically doped graphene via contact angle measurements, finding an ambipolar enhancement of the wetting with doping.

Chapter 6

Structure and magnetism of Eu intercalation layers

Much of this chapter is published in Refs. [30, 162].

The coauthors of Ref. [30] are: S. Schumacher, F. Huttmann, M. Petrovic, C. Witt, D. F. Förster, C. Vo-Van, J. Coraux, A. J. Martínez-Galera, V. Sessi, I. Vergara, R. Rückamp, M. Grüninger, N. Schleheck, F. Meyer zu Heringdorf, P. Ohresser, M. Kralj, T. O. Wehling, and T. Michely. My contribution to the results described in this chapter are as follows: I conducted the STM and LEED measurements together with SS, thereby furthering the structural characterizations of the intercalation layers started by DFF. I participated in the beamtime at ID08 in 2012 contributing to the in-situ sample preparation. I evaluated the XMCD data jointly with SS and with help from PO, and contributed to that part of the manuscript that discusses the magnetization loops, in particular the shape anisotropy model. Other coauthors contributed to results described here as follows: VS managed the ID08 beamline and endstation. TM, SS, PO, JC, and CVV also worked at the beamtime, with the XMCD measurements mostly done by PO and SS. TOW contributed to the magnetic discussion, and the DFT calculations that are not discussed here. TM led the project. The other coauthors contributed to Ref. [30] the LEEM and ARPES parts which are also not discussed here.

The discussion here uses some unpublished data of DF and SS, and unpublished data of the 2011 beamtime, where I did not participate. More XMCD data on the $(\sqrt{3} \times \sqrt{3})\mathrm{R30}^{\circ}_{\mathrm{Gr}}$ was acquired in the 2016 beamtime at ID32, coworkers there see section 7.5.

The coauthors of Ref. [162] are F. Huttmann, D. Klar, N. Atodiresei, C. Schmitz-Antoniak, A. Smekhova, A. J. Martínez-Galera, V. Caciuc, G. Bihlmayer, S. Blügel,

T. Michely, and H. Wende. Their contributions are as follows: I conducted the LEED and STM experiments in cologne. DK evaluated the XMCD and carbon XAS data with contributions from CSA and AS. These three also managed the Wende group's chamber used for the XAS/XMCD measurements. DK, CSA, AS, AJMG, and myself worked at the BESSY beamtimes. NA, VC and GB conducted the DFT calculations. SB guided the theoretical work. TM and HW conceived the experiments and lead the project.

The desire to either contact Gr with magnetic materials or render Gr itself magnetic is motivated by possible spintronic applications [21], due to Gr's negligible spin-orbit coupling and consequently large spin diffusion length [20], as well as the emergence of spin-based quantum effects [163]. A wealth of approaches have been demonstrated: Gr was transferred onto a ferromagnetic insulator [163, 164], a ferromagnetic insulator was grown on top of Gr [165, 166], ferromagnetic $3d$ metal substrates were used for Gr growth [22], $3d$ [18, 84, 85, 167] or $4f$ [30] metals were intercalated after growth on a nonmagnetic substrate, $3d$ metal adatoms were adsorbed [168], or magnetic moments were generated via defects that break the Gr AB sublattice symmetry, such as zigzag edges [169–171], hydrogen adatoms [172], vacancies, or voids [173, 174].

In this chapter, we investigate systems with monolayers of Eu intercalated between Gr and its substrate. The choice of Eu is motivated by its lack of a d electron, such that the electronic structure of Gr is largely preserved [30]. In section 6.1, the substrate is Ir(111), which is nonmagnetic, such that the intrinsic magnetism of the Eu layer can be observed. In order to stabilize magnetic order in Eu intercalation layers to higher temperatures, we develop a method to have the Gr on nickel and cobalt thin films in section 6.2 to obtain a Gr-$4f$-$3d$ hybrid system.

6.1 Eu intercalation layers under graphene on Ir(111)

As described by S. Schumacher and D. Förster [121, 175], exposure of Gr/Ir(111) to Eu at 720 K leads to intercalation. At this temperature, any Eu left on top evaporates back into the vacuum, such that the process is self-limiting.

6.1.1 Structure

In Fig. 6.1 (a) to (f), we show the evolution of the structure on the sample with Eu coverage. The LEED image of pristine Gr/Ir(111) is shown for reference in Fig. 6.1 (a). Moiré satellite spots appear in addition to the Gr and Ir spots. The moiré satellites decrease in intensity when Eu is intercalated, even at low coverages, where superstructure spots associated with Eu are not yet visible. In this submonolayer regime, a complex pattern of stripes and islands of intercalated Eu is observed in STM [83, 175]. Only for a coverage of Eu near completion of a monolayer,

additional spots of a $(2\times2)_{\mathrm{Gr}}$ structure become visible as marked in Fig. 6.1 (b) and (c) by solid-green circles. The index to the Woods notation indicates the lattice with respect to which the superstructure occurs. Figure 6.1 (i) to (l) illustrate how to see whether a superstructure occurs w.r.t.Gr or Ir. Upon further deposition, a $(\sqrt{3}\times\sqrt{3})\mathrm{R30}^{\circ}_{\mathrm{Ir}}$ (marked with blue circles) develops, and coexists with the $(2\times2)_{\mathrm{Gr}}$ as shown in Fig. 6.1 (c). At the particular electron energy of (c),

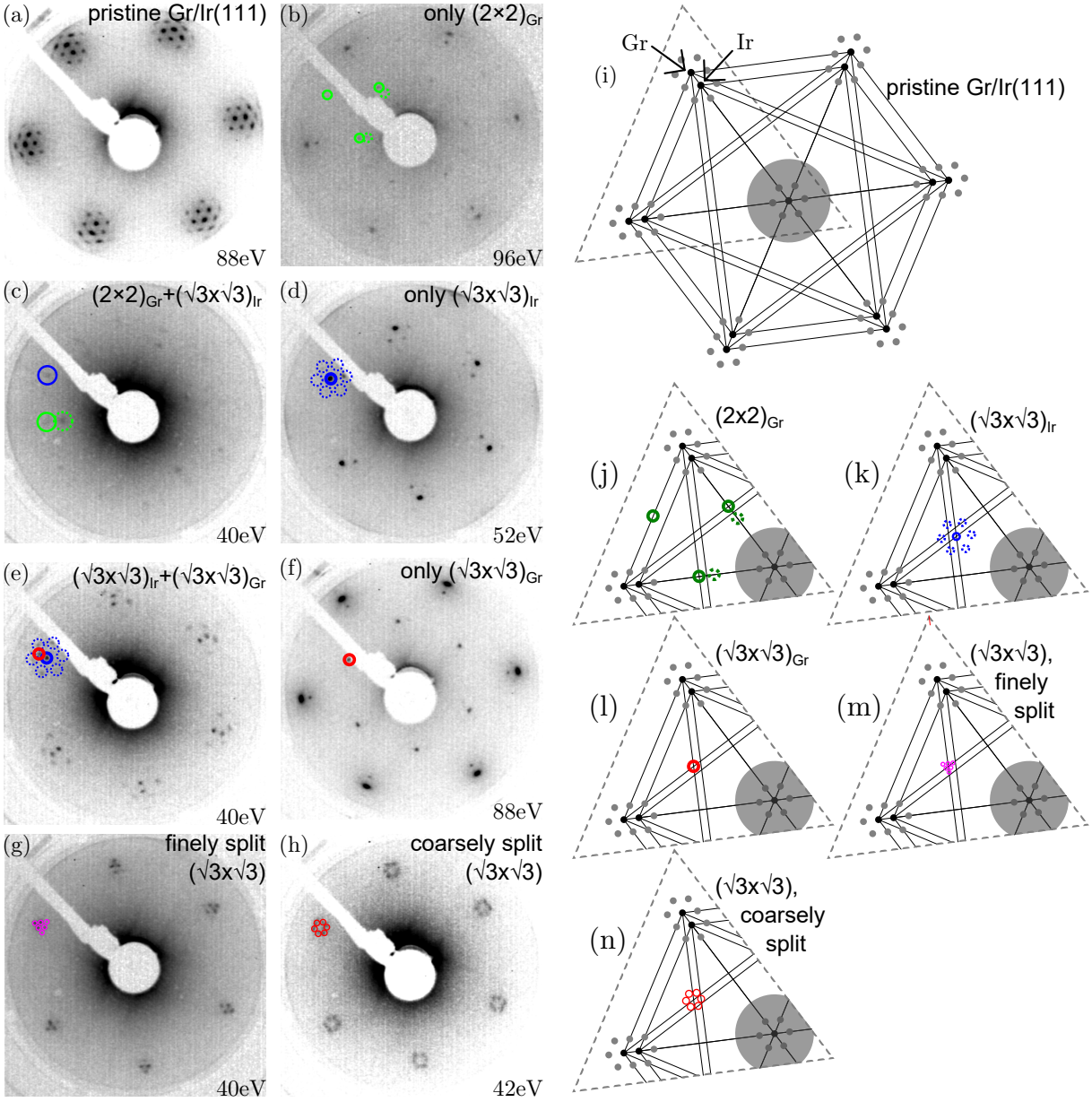

Figure 6.1: (a)–(h): LEED patterns at the indicated primary electron energies, before [(a)] and after intercalation of Eu [(b)–(h)]. The Eu coverages are increasing successively from (a) to (f). (g) and (h) presumably have coverage beyond (f), see text. (i): Schematic depiction of the LEED pattern of Gr/Ir(111), the lines allow to construct the positions of the superstructure spots with respect to Gr or Ir. (j)–(n): Regions of the dashed triangle in (i) with additional marked superstructure spots.

a moiré satellite appears to the inside of each of the $(2\times2)_{\mathrm{Gr}}$ superstructure spots and is marked by dotted-green circles in (c) and (j). With further increasing coverage, the $(\sqrt{3}\times\sqrt{3})\mathrm{R30}^\circ_{\mathrm{Ir}}$ becomes pure as seen in Fig. 6.1 (d). The $(\sqrt{3}\times\sqrt{3})\mathrm{R30}^\circ_{\mathrm{Ir}}$ has moiré satellites, marked dotted-blue in (d) and (k), which are more intense compared to those of the structures with respect to Gr, presumably because the low-energy electrons do not probe deeply, and the moiré affects the Gr layer more strongly when the Eu underneath is aligned to Ir. Visible at higher energies (not shown) is that the satellite spots are stronger for the $(\sqrt{3}\times\sqrt{3})\mathrm{R30}^\circ_{\mathrm{Ir}}$-intercalated sample also around the first-order Gr and Ir spots. A further small coverage increase in Fig. 6.1 (e) leads to a coexistence of $(\sqrt{3}\times\sqrt{3})\mathrm{R30}^\circ_{\mathrm{Ir}}$ with $(\sqrt{3}\times\sqrt{3})\mathrm{R30}^\circ_{\mathrm{Gr}}$, the latter marked red in (e), (f), and (l). Even further deposition makes the $(\sqrt{3}\times\sqrt{3})\mathrm{R30}^\circ_{\mathrm{Gr}}$ pure in (f).

In addition to these easily understood superstructures, we have on one occasion each observed two other $(\sqrt{3}\times\sqrt{3})\mathrm{R30}^\circ$-type structures with split spots as shown in (g) and (h). They are centered around the $(\sqrt{3}\times\sqrt{3})\mathrm{R30}^\circ_{\mathrm{Gr}}$ position as illustrated in (m) and (n). Furthermore in addition to the structures shown in (g) and (h), we observed more blurred or streaked $(\sqrt{3}\times\sqrt{3})\mathrm{R30}^\circ$-type structures not shown here.

A DFT relaxation of a moiré unit cell with $(2\times2)_{\mathrm{Gr}}$ Eu conducted by N. Atodiresei indicated that the Eu atoms prefer to be in hollow sites of the Ir substrate as well as in the carbon ring center. This can explain why the $(\sqrt{3}\times\sqrt{3})\mathrm{R30}^\circ$ forms w.r.t.Ir for lower and w.r.t.Gr for higher coverages. In contrast, the reason for the formation of the split-spot phases in (g) and (h) is less clear. Because the coexistence of $(2\times2)_{\mathrm{Gr}}$ with $(\sqrt{3}\times\sqrt{3})\mathrm{R30}^\circ_{\mathrm{Ir}}$ as well as the coexistence of the latter with the $(\sqrt{3}\times\sqrt{3})\mathrm{R30}^\circ_{\mathrm{Gr}}$ has been clearly demonstrated in (c) and (e), we exclude that phases (g) and (h) occur at intermediate coverages to those phases. I thus speculate that the split-spot structures in (g) and (h) originate from Eu coverages beyond a full layer of the $(\sqrt{3}\times\sqrt{3})\mathrm{R30}^\circ_{\mathrm{Gr}}$, where a further compression makes the Eu lattice incommensurate with both Gr and Ir, resulting in an even finer type of moiré spot splitting. In support of the interpretation of a coverage beyond the $(\sqrt{3}\times\sqrt{3})\mathrm{R30}^\circ_{\mathrm{Gr}}$ leading to the split-spot structures, we note that (g) transformed into $(\sqrt{3}\times\sqrt{3})\mathrm{R30}^\circ_{\mathrm{Ir}}$ after an annealing step at 823 K, while (h) resulted from an experiment where further Eu was deposited after completion of the $(\sqrt{3}\times\sqrt{3})\mathrm{R30}^\circ_{\mathrm{Gr}}$. Likely, the structures in (g) and (h) were not reproducibly observed because the temperature of 720 K is already close to where back-evaporation of Eu from the highly compressed intercalation layer sets in. It would be possible to lower the intercalation temperature somewhat without giving up the self-limiting back-evaporation of Eu from on top of Gr, and this could help to clarify this point.

Figure 6.2 (a) shows an STM topograph of the preparation with the LEED pattern of Fig. 6.1 (c). A Gr wrinkle passes diagonally through the image. With the same tip and tunneling conditions, two different moiré contrasts appear: in the lower left half, dark dots on bright background, and in the upper right half, bright dots on dark background, as most easily seen in the contrast-enhanced inset. This proves that there are indeed two distinct phases in

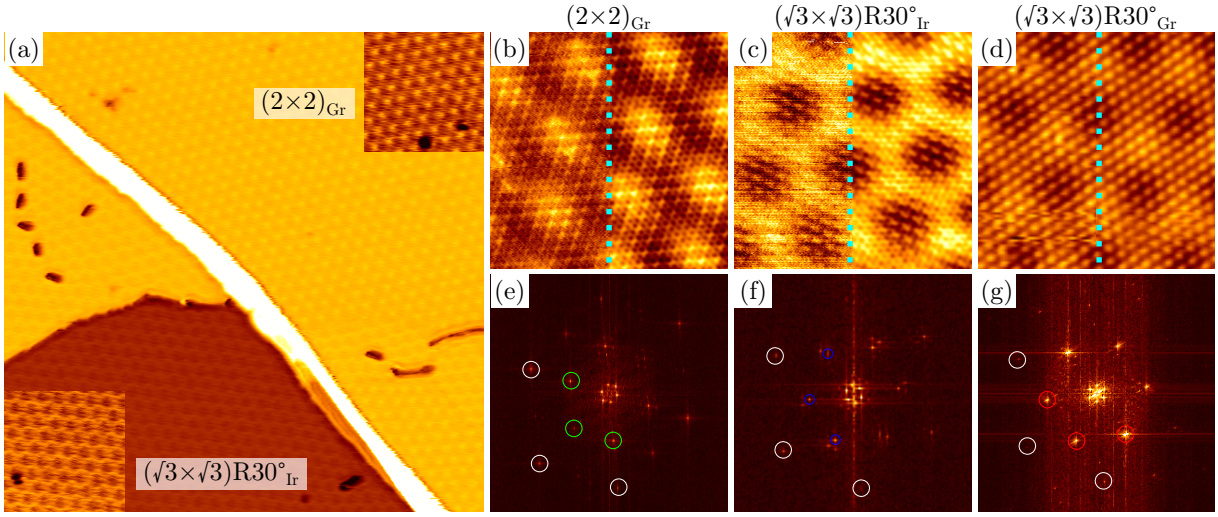

Figure 6.2: Different phases of Eu intercalation underneath Gr/Ir(111) in STM. (a): STM topograph of a preparation with coexistence of two different intercalation phases, distinguished by the inversed moiré contrast, $(90\,\mathrm{nm})^2$. Obtained on the same preparation as Fig. 6.1 (c). Insets: same image, enhanced contrast. (b,c,d): Atomic resolution STM topographs of Eu intercalation structures, $(8.4\,\mathrm{nm})^2$. The left half of the image is unfiltered, while the right one is Fourier-filtered. (b): $(2 \times 2)_{\mathrm{Gr}}$, obtained on the same preparation as (a). (c): $(\sqrt{3} \times \sqrt{3})\mathrm{R30}^\circ_{\mathrm{Ir}}$, obtained on the same preparation as (a) and (b). (d): $(\sqrt{3} \times \sqrt{3})\mathrm{R30}^\circ_{\mathrm{Gr}}$, obtained on a different preparation, where LEED indicated only this intercalation phase. (e,f,g): Corresponding Fourier transforms (FT) of larger versions of (b,c,d). Gr spots encircled white, superstructure spots with colors. Only three out of six equivalent spots each are encircled.

coexistence. From LEED, we would expect that one of them is the $(2 \times 2)_{\mathrm{Gr}}$, while the other one is the $(\sqrt{3} \times \sqrt{3})\mathrm{R30}^\circ_{\mathrm{Ir}}$. Note that the moiré contrast could depend upon tip and tunneling parameters, and it is not necessarily always the case that the two phases appear with opposite contrasts.

Figure 6.2 (b) and (c) show atomic resolution obtained on the same preparation as (a). From the corresponding Fourier transform (FT) images in (e) and (f), we can identify (b) as the $(2 \times 2)_{\mathrm{Gr}}$ structure and (c) as the $(\sqrt{3} \times \sqrt{3})\mathrm{R30}^\circ_{\mathrm{Ir}}$ using the construction as already sketched for the LEED patterns above. In the case of the $(2 \times 2)_{\mathrm{Gr}}$ structure, the moiré satellites observed are of low intensity and we assign all intense spots in the FT to Gr (encircled white) and $(2 \times 2)_{\mathrm{Gr}}$ (encircled green). In contrast, in the case of (f), groups of three spots occur in the superstructure position with similar intensities. The white-encircled spots are Gr and the inner one of the group of three is $(\sqrt{3} \times \sqrt{3})\mathrm{R30}^\circ_{\mathrm{Ir}}$. Groups of three spots in the superstructure position have been observed also for the $(\sqrt{3} \times \sqrt{3})\mathrm{R30}^\circ_{\mathrm{Ir}}$ superstructure in Cs-intercalated Gr/Ir(111) [78]. Figure 6.2 (d,g) were obtained on a different sample, where we expected the $(\sqrt{3} \times \sqrt{3})\mathrm{R30}^\circ_{\mathrm{Gr}}$ from LEED. The moiré satellites in the FT are again weak, such that we assign all high-intensity spots to be w.r.t.the Gr lattice.

I would like to compare the atomic resolution in (b,c,d). We observe that the Eu lattice

is visible in a similar contrast throughout all the moiré regions for the two structures that are w.r.t.Gr in (b) and (d). In contrast, for the structure w.r.t.Ir in (c), the atomic contrast of the Eu atoms consists of clear intensity maxima only in one region of the moiré, while elsewhere, the atomic resolution is hard to see. The hcp and fcc regions of the moiré are similar; thus, the one region with good atomic resolution of the $(\sqrt{3} \times \sqrt{3})\mathrm{R30}^\circ_{\mathrm{Ir}}$ must be top. The Eu atoms are in the center of the carbon ring only in the top region for those superstructure w.r.t.Ir, while for the superstructures w.r.t.Gr, the Eu atoms are always in the carbon ring center. Apparently, Eu in the carbon ring center gives a more instructive atomic resolution.

Here, I note that we failed to describe the $(\sqrt{3} \times \sqrt{3})\mathrm{R30}^\circ_{\mathrm{Ir}}$ in Ref. [30]. Furthermore, Ref. [30], Fig. 1 (c) does not show atomic resolution of the $(2 \times 2)_{\mathrm{Gr}}$ as stated therein, but rather of the $(\sqrt{3} \times \sqrt{3})\mathrm{R30}^\circ_{\mathrm{Ir}}$. The same mistake is found in Refs. [175, 176]. Furthermore, what is shown in Fig. 6.2 (d,g) here was not obtained on the same sample as the other images of Fig. 6.2, contrary to what is suggested in Refs. [175, 176]. The confusion arose partly because the small-angle scatter of the Gr lattice was comparably large in this preparation (i.e., few degree misorientation of Gr w.r.t.the Ir lattice), due to a low CVD growth temperature in the preparation. This results in large misorientations of the moiré via its magnifying effect [54], as evident in the insets in Fig. 6.2 (a). Therefore, I selected images with comparably small misorientations for Fig. 6.2 (b–g), although the superstructures exist on the more misoriented Gr as well.

6.1.2 Magnetism

The magnetism of the Eu intercalation layers was investigated by XMCD at their $\mathrm{M}_{5,4}$ edges in 2011 and 2012 at ESRF ID08 and in 2016 at ESRF ID32. One preparation with the $(\sqrt{3} \times \sqrt{3})\mathrm{R30}^\circ_{\mathrm{Gr}}$ structure was investigated in each beamtime, while the $(2 \times 2)_{\mathrm{Gr}}$ structure was investigated only in 2012. The lowest indicated temperature was $T_{\mathrm{min,\,ind}} = 7\,\mathrm{K}$ and highest magnetic field $B_{\mathrm{max}} = \pm 5\,\mathrm{T}$ in 2011 and 2012 at ID08, while in 2016, the better setup at ID32 gives $T_{\mathrm{min,\,ind}} = 5.5\,\mathrm{K}$ and $B_{\mathrm{max}} = \pm 9\,\mathrm{T}$. The actual lowest temperatures at the sample $T_{\mathrm{min,\,real}}$ are somewhat higher, but not precisely known, because there is no temperature sensor directly on the sample, and the thermal contact of the cryostat cold finger to the sample can change every time the sample is changed. However, values of $T_{\mathrm{min,\,real}} = 10\,\mathrm{K}$ at ID08 and $T_{\mathrm{min,\,real}} = 7$ at ID32 are realistic, and are called just T in the following. When the sample is heated to achieve higher temperatures, the indicated and real temperature are presumed the same, as the thermal conductivity of the sample holder increases rapidly with T.

Figure 6.3, left side, exemplarily shows the spectra obtained on the $(\sqrt{3} \times \sqrt{3})\mathrm{R30}^\circ_{\mathrm{Gr}}$ structure in 2016 under grazing incidence with $\theta = 60^\circ$ at $T = 7\,\mathrm{K}$ and in an external magnetic field of $B = \pm 9\,\mathrm{T}$. The absorption spectra for two opposite helicities are plotted in (a), the resulting difference (XMCD) spectrum in (b), and the polarization-averaged one in (c). The average spectrum is indistinguishable from previous measurements on metallic Eu [107] and stoichiometric

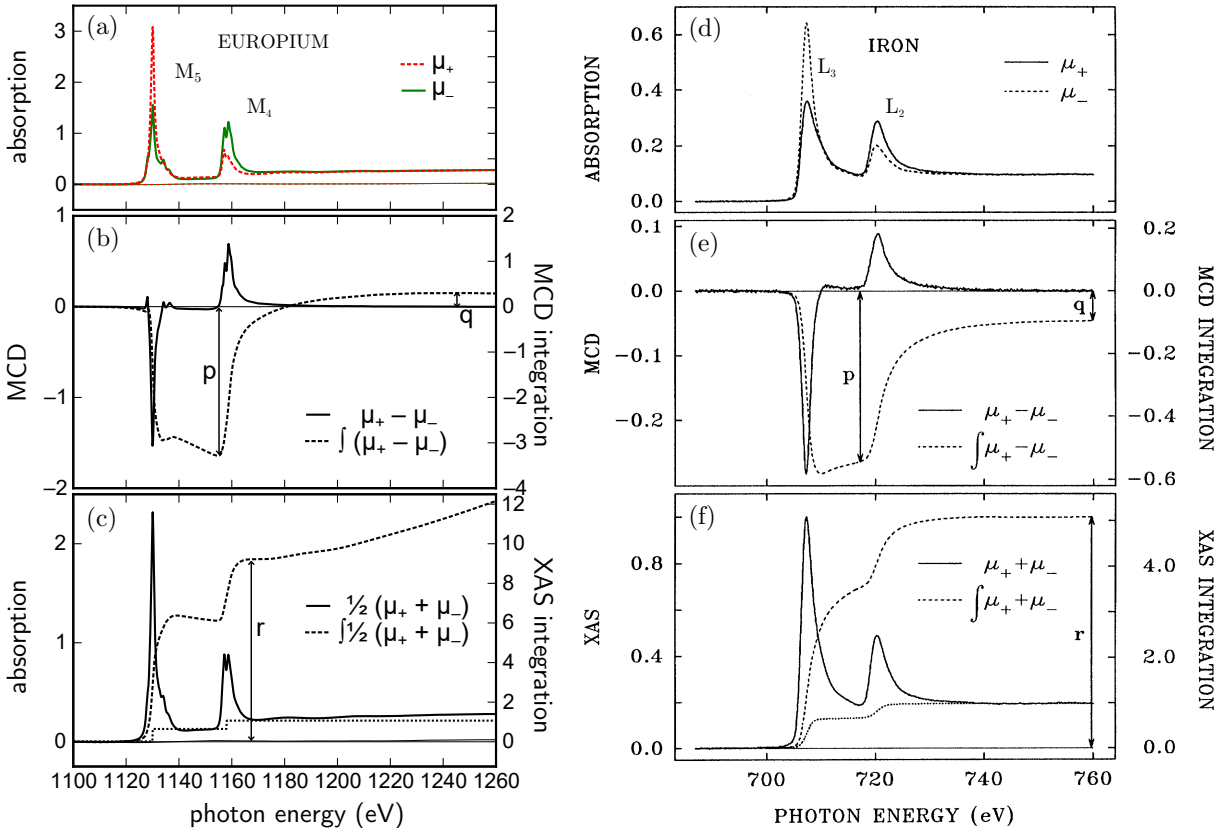

Figure 6.3: Left side: XAS and XMCD spectra of the $(\sqrt{3}\times\sqrt{3})\mathrm{R30}^\circ_{\mathrm{Gr}}$ intercalation structure structure measured in 2016 at an indicated temperature of $T = 5.5\,\mathrm{K}$ and $B = \pm 9\,\mathrm{T}$ in grazing incidence ($\theta = 60^\circ$). Right side: Results of Chen et al. [113] obtained on Fe thin films in transmission mode, © APS 1995. Top panels: XAS for opposite helicities. Middle panels: XMCD and its integral. Bottom panels: XAS for opposite helicities, double-step background, and integral. In this energy region, the XAS of pristine Gr/Ir(111) is a practically flat line at zero in (a) and (c). Note the factor 2 between our definition of r and that of Ref. [113].

EuO [177], where Eu is present in a $4f^7$ configuration. It is also clearly distinguished from the $4f^6$ spectra reported there. Calculations of the XMCD spectrum in Ref. [178] of a $4f^7$ configuration also agree well with the measured spectra. These statements furthermore hold for all our measurements on Eu-intercalated Gr.

We have used the XMCD sum rules to evaluate the orbital and spin magnetic moment [118, 119]. This requires integration of the XMCD and XAS spectra. As far as possible, we followed Chen et al. [113], who applied the sum rules to spectra obtained in transmission-mode XAS of thin films of ferromagnetic $3d$ metals. Figure 6.3 (d) to (f) depicts their spectra and analysis for iron.

The dashed-black lines in (b/e) give the integrals over the XMCD, to obtain the values for p and q as defined in section 3.5.1. The ratio of orbital to spin moment depends only on the ratio of p and q, and becomes zero for $q = 0$. For iron and cobalt, Chen et al. found agreement of

this ratio determined by sum rules with that obtained in gyromagnetic experiments within a few percent. In the case of Eu, due to the $4f^7$ configuration, we expect a vanishing orbital moment and therefore $q = 0$. Strictly following Chen et al. we find an absolute value of the integral over the whole XMCD spectrum q as indicated in Fig. 6.3 (b) of about 10% of p. Yet the deviation of the integral q from zero entirely results from a long, high-energy tail of the XMCD in an energy region more than 20 eV above the center of the M_4 line, suggesting that this XMCD does not originate in simple transitions from $3d$ to $4f$. Therefore, we conclude that the orbital moment is zero within an error of $0.3\,\mu_B$. Note that also for p, about 10% is contributed between the M_5 and M_4 edges, where the XMCD is non-zero yet almost constant, which again suggests an origin unrelated to the $3d$ to $4f$ transition.

In contrast to the determination of the ratio m_L/m_S, the individual moments depend also on the integral over the XAS. A double-step background as indicated by dotted lines in (c/f) must be assumed to account for transitions into continuum-like states. The theoretically expected ratio of step heights is 3:2 for the $4f$ elements (it is 2:1 for the $3d$ ones). In the energy region of the Eu $M_{5,4}$, the absorption of Gr/Ir(111) measured as a reference is essentially flat as indicated by the fine lines around zero in (a). However, the background is still partially arbitrary, because the energy of the onset of the continuum is not known and masked by the high intensity of the $3d$ to $4f$ transitions. Furthermore for Eu, we encountered the problem that EXAFS oscillations in the post-edge region mean that the absorption there is not constant, a feature that is not apparent in the data of Ref. [113].

Nevertheless, taking a suitable background and integration boundary, and assuming the number of holes in the $4f$ shell at $n_H = 7$, we obtain spin moments of 6.3 to $6.8\,\mu_B$ for measurements on the $(\sqrt{3} \times \sqrt{3})$R30°-type structures in grazing incidence, near the expected saturation values. We estimate a relative error of 10 %. In contrast, the moments for the (2×2) are significantly lower; furthermore, for all investigated Eu intercalation systems, the moments in normal incidence were slightly ($< 10\%$) less than in grazing. These points become clearer in the discussion of the magnetization loops later, where the calculated moments were used to scale the curves.

Before that, I wish to discuss briefly on the expectable accuracy of sum rules at the $M_{5,4}$. Principally, the derivation of the sum rules is based on an atomic picture, where angular momentum is a good quantum number due to the spherical symmetry of the free atom. From this point of view, the sum rules could be expected to give better results at the $4f$ metal's $M_{5,4}$ transitions than at the $L_{3,2}$ edges of the $3d$ metals, because the $4f$ is more core-like and less influenced by the environment. Indeed, the multiplet structure at the $4f$ $M_{5,4}$ is generally sharper than at the $3d$ $L_{3,2}$. While the $4f$ $M_{5,4}$ have been less analyzed by sum rules in the literature compared to $3d$ $L_{3,2}$, values from sum rules at the Eu $4f$ $M_{5,4}$ edges with errors as low as 5% have been given [179].

The application of sum rules is limited by both theoretical and experimental complications

as discussed by van der Laan [180]. For Eu^{2+}, one significant complication fortunately does not arise: Because there is no orbital moment in the spherically symmetric $4f^7$, the dipolar term is $T_Z = 0$, and the linear dichroism vanishes. Furthermore, self-saturation effects as discussed in Refs. [107, 108] should play no role as our samples are always atomically thin.

The obviously largest error is thus the ambiguity in the extraction of the integrals p, q, and r; here, we estimate an error of the spin moments of at most 10% from this factor. Yet this value could be rather pessimistic particularly compared to works on $3d$ metals, e.g., that of Chen et al., who reports the excellent agreement (within 7%) of spin- and orbital moment obtained on ferromagnetic thin films of Fe and Co. This is because the choices made in the integration of $3d$ spectra are more difficult for several reasons: Firstly, the $L_{3,2}$ edges in the $3d$ elements are less well separated in energy, and therefore more difficult to integrate separately, than the $M_{5,4}$ of the $4f$ elements, due to the smaller spin-orbit coupling in the former. Thus, in the Eu spectrum, an extended, comparably flat area is seen between the edges in the XAS, while in the Fe spectrum of Chen et al., this area still has significant slope from the high-energy tail of the L_3. The XAS also does not go down to the assumed double-step background between the edges in (f), while it does in (c). Secondly, also the separation of the $2p \rightarrow 3d$ peak from the $2p \rightarrow ns$ ($n \geq 4$) continuum is more difficult for the $3d$ metals, as the dominance of the former process over the latter is not as pronounced as the dominance of the $3d \rightarrow 4f$ peak over the $3d \rightarrow np$ ($n \geq 6$) in the $4f$ metals. This is visible when comparing the ratios of the peak height to the continuum step height in (c) and (f). On the other hand, the spin polarization in s electrons should be less than in p electrons, due to the more localized nature of the latter. Thole et al. [107] have a short discussion on the contribution of the $3d$ to $6p$ channel to the XAS in the rare earth.

Next, we discuss the magnetization loops, all of which are shown in Fig. 6.4.

In 2011, only one sample with the $(\sqrt{3} \times \sqrt{3})\mathrm{R30}^\circ_{\mathrm{Gr}}$ structure was measured as shown in Fig. 6.4 (a/b). This preparation exhibited significant ferromagnetic coupling, clear in-plane anisotropy and near-saturated magnetization at 5 T. Furthermore, there is a hysteresis of the magnetization loop in a field region between ±50 mT around zero in grazing incidence. Temperature-dependent measurements in this low-field region showed that a hysteresis is present up to 40 K but has vanished at 60 K.

Due to experimental limitations, the 2011 preparation was produced by deposition of Eu at room temperature, followed by a transfer step, and was only then annealed to allow intercalation of Eu underneath Gr. In contrast to deposition of Eu directly at elevated temperature, which leads to either rapid intercalation or equally rapid back-evaporation, the post-annealing method implies that there is a lot of time during which the Eu adsorbed on top of Gr is exposed to the chamber background pressure, which is problematic especially during the transfer process through narrow and thus poorly pumped tubes.

Thus in 2012, a $(\sqrt{3} \times \sqrt{3})\mathrm{R30}^\circ_{\mathrm{Gr}}$ sample was prepared by deposition of Eu at elevated temperature, so that such contamination may be excluded. As shown in Fig. 6.4, (c/d), the shape

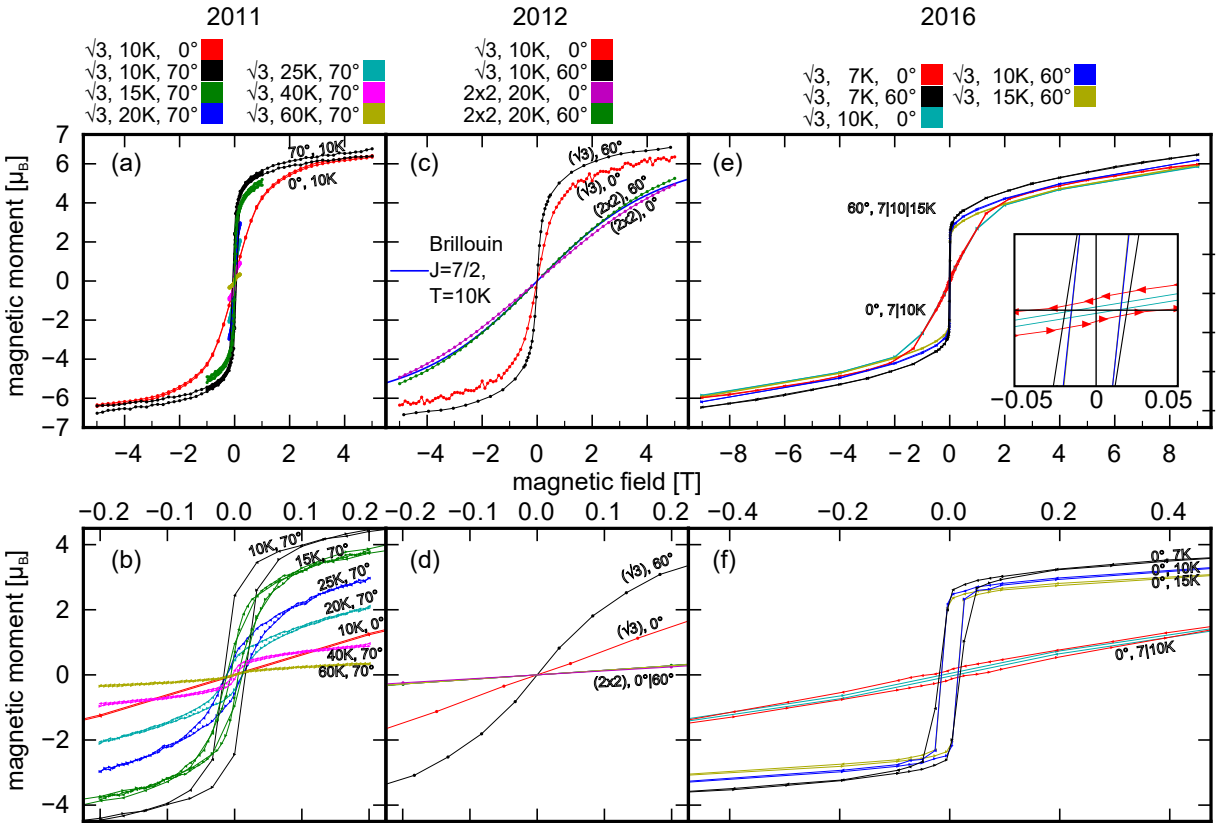

Figure 6.4: Magnetization loops measured in (a/b) 2011, (c/d) 2012, and (e/f) 2016 on Eu intercalation layers under Gr/Ir(111) by XMCD. Full measured B-field range in top row, zoom-in onto the low-field region in bottom row. The curves in (c/d) were averaged over field-up and field-down directions, while those in (a/c) and (e/f) were not. All curves were symmetrized according to $M(B) = -M(-B)$. Thin line in (c) between (2×2) curves is a Brillouin function for $J = 7/2$ and $T = 10\,\mathrm{K}$.

of the curve is similar on a scale of $B = \pm 5\,\mathrm{T}$ and still indicates a significant ferromagnetic coupling: The susceptibility in grazing incidence, at $24\,\mu_\mathrm{B}/(\mathrm{T} \cdot \mathrm{atom})$, is far larger than a paramagnetic $J = 7/2$ system at $T = 10\,\mathrm{K}$, which would be $1.41\,\mu_\mathrm{B}/(\mathrm{T} \cdot \mathrm{atom})$. However, a loop opening was no longer observed. Therefore, in Ref. [30], we attributed the hysteresis in 2011 to ferromagnetic EuO impurities on top of Gr. EuO has a bulk Curie temperature of 69 K, and is known to grow on Gr by exposure of Gr to Eu and O at room temperature in an Eu excess, followed by post-annealing to 700 K [32, 181]. We presumed it formed in the 2011 preparation by the reaction $\mathrm{Eu}+\mathrm{H_2O} \rightarrow \mathrm{EuO}+\mathrm{H_2}$ from Eu and water vapor, a common residual gas in imperfectly baked UHV systems. The Curie temperature would be lowered in small clusters on Gr to below 60 K.

Although we find evidence for ferromagnetic coupling in the 2012 $(\sqrt{3} \times \sqrt{3})\mathrm{R30}^\circ_\mathrm{Gr}$ preparation, there is no spontaneous magnetization or hysteresis. This indicates that at 10 K the layer is either (i) just above its Curie temperature T_C or (ii) composed of magnetic units that display su-

perparamagnetic behavior. Finally, one might argue that (iii) according to the Mermin-Wagner theorem in two dimensions there cannot be spontaneous magnetization at all at non-zero temperature [182].

Considering (i), we note that according to the Curie-Weiss law the susceptibility of a ferromagnet diverges as T approaches T_C from above, which explains the high susceptibility without hysteresis if measuring close to, but above T_C. Based on the calculated Curie constant C for $J = \frac{7}{2}$, we estimate that our measurement temperature would need to be just 7% above T_C to get the observed susceptibility χ.

Considering (ii), the superparamagnetic unit could be constituted by the moiré unit cell given that the Eu atoms' adsorption positions relative to the Ir surface atoms (e.g., top, hollow, bridge) are dependent on the position within the moiré unit cell and so will the magnetic coupling between these Eu atoms. Indeed, calculating the paramagnetic susceptibility of a magnetic moment equal to the sum of Eu moments in a moiré unit cell at $T = 10\,\mathrm{K}$ yields

$$\frac{1}{3} \cdot 10.23^2 \cdot 1.410\,\mu_\mathrm{B}/(\mathrm{T}\cdot\mathrm{atom}) = 49.2\,\mu_\mathrm{B}/(\mathrm{T}\cdot\mathrm{atom})$$

In this expression, $\frac{1}{3}\cdot 10.23^2$ is the number of Eu atoms per moiré unit cell, and this is multiplied with the paramagnetic susceptibility at 10 K of a single $4f^7$ spin. If we further assume that, because of shape anisotropy, the spins are constrained completely to lie in the plane, then we would only see the projection of the magnetization onto the direction of the beam, and the spin sees only the projection of the external field onto the plane (i.e., factor $\cos^2\theta$ in total), thus the value would be

$$10.23^2 \cdot \frac{1}{3} \cdot 1.410\,\mu_\mathrm{B}/(\mathrm{T}\cdot\mathrm{atom}) \cdot \cos^2 60^\circ = 36.9\,\mu_\mathrm{B}/(\mathrm{T}\cdot\mathrm{atom})$$

which is not that far away from the measured value of $23(2)\,\mu_\mathrm{B}/(\mathrm{T}\cdot\mathrm{atom})$.

Finally, considering (iii), we note that the Mermin-Wagner theorem is based on an *isotropic* model. As we will argue below, magnetocrystalline anisotropy is indeed absent or at least negligible in our system. However, it has been shown that the long-range dipolar interaction present in our case is sufficient to change the magnon dispersion such that the Mermin-Wagner theorem no longer applies [183]. In this case, there is a temperature $T_1 \sim JS^2$ at which short-range order occurs, and a logarithmically lower temperature $T_\mathrm{C} \sim JS^2/\ln(J/\Delta)$ below which long-range order evolves. Herein, Δ is an energy determined by the dipole-dipole interaction. It may be plausible that our measurement temperature lies between these two temperatures, where one would expect long-wavelength spin waves to lead to an average magnetization of zero in the zero-field case, but a much larger response of the magnetization to small fields than in the paramagnetic case. Unfortunately, a simple analytical solution to this problem does not exist.

In conclusion, it is understood that the large susceptibility of the 2012 $(\sqrt{3}\times\sqrt{3})\mathrm{R}30^\circ_\mathrm{Gr}$ preparation must arise from ferromagnetic regions, although it remains unclear whether these

regions are limited in size by thermal fluctuations, as in (i) and (iii), or are of structural origin, as in (ii). Temperature-dependent magnetization loop measurements would have allowed to resolve this issue.

In addition to the $(\sqrt{3}\times\sqrt{3})\mathrm{R30}^\circ_{\mathrm{Gr}}$, one sample with the $(2\times2)_{\mathrm{Gr}}$ structure was investigated in 2012 as shown in Fig. 6.4 (c). The magnetization curve is much flatter than the curve obtained on the $(\sqrt{3}\times\sqrt{3})\mathrm{R30}^\circ_{\mathrm{Gr}}$ structures. Furthermore, the grazing incidence curve is only slightly steeper than the normal one. In Fig. 6.4 (c), we have plotted a Brillouin curve as expected for a paramagnet with $J = 7/2$ at $T = 10\,\mathrm{K}$, which lies just between the normal and grazing curves, suggesting that the $(2\times2)_{\mathrm{Gr}}$ behaves as a plain paramagnet.

To clarify the situation on the $(\sqrt{3}\times\sqrt{3})\mathrm{R30}^\circ_{\mathrm{Gr}}$ via temperature-dependent measurements, this structure was prepared and measured again in the 2016 beamtime, as shown in Fig. 6.4 (e,f). The curves for normal and grazing incidence differ markedly around $B = 0$. For grazing incidence, a jump in $M(B)$ occurs, while in normal incidence, $M(B)$ exhibits an extended linear regime. At higher field, the curves behave qualitatively similar, although the grazing incidence curve always has larger absolute values of the magnetization. For grazing incidence, the loops show an apparent hysteresis with a coercive field of a few ten mT up to the highest measured temperature of $T = 15\,\mathrm{K}$. However, the normal incidence curve has a very similar coercive field, although the system is obviously highly anisotropic. Therefore, most of the coercive field should be an artifact of a non-zero remnant field of the superconducting magnet, i.e., a magnetic field remains even when the current in the coil is set to zero. This is rather typical of superconducting magnets [184]. Thus we cannot resolve the near-zero-field region, yet we say that the 2011 and 2016 $(\sqrt{3}\times\sqrt{3})\mathrm{R30}^\circ_{\mathrm{Gr}}$ preparations exhibited spontaneous in-plane magnetization and are thus ferromagnetic and below T_C, while the 2012 preparation is not.

There is a strong discrepancy in the measurement results on the $(\sqrt{3}\times\sqrt{3})\mathrm{R30}^\circ_{\mathrm{Gr}}$ phase when comparing the 2012 and 2016 measurements, even for the same temperature: (1) The extended linear regime in normal incidence around $B = 0$ occurs only in 2016. (2) The quasi-spontaneous magnetization is not seen in the 2012 data. (3) The 2016 $M(B)$ curves saturate much slower, such that a significant slope is present even at $B = 9\,\mathrm{T}$.

The extended linear regime is very well described by the dipolar anisotropy model, as is the jump in grazing incidence, assuming a soft-magnetic ferromagnet, as discussed below. On the other hand, the slow saturation behavior is rather difficult to explain. Because the spontaneous magnetization occurs in 2016 for temperatures as high as 15 K, and because the trend of the size of the spontaneous magnetization with temperature suggests $T_C > 20\,K$, I exclude a poor thermal contact in the 2012 measurements. I thus imply that the 2012 and 2016 $(\sqrt{3}\times\sqrt{3})\mathrm{R30}^\circ_{\mathrm{Gr}}$ preparations were subtly different in an unknown way.

Next, we are going to discuss the strong anisotropy apparent in the magnetization loops of the $(\sqrt{3}\times\sqrt{3})\mathrm{R30}^\circ_{\mathrm{Gr}}$ preparations: Saturation is reached faster for grazing incidence, pointing to a preferred in-plane direction for the magnetization. There are two main classes of magnetic

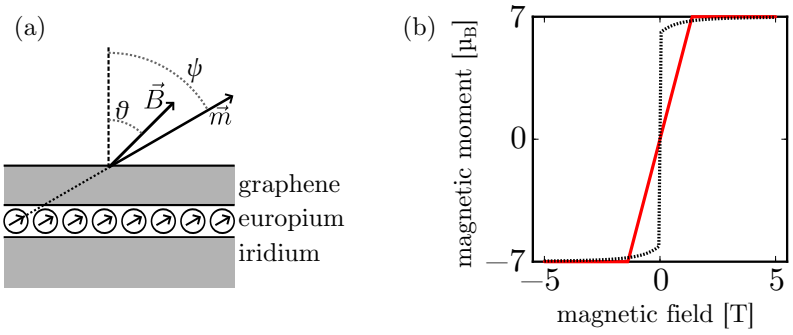

Figure 6.5: (a) Sketch of the situation assumed in the calculation of the shape anisotropy energy per Eu atom. (b) Resultant magnetization curve of a fully ferromagnetically coupled hexagonal monolayer of Eu atoms with lattice constant $\sqrt{3}a_{\mathrm{Gr}}$ in normal incidence ($\theta = 0°$, solid-red) and grazing ($\theta = 60°$, hashed-black).

anisotropy: dipolar (also called shape) anisotropy, which is an effect of simple magnetostatics, and single-ion (also called magnetocrystalline) anisotropy, which is an effect of the spin-orbit coupling. As we have already established for all intercalated Eu that the magnetic shell has $4f^7$ configuration and thus $L = 0$, the spin-orbit interaction as a source of the anisotropy in our system must be largely suppressed. Indeed, DFT calculations on Eu^{2+} even in a very anisotropic crystal field of molecular ligands have yielded a value of the single-ion anisotropy energy in the range of only a few µeV [43]. On the other hand, as this system is so exceptionally thin, and the magnetic moment of Eu is comparably large, a strong shape anisotropy can be expected. In order to gain quantitative insights, I will assume for simplification a complete ferromagnetic order of the spins and calculate the ensuing shape anisotropy energy per atom, and from this, the response of the magnetization to external fields away from the easy plane, as sketched in Fig. 6.5 (a). The dipole-dipole interaction Hamiltonian for two magnetic moments $\vec{m}_j$, $\vec{m}_k$ with a distance vector $\vec{r}_{jk}$ and $\vec{e}_{jk} = \vec{r}_{jk}/|\vec{r}_{jk}|$ is:

$$H = -\frac{\mu_0}{4\pi r_{jk}^3}\left(3(\vec{m}_j \cdot \vec{e}_{jk})(\vec{m}_k \cdot \vec{e}_{jk}) - \vec{m}_j \cdot \vec{m}_k\right)$$

with $\vec{m}_j = \vec{m}_k = 7\,\mu_{\mathrm{B}} \cdot \vec{e}_m$ and $\vec{e}_m$ the unit vector in the direction of magnetization. We can then calculate the dipole-dipole interaction energy of one Eu atom with all others as a function of the magnetization direction:

$$E_{\mathrm{dip-dip}} = -\frac{1}{2}\sum_{\vec{r}_{mn}\neq\vec{0}} \frac{\mu_0}{4\pi r_{mn}^3}(7^2\mu_B^2)\left(3(\vec{e}_m \cdot \vec{e}_{jk})^2 - 1\right)$$

with $\vec{r}_{mn} = (m(1,0,0) + n(-1/2,\sqrt{3},0))^T \cdot \sqrt{3} \cdot a$ all position vectors of the Eu atoms, and a the lattice constant of Gr. A factor of one-half has been added to avoid double counting of pairwise interactions, such that E can be properly understood as an anisotropy energy per Eu atom.

Performing the summation numerically for many values of ψ and guessing the formula, I obtain

$$E_{\mathrm{dip-dip}} = E_{aniso} \cdot \left(-\frac{1}{3} + \cos^2(\psi)\right)$$

with ψ the angle between magnetization and surface normal and $E_{\mathrm{aniso,\,Gr}} = 281\,\mu\mathrm{eV}$ per Eu atom. For comparison, the magnetocrystalline anisotropy energy of hcp Co and FePt are of the order $60\,\mu\mathrm{eV}$[1] and $3000\,\mu\mathrm{eV}$[2] per Co/Fe atom, respectively. In an external magnetic field of modulus B oriented at an angle θ with respect to the surface normal, an additional Zeeman energy occurs to yield a total magnetic energy per Eu atom:

$$E_{\mathrm{total}} = E_{\mathrm{aniso}}(-\frac{1}{3} + \cos^2\psi) - mB\cos(\psi - \theta) \tag{6.1}$$

The intuition for this equation is as follows: to minimize the anisotropy energy that results from dipolar interactions, the magnetization would prefer to be in plane (i.e., $\phi = 0$); this is captured by the anisotropy energy (left summand). However, the external field is able to pull the magnetization out of the plane by means of the Zeeman energy (right summand). So if we minimize E_{total} by setting its derivative to zero, we can calculate ψ as a function of the magnitude B and angle to the surface normal θ of the external field.

$$\frac{\partial E_{\mathrm{total}}}{\partial \psi} = -2E_{aniso}\sin\psi\cos\psi + mB\sin(\psi - \theta) \stackrel{!}{=} 0$$

For the case $\theta = 0$ (normal incidence), we thus obtain:

$$\cos\psi = \frac{mB}{2E_{\mathrm{aniso}}}$$

What we measure, however, is not $\psi(B)$, but the projection of the magnetization onto the direction of the beam. At ID08 and ID32, the beam and the magnetic field are always parallel and fixed in direction; the incidence angle is varied by rotating the sample. Thus, the measured magnetization is $M = m\cos(\psi - \theta)$. In normal incidence, we can easily calculate a theoretical expectation for the zero-field susceptibility (again for $a = a_{Gr}$):

$$\chi_{theo} = \frac{\partial M}{\partial B} = \frac{\partial(m\cos\psi)}{\partial B} = \frac{m^2}{2E_{\mathrm{aniso}}} \tag{6.2}$$

$$= 5.0\,\mu_{\mathrm{B}}/(\mathrm{T}\cdot\mathrm{atom}) \tag{6.3}$$

For non-zero θ or B, the calculation of $M(B)$ was performed numerically. Figure 6.5 (b) shows the resulting curve for normal (solid-red) and grazing ($\theta = 60°$, hashed-black) incidence. In grazing incidence, the curve jumps to $\sin(\theta) \approx 87\%$ of the saturation value at zero field, then

[1] At 4.2 K; Ref. [185]

[2] Ref. [186] gives $1 \times 10^8\,\mathrm{erg/cm^3}$ for MBE-grown $L1_0$ FePt films, corresponding to $1 \times 10^8\,\mathrm{erg/cm^3} \cdot \frac{\sqrt{3}}{2}a^2c = 2979\,\mu\mathrm{eV}$ with $a = 3.853\,\text{Å}$ and $c = 3.713\,\text{Å}$.

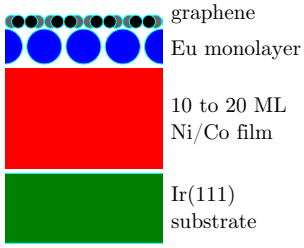

Figure 6.6: Schematic cross-sectional sketch (along the substrate's (110) direction) of the investigated system.

saturates smoothly on a scale of about 1 T. In contrast, the normal incidence curve is a line with slope χ_{theo} that sharply transitions into the saturated value at $B \approx 1.4\,\mathrm{T}$. The value of χ_{theo} is quite close to the experimentally determined zero-field susceptibility in 2012 in normal incidence of $\chi_{\mathrm{exp},2012} = 8.0(8)\,\mu_\mathrm{B}/(\mathrm{T}\cdot\mathrm{atom})$, demonstrating the relevance of the above calculation. In contrast, the 2016 value for the zero-field susceptibility is significantly smaller, only $\chi_{\mathrm{exp},2016} = 2.7(3)\,\mu_\mathrm{B}/(\mathrm{T}\cdot\mathrm{atom})$. However, the extended linear regime of the $M(B)$ for $\theta = 0°$ in 2016 indeed ends between 1.3 and 2.1 T, as predicted by the model. This would be consistent with the 2016 preparation being a phase mixture with another, harder to magnetize part as suggested by the high-field behavior.

6.2 Graphene-4f-3d hybrid systems

In order to stabilize ferromagnetic order in intercalated europium layers to higher temperatures, we have sought to replace the non-magnetic iridium metal underneath by nickel and cobalt. Nickel and cobalt have been chosen for the following reasons: (1) They are ferromagnetic at room temperature. (2) In contrast to iron, they do not have a bulk carbide, such that Gr can exist on a bulk surface in equlibrium. (3) Because thin films are strongly influenced by interface effects, iron can occur in such thin films in both fcc and bcc structure, a serious complication, because Fe is ferromagnetic only in the bcc structure, but not in the fcc structure. Because nickel is much better characterized in the literature as a Gr substrate, most experiments were conducted only with nickel, and we focus on the Ni discussion in the following. However, cobalt was not observed to behave differently where it was investigated. We are not interested in growing Gr on Ni single crystals, because single crystals are comparably hard to bring into magnetic saturation. In contrast, thin films can be easily magnetically saturated as long as the material is magnetically soft and the anisotropy is in plane. This is because the demagnetization factor of a thin film is zero for in-plane magnetization. A nickel film thickness of 10 ML or more would seem ideal to obtain ferromagnetic properties as in bulk nickel. Figure 6.6 shows a sketch of the systems that we have sought to produce.

Two different pathways were chosen to obtain Gr on nickel films. Firstly, Gr was grown on

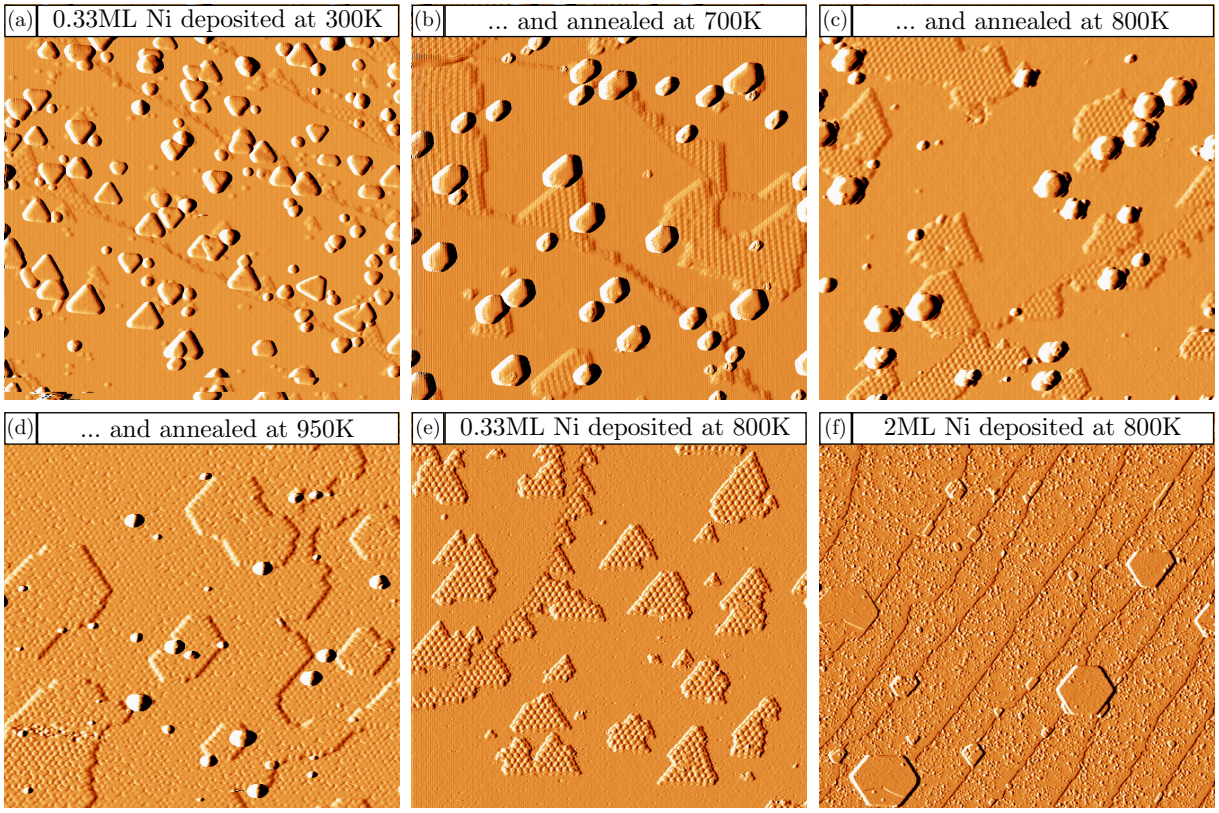

Figure 6.7: Differentiated STM topographs of Gr/Ir(111) exposed to Ni vapor. (a): After deposition of 0.33 ML Ni at RT. (b-d): Same sample as (a), but with additional annealing steps to (b) 700 K, (c) 800 K, and (d) 950 K. (e): After deposition of 0.33 ML Ni at 800 K. (f): Same sample as (e), but with additional deposition of 1.67 ML Ni at 800 K. Image sizes: (a)–(e): $(160\,\mathrm{nm})^2$; (f): $(660)\,\mathrm{nm}^2$.

Ir(111), and was subsequently intercalated with Ni. Secondly, Gr was grown on Ni thin films grown on the clean Ir(111) surface. The first approach initally seemed preferable to us due to the very high quality of Gr that can be obtained on Ir(111), and will be discussed next.

6.2.1 Intercalation of graphene on Ir(111) with Ni

The commonly described literature recipe to obtain Gr intercalated with metals is to deposit the metal at room temperature, and subsequently anneal [8, 18, 84]. The interface energies make it energetically favorable for the deposited metal adsorbed on top of Gr to go underneath, where a strong metallic bond to the iridium substrate can form.

Figure 6.7 (a) to (d) show differentiated STM topographs of 0.33 ML Ni deposited at (a) room temperature and subsequently annealed to (b) 700 K, (c) 800 K, and (d) 950 K. After deposition at room temperature, only very small patches near the step edges are intercalated with Ni. The largest part of the deposited amount seems to reside in the form of triangular, multi-layer high clusters on top of the Gr sheet. The triangles have their sides parallel to the substrate's

dense-packed rows. Upon annealing of this sample to 700 K, the intercalated patches take up a much larger area, and fewer Ni clusters reside on top of the surface. The Ni clusters on top have reshaped into truncated triangles. We annealed further to 800 K, but clusters are still present. Only at 950 K have the clusters almost completely disappeared. However, at this temperature, it is no longer possible to distinguish nickel-intercalated and non-intercalated areas. This means that a homogenous alloy of Ni and Ir has formed. Thus, the post-annealing method is unable to intercalate all deposited nickel without alloying it with the iridium substrate. Alloying with the substrate is expected to degrade or destroy the ferromagnetic property of nickel, and it thus not acceptable.

When metal atoms are evaporated onto Gr at low temperature, they form clusters on top, because the thermal energy is insufficient to activate the intercalation. Intercalation then requires that the clusters are first dissolved, which apparently requires a higher temperature than the intercalation itself. To avoid this, we have deposited nickel directly at elevated temperature, such that the material can intercalate as atoms before forming any clusters. We chose 800 K as the deposition temperature for this experiment, because this seemed the highest temperature where still no strong alloying has occured. Figure 6.7 (e) shows the results of the experiment for a deposited amount of 0.33 ML. Intercalated areas are seen and are fully distinguishable from the pristine Gr/Ir. At the same time, no clusters have formed on top, which means the deposition-at-elevated-temperature method is superior. However, when we attempted to intercalate a larger amount by deposition of a total of 2 ML of Ni, clusters still formed on top of Gr as seen in Fig. 6.7 (f). These clusters are larger and spaced further apart as expected from the larger diffusion length at 800 K compared to room temperature. Clearly, when even larger amounts of nickel are deposited, the clusters on top absorb a disproportionate share of the material. While nucleation of cluster on top might be further delayed by increasing the deposition temperature, this would risk alloying. We have therefore concluded that growth of Gr on iridium followed by intercalation with nickel is not a suitable pathway if the desired thickness of the Ni film is on the order of 10 ML.

After we performed this work, we became aware of a similar work on Co and Fe intercalation [187], where the authors also concluded that deposition at elevated temperature is preferable. Furthermore, Ref. [66] presents an in-depth study of the alloying process of intercalated iron with iridium with a focus on the resulting changes to the interaction with the Gr sheet.

6.2.2 Structure of Eu intercalation layers under graphene grown on Ni and Co thin films on Ir(111)

Having concluded that nickel intercalation of Gr on Ir(111) is problematic, we instead tried to grow the nickel films on Ir(111) first, and then grow the Gr on the nickel films afterwards. Ni and Co films were grown at room temperature on the clean Ir(111) surface. Subsequent Gr growth growth was performed at 800 K.

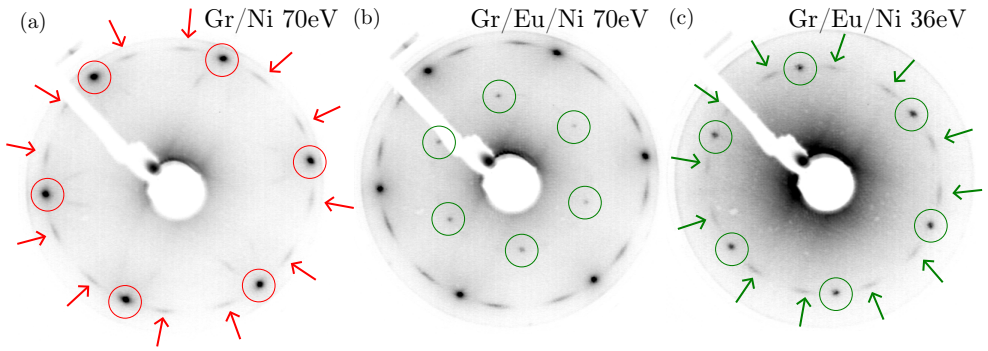

Figure 6.8: Inverted contrast LEED patterns of Gr on Ni thin films. (a): At $\approx 70\,\mathrm{eV}$ electron energy, before intercalation of Eu. (b): Same electron energy as (a), after intercalation of Eu. (c): Same as (b), but at a lower electron energy of $\approx 36\,\mathrm{eV}$.

Figure 6.8 (a) shows a low-energy electron diffraction (LEED) pattern of Gr grown on a Ni thin film. Marked by red circles are the spots of Gr in a (1×1) superstructure with respect to the substrate. Also visible and marked by red arrows are segments of a circle around the central spot, with the same distance from the central spot as the Gr (1×1) spots. These have been previously assigned [63] to Gr rotated in-plane with respect to the Ni substrate by angles $17 \pm 7°$.

After exposure of the sample to Eu vapor at elevated temperature, the LEED pattern in Fig. 6.8 (b) has additional spots in the $(\sqrt{3} \times \sqrt{3})$R30° superstructure position, encircled green. We ascribe this to the formation of an ordered, intercalated monolayer of Eu in between Gr and its metal substrate, as has been previously shown to be the case for Gr on Ir(111) [30]. The LEED pattern seen at a lower electron energy in Fig. 6.8 (c) reveals that segments of an arc of the diameter of the $(\sqrt{3} \times \sqrt{3})$R30° superstructure spots are also present. It is thus apparent that when the crystallographic directions of Gr and the substrate are rotated against each other, the Eu layer orients by the Gr, rather than by the substrate. We made the same observations also when using a Co instead of a Ni film.

In order to extend our investigation to real space, we have conducted STM measurements on the Ni-based system. Figure 6.9 shows an STM topograph acquired on a sample where the deposition time was reduced so that only submonolayer amounts of Eu were intercalated. The atomic resolution allows to identify the (1×1) superstructure of Gr on Ni in the lower part and the $(\sqrt{3} \times \sqrt{3})$R30° of Eu-intercalated Gr in the upper part of the image. The Eu-intercalation island exhibits a sharp edge which is oriented along the dense-packed rows of the Eu layer, rather than the dense-packed rows of Ni or Gr. The small height difference of only about 1 Å between intercalated and non-intercalated regions suggests that the Eu-intercalation island is attached to the lower side of a Ni step edge. We note that, despite the sharp LEED patterns, larger-scale STM images generally showed a high density of obtrusive point defects already prior to Eu intercalation, not untypical for Gr on Ni. Nevertheless, flat areas could be found where

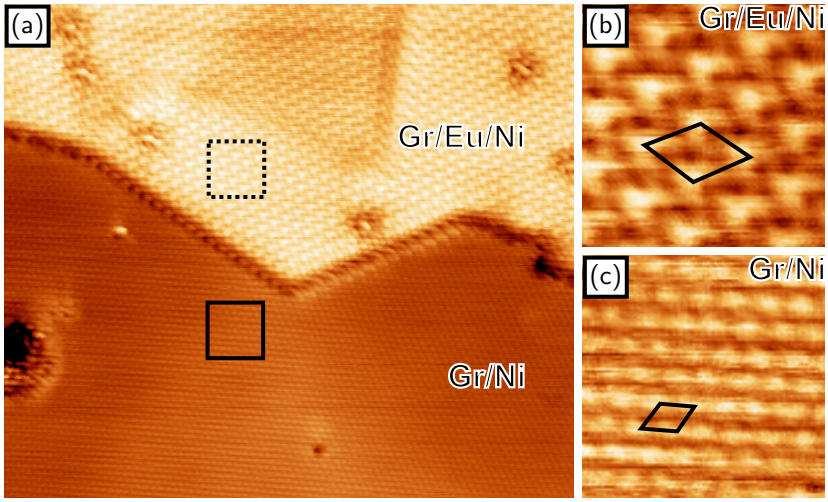

Figure 6.9: (a) $(20\times17)\,\mathrm{nm}^2$ STM topograph acquired on partially Eu-intercalated Gr/Ni ($U_B = 190\,\mathrm{mV}$, $I_t = 150\,\mathrm{nA}$). (b/c) $(2.1\,\mathrm{nm})^2$ zoom-in of the area indicated by the dashed/solid square in (a). Unit cells of the $(\sqrt{3}\times\sqrt{3})\mathrm{R30}^\circ$ superstructure in (b) and of the (1×1) superstructure of Gr/Ni in (c) indicated by diamonds.

stable imaging is also possible with small tunneling resistances that facilitate higher resolution. Eu intercalation did not cause any measurable increase in the point defect density. Together with the homogenous and well developed $(\sqrt{3}\times\sqrt{3})\mathrm{R30}^\circ$ intercalation pattern in intercalated areas and the negligible respective solid solubilities of Eu and Ni [188], we rule out intermixing of Eu and Ni to any significant extent in our samples.

6.2.3 Magnetism of Eu intercalation layers under graphene on Ni and Co thin films

The samples with Eu-intercalated Gr on Ni and Co thin films were investigated by X-ray magnetic circular dichroism (XMCD). In our setup, the magnetic field is always parallel or antiparallel to the beam, while the angle θ between the sample surface normal and the beam can be varied. By comparing the XMCD signals under grazing incidence, shown here, and under normal incidence, with very small XMCD signal, we concluded that our Ni and Co films always exhibited an easy-plane anisotropy. Therefore, all following measurements have been conducted under 65° grazing incidence.

Figure 6.10 shows the XAS for different helicities and resulting XMCD of Ni, Co and Eu measured at the lowest attainable temperature of 70 K. Measurements on the Gr/Eu/Ni system are shown in Fig. 6.10 (a) and (b), while measurements on the Gr/Eu/Co system are shown in Fig. 6.10 (c) and (d). The obtained XAS and XMCD lineshapes of Ni and Co are in agreement with previous observations at their $L_{3,2}$ edges [189, 190], confirming that the films are sufficiently thick to be considered bulk-like. A comparison of our measurements with Refs. [107, 177] clearly indicates that Eu is present in a $4f^7$ configuration, as was previously found also for Eu

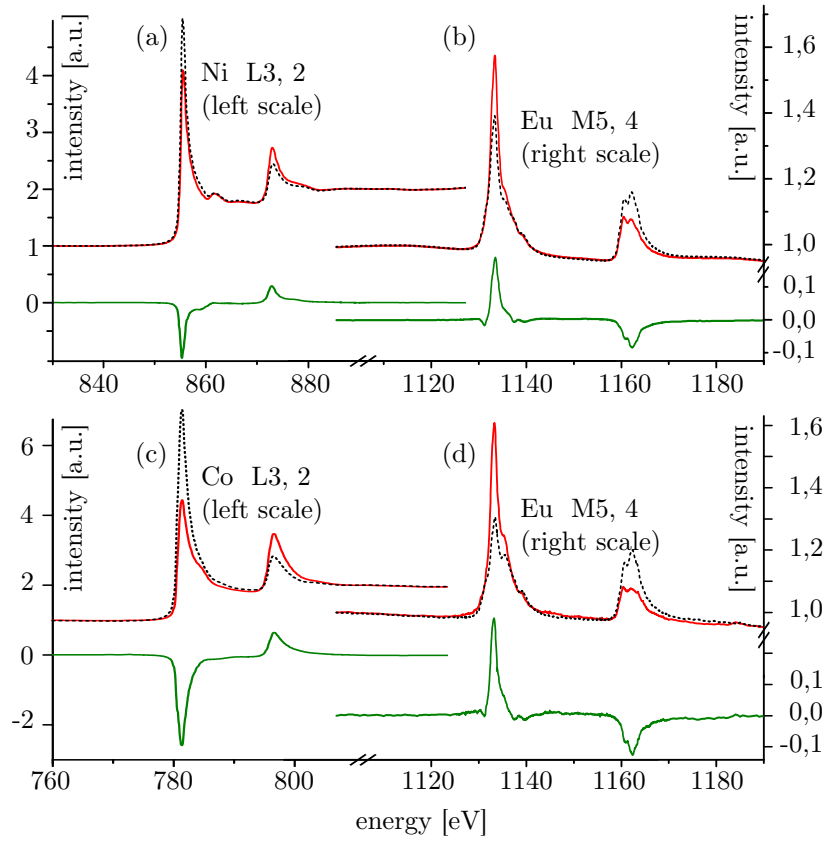

Figure 6.10: XAS spectra for different helicities (dashed black and solid red) and resulting XMCD signal (solid green) obtained under grazing incidence ($\theta = 65°$) at 70 K and in a field of 35 mT for Ni/Co (left side, a/c) and Eu (right side, b/d) in the Gr/Eu/Ni system (upper part, a/b) and Gr/Eu/Co system (lower part, c/d).

intercalated under Gr on Ir(111) [30]. More interestingly, however, the XMCD measurements show that the Eu monolayer has a net moment. This moment is anti-parallel to the Ni/Co moment as evidenced by the opposite sign of the XMCD signal. Similar coupling has been detected by Sanyal *et al.* [191] for thin layers of Gd on Fe. We have previously shown that an Eu monolayer under Gr on Ir exhibits a net magnetization of comparable size only at a much lower temperature (10 K) and much higher field ($\approx$ 1 T) [30] indicating a clear magnetic coupling of Eu to the ferromagnetic substrates in the present case. The Eu XMCD signal at 70 K on the Co film is larger than on the Ni film. This points to a stronger coupling of Eu to Co compared to Ni, as we will confirm below. The XMCD lineshape for Eu on Co and Eu on Ni is identical, as is the Eu polarization-averaged absorption spectrum (not shown). The polarized Eu absorption spectra on Co and Ni are only slightly different due to incomplete saturation of the Eu moment on the Ni film.

In order to learn more about the relation of the Eu moment to the moment of the underlying 3*d* metal film, we have measured element-specific magnetic hysteresis loops, which are shown for Eu on Ni in Fig. 6.11 (a). The identical shape of the hysteresis loops of Eu and Ni and their

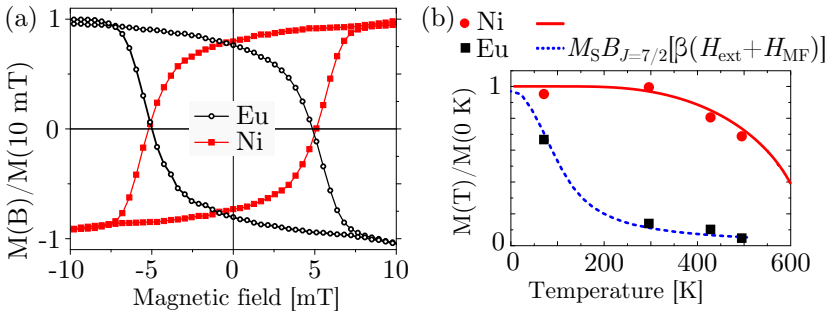

Figure 6.11: (a): Hysteresis loop obtained for Eu (red squares) and Ni (black circles) obtained at 70 K. The field was changed stepwise, and for each field the signal at the energy of the maximum of the XMCD is recorded and normalized to the field-dependent pre-edge value. (b): XMCD signals in dependence of temperature for Ni and Eu. Lines are fits to $M(T)$, see text. The XMCD signals are normalized to their expected value at $T = 0\,\mathrm{K}$ as obtained from the respective fits of $M(T)$ for Ni/Eu.

opposite magnetization indicate that the ordering of the moment of the Eu monolayer is induced by an antiferromagnetic coupling with the Ni film.

We performed temperature-dependent measurements of the XMCD signals of Eu and Ni as shown in Fig. 6.11 (b) to investigate the coupling strength. The Ni signal significantly declines only above 400 K, consistent with a bulk-like film given the bulk Ni Curie temperature of 627 K. The solid, red line gives the $M(T)$ curve from mean-field theory, which describes Ni approximately [192].

In contrast, the Eu signal decreases strongly already when going from 70 K to room temperature, yet a nonvanishing XMCD is still detected even at 500 K. A simple mean-field approach is able to describe this: We assume that the Eu monolayer behaves paramagnetically with $J = 7/2$ in an effective external field corresponding to the sum of the actual external field H_{ext} and an exchange field $H_{\mathrm{MF}}(T)$ proportional to the temperature-dependent Ni magnetization, *i.e.*:

$$M_{Eu} = M_S \cdot B_{J=7/2}[\beta(H_{\mathrm{ext}} + H_{\mathrm{MF}}(T))] \tag{6.4}$$

Here, M_S is the saturation magnetization, β is $g\mu_{\mathrm{B}}\mu_0 J/k_B T$ and B is the Brillouin function. We find a good fit to the experimental data as seen in the dashed, blue line in Fig. 6.11 (b), in the process obtaining $H_{\mathrm{MF}}(T = 0\,\mathrm{K}) = (30 \pm 6)\,\mathrm{T}/\mu_0$. For the Co-based system, measurements were only taken at temperatures of 70 and 500 K, and indicated roughly a factor of 2 stronger coupling.

For a better understanding of the magnetic exchange interaction between the Eu atoms and these ferromagnetic substrates, first-principles calculations were conducted by N. Atodiresei, V. Caciuc, and G. Bihlmayer of the group of S. Blügel. As suggested by the experiments, they used a $(\sqrt{3} \times \sqrt{3})\mathrm{R}30°$ surface unit cell. Three high-symmetry positions were considered, *i.e.*, the Eu atom adsorbed in the fcc, hcp, and top sites w.r.t.the Ni/Co substrates. In the case of

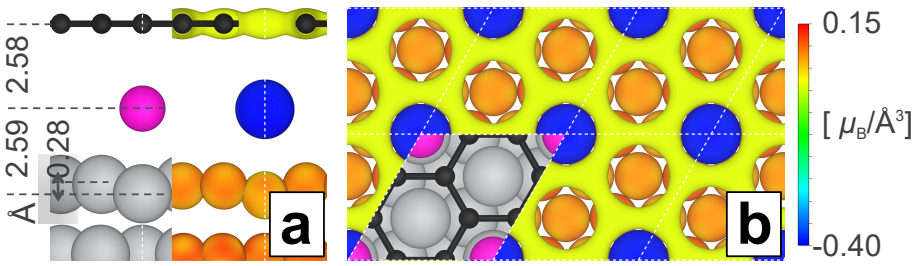

Figure 6.12: Ground-state relaxed structure and an isosurface of the total charge density (at $0.2\,e^-/$ Å^3) colored according to its total magnetization density for the Gr/Eu/Ni(111) system. (a): side view along the $[11\bar{2}]$ direction; structure on the left, isosurface plot on the right. (b): top view along the [111] direction; structure in the rhombus (surface unit cell), isosurface elsewhere. Color code for the structure: C-black, Ni-gray, and Eu-magenta. The crystallographic directions are given with respect to the Ir(111) substrate. Note that the plotted isosurface at the Gr site is ≈ 0.5 Å away from the carbon atoms. The Ni and C atoms have a positive magnetization (i.e. larger number of electrons in the spin-up channel) while the Eu atoms have a negative magnetization (i.e. larger number of electrons in the spin-down channel).

the Ni substrate, the calculation finds the top adsorption site to be the most stable, while the hcp (fcc) adsorption site is higher in energy by 30 meV (75 meV). For the Co substrate, the hcp adsorption site is the most stable, followed by the fcc (+20 meV) and top (+141 meV) sites. The resulting relaxed geometry for the Gr/Eu/Ni system is shown in Fig. 6.12 (a), left side. In the energetically favored adsorption geometry, the difference between the ferromagnetic (FM) and antiferromagnetic (AFM) structures is ≈ 55 meV for Ni and ≈ 104 meV for Co, in agreement with the experimental observations that suggest a stronger magnetic exchange coupling between Eu and Co atoms. Yet the preference for antiferromagnetic coupling is not limited to the energetically favored adsorption geometry: In fact for all optimized Gr/Eu/Ni(111) and Gr/Eu/Co(0001) configurations considered in our study we obtained that Eu is antiferromagnetically coupled to the metal underlayer. A visualization of the magnetic structure is given in Fig. 6.12 (a), right side and Fig. 6.12 (b), where the magnetization density on a selected isosurface of the charge density is given on a color scale.

To compare the calculated value for the Eu-Ni magnetic exchange coupling quantitatively to our experimental results, the experimental value can be estimated as $E_{\mathrm{FM-AFM}} = 2\mu_0\mu_{\mathrm{B}}gJH_{\mathrm{MF}}$ to obtain (24 ± 4) meV. The factor of two larger exchange coupling constant in theory compared to experiment could be the result of a typical overestimation of the exchange coupling due to self-interaction errors in DFT [193, 194].

In the following, we would like to discuss the magnetic exchange coupling mechanism. Campbell proposed a model to explain the antiferromagnetic alignment of $4f$ and $3d$ magnetic moments in intermetallic alloys of these elements [195]. There, the coupling is mediated by the $5d$ electrons of the rare earth [196, 197], because the strong localization of the $4f$ leads to too small direct overlap with the $3d$. In contrast, the $5d$ are spatially more extended. As the $5d$

shell on the rare earth site is less than half filled, while the 3d shell of Fe, Co, or Ni is more than half-filled, an antiferromagnetic alignment allows a stronger hybridization of 3d and 5d states near the Fermi level, and is therefore energetically favored. The intra-atomic 4f–5d exchange is always ferromagnetic, and thus in total, antiferromagnetic coupling of 4f to 3d results.

However, in contrast to most other rare earth, which assume a $6s^2 5d^1 4f^n$ electron configuration in bulk form, Eu is commonly assumed to have a $6s^2 5d^0 4f^7$ electron configuration not only as a free atom, but also as a bulk metal. Therefore, the occupation of the 5d orbitals of Eu was calculated in a number of different structures by DFT:

	Eu monolayer	Eu bulk	Eu/Ni(111)	Gr/Eu/Ni(111)
5d occupancy	0.17	0.27	0.39	0.46

Clearly, a small occupation number of the 5d is present also in the bulk. A comparison with the Eu monolayer shows that a higher coordination of the Eu atoms leads to more occupation of the 5d orbitals. Yet while the Eu 5d channel occupancy increases slightly with the coordination number from the Eu monolayer to the Eu bulk, a more substantial increase is caused by the specific chemical environment: from 0.17 for the Eu monolayer to 0.39 for the Eu-layer on Ni(111) and to 0.46 for the Eu layer sandwiched between Ni and Gr.

The magnetic moments found are:

	Ni 3d below Eu	Eu 4f	Eu 5d	C
spin moment [μ_B]	+0.423	−6.89	−0.16	+0.004

Thus, the magnetic coupling of Eu with Ni can be mediated by the 5d electrons in our system. We note that insofar as the same quantities were computed [*i.e.*, magnetic moment on carbon and Gr-Eu distance in Fig. 6.12 (a)], our results compare well with an earlier theoretical study of this system [198], despite there, a different adsorption position of the Gr/Eu layers relative to the Ni substrate was assumed.

In Fig. 6.13, we give the spin-resolved partial density of states in the carbon p_z, europium 4f and 5d, and first-layer nickel 3d orbitals. The Gr is strongly n-doped as expected from the Eu intercalation. Yet more interestingly, the electronic structure of Gr in (c) displays a substantial energy-dependent spin polarization. It amounts to about 15% at the Fermi level and reaches a factor 3 to 4 close to the Dirac point. It would be attractive to exploit the large spin polarisation close to the Fermi level, but this would require a considerable shift of the chemical potential by doping. Yet the calculated total induced magnetic moment of $0.004\mu_B$ per atom in Gr is still small.

Considering that the calculated induced magnetic moment on the carbon atom for the Eu-intercalated system is on the order of a factor 5 smaller than what has been calculated for Gr in direct contact with underlying Co or Ni (for which in Refs. [22] and [84] nonvanishing XMCD signals at the C K edge were reported), it is not surprising that our XMCD measurements at

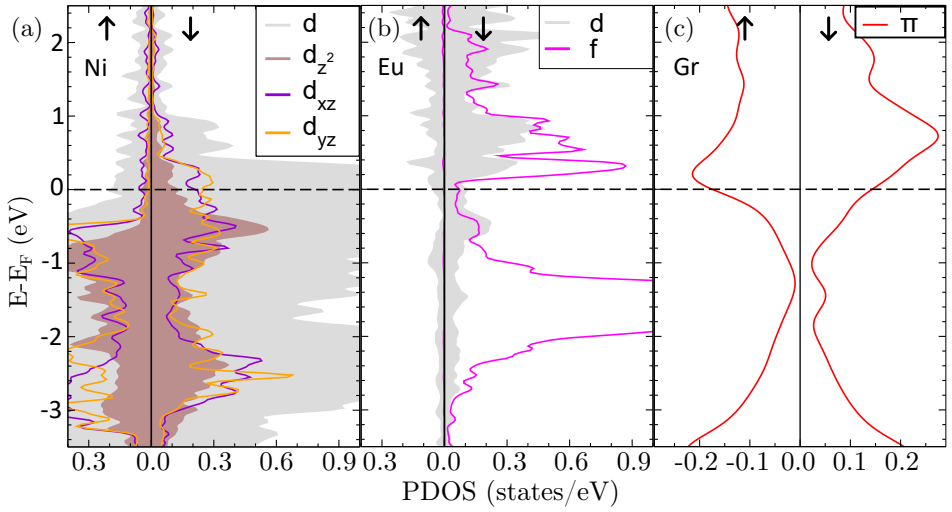

Figure 6.13: Spin-polarized local projected density of states (SP-PDOS) of the (a) surface $3d$ orbitals of the Ni atom below Eu, (b) Eu $4f$ and $5d$ orbitals, and (c) Gr π orbitals. The black arrows indicate the spin-up and spin-down channels.

the C K edge failed to display an unambiguous dichroic signal. Generally, such measurements are inherently difficult due to the lack of spin-orbit splitting in the carbon $1s$ initial state of the transition probed by X-rays at the K edge, which means that only orbital magnetism can be detected [199–201], and we expect that this orbital magnetic moment is much smaller than the spin moment [199].

Lastly, we discuss the near-edge X-ray absorption fine structure (NEXAFS) at the carbon K edge. Graphite was an early case where features in NEXAFS were directly mapped to transitions into specific valence bands [109]. Figures 6.14 (a) to (c) show the NEXAFS spectra of Gr/Ni (redrawn from Ref. [22]), of graphite (redrawn from Ref. [109]), and of Gr/Eu/Ni, respectively. Note that our measurements on Gr/Eu/Ni have been performed with circularly polarized X-rays at an incidence angle of 65°, while the spectra on graphite and Gr/Ni have been measured with linearly polarized X-rays at 60°. The pronounced feature at $\approx$ 286 eV (highlighted with gray background) is a double peak in the case of Gr/Ni, while it is a single peak in the case of graphite. In Refs. [152] and [202], the double-peak structure has been ascribed to transitions into two interface states that result from the hybridization of Gr π with Ni $3d$ states. It was furthermore found that upon intercalation of Al, this hybridization is lifted and the single peak as found in freestanding Gr as well as graphite is recovered. Here, we find that also by intercalation of Eu, the single-peak structure is recovered as seen in Fig. 6.14 (c), demonstrating that Gr can be brought into contact with a magnetic metal without destruction of its electronic structure.

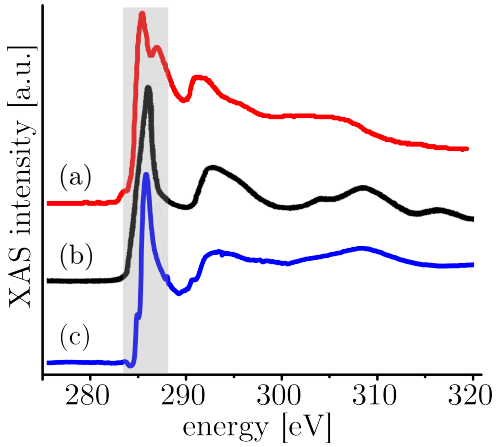

Figure 6.14: XAS at the carbon K edge for (a) Gr on Ni (redrawn from Ref. [22]), (b) graphite (redrawn from Ref. [109]), and (c) Eu-intercalated Gr on Ni (own data).

6.3 Conclusion and outlook

Europium intercalates easily under Gr/Ir(111), as well as Gr/Ni and Gr/Co, where it orders in atomically well-defined superstructures.

Under Gr/Ir(111), three different intercalation structures were understood, in order of increasing Eu coverage: $(2 \times 2)_{\mathrm{Gr}}$, $(\sqrt{3} \times \sqrt{3})\mathrm{R30}^{\circ}_{\mathrm{Ir}}$, and $(\sqrt{3} \times \sqrt{3})\mathrm{R30}^{\circ}_{\mathrm{Gr}}$. The magnetic behavior was investigated by XMCD. One sample with the $(2 \times 2)_{\mathrm{Gr}}$ Eu monolayer phase under Gr/Ir(111) exhibited a magnetization loop consistent with paramagnetic behavior at $T = 10\,\mathrm{K}$. Of the $(\sqrt{3} \times \sqrt{3})\mathrm{R30}^{\circ}_{\mathrm{Gr}}$ structure under Gr/Ir(111), three samples were investigated in three different beamtimes in 2011, 2012, and 2016. In all, ferromagnetic coupling was found, as well as an in-plane anisotropy, which could be explained using a model with only dipolar interaction. However, the preparations differed in significant details of the magnetic behavior: The 2011 likely was contaminated with EuO on top of Gr, due to issues with the preparation conditions. But also the later two samples in 2012 and 2016, which were both prepared without EuO contamination, differed in their magnetic behavior: The 2012 sample had no quasi-spontaneous magnetization, while the 2016 had; while at high fields, the 2012 preparation saturated faster. A consistent interpretation was not obtained and more measurements are needed for a full understanding. The intercalation systems Gr/$(\sqrt{3} \times \sqrt{3})\mathrm{R30}^{\circ}$/Ir(111) could principally be a nice model system to explore the physics of a truly two-dimensional Heisenberg ferromagnet, where only the dipolar interactions break the conditions of the Mermin-Wagner theorem [183, 203]. This is because the shape anisotropy, which scales with the square of the magnetic moment and the inverse of the layer thickness, is uniquely high at $\approx 300\,\mu\mathrm{eV}$ (i.e., 3 K), comparable to the temperature, while the spherically symmetric and highly localized $4f^7$ strongly suppresses single-ion anisotropy. However, the occurrence of several different phases in this system, which are close in coverage, is likely responsible for difficulty in preparing samples with reproducible

magnetic properties.

The ordering temperatures of the Eu monolayer can be drastically enhanced by coupling to thin films of the 3*d* ferromagnets Ni and Co. In an attempt to achieve such hybrid 3*d*–4*f* systems, we investigated Ni intercalation under Gr/Ir(111). To achieve full intercalation, the deposition of Ni onto Gr/Ir(111) at elevated temperature (800 K) is preferable over the deposition at room temperature followed by annealing. Yet films with a thickness on the order of 10 ML could not be intercalated under Gr/Ir(111) without forming metal clusters on top of Gr or starting to alloy. To obtain Gr on Ni and Co thin films, it is instead possible to grow Ni and Co films on Ir(111), followed by Gr growth on the films at 800 K. Subsequent Eu intercalation results exclusively in a $(\sqrt{3} \times \sqrt{3})$R30° structure with respect to Gr, including under rotated Gr. The magnetic behavior of this 3*d*-4*f* hybrid system is characterized by an antiferromagnetic coupling of the Eu monolayer to the 3*d* metal, which can be described as an exchange field on the order of a few ten tesla. The antiferromagnetic coupling results from indirect exchange via the Eu 5*d* orbitals, which become partially occupied due to the chemical environment in the intercalation layer. In NEXAFS, we observe that the Gr is electronically decoupled from the 3*d* metal substrates by Eu intercalation. A magnetic moment is induced in Gr, which is however even smaller than the induced moment in non-intercalated Gr on Ni. The desired decoupling via the intercalation layer apparently works against the equally desired, induced magnetization in Gr.

Chapter 7

On-surface synthesis of organometallic compounds and sandwich molecular nanowires on graphene

The introduction and first section of this chapter are mostly adapted from our publication in Ref. [204], the authors of which are: F. Huttmann, N. Schleheck, N. Atodiresei, and T. Michely. Their contributions are as follows: NA woke the experimentalist's interest into cyclooctatetraene and contributed the DFT calculations and discussion on the EuCot imaging contrast. NS conducted the experiments under my guidance as part of his master thesis. I wrote most of the manuscript and the supplement. TM guided all efforts and wrote the abstract, conclusion and parts of the introduction. The results are also the subject of the master thesis of NS.

In this chapter, we pursued the growth of organometallic sandwich compounds from vapors of the metal and the ligand on graphene. Previously, most of these compounds have been synthesized only by pulsed laser vaporization of the metal and reaction with vapor of the organic ligand in a noble gas stream, followed by mass spectrometry [96, 205, 206]. Using a beam deflection method, it was then found that the magnetic moments of VBz [100] and EuCot wires [98] increase with the number of metal atoms in the wire, while for TmCot, evidence for antiferromagnetic coupling was seen. However, the length of the wires obtained by the gas-phase synthesis was limited to about 30 metal atoms in the case of EuCot [207], and only 6 for VBz [205, 208]. For EuCot, also synthesis in solution has been described even before such materials were considered for molecular spintronics [97]. A recent study characterized the product obtained in this way with a variety of methods [209], showing that it is polycrystalline, but contaminated

with ferromagnetic EuO ($T_C = 69\,\mathrm{K}$).

Due to the high inertness of graphene, deposited metals have a tendency to dewet the surface, and a weak interaction with the substrate appears as an ideal condition to facilitate the reaction of the metal atom with the organic ligand. Thus, we hope for a case of van der Waals epitaxy, where sharp interfaces and high-quality growth may be realized despite large structural mismatches [210, 211]. Furthermore, when the bond to the substrate is of the van der Waals kind, the electronic structure of the organometallic compounds can be preserved. Beyond these rather technical arguments, graphene is a conductor with not only a high electron mobility but also a high spin diffusion length due to its negligible spin-orbit coupling, and the strong interest into magnetic contacting of graphene provides another motivation to use this substrate [212–214].

In contrast to the use of covalent linking in on-surface synthesis [215–221], where the bond formation requires activation, for instance thermally, and where the substrate is often necessary as a catalyst, our on-surface synthesis necessitates a fully inert substrate, but no activation, as it is based on the reactivity of the metal atoms, as in vapor synthesis [222]. In a way, we thus extend the previously reported metalation of cyclic π-conjugated systems [223–226] and synthesis of double- and triple-decker complexes [227]. Compared to other metal-coordinated structures [228–232], the systems pursued here differ also in that the internal bonding fully dominates over the interaction with the surface. This strong internal bonding is signified by our observation of upright-standing planar molecules as the result of the organometallic synthesis.

Generally in our growth experiments, the amount of molecules was significantly larger than the amount of metal in order to avoid any of the latter being left over. The high vapor pressure of the small ligands used already at room temperature led to re-evaporation of the excess. This method of intentional overdosing of one of the components and back-evaporation of the excess has been on occasion termed MBE distillation [33]. It was shown to be most suited to achieve single-phase, stoichiometric thin films for binary compounds, *e.g.*, EuO with Eu excess [33], Bi_2Te_3 with Te excess [233], or FeSe with Se excess [234].

The chapter is organized as follows: Sections 7.1, 7.2, and 7.3 describe the results of growth experiments on EuCot, VBz, and TmCot, respectively. In section 7.4, we develop a substrate for orienting the growth of EuCot nanowires. In sections 7.5 and 7.6, we investigate some of the magnetic properties.

7.1 Growth of europium cyclooctatetraene wires

7.1.1 Carpet structure, bonding, and imaging contrast

Figure 7.1 (a) shows a large-scale scanning tunneling microscopy (STM) topograph after simultaneous dosing of Cot and Eu onto the graphene film resting on Ir(111) held at room temperature.

The surface is covered by compact islands in the shape of anisotropic crystallites with mostly straight edges. Often, the islands overgrow the atomic steps of the underlying Ir substrate in a carpet-like fashion. The in-plane orientation of the crystallites is apparently random. Depending on the tip and the tunneling conditions, the apparent height of the islands is in the range (6.1 ± 0.5) Å.

In Fig. 7.1 (b), a higher-resolved, Laplacian-filtered STM topograph shows that the crystallites are made of wires lying mostly parallel to each other. The moiré of graphene with Ir(111) [54] is shining through the nanowire carpet as seen in the inset of Fig. 7.1 (b). The molecular structure inside the wires is indicated in Fig. 7.1 (c) with an overlaid structural model, where the bond length are to scale. The periodicity along the direction of the wires is $a = (0.44 \pm 0.02)$ nm. This indicates that either only the Cot molecules or only the Eu atoms are imaged bright by the STM. Measurement of the distance between the centers of the wires shows a separation of only $b = (0.68 \pm 0.02)$ nm. This small value cannot be understood if the wires are seen as touching cylinders with a radius that is given by the van der Waals radius of the Cot molecules. Indeed, we find that the wires are always offset against their nearest neighbors by half an intra-wire repeat distance, which makes it possible for the Cot rings of neighboring wires to hook into each other and interlock.

N. Atodiresei conducted calculations within density functional theory (DFT) on such a two-dimensional EuCot carpet. The computational parameters of the DFT calculations have been previously described elsewhere [43, 126]. The resulting unit cell dimensions of $a = 0.435$ nm and

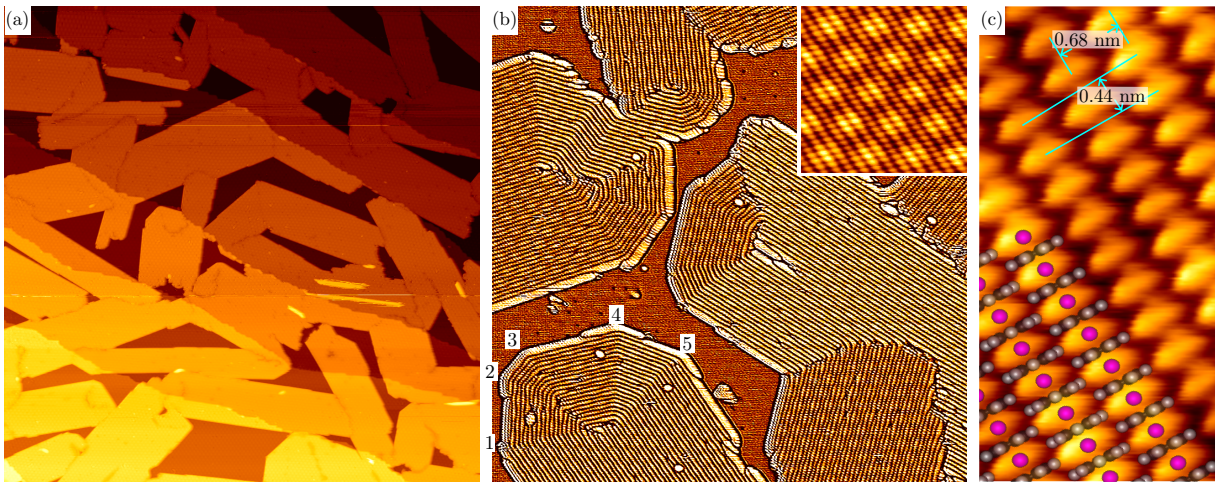

Figure 7.1: (a)-(c): STM topographs of a submonolayer film of EuCot nanowires on graphene on Ir(111). (a) $[(330\,\text{nm})^2, U = -3.4\,\text{V}, I = 36\,\text{pA}]$ overview of 2D crystallites covering the surface. (b) $[(82\,\text{nm})^2, U = -3.1\,\text{V}, I = 67\,\text{pA}]$, Laplacian-filtered to reveal the line structure in the islands, unfiltered inset $[(10\,\text{nm})^2, U = -0.9\,\text{V}, I = 40\,\text{pA}]$ to reveal the moiré superstructure of graphene on Ir(111) visible "through" the nanowire layer. (c) $[(5.1 \times 2.5)\,\text{nm}^2, U = -0.9\,\text{V}, I = 40\,\text{pA}]$, higher resolution partially overlaid with a structural model and indicated experimentally measured geometry.

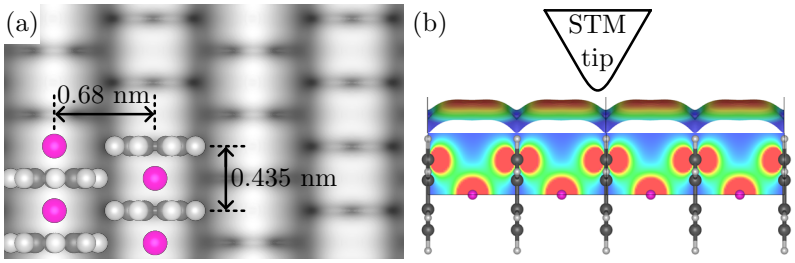

Figure 7.2: (a) Simulated STM image at sample bias voltage −2 V with overlaid structural model. (b) Side views of the charge density found in the energy interval $[E_F - 2\,\text{eV};\ E_F]$ corresponding to the simulated STM image in (a). The eightfold-rotation axis of the wire is in the horizontal. Lower part: Only structural model [atoms in (b) are drawn smaller than elsewhere]. Middle part: Color-coded plot of the charge density on a cut plane through the wire axis overlaid with the structural model shows contributions from the π-orbitals of the intersected carbon atom as well as from the Eu atom. Top part: Isosurface of the charge density further above the nanowire has its minimum at the Cot ring due to the nodal plane of the π orbitals; color encodes the height of the isosurface.

$b = 0.68\,\text{nm}$ are in agreement with the experiment. Tersoff-Haman type STM image simulations were performed as shown in Fig. 7.2 (a). When imaging the occupied states as done throughout this work (negative sample bias voltage U), the intensity maxima are located above the Eu atoms. However, a closer look at the electronic character of the imaged orbitals reveals that they are of π character, *i.e.*, belonging to the Cot rings. Figure 7.2 (b) shows a plot of the charge density on a cut plane through the wire axis [the wire axis is horizontal in Fig. 7.2 (b)]. Contributions to the charge density on this cut plane are from the Eu atom and from the π orbitals of the intersected carbon atom of the Cot ring. However, due to the faster asymptotic decay of the $4f$ orbitals, the charge density is completely dominated by the π states of the Cot ring further away from the wire axis, *i.e.*, at a distance relevant for STM imaging. There, the π charge density of two adjacent rings overlays into one flat maximum above the Eu atom, and the minimum is just above the Cot ring due to the nodal plane of the π orbitals. This finding is consistent with the known difficulty of tunneling into the localized $4f$ states in STM [103].

Other quasi-one-dimensional materials such as carbon nanotubes [235, 236] or MoSI molecular wires [237] are also known to occur in bundles. Yet while carbon nanotubes have a covalent and nonpolar bonding that leads to only van der Waals interaction between the tubes, EuCot wires have an ionic bonding character with alternating Eu^{2+} cations and Cot^{2-} anions [206]. That EuCot SMWs interlock with each other could then be seen to imply an ionic bonding component also between the wires, where Eu^{2+} ions of one wire are neighbored by Cot^{2-} ions of an adjacent wire, and vice versa. However, our DFT calculations reveal that the inter-wire bonding is predominantly of van der Waals character: The inter-wire binding energy is 189 meV when van der Waals interactions are included (using the functional as in Ref. [126]), but only 20 meV with a semilocal exchange-correlation functional (as used in Ref. [43]). The inter-wire

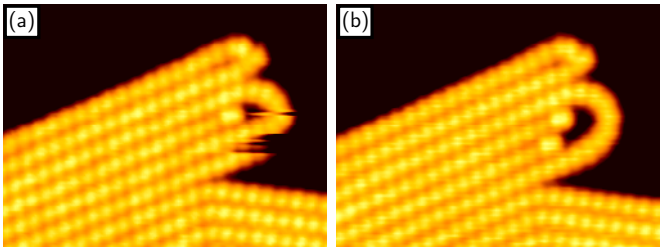

Figure 7.3: Successive STM topographs of a wire bundle end [$(10.2 \times 7.7)\,\mathrm{nm}^2$, $U = -2.4\,\mathrm{V}$, $I = 48\,\mathrm{pA}$].

binding energy is thus of a similar magnitude as the pure van der Waals interaction that holds, *e.g.*, polyethylene crystals together [238]. This underlines the one-dimensional character of the binding, even when the nanowires are present in a carpet, because the inter-wire binding pales in comparison to the intra-wire binding energy of 5.3 eV [239].

The strong ionic binding within a wire explains a peculiar observation in Fig. 7.1 (b): At the end of a crystallite, the wires do not end, but rather bend and turn around, forming mostly closed lines, sometimes reminiscent of the lines of a fingerprint. Naively, due to the ionic intra-wire bonding, a wire end will always have an unsaturated bond: Depending on whether the wire is Cot- or Eu-terminated, either a Cot ring is missing one electron so that it cannot achieve its favorable configuration with 10 π electrons, or a Eu atom has one $6s$ electron left over. The end of a wire could also be called a polar termination [240] of the ionic nanowire crystals, because a wire would have to be electrically charged in order to possess at its ends the oxidation state that it has inside the wire. The unique electronic properties of the wire ends sometimes let them appear as bright protrusions in STM topographs as seen in Fig. 7.3. Even though a polar catastrophe cannot occur in a one-dimensional crystal, and although the structure at the wire end in our experiments is unknown, wire ends are clearly expected to be energetically unfavorable and thus possibly unstable. We observed such an instability manifesting itself in the reconfiguration of a wire bundle end while the STM tip is scanning over it, as seen in Fig. 7.3 (a). Likely, the switching is induced by the STM tip.

7.1.2 Bending angle quantization

Next, we would like to explain why the wire bundles in Fig. 7.1 (b) do not bend continuously, but rather by discrete angles. The idea is as follows: If a wire bundle bends, the wire on the outside of the curve must have a longer path than the wire on the inside of the curve. However, if the energetically very favorable interlocking is to be kept, the path length of adjacent wires can differ only by multiples of the intra-wire repeat distance a, and exactly one times a in the simplest case. To illustrate this concept, Fig. 7.4 (a) shows two successive, discrete bends of a bundle in an STM topograph with intra-wire resolution. Note that the longer-range, 2.5 nm

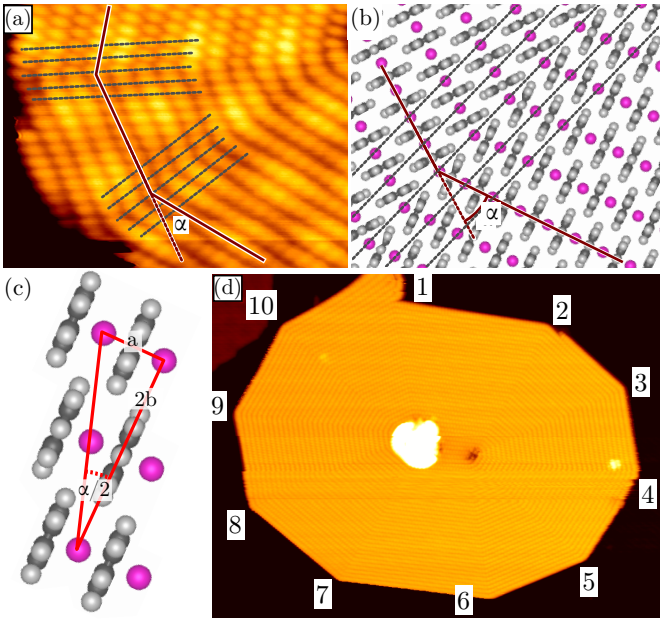

Figure 7.4: (a) STM topograph [$(11 \times 8.6)\,\mathrm{nm}^2$, $U = -1.6\,\mathrm{V}$, $I = 61\,\mathrm{pA}$] of two successive bends of a nanowire bundle by a characteristic angle. Dashed black lines connect intensity maxima in lines parallel to the bend line. (b,c) Sketch of the model to explain the characteristic bending angle. Atom colors: pink Eu, black C, white H. (d) STM topograph of a decagonal spiral of nanowires [$(67 \times 52)\,\mathrm{nm}^2$, $U = -2.4\,\mathrm{V}$, $I = 48\,\mathrm{pA}$].

periodicity of bright maxima is a result of the underlying moiré of graphene on Ir(111) and is irrelevant here. The model for one such bending is seen in Fig. 7.4 (b). That this model fits the observation well is seen if one connects either the Eu atoms or Cot rings by lines the way it is done in both Fig. 7.4 (a) and 7.4 (b). The fact that these lines are parallel to each other on both sides of the bending in the STM topograph is strong support for the model. By geometrical construction as displayed in Fig. 7.4 (c), we obtain that the bending angle α must be discrete and results from the ratio of inter-wire distance b to intra-wire distance a via the relationship

$$\alpha = 2\arctan\left(\frac{a}{2b}\right) \approx 2\arctan\left(\frac{4.4 \pm 0.2}{2(6.8 \pm 0.2)}\right) \approx (36 \pm 2)^\circ.$$

It follows that 10 bends are necessary to obtain a full circle (*i.e.*, $10 \cdot 36^\circ = 360^\circ$), or 5 bends for a half circle. A half-turn is nicely observed on the crystallite in the lower left corner in Fig.7.1 (b), where we numbered the turns 1 to 5 for clarity. If we use graphene on Ir(111) intercalated by Eu till saturation [30] instead of pristine graphene for growth, decagonal spirals like the one in Fig. 7.4 (d) are commonly observed, which exhibit the full 10 turns. The growth in spirals implies that wires can become very long, up to 1 μm. We note that growth on the strongly n-doped Eu-intercalated graphene does not change the structure of the wire bundles, but affects the overall morphology to some extent and favors spiral formation, for reasons that are not obvious. Another effect is the occasional growth of a second layer of EuCot wires on top

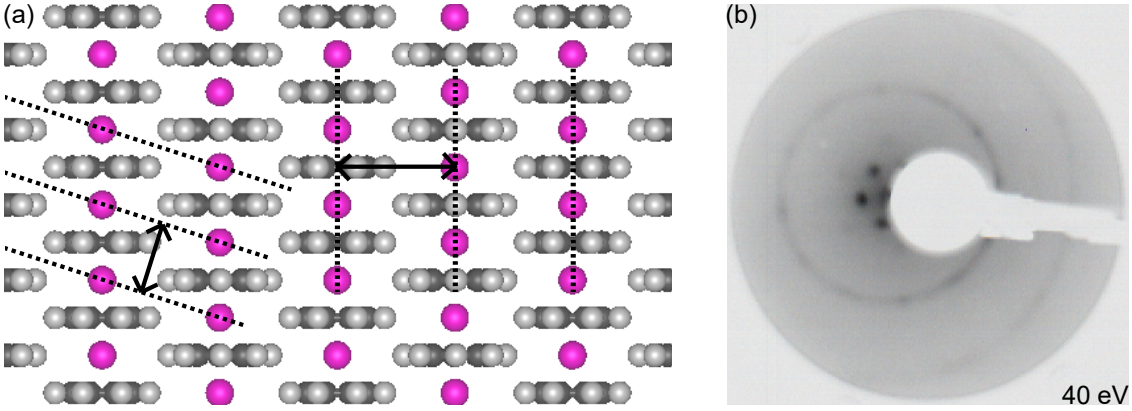

Figure 7.5: (a): EuCot carpets as a two-dimensional crystal with centered rectangular lattice and 2 EuCot formula units per conventional unit cell with the two sets of Bragg lines corresponding to the longest Bragg lines separation and thus shortest reciprocal space vectors. (b): MCP-LEED image of monolayer EuCot carpets, two rings result from scattering from the Bragg lines as indicated in (a).

of an existing carpet.

7.1.3 Diffraction from carpets

The EuCot carpet is a two-dimensional crystal with a centered rectangular lattice and 2 EuCot formula units per conventional unit cell. Due to the centered lattice, there are systematic extinctions of reflections. In analogy to the Bragg planes of a three-dimensional crystal, we use the term Bragg lines here. The two non-extincted sets of Bragg lines with the largest lattice spacings and thus shortest reciprocal lattice vectors are indicated in Fig. 7.5 (a). Notably, the reciprocal lattice vector with $k = 2\pi/a$ is extinct. A LEED pattern of a sample with EuCot carpets prepared as in Fig. 7.1, taken with an MCP-LEED, is shown in Fig. 7.5 (b). The two rings correspond to scattering from the two sets of Bragg lines indicated in (a). The intensity on the rings is slightly enhanced for rotations of both 0° and 30° with respect to the dense-packed rows of the substrate, implying a preferential orientation of the crystallographic axes of the EuCot along both, the zigzag and armchair direction of the Gr.

7.1.4 Isolation of wires

Up to now, the nanowires have always been part of extended carpets. In order to obtain nanowires well separated from each other, we have to overcome the significant attractive interaction between them. To achieve this, we pre-patterned the graphene substrate to guide the growth of isolated wires. This is shown in Fig. 7.6. When graphene on Ir(111) is intercalated with submonolayer amounts of Eu by exposure at elevated temperatures, a complex pattern of Eu-intercalated and non-intercalated graphene areas emerges as previously described in detail in Ref. [83]. We have used an Eu amount of $\approx 80\%$ ML, so that about 80% of the sample surface

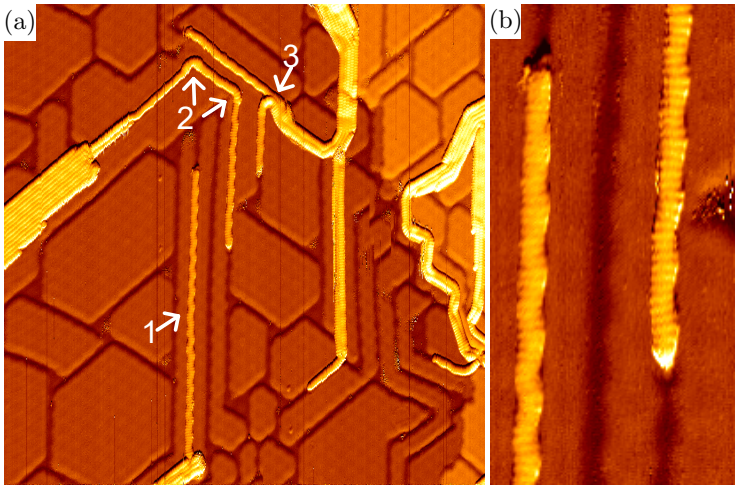

Figure 7.6: STM topographs ($U = -1.8\,\mathrm{V}$, $I = 25\,\mathrm{pA}$) of a sample prepared by simultaneous deposition of Cot and Eu at 300 K onto partially ($\approx 80\%$ ML) Eu-intercalated graphene. Some nanowires outside of wire bundles are present in trenches formed by the Eu intercalation pattern. (a) $(82\,\mathrm{nm})^2$. (b): Zoom into an area in (a) reveals intra-wire resolution, $(22 \times 11)\,\mathrm{nm}^2$. Topographs were overlaid with their horizontal derivatives to enhance visibility.

consists of islands with intercalated Eu underneath graphene, and 20% of the sample surface consists of trenches in between these islands, where the graphene is not intercalated. The trenches have a quantized width of around 1.4 nm. The graphene itself is continuous all over the sample. When EuCot wires are then grown by simultaneous exposure at room temperature, isolated wires appear in these trenches. The long straight wire marked "1" in Fig. 4 (b) has a length of about 103 EuCot units, determined by counting. The light wiggling of the wires in the trenches follows the periodicity of the moiré superstructure of graphene on Ir(111). Occasionally, single wires turn around the edges of intercalation islands, such as at "2", or a bundle of two wires separates into two isolated wires at a threefold crossing of intercalation trenches, like at "3". Due to the consistency and excellent order, the isolated wires prepared in this way appear very well suitable for investigation by local scanning tunneling spectroscopy. On the other hand, in measurement techniques that average spatially over the sample, such as photoemission or x-ray absorption, the signal from isolated wires will still be small compared to the signal from wire bundles, because the latter contains most of the EuCot material. Thus, for spatially averaging measurements, an approach that separates the wires differently, *e.g.*, by adding inert alkyl side chains on the Cot ring, appears more promising.

7.1.5 Growth morphologies under various preparation conditions

We have investigated the growth of EuCot on graphene using five different preparation recipes that we labeled (a) to (e), as shown in Fig. 7.7. Remarkably, EuCot nanowires form in all cases where Cot and Eu can meet on the surface, regardless of the deposition temperature (20 K or

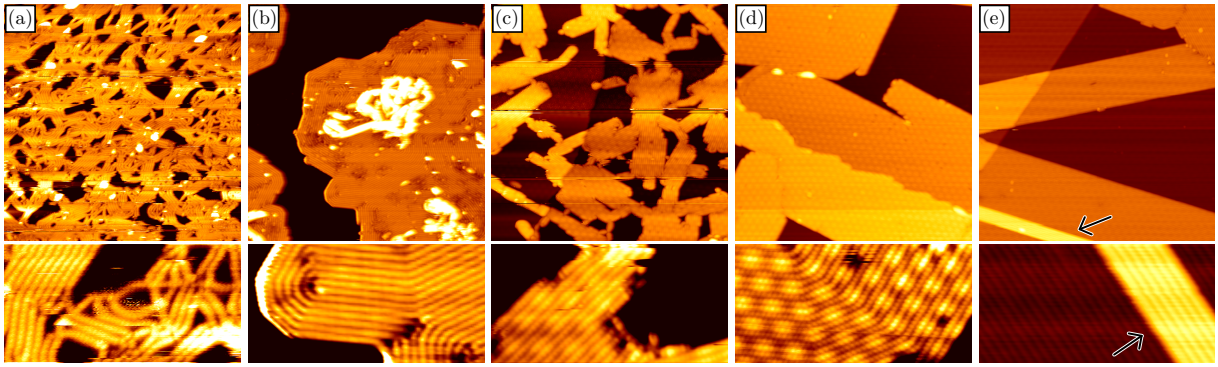

Figure 7.7: STM topographs of EuCot nanowires formed under five different preparation conditions, see text. Image size top row: $(82\,\mathrm{nm})^2$. Bottom row: $(20 \times 10)\,\mathrm{nm}^2$.

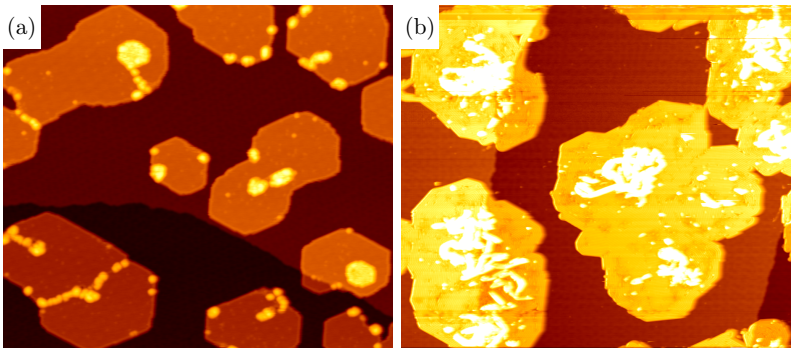

Figure 7.8: STM topographs of Eu deposited onto Eu-intercalated graphene at room temperature (a) before exposure to Cot vapor (b) after exposure to Cot vapor. Image size: $(164 \times 144)\,\mathrm{nm}^2$.

300 K) and deposition order (simultaneous, Cot first, or Eu first). However, each recipe results in a different morphology of the growth, and each of these morphologies yields insights, as will be discussed in the following. The amount of Eu is the same in all cases at 0.44 monolayer (ML) Eu. 1 ML of Eu here is defined as corresponding to one layer of Eu in the $(\sqrt{3} \times \sqrt{3})R30°$ superstructure, which Eu forms on graphene.

In recipe (a), a layer of Cot with a thickness on the order of 10 ML is firstly deposited onto the cold sample, at $T = 20\,\mathrm{K}$. Subsequently, Eu is deposited, and only then the sample is warmed up to room temperature. As seen in Fig. 7.7 (a), this results in a disordered, spaghetti-like growth mode. This is explained as follows: At 20 K, mobility of both the Cot molecule and the Eu atoms is likely frozen. The reaction between Eu and Cot therefore will take place during the warm-up from 20 K to room temperature as soon as a temperature is reached where the mobility becomes high enough. However, once Eu and Cot have reacted into nanowires in the first best and thus chaotic way, the wires cannot separate and rejoin with the available thermal energy even at room temperature. Therefore the arrangement is frozen in.

In recipe (b), graphene was first intercalated with Eu to saturation by sufficiently long

deposition at a sample temperature of 700 K [30]. Then, an amount corresponding to 0.44 ML Eu was deposited onto the sample at 300 K. This results in the formation of hexagonal, mostly single-layer islands of Eu on top of graphene as seen in Fig. 7.8 (a). Upon exposure of these islands to a Cot excess, the coverage of the islands expands from ≈0.44 ML to ≈0.66 ML, as seen in Fig. 7.8 (b). The monolayer-high islands are now completely composed of EuCot wires as seen in Fig. 7.7 (b). The structures on top of the monolayer-high islands are much less well-ordered, but consist of nanowires, too. This proves that even when Eu is already present in the form of compact metal islands, the reaction with Cot is able to break the Eu-Eu bond to form EuCot.

That all Eu deposited onto graphene at room temperature (without Cot) arranges into extended hexagonal islands is only the case if the graphene has been previously fully intercalated with Eu. Deposition of Eu onto only partially or non-intercalated graphene instead yields small and mobile Eu clusters in equilibrium with islands [29, 86].

Thus to compare, we also deposited 0.44 ML Eu at 300 K and subsequently a Cot excess just as in recipe (b), but this time, on non-intercalated graphene. The morphology as shown in Fig. 7.7 (c) is then indeed very different. The nanowires are now arranged in elongated crystallites, a shape clearly unrelated to the morphology of the Eu adsorption, which we attribute to the mobility of Eu during the growth.

To increase the mobility of Eu during deposition even further, we should make Eu available on the surface as atoms, rather than as clusters. To do so, we simultaneously expose the sample to Cot and Eu vapors, so that the reaction will occur before the clustering of the Eu metal. We have opened the Cot dosing valve always before and closed it after the shutter to the Eu evaporator, so that there is not only more Cot than Eu in total, but also at every single point in time. Without Eu intercalation, this is the recipe (d) shown in Fig. 7.7 (d), which is the one that is also shown in Fig. 2 and 5 (a) of the main paper. We observe that the crystallites have become much larger, indicating a reduced nucleation density, in line with our expectations. The defect density is also reduced, because Eu in metal clusters does not have to rearrange into EuCot islands, but rather the EuCot islands can grow by direct incorporation of Eu adatoms.

Fig. 7.7 (e) is an STM topograph obtained when graphene is first intercalated with Eu to saturation, and afterwards simultaneously exposed to 0.44 ML Eu and Cot vapor as before. In contrast to recipe (d), small areas of a second layer of nanowire bundles on top of the first layer have formed as indicated by the arrows in Fig. 7.7 (e). This is despite the fact that the first layer is not completed at this coverage. Nanowires in the second layer lie mostly parallel to the first layer. Whether and at which coverage a second layer tends to form before completion of the first layer is a typical question in microscopic investigations of thin film growth (*e.g.*, Ref. [241]). In our case, we explain the higher tendency of EuCot to form a second layer on Eu-intercalated compared to non-intercalated graphene by the energetics of the adsorption of Eu atoms: The binding energy of a Eu atom on Eu-intercalated graphene is significantly lower than the binding energy on non-intercalated graphene, a result of the ionic bonding character and resulting charge

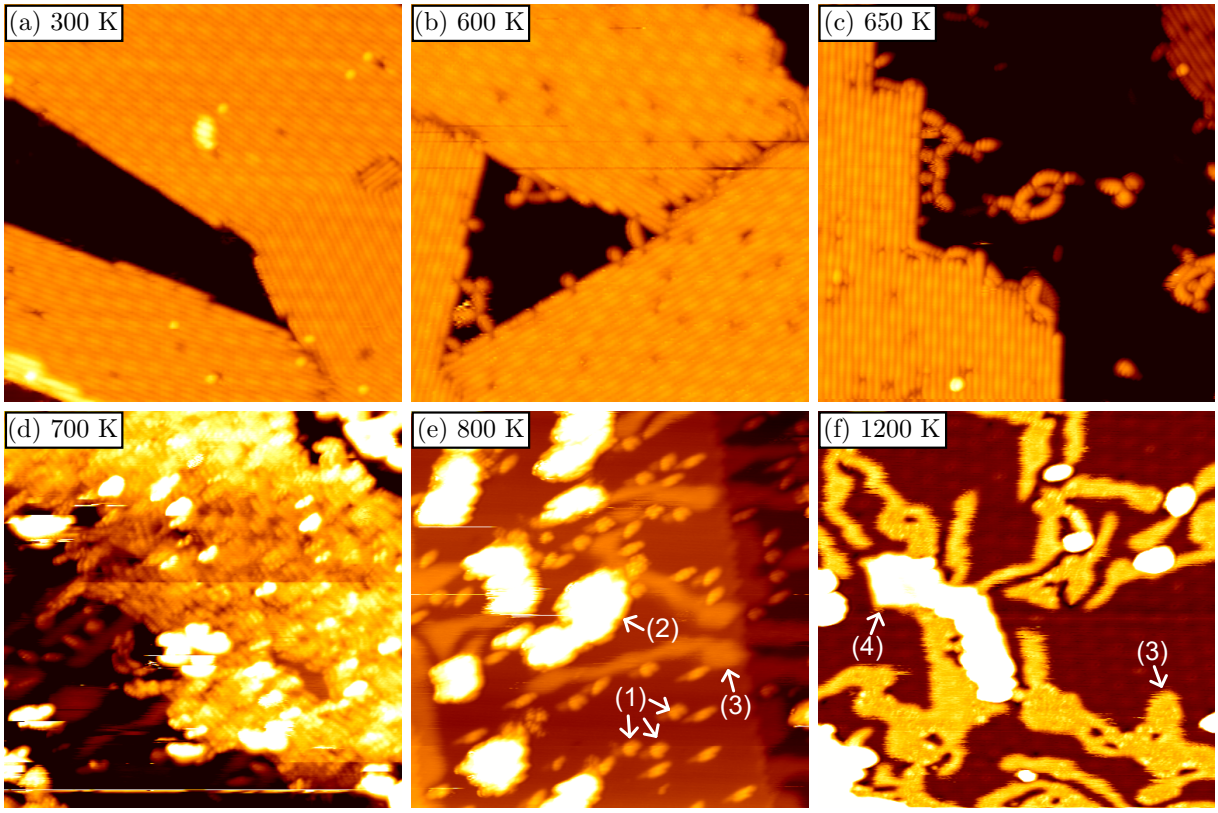

Figure 7.9: STM topographs of nanowire crystallites formed by simultaneous exposure on non-intercalated graphene at room temperature [(a)], and subsequently stepwise annealed to the indicated temperatures [(b-f)]. Image size: 41 nm^2. Note that (d) suffers from a double-tip artifact. For an explanation of numbers (1)–(4), see text.

transfer [86]. If a Eu atom binds more strongly to graphene, it is more likely to reside there while waiting to react with a Cot molecule, and the formation of a second layer, which presumably requires the presence of Eu atoms on top of the nanowire islands, will be inhibited. We thus explain the stronger tendency toward multilayer formation on Eu-intercalated graphene as a kinetic effect during growth.

7.1.6 Temperature stability

To assess the thermal stability of the wire bundles, we have grown EuCot at room temperature and annealed to successively higher temperatures. Figure 7.9 shows STM topographs before [Fig. 7.9 (a)] and after stepwise annealing for 3 minutes at the indicated temperatures [Fig. 7.9 (b) to (f)]. Imaging was performed after cool-down to room temperature in all cases.

Annealing at 600 K [Fig. 7.9 (b)] leaves the wire bundle structure mostly intact. Only at the edges of the islands, what seems like small wire segments sticks out. More of this is seen at 650 K [Fig. 7.9 (c)]. The small wire segments detached from the islands form a network-like structure, where usually three nanowire segments meet in one point.

Annealing at 700 K [Fig. 7.9 (d)] destroys the ordered nanowire carpets, although a certain texture still seems to hint at the original orientation of the wires. The temperature where we observed decomposition to start is thus somewhat lower than the $500°\mathrm{C} \mathrel{\hat{=}} 773\,\mathrm{K}$ value given by Ref. [97] for bulk EuCot obtained by their solution method. It is plausible that the dense packing of nanowires in a 3D structure leads to a stabilization compared to nanowires in a 2D carpet on a surface, especially considering that the decomposition of the 2D carpets appears to start at the edges.

Annealing at 800 K leads to complete decomposition as seen in Fig. 7.9 (e). We identify the following structures on the sample and marked them in the figure: (1) protrusions of almost uniform shape and a typical height of 3 Å arranged in the moiré lattice; (2) clusters of typically around 10 Å height with irregular shapes; (3) stripes and small islands of a height of about 2 Å. The nature of (1) and (2) is unclear to us, while (3) is easily attributed to Eu which has intercalated underneath the graphene sheet [83], as the decomposition of nanowires releases the Eu.

Annealing at 1200 K [Fig. 7.9 (f)] makes (1) and (2) disappear, while the amount of intercalated Eu seems to have increased. The irregularities in the pattern of intercalated Eu indicate a defective graphene layer (compare with Ref. [30], Fig. 3). In addition to the Eu intercalation islands, a new type of island appears, marked (4) in Fig. 7.9 (f), with a height of roughly 5.5 Å. We suspect that this structure consists of a bilayer of graphene intercalated with one layer of Eu, as $(5.5\,\text{Å} - 2\,\text{Å}) \approx 3.35\,\text{Å}$ approximately corresponds to the distance between two graphene layers in graphite.

In order to test whether Cot desorbs in molecular form from the sample during the decomposition, we have placed the sample under a mass spectrometer and monitored the signal at a mass-to-charge ratio of $m/q = 104\,e/u$, corresponding to singly ionized Cot, while applying a heating ramp with a few Kelvin per second. No signal was observed, indicating that Cot does not desorb in molecular form. This is consistent with the bilayer graphene found after annealing to 1200 K and clusters of carbonaceous material if some or all of the carbon deposited on the sample in the form of Cot does not desorb during heating.

One could imagine that the nanowire islands are actually not stable up to 600 K, but rather, that they dissolved during heating and re-assembled during cool-down, and thus appear unchanged when imaged again at 300 K. The fact that different growth morphologies can be produced as shown in Fig. 7.7 allows us to test this hypothesis: If the wires dissolved during heating, then there is no reason why the morphology after annealing should be the same as before annealing; in fact, the morphology after annealing should be independent of what was before, because the islands after annealing would always condense from the same "fluid" high-temperature phase. In Fig. 7.10, we compare the morphology obtained as in Fig. 7.7 (b), before [Fig. 7.10 (a)] and after [Fig. 7.10 (b)] annealing to 600 K, just below the onset of decomposition. It is seen that the morphology after annealing is very similar to before anealing, and at the

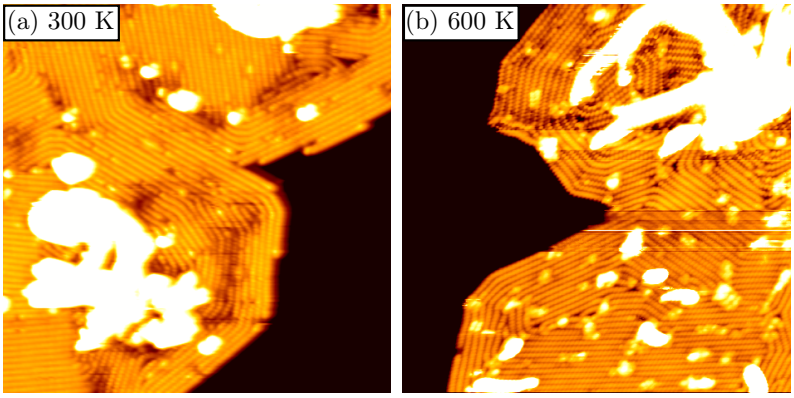

Figure 7.10: STM topographs of nanowire islands formed by evaporation of Eu onto Eu-intercalated graphene and subsequent exposure to Cot at room temperature [*i.e.*, as in Fig. 7.7 (b)]. (a): Before annealing. (b): After annealing to 600 K. Image size: $(41\,\mathrm{nm}9)^2$.

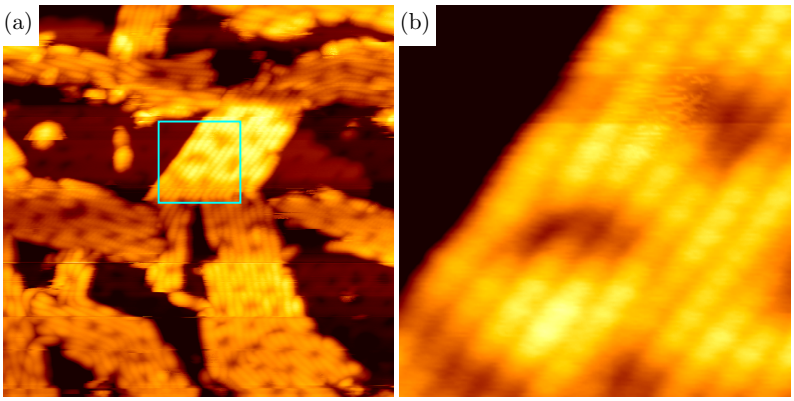

Figure 7.11: STM topographs of nanowire crystallites formed by simultaneous exposure on hexagonal boron nitride. (b) is a zoom into the area in (a) indicated by the square. Image size: $(41\,\mathrm{nm})^2$, zoom-in $(7\,\mathrm{nm})^2$.

same time very different from another morphology annealed to the same temperature as seen in Fig. 7.9 (b). In particular, islands in Fig. 7.9 (a) and (b) have longer straight edges than the islands of Fig. 7.10 (a) and (b), and the wires themselves are also mostly straight for the former and convoluted for the latter. Based on these observations, we exclude dissolution of islands before decomposition.

7.1.7 Growth on hexagonal boron nitride

If the growth of the EuCot wires on graphene is a case of van der Waals epitaxy, then this implies that any sufficiently inert substrate will enable the growth. A h-BN monolayer is isostructural and isoelectronic to graphene, however, in contrast to graphene it is a good insulator. Therefore, h-BN may be a better substrate if one would want to study the electronic structure by scanning tunneling spectroscopy or even the transport properties of the nanowire carpets. Figure 7.11

shows the result of the exposure of h-BN/Ir(111) to Eu and Cot vapor, using the same parameters as in the experiment on graphene shown in Fig. 7.7 (d) and Fig. 2 of the main paper. We can observe that also in the case of h-BN, nanowire crystallites grow. However, the crystalline quality is significantly worse in the case of h-BN. For example, the typical size of a nanowire crystallite is on the order of 10 to 20 nm for h-BN, but is 50 to 100 nm for graphene. Possibly, this is related to the stronger interaction of h-BN with the Ir(111) surface compared to graphene, which leads to a higher corrugation and a more chemisorbed binding character of h-BN to Ir(111) [1], and could be remedied by using a more weakly interacting substrate for h-BN, such as Cu or Ag(111) [244–246].

7.2 Growth of vanadium benzene sandwich molecules

This section is not published or in preparation for publication, but the results are described in the bachelor thesis of M. Seçkin. I conceived to attempt growing vanadium-benzene wires, and suggested to T. Michely to offer this as a bachelor thesis project for M. Seçkin. The experiments were conducted by M. Seçkin under my guidance. Some experimental guidance was also by N. Schleheck when I was away.

After the experiments with EuCot were so surprisingly successful, we asked ourselves: How general is this method, i.e., can we make nanowires with other metals, and with other ligands,

[1] While the work of Schulz *et al.* [242] gives a peak-to-peak corrugation of ≈ 0.4 Å for h-BN/Ir(111), about the same as found for graphene/Ir(111) [56, 73] and thus indicating a similar strength of interaction with the substrate,

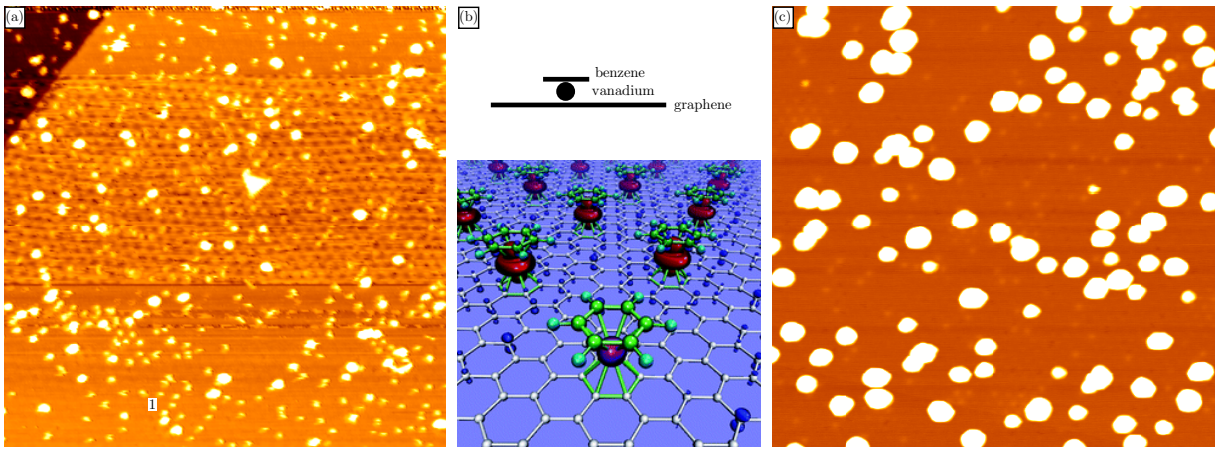

Figure 7.12: STM topographs taken at room temperature, both $(88\,\mathrm{nm})^2$. (a) Submonolayer amounts of vanadium deposited in a benzene background pressure of $5 \cdot 10^{-7}$ mbar onto Gr/Ir(111). "1" indicates an area where ordering of the small dots in the moiré periodicity is visible. (b) Upper part: Sideview sketch of supposed benzene-vanadium-graphene complex. Lower part: Structural model of periodic benzene-chromium-graphene, reproduced from Ref. [247], © 2011 ACS. (c) Submonolayer amounts of vanadium deposited without benzene onto Gr/Ir(111).

as well? Vanadium-benzene (VBz) is another sandwich molecular wire that was predicted to possess outstanding electronic properties: Ferromagnetic and half-metallic, i.e., conducting for one spin direction and insulating for the other [37]. This material was therefore our next choice.

In a first experiment, we tried to dose an excess of benzene (chamber pressure $5 \cdot 10^{-7}$ mbar) and submonolayer amounts of vanadium at the same time onto the Gr/Ir(111) substrate held at room temperature, in analogy to the best recipe for EuCot as shown in Fig. 7.1. The result is shown in Fig. 7.12 (a). Small clusters and even smaller, uniform dot-like objects cover the surface, but no nanowires or islands of any other material are visible. The smaller dot-like objects are seen ordering according to the moiré in some parts. Because the small dot-like objects are rather uniform in appearance, and very different from the larger clusters, they likely consist only of a small number of constituents. I speculate here that they are made of a benzene molecule on top of a vanadium atom, which is adsorbed to the graphene in the center of a carbon ring, as sketched in Fig. 7.12 (b), upper panel. Such a structure was calculated to be rather stable for the analogous case of chromium [247], and the complexation of graphene with chromium-benzene has already been experimentally reported, based on the reaction of chromium hexacarbonyl $Cr(CO)_6$ with ultrasonically exfoliated graphite in solution. The lower panel of Fig. 7.12 (b) shows a rendering of the structure of Bz/Cr/Gr taken from Ref. [247]. We suppose that this structure should be stable for vanadium as well, because the molecule VBz_2 exists, in analogy to $CrBz_2$ [248, 249].

We have conducted experiments depositing vanadium on Gr/Ir(111) without benzene, the result is shown in Fig. 7.12 (c). Without benzene, the V clusters are larger and higher, and the clusters are hexagonal in shape with a hexagon's straight edge aligned with the dense-packed rows of the substrate. This shows that these clusters are single crystals of vanadium with a well-defined epitaxial orientation with respect to the substrate. Thus, while the benzene exposure did prevent the V from forming larger clusters, no VBz wires were obtained in experiments with deposition at room temperature.

We have therefore tried an alternative recipe, where we deposited firstly an amount of $\approx$ 10 ML of benzene onto the sample held at 20 K, and subsequently deposited submonolayer amounts of vanadium atoms onto this film. This recipe would be analogous to what is shown in Fig. 7.7 (a) for EuCot, where this recipe worked to create wires, but led to worse ordering compared to room-temperature simultaneous exposure. The sample was then annealed at 200 K in order to desorb the benzene excess, and cooled down again for STM imaging. Figure 7.13 (a)-(c) shows overview topographs of these experiments for three different amounts of deposited vanadium. Islands have formed, which are coalesced for the highest vanadium coverage. Because the benzene and vanadium were deposited at 20 K, and the annealing took place at only 200 K, the formation of extended islands implies a low diffusion barrier and low barrier of detachment from islands, which is typical for small van-der-Waals-type adsorbates. For the smallest coverage,

recent investigations of Farwick zum Hagen *et al.* [243] point to a much stronger corrugation of h-BN/Ir(111).

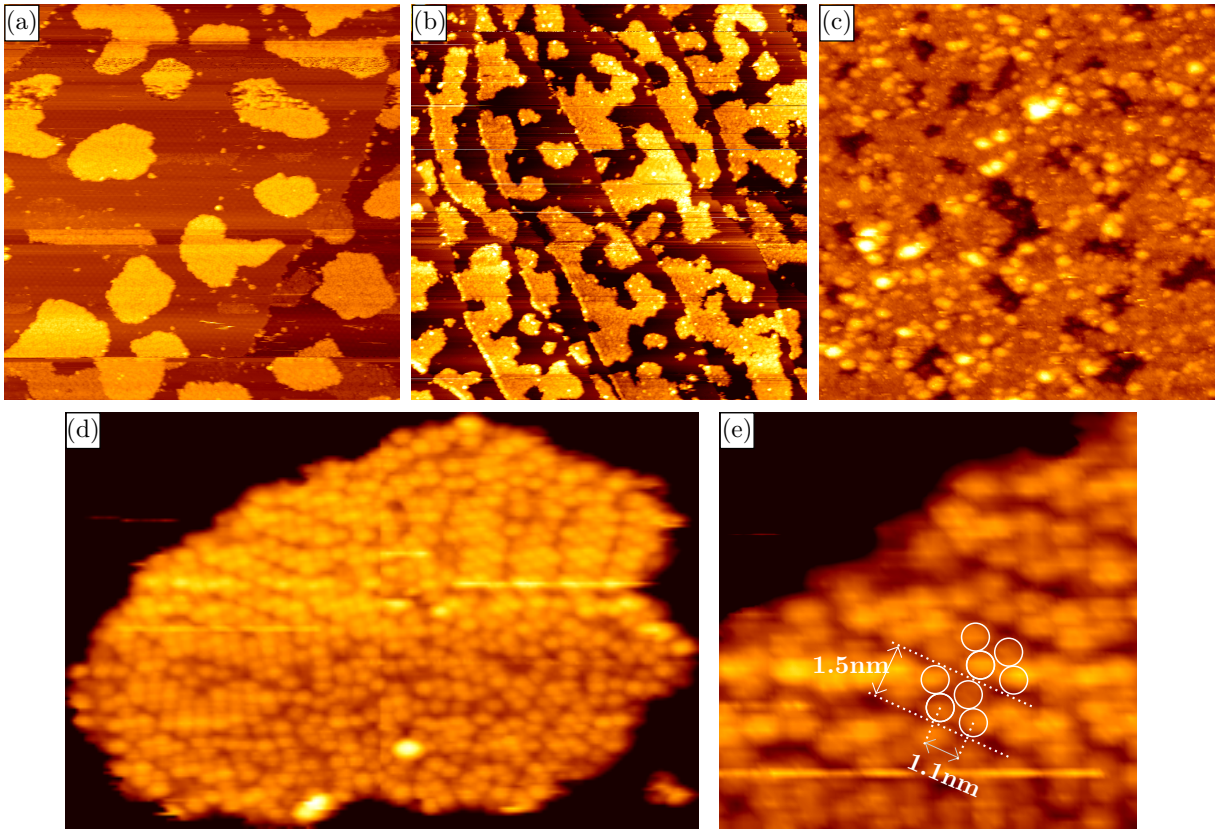

Figure 7.13: STM topographs taken at 20 K. Image sizes: (a), (b) $(328\,\mathrm{nm})^2$, (c) $(47\,\mathrm{nm})^2$, (d) $(37 \times 24)\,\mathrm{nm}^2$, (e) $(11\,\mathrm{nm})^2$. Vanadium was deposited at 20 K into a 10 ML thick preadsorbed benzene film, and subsequently annealed to 200 K. The amount of deposited vanadium increases from (a) to (c). (d) is a zoom-in into an area in (a). (e) is a further zoom-in into an area in (d), where a few double-row strands of dots are seen. The periodicity along the axis of a double-row strand as well as the width of a double-row strand are indicated.

the islands are relatively more homogenous in height, while higher coverages lead to a rougher and more grainy appearance.

Only for the smallest coverage, a structure inside the islands could be resolved, shown in the zoomed-in image in Fig. 7.13 (d). Round dots are seen all over the islands. They are in disordered arrangements in some regions, while in others, they appear in strands made of 2, 3, or more rows of dots. Figure 7.13 (e) shows the structure of the most ordered and periodic region of double-row strands that was seen in the image in Fig. 7.13 (a). A periodicity along the strand direction of about 1.1 nm and a separation between double-strands of 1.5 nm is observed.

Already several decades ago, chemists have produced metal-organic complexes by the co-condensation of, e.g., benzene and vanadium vapors onto a liquid-nitrogen-cooled surface in high vacuum [250]. These works typically use very large excesses of benzene, e.g., a factor of 100, and the evaporation rate of the metal allows to produce on the order of 1 gram per hour. The co-condensation of vanadium with a large excess of benzene results in the formation of VBz_2. We have therefore heated the sample at a rate of 1 K/s while recording the signal of

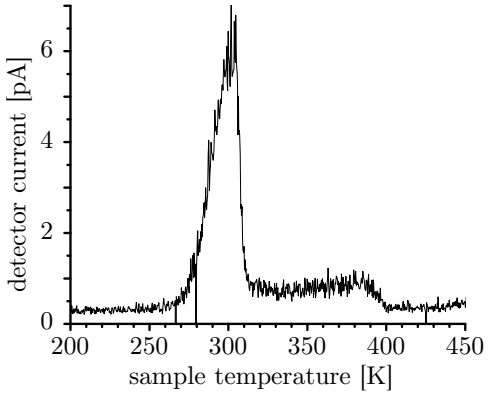

Figure 7.14: Mass spectrometer signal at $m/(2q) = 103.5\,e/u$, corresponding to doubly-ionized VBz_2, vs. the sample temperature as the sample is heated under the mass spectrometer with a rate of 1 K/s. The sample was prepared by deposition of submonolayer amounts of vanadium into a thick benzene film at 20 K.

a quadrupole mass spectrometer tuned to the charge-to-mass ratio of $m/q = 103.5\,e/u$, corresponding to doubly-ionized VBz_2. Singly ionized VBz_2 would have been inaccessible because the spectrometer could only measure up to $m/q = 200\,e/u$. We observed a desorption maximum at $T = 302 \pm 2$ K. This is a realistic desorption temperature as seen in the comparison with a work of Mitsui et al. [251], who measured desorption of VBz_2 from gold and molecularly functionalized gold surfaces to occur with the desorption maxima at ≈ 270 K and ≈ 320 K, respectively.

On another preparation of VBz_2 prepared in the same way, we conducted STM not only after short annealing at 200 K, but also after warming up to room temperature. Islands were not visible then any longer, indicating that the material covering the surface is made mostly out of VBz_2 molecules.

Now that we know the chemical nature of the molecules in the islands, we can come back to the structure visible in Fig. 7.13 (d) and (e). It is unclear how the molecules arrange in the islands to form the "strands of dots" structure. We refrain here from making an attempt of a structural model, but would like to point to the case of the structurally similar iron-cyclopentadienyl ($FeCp_2$) sandwich molecules adsorbed to the copper (111) and (100) surfaces reported by Ormaza et al. [252]. Their work reports fully periodic overlayers made by evaporation of ex-situ-synthesized ferrocene molecules onto the copper surface. Confirmed by comparison with DFT calculations, they find that ferrocene molecules in the overlayer are adsorbed both with the molecular axis parallel and normal to the surface ("horizontal" and "vertical"), within the same phase. Vertical ferrocene molecules appear as protruded dots, while horizontal ones appear as depressed space between them. This would be a good starting point to create a full structural model.

That the best results were obtained for the lowest amounts of deposited V indicates that a larger excess of molecules would be better. When the amount of V deposited is higher, the chance of a V atom hitting an already reacted VBz_2 molecule or even another V atom are higher,

and this will lead to side products. I suggest here that the Bz flux should have been applied not only for some time before but also during the V deposition at cryogenic temperature, such that the Bz excess is not limited by the surface coverage.

Our original motivation was to investigate vanadium-benzene for the magnetic properties. However, VBz_2 molecules have already been magnetically characterized by electron paramagnetic resonance [253]. Because we were not successful in producing wires, VBz was not pursued further. But especially when comparing to our previous work on EuCot, which worked under all conditions with Cot/Eu>1, it begs the question: Why was the VBz nanowire synthesis not successful?

Reference [205] describes the gas-phase synthesis of V_nBz_m sandwich clusters, with $n = m\pm1$ and $n \leq 5$, i.e., very short nanowires. In their discussion, the authors consider two possible pathways toward the formation of multidecker sandwiches. (i) A vanadium cluster could react with benzene. (ii) only vanadium atoms react with benzene; or V atoms react with benzene-terminated ends of a previously-formed sandwich cluster, making it one unit longer. The authors exclude pathway (i), because the binding energy even of vanadium dimers is too large to separate them, which is necessary if a benzene molecule were to be inserted between them. During our experiments, we noticed that the quality and ordering in the VBz_2 islands that we obtained was generally better for lower amounts of deposited vanadium. Because the amount of benzene was always the same, less vanadium implies higher Bz-to-V ratios. As previously mentioned, also chemists who synthesize complexes of transition metals with benzene by co-condensation from the vapors use very high Bz/metal ratios. We believe that the large excess ratios of Bz/V are necessary in order to avoid vanadium atoms meeting each other, because once they have formed a dimer or larger cluster, they can no longer be separated. This reasoning is consistent with our experience with europium, which forms long nanowires with Cot even if present on the sample as metal clusters or islands before the exposure, because the cohesive energy of europium is much less than that of vanadium. The difference in the cohesive energy of the two metals is reflected in the differing temperatures that are necessary to obtain a typical vapor pressure for deposition in UHV on the order of 10^{-4} mbar, being 723,K for Eu, and 1814 K for V [254].

Yet another independent and important difference exists between EuCot and VBz. When Eu atoms are evaporated into a thick layer of Cot adsorbed onto the sample at LHe temperature, and the Cot excess is then removed by heating above the desorption temperature of Cot, EuCot nanowires form (see Fig. 7.7 (a)). No indication of anything else – such as $EuCot_2$ – was ever observed. Because the Eu atoms are surrounded by many Cot molecules initially, it is most plausible that $Eu^{+2}(Cot^{-1})_2)$ was formed immediately after deposition, but one of the Cot molecules was then released from this chemical bond and desorbed. In contrast, the same procedure with vanadium and benzene results in VBz_2. The difference here is that the vanadium–benzene bond is covalent, and VBz_2 is an electronically saturated molecule (except for one d hole localized on the vanadium), and VBz_2 is thus stable. In contrast, EuCot is ionically bound,

and the Cot is electronically unsaturated if in the -1 oxidation state. Thus, two $Eu^{+2}(Cot^{-1})_2$) molecules will react to one $Eu_2^{+2}(Cot^{-1.5})_3$) and one neutral Cot, which will desorb, and so on, until long wires have formed with all Cot in the -2 oxidation state.

The reasoning given in the two previous paragraphs will guide our choice for another organometallic nanowire that we will attempt to produce in the next section.

7.3 Growth of thulium cyclooctatetraene, from dots and coffee beans to wires

This section is not published, but the results have been described in the master thesis of S. Kraus. I developed the reasoning behind the choice of Tm for the next attempt at growing another kind of nanowire. Experiments were conducted by S. Kraus under my guidance. Of the interpretational aspects, I performed the filtering for Fig. 7.18 (a), developed the growth model with Tm trimer riceballs dimerizing into coffee beans of Fig. 7.18, and started with the geometrical methodology of assembling the unit cell of the coffee bean phase. The observation of the opposite chirality of the coffee beans in adjacent rows of the herringbone, and how to assemble the coffee beans such as to reproduce the star feature, are by S. Kraus. All figures in this section were adapted from the master thesis of S. Kraus.

We have drawn two lessons from the experience with VBz: Firstly, nanowires should grow best with an ionic ligand like Cot. Secondly, the cohesive energy E_{coh} of the metal should be low. Looking at the metals with magnetic $3d$ and $4f$ shells, we see that the lowest E_{coh} occur in the rare earth. Specifically, samarium (Sm), europium, thulium (Tm), and ytterbium (Yb) have the lowest ones among the magnetically interesting elements, summarized in Tab. 7.1. Because the rare-earth metals are in the $+2$ oxidation state in nanowires with Cot, we are not interested in samarium and ytterbium. This is because Sm^{+2} has $4f^6$ configuration, where the spin and orbital moment are equal and opposite in sign, so that the total moment is zero. And in Yb^{+2}, the $4f^{14}$ configuration corresponds to a closed shell and thus also carries no magnetic moment. Because we already investigated Eu, we are only left with Tm.

Tm^{2+} would have a $4f^{13}$ electron configuration, yielding $J = 7/2$, the same as Eu. But in contrast to Eu, which has no orbital moment, Tm has a large orbital moment of $L = 3$. This should lead to a much larger single-ion anisotropy for Tm, and we may expect to learn something from the comparison of the magnetic behavior of Eu and Tm in nanowires with Cot.

In a first attempt at growing TmCot nanowires, we have deposited Tm and Cot at the same time onto non-intercalated Gr/Ir(111), in analogy to the best recipe found for EuCot. In contrast to the case of Eu, this recipe did not yield sandwich molecular nanowires of Tm with Cot, but yielded other interesting organometallic structures, as discussed in the next subsection

element	shell	S	L	J	g_J	E_{coh}
Sm	$4f^6$	3	3	0	–	2.14 eV
Eu	$4f^7$	7/2	0	7/2	7/2	1.86 eV
Tm	$4f^{13}$	1/2	3	7/2	8/7	2.42 eV
Yb	$4f^{14}$	0	0	0	–	1.60 eV

Table 7.1: The four elements of the rare-earth series with the lowest cohesive energies, with the properties of their magnetic shell given in the +2 oxidation state. The next-highest cohesive energy would be significantly higher, dysprosium at 3.04 eV.

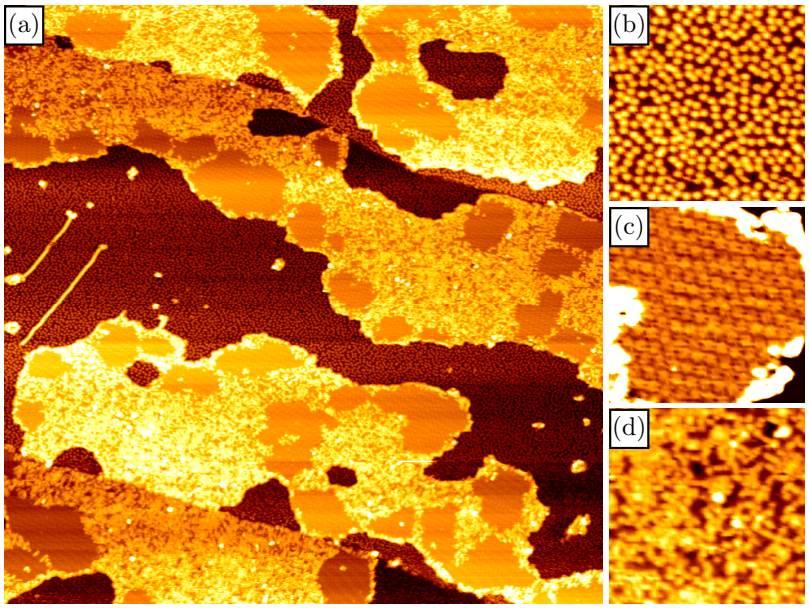

Figure 7.15: STM topographs taken at LHe temperature after deposition of 0.14 ML Tm with Cot excess. The $(235\,\mathrm{nm})^2$ overview topograph in (a) has three distinct types of areas, for which (b), (c), and (d) show zoom-ins of $(25\,\mathrm{nm})^2$. (b) Areas between the islands show the "dot phase". (c) Flat island areas show a superstructure, higher-resolved images later reveal this to be the "coffee bean phase". (d) Rough parts of islands show disorder.

7.3.1. Yet, TmCot nanowires could be produced by growth on graphene that was n-doped by intercalation of Eu before the TmCot growth, and these results are described in subsection 7.3.2.

7.3.1 Thulium-cyclooctatetraene dots and coffee beans grown on undoped graphene

Figure 7.15 (a) shows an overview topograph of a sample where submonolayer amounts of Tm were deposited in an excess Cot pressure at room temperature. The precise value of the flux ratio appeared to be irrelevant so long as $f_{\mathrm{Tm}}/f_{\mathrm{Cot}} > 1$, as previously observed for EuCot nanowires. Thus, the Tm-to-Cot stoichiometry is self-limiting here. The sample was subsequently imaged at LHe temperature. Three different regions cover the sample, which are shown in the zoom-ins in Figure 7.15 (b) to (d).

A phase with disperse dots shown in Figure 7.15 (b) appears between the islands and is

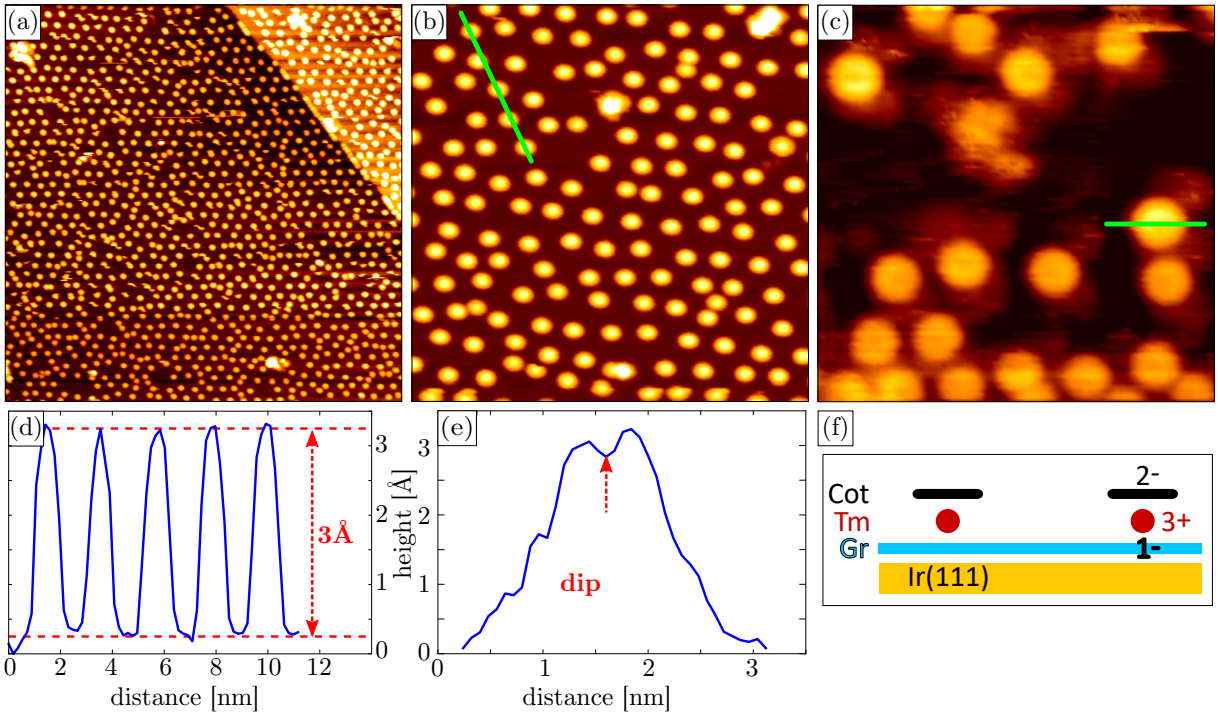

Figure 7.16: Disperse dot phase after deposition of (a) 0.013 ML Tm or (b,c) 0.08 ML Tm. (a): STM topograph, $(75\,\mathrm{nm})^2$; (b): STM topograph, $(26\,\mathrm{nm})^2$; (c) STM topograph $(9\,\mathrm{nm})^2$; (d): Height profile indicated by the green line in (b). (e): Height profile indicated by the green line in (c), each dot shows a dip in its center.

discussed first. Afterwards, we will discuss the flat island phase, shown in the zoom-in in Figure 7.15 (c), which will be revealed to be the "coffee bean" phase. The disordered, rough phase shown in Figure 7.15 (d) disappears upon mild annealing as discussed last.

The dot phase

Figures 7.16 (a) to (c) show STM topographs of the dot phase. For sufficiently low deposited amounts of Tm, the dot phase is the only phase and covers the whole sample. The density of dots depends on the coverage, but is never much more than on the order of 1 per moiré site. The dots are uniform in height as shown in the line profile in Figure 7.16 (d), taken along the green line in Figure 7.16 (b). While the long-range order of the dot phase is poor, locally, a hexagonal ordering is observed. The arrangement is not random: Very short distances occur much less than expected for a random distribution. Such a behavior is typical for repulsively interacting adsorbates on a surface, as shown previously for the model system potassium on graphite [255]. The origin of the repulsion is the Coulomb interaction of the dipole moments of the adsorbates, which results from charge transfer into the substrate.

What are the dots made of? Firstly, they cannot be single Cot molecules, because these desorb below 210 K [256]. They can also not be single Tm atoms, because thulium forms clusters on graphene upon deposition at room temperature [117]. It is also implausible that Tm

atoms would reside on the surface without reacting with Cot, because undercoordinated atoms are reactive, and Cot is a very unsaturated hydrocarbon. The model shown in Figure 7.16,(f) explains all observations. A thulium atom sandwiched between a Cot ring and the graphene surface donates two electrons into the Cot ring and one (or perhaps a bit less) into the graphene substrate. The resulting dipole leads to the Coulomb repulsion. As the Tm atom is covered by the Cot ligand, this object should be relatively inert toward reaction with contamination residual gas, in agreement with our observation that the dot phase survives relatively high pressures, on the order of 1×10^{-9} mbar, for more than an hour without degradation. Metallic Tm would be expected to degrade faster through reaction with background gas. Further support for the model is seen looking at the height profile in Figure 7.16 (e) taken along the green line in Figure 7.16 (c), which shows a small depression ("dip") in the center of the dot, expected due to the ring-shaped Cot molecule and its equally ring-shaped π orbitals.

Why can sandwich dots form with thulium, but do not form with europium? The reason must be the differing preference for the formation of the 2+ and 3+ oxidation state. The half-filled $4f$ shell of Eu^{2+} is especially stable because all spins are parallel, optimizing the Hund's rule energy. Europium therefore appears in divalent form in many more compounds than Tm. Likely, the cyclooctatetraene molecule and/or graphene are simply not sufficiently electronegative to oxidize Eu into the 3+ state. The dot phase forms because this way, the Tm atom can bind and donate charge to both graphene and the Cot ring. In contrast, for Eu the 2+ state obtained by reaction of Eu with Cot alone is already the highest oxidation state possible with the ligands Cot and Gr, thus no driving force to bind down to the substrate exists for Eu, and no dots will form. That graphene must be a sufficiently strong electron acceptor to enable the formation of the TmCot dot phase is evident from the suppression of this phase upon n doping of graphene as discussed in section 7.3.2.

The coffee bean phase

When a certain critical amount of deposited Tm is exceeded, an island-forming phase grows and coexists with the dot phase: It is the coffee bean phase shown in high resolution in Figure 7.17 (a) and (b). Note that what appears as empty (or only somewhat dirty) area between the islands is actually filled with dots just the same as seen in Figure 7.15, but the dots in Figure 7.17 are not seen, because in order to image the coffee beans in the highest resolution, tunneling parameters were chosen such that the tip is relatively close to the sample, and moves the dots around, so that they are not seen. The coffee beans are arranged in the islands in a herringbone pattern, i.e., a rectangular lattice with two coffee beans in the unit cell and mirror glide symmetry that maps the two coffee beans in the unit cell onto each other. The point group is D2 and the wallpaper group is pgg. The dimensions of the unit cell are $a = 1.8\,\text{nm}$ and $b = 4.0\,\text{nm}$. The height of the coffee bean islands is about 0.5 nm as seen in the line profile in Figure 7.17 (c) taken along the green line in Figure 7.17 (a). This is similar to the heigth of EuCot islands.

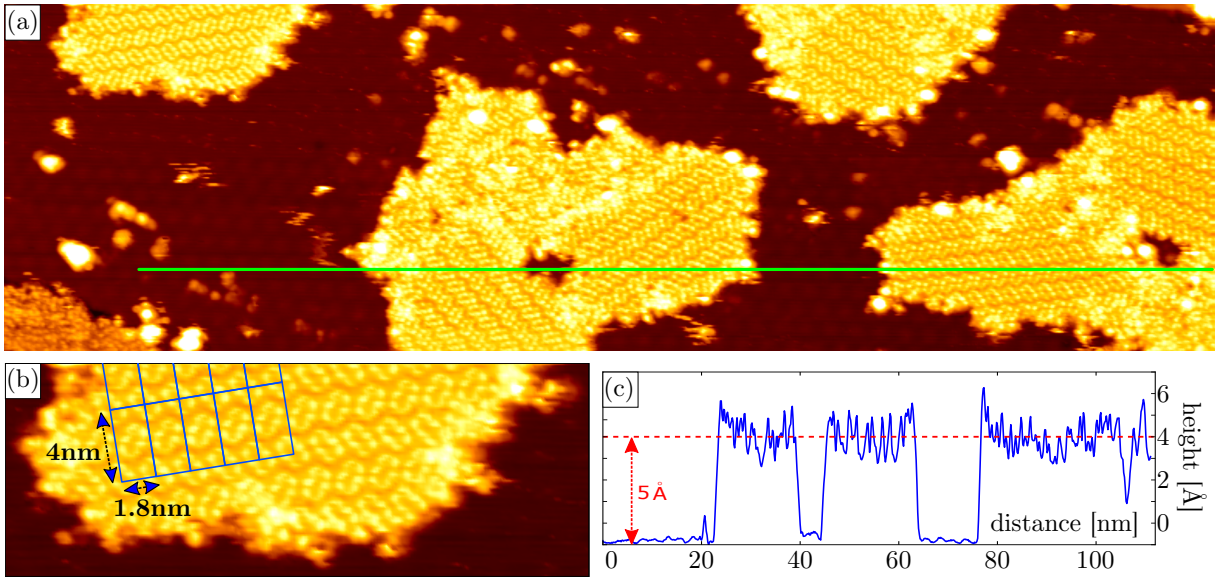

Figure 7.17: (a, b, d): STM topographs of coffee beans after deposition of 0.08 ML Tm. (a) Overview ((125 nm × 36 nm)) of the island structure. (b) Zoom on one island (30 nm × 12 nm), lattice of the herringbone structure indicated. (c) Height profile along the green line in (a).

Arbitrary different crystallographic orientations of the coffee bean islands relative to the underlying graphene substrate occur. In low-energy electron diffraction, one therefore expects to observe a ring, as seen for EuCot. However, because of the much more complex unit cell of the coffee bean islands, the intensity will be distributed over more spots, and because the unit cell is larger than for EuCot, the spacing of the intensity maxima on the screen will be closer. Furthermore, the coffee bean islands are rarely larger than about ten repeat periods of the superstructure in any direction, such that an intrinsic spot smearing due to finite size domains is also present. In the end, we only observed diffuse intensity from the coffee bean phase in LEED, even with an MCP LEED available at the ESRF's ID32 beamline. This cannot be traced to a possibly poor quality of the preparation, because STM taken at ID32 on the same sample confirmed the quality and an about half-monolayer coverage with coffee bean islands.

The lower left corner of Figure 7.18 (a) shows a closer zoom into the STM topograph in Figure 7.17 (a), where the image has been rotated such as to align the short axis with the horizontal. The coffee beans appear to consist of six protrusions, and these protrusions sometimes appear to be elongated in particular directions. However, an STM image always results from a convolution of the electronic states of the tip with those of the sample. Therefore, a feature might result from the shape of the tip just as well as from the shape of the molecules on the sample. However, if the feature occurs in the same way in several different orientational domains of the adsorbate phase, then it must be real, i.e., it must be a property of the sample, and not of the tip.

We have applied an elaborate filtering procedure in order to obtain the image shown in Figure 7.18 (a) outside the lower-left corner. The idea is as follows: We are imaging with the STM tip a periodic structure that exhibits a number of symmetries and is observed in a number

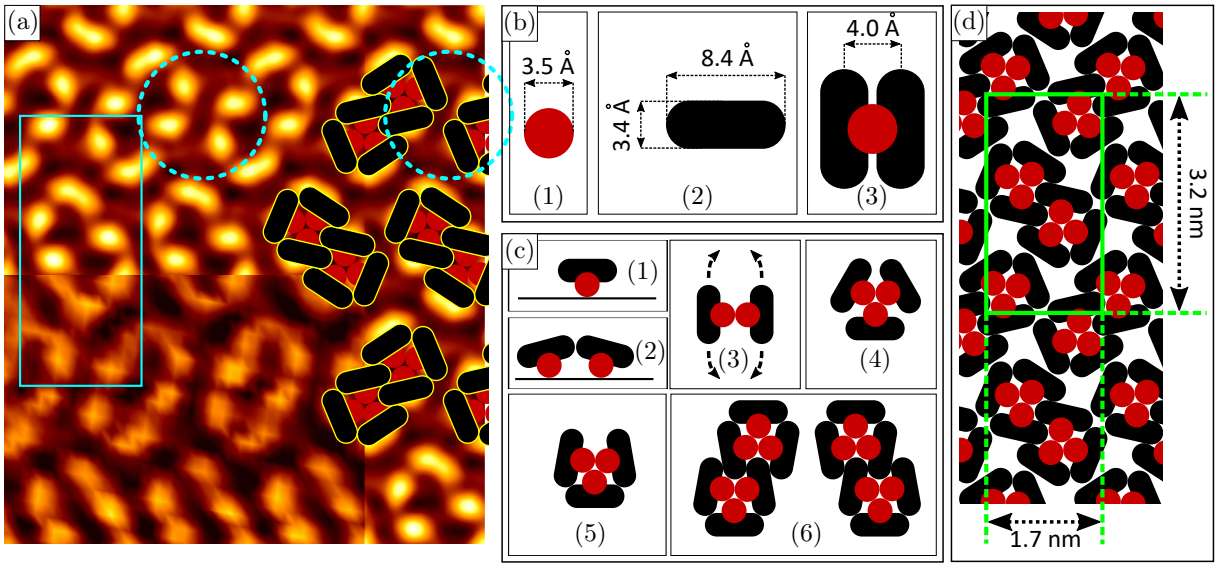

Figure 7.18: (a) Zoom on (4×2) coffee bean herringbone unit cells. Cyan rectangle indicates the unit cell. Lower left corner unfiltered, other quarters filtered as described in the text. Dashed cyan circles around the characteristic "star feature". (b) Building blocks for the structural model of the coffee beans. (1) Tm atom. (2) Cot ring. (3) TmCot sandwich. (c) Growth model from (1) half-sandwich dots to (6) coffee beans. (d) Packing of the coffee beans based on the dimensions shown in (b) leads to a too small long axis of the rectangular unit cell. Therefore, in (a) we increased the separation of the coffee beans along the rectangle's long axis to obtain the good match of model and experiment seen in (a).

of different rotational domains. For each rotational domain, we average the STM image over several measured unit cells, in the same way that a lock-in amplifier extracts a higher-quality signal by phase-correct addition of the signal obtained over many periods. Then, we rotate each of these averages to make the orientation of the lattice identical and then average the different rotational domains into one image. Then, we again average this image with its own mirror-glided copy, and then average this again with its twofold-rotated copy. The result is an image where the rotational asymmetry of the tip mostly cancels out. To enhance the high frequencies, we apply a Laplace filter, and then use a Fourier filter to remove high-frequency noise. In the resulting image, the elongated shape of the protrusions is clear.

To arrive at a structural model of the coffee beans, we apply the following reasoning: (1) The height of the islands is very similar to the height of EuCot, suggesting that the Cot rings are upright-standing. (2) The sample bias voltages for best imaging of $-1\,\mathrm{V}$ and below are the same as for EuCot, suggesting the same entities are imaged, and we know for EuCot that it is the Cot rings which are imaged, not the Eu[2]. (3) The elongated shape of the protrusions likewise indicates upright-standing Cot rings. (4) Upon annealing of the sample at only 400 K,

[2]As discussed for Fig. 7.2, a single upright-standing Cot ring will appear as two protrusions separated by the nodal plane of the π orbitals. However, we speculate that when a metal atom is attached to only one side of the ring, as implied by the model developed for the coffee bean phase here, a distortion of the π system's nodal plane should lead to a much higher intensity of that protrusion which is on the metal-bonded side of the ring.

the islands re-arrange and expel impurities, as described later. The units comprising the coffee bean islands must therefore be only weakly bound toward each other, i.e., only by van der Waals bonds. This is in contrast to the case of EuCot nanowire islands, where the entire islands are held together by ionic bonds and do not rearrange during annealing until they decompose at $\approx 650\,\mathrm{K}$. (5) Because the sandwich dot phase forms first one the sample, and the coffee beans occur later with increasing amounts of deposited Tm, it is plausible that the coffee beans result from the merging of dots in some way.

To estimate the bond length in our structural model, we took the numbers as indicated in Fig. 7.18 (b). Tm-Tm bonds were taken to have the same length distance as in Tm metal, i.e., 3.5 Å. A value of 8.4 Å for the diameter of the Cot ring is calculated from the tabulated values of the van der Waals diameter of the hydrogen atom, the hydrogen-carbon bond, and the carbon-carbon bond in graphene. The thickness of the Cot ring of 3.4 Å is taken from the stacking distance of graphene sheets in graphite. The separation of the center of a Cot ring from a Tm atom to which it binds is assumed at 2.0 Å. This taken as one-half of the periodicity in a TmCot infinite nanowire, which itself is estimated from the EuCot nanowire periodicity and the difference in ionic radii of Tm and Eu.

We propose a multistep growth model for the coffee beans as seen in Figure 7.18 (b). Half-sandwiches of TmCot adsorbed to the graphene surface are step (c,1). As the coverage is increased, the dots will get closer and closer to each other. At some point, thermal excitation will be sufficient to bring two TmCot units so close that a steric repulsion of Cot rings will make two neighboring TmCot units tilt as indicated in (c,2). With the metal centers now toward each other, a covalent bond can form via the remaining $5d$ electrons [(c,3)]. The resulting dimer will have a very soft vibrational mode where the two halfs tilt against each other as indicated by the arrows in (c,3). It will also have a much lower dipole moment compared to the half-sandwich monomer bonded to graphene. Therefore, the repulsion from the surrounding TmCot monomers that are still bound to graphene will be lower, and it will be easy for the dimer to bind another TmCot monomer and form a trimer [(c,4)]. Trimers with this structure have been called "riceballs" and were observed to result from the gas-phase reaction of late $3d$ transition metals (e.g., Co, Ni) and benzene in mass-spectrometry experiments [96]. The riceball (c,4) no longer has the very soft vibrational mode of (c,3), and if it is arranged with its three Cot rings perpendicular to the graphene, it will have its relatively reactive metal core sterically protected from reactions with the remaining TmCot monomers. Yet in the riceballs, a slight freedom to rotate the Cot rings around the core is still present [(c,5)]. This can be exploited to dimerize two riceballs into one coffee bean [(b,5)]. When the coffee beans are with their Cot rings perpendicular to the surface, and they are not allowed to "flip over", then they exist in two different chiralities, which are mirror twins of each other.

We can arrange the coffee beans into the herringbone structure as shown in Figure 7.18 (d). The two mirror twins are needed in equal amounts in order to produce the coffee bean islands,

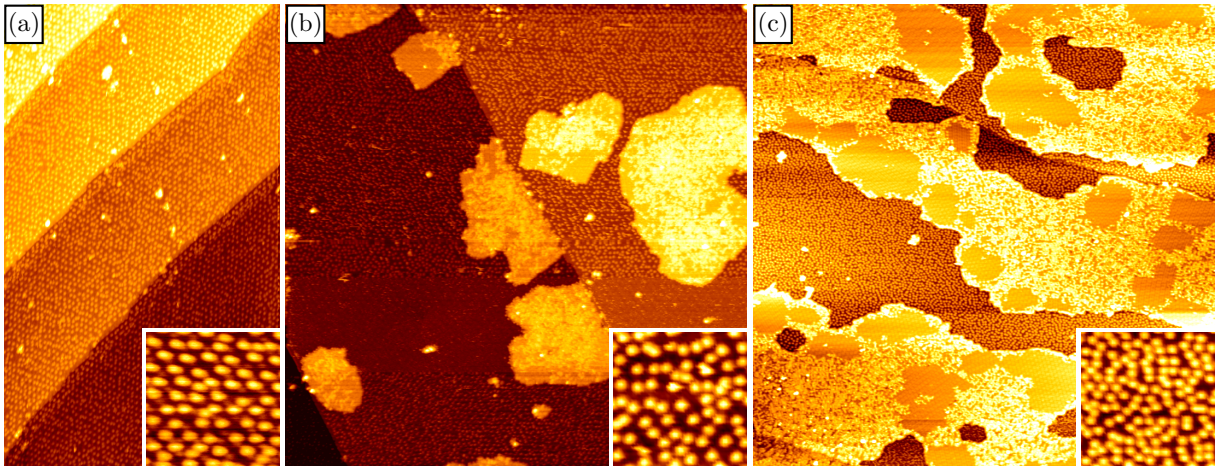

Figure 7.19: STM topographs of submonolayer amounts of Tm with Cot excess deposited at 300 K and imaged at LHe temperature. The amount of deposited Tm increases from (a) via (b) to (c). Islands form only after a certain critical amount of deposited Tm has been exceeded. Image sizes: (a): $120 \times 200\,\mathrm{nm}^2$, (b): $(200\,\mathrm{nm})^2$, (c): $(235\,\mathrm{nm})^2$.

because in alternating rows of the herringbone, oppositely chiral coffee beans occur. We did not use a closest packing to build the model, but rather arranged the coffee beans such that the experiment is best reproduced, in particular the "star" feature indicated by the dashed circles in Figure 7.18 (a).

The structural model results in dimensions of the rectangular unit cell of $(1.7 \times 3.2)\,\mathrm{nm}^2$, compared to $(1.8 \times 4.0)\,\mathrm{nm}^2$ in the experiment. The disagreement is above the error of the STM measurements for the longer axis. Therefore, in order to match the STM image with the model in Figure 7.18 (a), the separation of the coffee beans along the long axis had to be increased. After that adjustment, a very good agreement is obtained.

To explain the disagreement in the lattice constant, we consider that in the vdW dimensions of the Cot ring, it was entirely neglected that the Cot ring is doubly-negatively charged, and its electron cloud will therefore be larger than that of, e.g., a neutral benzene ring. This is a large effect; for example, a thulium atom that changes oxidation state from 3+ to 2+ expands its ionic radius from 102 pm to 117 pm. This effect would lead to an expansion of the unit cell, and it would expand the cell more strongly in the direction of the long axis, because in the direction of the long axis, the Cot rings of two adjacent coffee beans touch more parallely, while in the direction of the short axis, the Cot rings touch more head-on-head in the start geometry. In the future, we hope that density-functional theory calculations that include the van der Waals interactions will be able to give better values for the unit cell dimensions and thereby confirm the model.

Coverage dependence

For the lowest coverages of deposited Tm, the sandwich dot phase covers the entire sample as seen in Figure 7.19 (a). Only when the deposited amount of Tm surpasses a certain threshold do islands nucleate as seen in Figure 7.19 (b). The islands grow with the deposited amount as seen in Figure 7.19 (c).

We next consider the insets of Figure 7.19 (a) to (c). The dot density per moiré cell is about 1.2 in (a), 1.6 in (b), and 3.3 in (c). These number were determined from larger images to obtain better statistics. Thus, the dot density increases even after islands have formed. This cannot be understood if the dots are believed to form coffee beans after a sharp limit in coverage is exceeded, i.e., simply as a result of the compression of the sandwich dot phase with increasing coverage. We speculate that hot thulium adatoms, i.e., adatoms that are in a vibrationally excited state in the microscopically short time following the adsorption process, are responsible for activating the formation of coffee beans from sandwich dots.[3] In this conception, Tm atoms arriving on the surface can either activate the formation of a coffee bean, or become one more sandwich dot, with a branching ratio that depends on the dot coverage.

Hexagonal ordering of the dots is observed for dot densities up to somewhat above 1 dot per moiré cell as seen in Figure 7.19 (a), while at higher dot densities, the ordering disappears as seen in the insets of Figure 7.19 (b) and (c). For dot coverages with densities below 1 per moiré cell (not shown), the dots also order in the moiré, but some cells remain empty.

Dependence upon annealing

We already mentioned that the "rough phase" seen in Figure 7.15 (d) disappears upon annealing. Figure 7.20 shows a direct comparison of a sample with 0.08 ML_{Ir} Tm deposited in Cot excess at room temperature, before [Figure 7.20 (a)] and after [Figure 7.20 (b)] annealing to 400 K.

Before annealing, the islands almost everywhere have a rough surface. Only a small fraction of the island area consists of extended flat parts, the larger of which are indicated by the arrows in Fig. 7.20 (a). Higher resolution imaging of these flat parts (not shown) reveals that they already consist of coffee beans herringbone islands. The phase separation into extended disordered and ordered areas is a remarkable testament to the purifying power of crystal growth. After short annealing at 400 K, the islands are flat almost everywhere. Rough protrusions occur only at grain boundaries, of which there are many inside the islands. Notably, the coverage with islands has not decreased, such that the rough island parts must have transformed into flat coffee bean herringbone islands.

Another effect of the annealing is a change in the island morphology. Before annealing, the islands are comparably compact, while after annealing, the less compact shape means that the

[3] The adsorption of molecular oxygen on aluminium (111) is an example for the relevance of hot adatoms as described in Ref. [257].

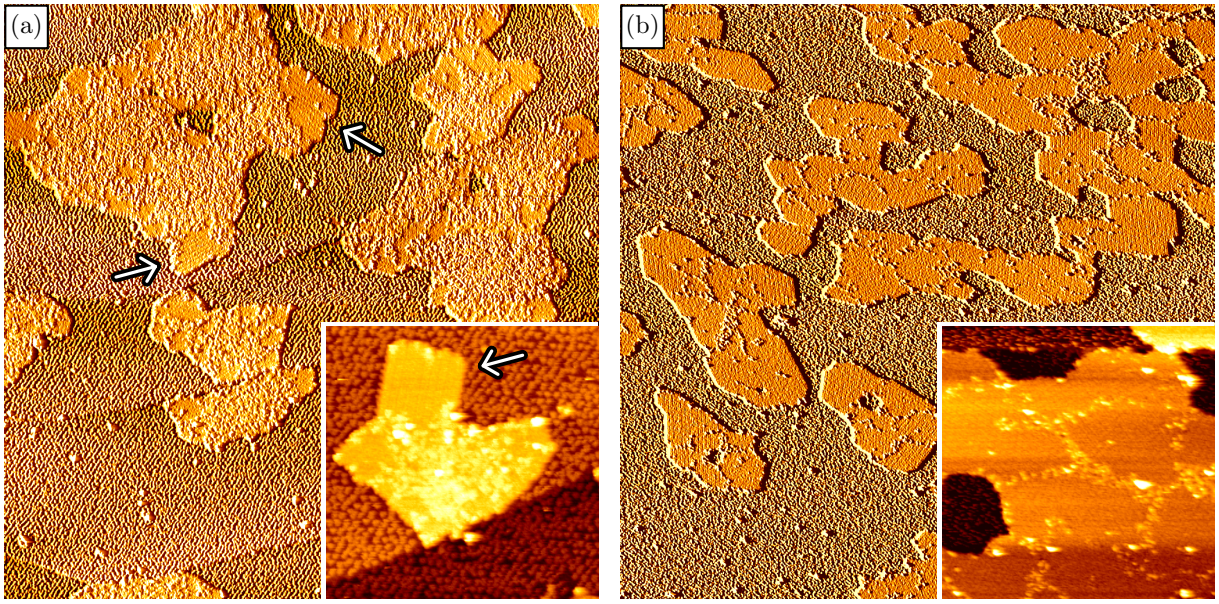

Figure 7.20: STM topographs of submonolayer amounts of Tm with Cot excess deposited at 300 K and imaged at LHe temperature. (a) is directly after growth, (b) is after additional short annealing at 400 K. The main images have been overlaid with their derivatives and are $(328\,\mathrm{nm})^2$ in size. The insets are $(72\,\mathrm{nm})^2$ in size and are without derivative.

islands come closer to percolation without a notable increase in island coverage. The observation of islands becoming less compact with temperature is opposite to the behavior of, e.g., islands of a typical metal like Ir homo-epitaxially grown on top of itself. The coffee bean islands expel impurities into the grain boundaries, and kinks in the edges of islands are always linked to grain boundaries. We believe that it is due to the strong anisotropy of the edge energy of coffee bean islands, that the islands become less compact during the growth of crystalline areas from previously more amorphous ones. The impurities at the grain boundaries are responsible for insufficient grain coarsening, such that the islands remain polycrystalline and non-compact.

7.3.2 Thulium-cyclooctatetraene nanowires grown on n-doped graphene

In the previous section, we have ascribed the stability of the dot phase on pristine Gr/Ir(111) to charge transfer from the thulium atoms to graphene. Thus, we have presumed that graphene is electronegative enough to oxidize thulium from the 2+ state (which results already from the reaction with Cot) to the 3+ state. There is an easy way to modify graphene's electronegativity: dope it with electrons from the backside. Here, we want to suppress the formation of the dot phase, because we believe that it blocks the formation of nanowires. Therefore, we have to make graphene less electronegative. We use a monolayer of europium intercalated between graphene and the iridium substrate to dope graphene with electrons from the backside, while graphene's frontside stays available as a substrate for the TmCot growth. The intercalation of europium to saturation results in an upward shift of the Fermi level in graphene by about 1.5 eV. Hence, the

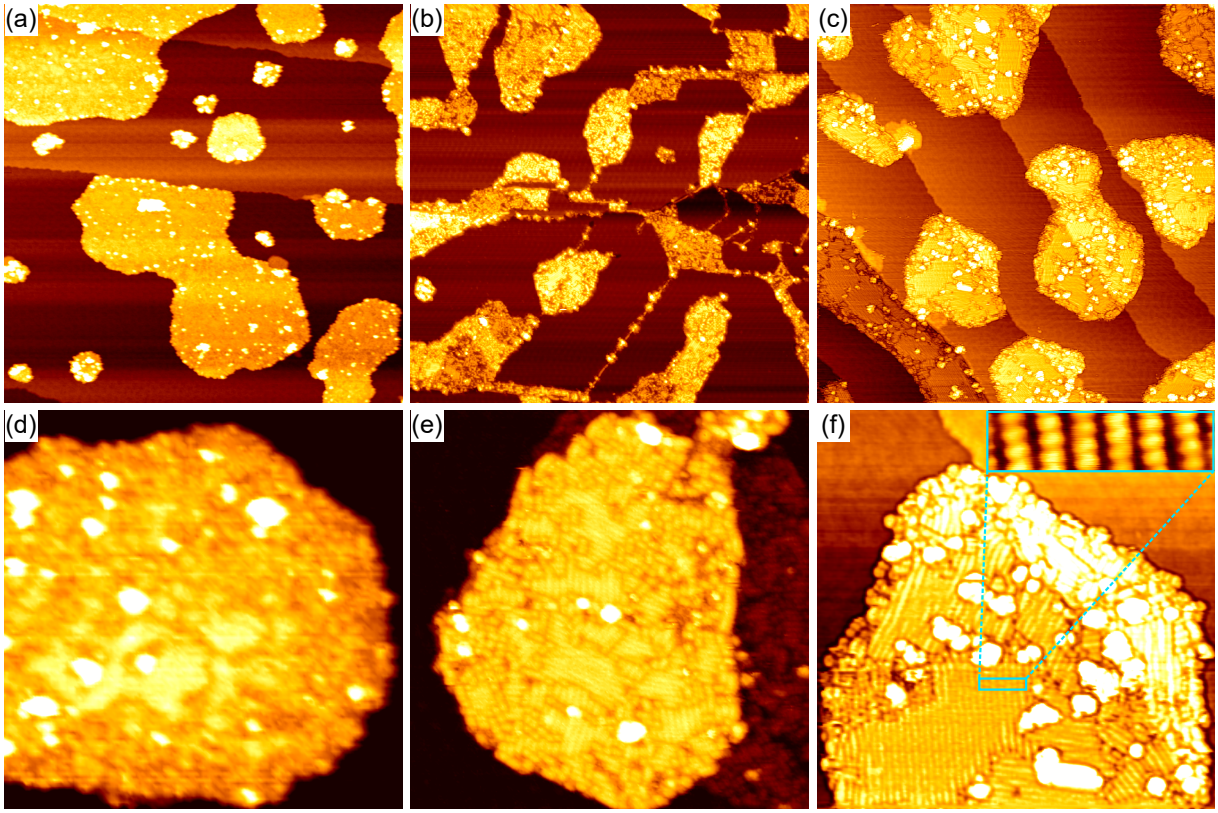

Figure 7.21: STM topographs from a series of experiments where the flux ratio $f_{\mathrm{Tm}}/f_{\mathrm{Cot}}$ was varied during growth at $T = 300\,\mathrm{K}$. (a/d): 10 min Tm deposition, 0.008 ML/min, $p_{\mathrm{Cot}} = 3.6{\cdot}10^{-9}$ mbar; (b/e): 2 min Tm deposition, 0.04 ML/min, $p_{\mathrm{Cot}} = 3.6{\cdot}10^{-9}$ mbar, subsequently annealed to 400 K; (c/f): 1.5 min Tm deposition, 0.08 ML/min, $p_{\mathrm{Cot}} = 3.6{\cdot}10^{-9}$ mbar. Image sizes: Top row: $(165\,\mathrm{nm})^2$. Bottom row: $(40\,\mathrm{nm})^2$. Inset in (f): $(5 \times 1)\,\mathrm{nm}^2$.

energy gain from additional charge transfer into graphene will be reduced by 1.5 eV.[4] It turned out that this is sufficient to suppress the dot phase and the coffee bean phase, and TmCot nanowires formed on the surface.

In contrast to the case of EuCot, the length of the TmCot nanowires depends sensitively on the flux ratio $f_{\mathrm{Tm}}/f_{\mathrm{Cot}}$. Figure 7.21 shows STM topographs from a measurement series where the Cot flux stayed constant while the Tm flux was varied over one order of magnitude, from 0.008 ML/min in Fig. 7.21 (a/d) via 0.04 ML/min in (b/e) to 0.08 ML/min in (c/f). The total amount of deposited Tm was kept constant by adjusting the deposition time. In (a/d), only a small fraction of the islands consists of flat parts. Although not resolved in this particular topograph, these are the areas with patches of parallel nanowires. Going toward higher $f_{\mathrm{Tm}}/f_{\mathrm{Cot}}$ ratios in (b) and (c) these patches become larger and fill most of the islands.

Why does the wire length change for TmCot, but not for EuCot? The explanation is again in

[4] This reasoning overestimates the effect, because it assumes that the shift in the Fermi level in graphene by charge transfer from Tm is the same for undoped and doped graphene, or that the charge transfer from Tm hardly changes the Fermi level. This is not the case, because the density of states at the Fermi level is close to zero for undoped graphene and changes strongly upon doping.

the different preference for the oxidation state 3+. Due to the excess of Cot molecules supplied during the growth, all wire ends are in general Cot-terminated. It has been shown by gas-phase photoemission spectroscopy [96] that in the case of EuCot, a Cot-terminated end has the Eu in the 2+ state and the Cot ring in the 1- state, i.e., the Cot ring is not electronegative enough to oxidize Eu from 2+ to 3+. The opposite is the case for Tm [96]. Thus, if two Cot-terminated EuCot wire ends touch, we expect that the two wires fuse. From the two single-negatively-charged Cot rings, one will become doubly-negatively-charged and become part of the fused wire, while the other one will become neutral and desorb. In contrast for TmCot, all Cot-terminated wire ends have the Cot in the 2- oxidation state, and are thus electronically saturated. Consequently, there is no reason to expel one of the Cot rings.

That the wire length depends on the flux ratio for TmCot is a major complication, because it is typically difficult to control fluxes precisely. When $f_{\mathrm{Tm}}/f_{\mathrm{Cot}}$ is too high, metallic Tm clusters will form on the surface, especially when $f_{\mathrm{Tm}}/f_{\mathrm{Cot}} > 1$. And when $f_{\mathrm{Tm}}/f_{\mathrm{Cot}}$ is too low, only exceedingly small wire segments will form, and the resulting crystalline order will be poor.

7.4 Alignment of wires through growth on graphene on Ir(110)

This section is entirely my own work.

The growth of EuCot nanowires on the surface of Gr/Ir(111) works very well, but they lack a highly desirable property: a global orientation. Without it, any measurement technique that is sensitive to the in-plane orientation, and which is spatially averaging over an area that is larger than the size of a single crystallite, is complicated or even made impossible by the lack of a global orientation. I discuss here only two such measurement techniques that are interesting for EuCot:

(1) Angle-resolved photoemission (ARPES) could be used to investigate the band structure of the system. However, in a conventional ARPES experiment, the sample is illuminated with monochromatic light, where the diameter of the light spot is $< 100\,\mu$m, i.e., far larger than one EuCot crystallite. A measurement will therefore yield an angular average intensity, which is of hardly any use for anything except features that are radially symmetric around the Γ point, such as Shockley states.

(2) X-ray magnetic circular dichroism (XMCD) could be used to determine magnetic properties, and in particular the magnetic anisotropy. Yet also in XMCD measurements, the spot size of the X-ray beam is typically $> 100\,\mu$m. While some information about the anisotropy can be gained from the dependence of the XMCD on angle between surface normal and incident x-ray beam, globally oriented samples would provide a far clearer picture.

The lack of a global orientation is a direct consequence of the threefold rotation symmetry of the Ir(111) substrate: No matter how we might tune the growth conditions, at least three directions for the nanowire growth will always be equally preferred, and unless nucleation occurs

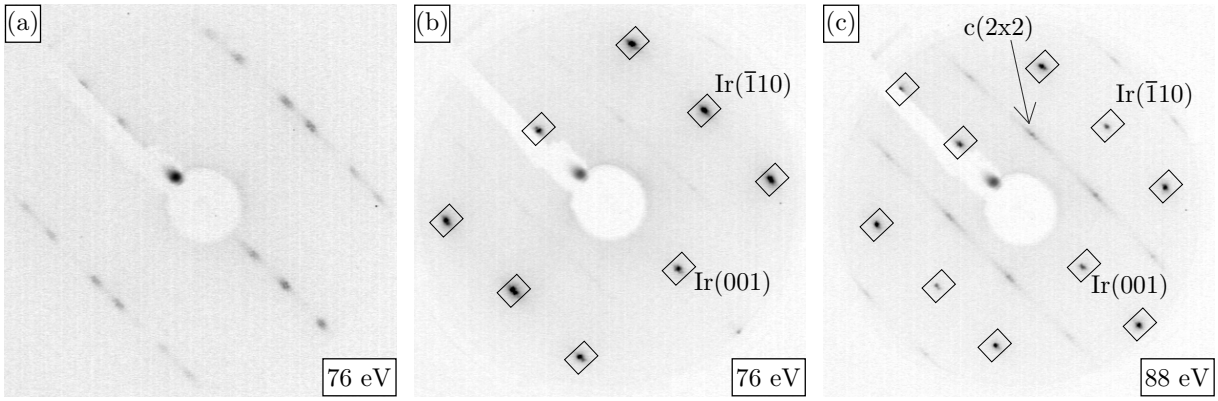

Figure 7.22: LEED patterns of the Ir(110) crystal taken at the indicated electron energies. Spots expected for an unreconstructed, truncated-bulk Ir(110) surface marked by black rectangles. (a): After sputtering and annealing to 1500 K. (b): After exposure to oxygen at 1400 K and cooldown with the oxygen valve open until the sample stopped to glow. (c): Like (b), but at a higher electron energy.

at a single point on the sample – obviously not the case for EuCot – differently oriented islands will form during growth.

Part of the solution must be to choose a substrate of only twofold or even lower symmetry. The reduced symmetry of the substrate is a necessary but not sufficient condition for oriented growth. This is easily seen from EuCot on Gr/Ir(111), where all orientations occur as seen by the formation of a ring in LEED despite only three are necessitated by the symmetry.

Iridium in general and not just its (111) surface is expected to be a good substrate for graphene growth: The carbon solubility is lower than in, e.g., nickel, ruthenium, or rhodium, which allows to exclude dissolved carbon in experiments at typical growth temperatures. Dissolved elements are difficult to control in surface science experiments, because they are not seen by surface-sensitive methods and can give the sample an undesirable history dependence. We thus chose to investigate the growth of graphene on Ir(110), the lowest-index face with at most twofold rotation symmetry.

The newly bought Ir(110) crystal was treated with cycles of sputtering, oxygen firing, and flash annealing at 1500 K, the same way we would prepare a new Ir(111) crystal. Figure 7.22 (a) shows a LEED image of the sample after the last sputtering and annealing at 1500 K. The spots are arranged on lines and move along those lines as the electron beam energy is changed, rather than toward the center, as is usual. This shows that the Ir(110) is unstable and decomposes into facets. Our LEED observations are identical to those of Koch et al. [258], who determined not only from LEED but also from STM measurements that the facets are (331), i.e., the decomposition occurs as $(110) \sim (331) + (33\bar{1})$.

The faceted surface can be brought back to a non-faceted state by exposure to oxygen. The LEED image in Fig. 7.22 (b) has been taken after exposure of the sample at 1400 K for a few minutes to a local oxygen pressure on the order of 10^{-6} mbar, and the oxygen was supplied

during cool-down until the sample was no longer glowing, because oxygen might desorb rapidly at high temperatures. The LEED image in Fig. 7.22 (b) then has all spots in the positions where we would expect them for an unreconstructed Ir(110) surface, resulting in a pattern of rectangular symmetry.

When the electron energy is changed a bit, additional spots in positions that would correspond to a c(2 × 2) superstructure are visible for this oxygen-exposed sample as seen in Fig. 7.22 (c). These superstructure spots are smeared out along the (001), indicating a small domain size of the reconstruction in this direction. Note that while the streakiness of the spots along (001) might at first appear similar to what was observed for the facetted surface in Fig. 7.22 (a), the movement of the c(2 × 2), including the streaks, is only radially to the center of the pattern as the energy is changed. The oxygen-exposed surface is therefore clearly not faceted. A variety of reconstructions of the O-covered Ir(110) surface are reported in the literature depending on the coverage, and c(2 × 2) is among them. Here, I point only to Ref. [259]. A summary of experimental results with references is contained therein, and its Fig. 1 (2) shows the geometry of the c(2 × 2).

Now that we have confirmed the structure of our Ir(110) surface to be as described in the literature, we turn our attention to the growth of Gr. The starting point for the Gr growth was always given by the non-faceted, O-covered surface. It is questionable, though, whether this is relevant: Firstly, because according to Ref. [260], the faceting of Ir(110) is lifted above 800 K anyways and other reconstructions are formed. Secondly, because ethylene will likely react with adsorbed oxygen and desorb as CO or CO_2 first, until no oxygen is left on the surface. Then, the situation would be the same at the onset of Gr growth as if oxygen had never been on the surface, provided that the equilibration of the surface reconstructions is fast enough, which seems realistic at the high growth temperatures of Gr.

To minimize the number of experimental parameters, we exposed the Ir(110) surface to ethylene only after heating it to a high temperature, i.e., no ethylene pre-adsorption at low temperature as in the TPG+CVD method used on Ir(111) [124]. In dependence of the growth temperature of either 1250 K or 1380 K we find two different phases of Gr, in the following just termed low-T and high-T phase. As a general remark for this section on Gr/Ir(110), we note that all temperatures have been measured by a pyrometer that was possibly poorly calibrated at the time of usage. Given temperatures could be off by up to 100 K, but consistently so between measurements.

Figure 7.23 (a) shows the LEED pattern after exposure to ethylene at 1250 K. The spots marked by the black rectangles again belong to Ir-(1 × 1). The pattern can be consistently interpreted as two domains of graphene, marked with blue-solid and red-dashed circles, which are rotated slightly against each other, and can be mapped onto each other with a mirror plane symmetry of the substrate. In the pattern, one pair of spots of each Gr domain is coincident with one of the four equivalent iridium $(\bar{1}1\bar{1})$, $(\bar{1}11)$, $(1\bar{1}1)$, and $(1\bar{1}\bar{1})$ spots. Thus, the graphene

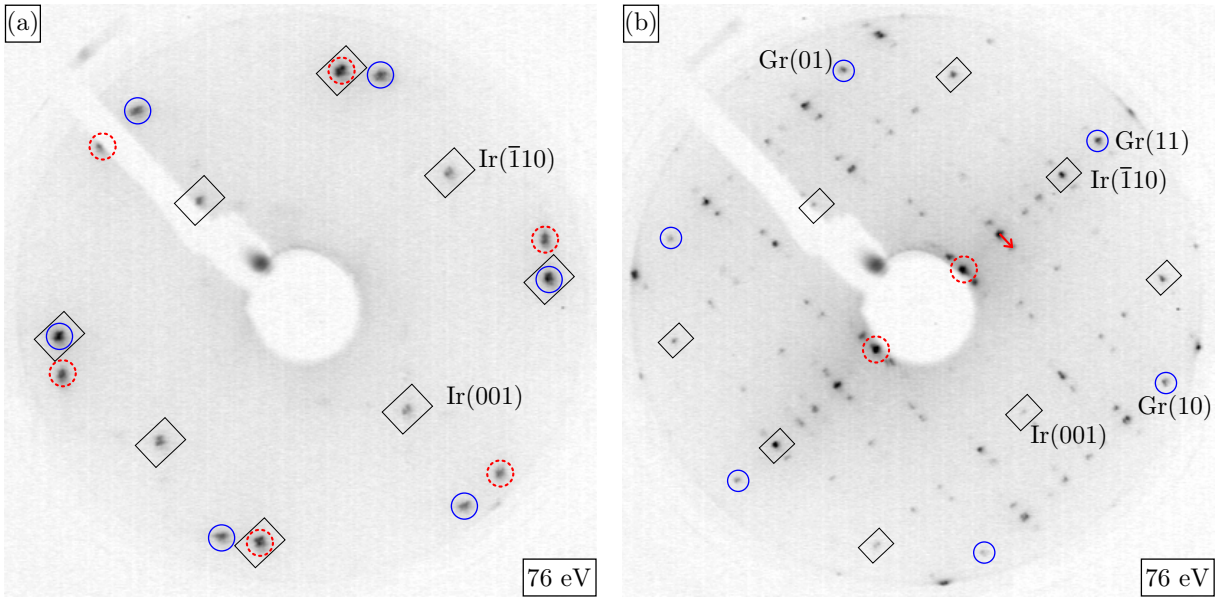

Figure 7.23: LEED patterns of the two phases of Gr/Ir(110) taken at 76 eV. Spots of unreconstructed Ir(110) marked by black rectangles. (a): After exposure of the clean Ir(110) surface to ethylene at 1250 K. The two rotated domains of the resulting low-temperature graphene phase are marked with solid blue and dashed red circles. (b): After exposure of the clean surface to ethylene at 1380 K. Only one rotational domain of Gr is present, marked by blue circles. Red circle marks a first order moiré spot, see text. All other spots result from mixing of Gr and substrate lattice vectors.

is commensurate along one of its zigzag directions. In contrast, perpendicular to that zigzag direction, the Gr and Ir spots do not coincide, and the graphene is most likely incommensurate in that direction. For lattice parameters of Ir $a_{Ir} = 271.5$ pm and graphene as in graphite $a_{Gr} = 246.1$ pm, the commensurability along one zigzag direction of graphene forces it to strech by 4.0%.

The structure of the low-T phase does not seem ideal to achieve a global orientation of all nanowires: If graphene is already present in two different orientations, it appears likely that EuCot nanowires will also grow in more than one direction. We have therefore went on with trials.

Figure 7.23 (b) shows the LEED pattern after exposure of a clean Ir(110) surface to ethylene at 1380 K. A large number of spots is visible. However, all of them can be explained as resulting from the moiré of Ir(110)-(1 × 1) with a single domain of graphene, discussed below. In Figure 7.23 (b), we have marked the spots belonging to Ir and Gr. In contrast to the low-T phase, the high-T phase is apparently incommensurate in all directions. One zigzag direction of Gr is aligned with the Ir($\bar{(}$1)10) direction. Rotational disorder, which is often observed for incommensurate overlayers (e.g., Gr/Ir(111) or polar bilayers of EuO/Ir(111) [261] or FeO/Pt(111) [262]), is not detected within the resolution of our LEED. As a side remark, poorly oriented high-T Gr/Ir(110) (LEED not shown) can be produced by ethylene adsorption at room temperature on

the facetted Ir(110) surface and subsequent annealing at 1380 K, but this is not our goal here.

A moiré spot in general results from an integer linear combination of k vectors belonging to two different lattices. We consider for illustration two k vectors that appear in the pattern in Fig. 7.23 (b). Firstly, a spot pair marked by dashed-red circles close to the center. We call the k vector belonging to this spot k_{m1}; it is given by $k_{m1} = (11)_{\mathrm{Gr}} + (\bar{1}10)_{\mathrm{Ir}}$, and we expect an associated lattice constant $2\pi/k_{m1} = 0.99\,\mathrm{nm}$ if graphene is not strained. Another k vector prominent in the pattern is seen around many spots as satellites in (001) direction. A very short red arrow marks this vector on one occasion. We call it k_{m2}, and it is given by $k_{m2} = (1\bar{1})_{\mathrm{Gr}} + (00\bar{1})_{Ir}$, resulting in the lattice constant $2\pi/k_{m2} = 3.19\,\mathrm{nm}$. k_{m1} and k_{m2} are the two shortest vectors visible in Fig. 7.23 (b), and point respectively in the $(\bar{1}10)$ and (001) directions of the subtrate. We see later that they appear most prominently in STM topographs as well.

The fact that the LEED pattern has so many more spots in the case of the high-T phase than in the case of the low-T phase begs the question: What's the difference? One part of the explanation is certainly that one reciprocal lattice vector of the low-T phase is coincident with a reciprocal lattice vector of the Ir(110) substrate, yielding no superstructure spot in this case. However, I believe that a further factor is at play. I would like to compare it to the difference between rotational domains of Gr on Ir(111). In addition to the aligned phase "R0" of Gr/Ir(111) that is most commonly investigated, including in this thesis, under some conditions Gr domains which are rotated against the substrate lattice can be produced as shown in Ref. [55], most prominently with 30° rotation. For the rotated domains, fewer and comparably less intense moiré spots are visible in the LEED patterns, and this coincides with an $\approx 8\times$ smaller apparent corrugation of the moiré lattice measured in STM for the R30 phase compared to R0 [55]. Most likely, the geometric corrugation of the moiré of R30 graphene is indeed less than that of R0 graphene, and this results in a lower intensity of the moiré spots in LEED. But why would the corrugation of the low-T phase be less than that of the high-T phase? We discussed before that a 4% stretch is imposed on the graphene to make the low-T phase commensurate in one direction. A recent study shows that compressive strain in R0 Gr on Ir(111) leads to a buckling of the Gr layer, i.e., an increased moiré corrugation [263]. I speculate that this mechanism works also in reverse, i.e., that stretching graphene will make it flatter, and that this is partially responsible for the lower number of moiré spots in LEED for the low-T compared to the high-T phase.

We conclude the discussion of the LEED results here and turn to the STM measurements. Figure 7.24 (a) and (b) show differentiated large-scale overview STM topographs of the sample after growth of the low- and high-T phase at 1250 K and 1380 K respectively. The differentiation results in an apparent illumination from the left. Both, (a) and (b), show a structure of almost periodic stripes along the $(\bar{1}10)$ made of high plateaus and low plains with step bunches in between. Note that the image size is 1.2 μm in (a) and 2.4 μm in (b). Thus, the typical stripe separation is roughly 300 nm for the low-T phase and 600 nm for the high-T phase.

One explanation for the stripe pattern would be as follows: The clean surface energetically prefers the (331)-faceted state, while the Gr-covered surface prefers the flat state. As graphene is grown, the faceted surface starts to transform into a flat one, but because this requires the diffusive transport of several layers of Ir atoms, the process might not complete, and a residual corrugation is observed. An alternative explanation could be that the pattern has nothing to do with the faceting of the surface, but is the result of sputtering, insufficient annealing, and anisotropic diffusion. The healing of sputter-induced surface corrugation proceeds via adatom diffusion, and the barrier to adatom diffusion on an fcc (110) surface is lower along $(\bar{1}10)$ than along (001). Thus, patterns of principally similar origin to what was observed by Michely et al. [264] on Pt(111) after ion erosion, but modified due to the anisotropic diffusion, could emerge. In either case, in order to explain the alternation of step bunches with largely flat areas, it seems necessary that growth of Gr/Ir(110) induces bunching of steps along $(\bar{1}10)$. Gr-induced step bunching has been observed before on the Ir(332) surface [265].

In the low-T case, in addition to the step edge bundles along $(\bar{1}10)$, a large number of step edges are present at an angle of 45° with respect to the substrate's high-symmetry directions. In contrast, in the high-T case, except the step edge bundles along $(\bar{1}10)$, preferential step directions are along the (001) and two or more directions that are in between $(\bar{1}10)$ and (001). In the low-T phase, the stripe structure appears with a more regular periodicity, while in the

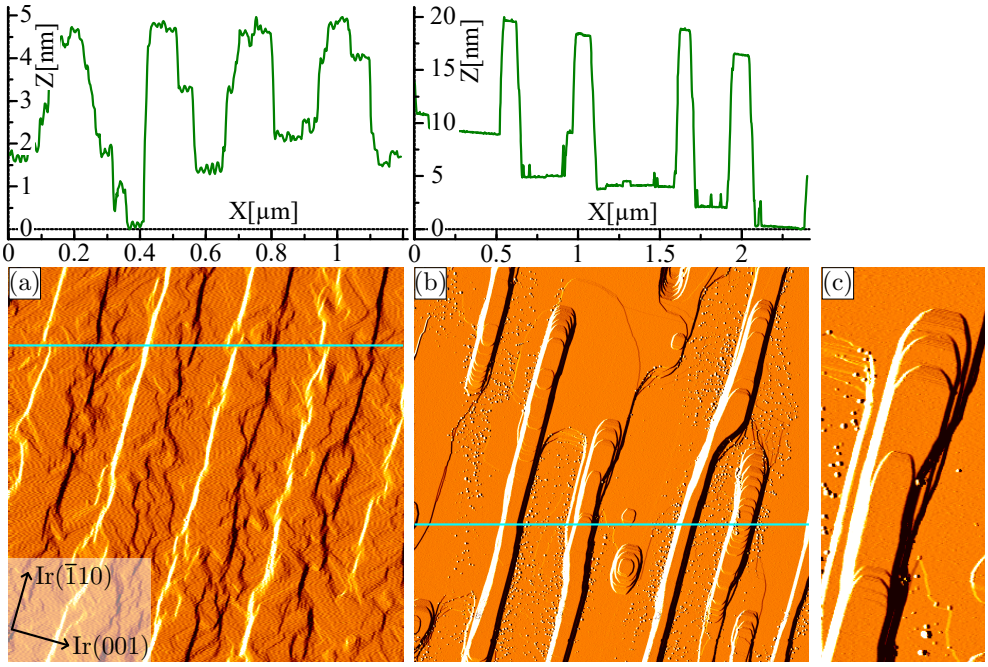

Figure 7.24: Large-scale differentiated topographs of the two different graphene phases on Ir(110), with height profiles along the indicated cyan lines. (a): Low-temperature phase, $(1.2\,\mu\text{m})^2$. This image suffers from humming due to vibrations. (b): High-temperature phase, $(2.4\,\mu\text{m})^2$. (c): Zoom into an area in (b), $(361 \times 874)\text{nm}^2$. The crystallographic directions given in (a) are valid for all STM images on the Ir(110) crystal.

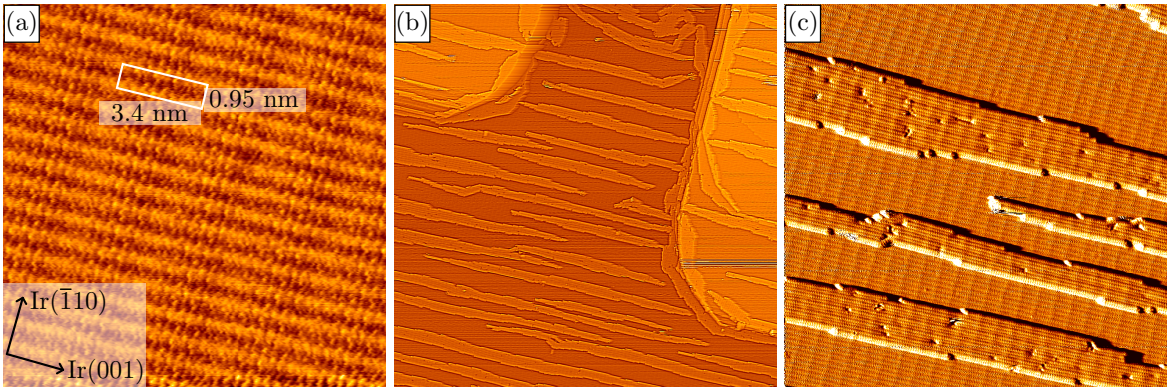

Figure 7.25: (a): STM topography of the moiré superstructure of the high-T phase of Gr/Ir(110), $(16\,\mathrm{nm})^2$. Corrugation with periodicity smaller than the moiré is visible, but no clear atomic resolution. (b): Overview after growth of submonolayer amounts of EuCot on the high-T phase of Gr/Ir(110), $(359\,\mathrm{nm})^2$. Needles are oriented with their long axis in (100) direction. (c): A closer view on the same sample as in (b) resolves the wires inside the EuCot needles, $(79\,\mathrm{nm})^2$. Many open wire ends are visible.

high-T phase, the structure appears as if it was in the process of dissolution by evaporation of adatoms from the non-($\bar{1}$10) step edges.

For the high-T phase, we have obtained one other large-scale STM image of this preparation, as well as an image taken with the STM at the ID32 HFM endstation on a different preparation (both not shown), neither of which exhibited such a regular stripe structure as Fig.7.24 (b), indicating that it should be possible to avoid the stripe pattern for the high-T phase by a more careful tuning of the growth parameters. Yet for our further work on EuCot growth, what appears as the most important distinction of the low- and high-T phases is the terrace diameter found on most of the surface, which is far larger, on the order of several 100 nm, on the high-T phase sample. As the high-T phase thus appears more promising from both LEED and STM, we focus exclusively on this phase from now on.

The higher-resolution STM topograph shown in Fig. 7.25 (a) shows what the moiré superstructure of the high-T phase looks like in real space. A longer periodicity in (001) direction has a small apparent corrugation of about 10 pm, while the shorter periodicity in ($\bar{1}$10) direction has a larger apparent corrugation of about 50 pm. The unit cell of this moiré is rectangular and is measured by STM with lattice constant of (0.95 ± 0.05) nm in ($\bar{1}$10) and (3.4 ± 0.2) nm in (001) direction, in agreement with the values expected from the lattice constants of Ir and graphite given earlier. It would be possible to determine the moiré periodicity with much greater precision if also the atomic lattices of Ir and Gr were resolved in the image [54], but this was not achieved here.

Finally, we have grown EuCot on this sample by simultaneous exposure to Eu and Cot at 300 K. Fig. 7.25 (b) shows an overview topograph, where needle-shaped crystallites are seen to be growing with their long axis along the substrate's (001) direction everywhere except at the

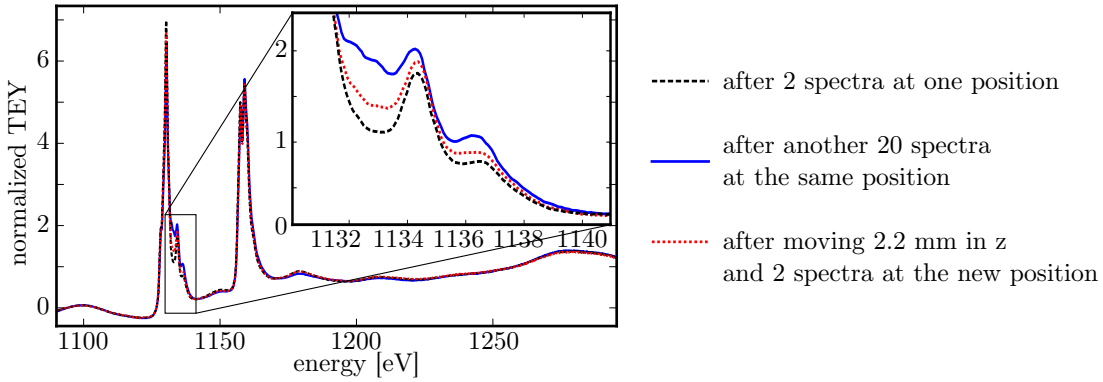

Figure 7.26: Spectra measured at negative helicity at the beginning of a measurement sequence, at the end of a sequence, and after the sample was moved 2.2 mm in z direction, before reducing the beam intensity. Changes in the spectral shape of Eu in EuCot from radiation damage are visible in the region between the M_5 main peak and a satellite on its high-energy side as shown in the inset.

substrate's step bundles, where the needles follow the step bundle's direction instead.

The differentiated STM topograph in Fig. 7.25 (c) shows that the needles indeed consist of parallel wire strands. Remarkably, the wires have exposed ends, in contrast to wires grown on Gr/Ir(111), which mostly bend around instead of ending. Our efforts to achieve growth of almost all EuCot nanowires in only one direction over a macroscopic area were thus successful.

7.5 Magnetism of europium cyclooctatetraene wires

This section is unpublished. The following persons took part in the beamtime at Bessy II's pm2/VEKMAG: N. Rothenbach and K. Ollefs of the group of H. Wende; A. Britton, L. M. Arruda, M. Bernien, L. Kipgen, and F. Nickel of the group of W. Kuch, who also arranged the beamtime; the beamline scientists of BESSY; and S. Kraus and myself of the group of T. Michely. The following persons took part in the beamtime at ESRF's ID32: N. Rothenbach, K. Ollefs, L. Arruda, S. Kraus, myself, and N. Brookes, who was the responsible ESRF beamline scientist. The XMCD data on EuCot of both beamtimes were evaluated by N. Rothenbach. During the beamtimes, S. Kraus and myself were predominantly occupied with the sample preparation and LEED/STM, while the others conducted the XMCD data acquisition. In particular during the ESRF beamtime, they identified the radiation damage and temperature reproducibility problems. Figure 7.27 was prepared by S. Kraus. I was the main proposer of the ESRF beamtime with co-proposers H. Wende, K. Ollefs, and T. Michely.

The magnetism of EuCot nanowires was investigated by XMCD, at first at the VEKMAG endstation at BESSY II's pm2 beamline, and later at the high-field-magnet endstation at ESRF's

ID32 beamline. After the graphene was prepared, the recipe for EuCot preparation could be easily reproduced and worked on the first try every time in both beamtimes. At VEKMAG, the existence of EuCot islands on the sample was confirmed by a MCP-LEED alone, because no STM is available on this chamber. At ID32, an STM is available, in addition to an MCP-LEED.

Samples were checked after the XMCD measurements by LEED and at ID32 also by STM; no degradation was observed. This excludes an effect of contamination by background gas, however, it does not exclude degradation by beam damage, because both the X-ray beam, LEED beam, and STM measurements see only a small part of the sample, and exceedingly likely do not see the same spot. That EuCot did not degrade, despite exposure to pressures of up to $1 \cdot 10^{-9}$ mbar for many hours, indicates a relative inertness of EuCot under typical UHV background pressures.

We now turn over to discussion of the XAS and XMCD. In all measurements, the lineshape indicated divalent Eu. New for EuCot compared to the previous Eu-intercalated samples is a sensitivity to radiation damage, which significantly complicated our measurements. In particular, data obtained later at ID32 let us conclude that all samples measured at BESSY had been damaged by too high x-ray doses. Only data taken at ID32 is therefore shown in this thesis.

Radiation damage was gauged by its effect on the Eu lineshape, and we discuss this aspect first. The change in the spectral shape is best visible in negative helicity. Figure 7.26 shows the absorption spectrum for a sample with ≈ 0.5 ML EuCot on Gr/Ir(111), for negative helicity, with different degrees of radiation damage. The effect is most clearly seen in the local minimum between the main M5 peak and a satellite peak to its right. This minimum is deepest at the beginning of a measurement sequence (black dashed line). After exposed to the beam for a certain time, this minimum has become much shallower. If we move the sample under the beam by 2.2 mm in z direction, such that the beam hits a different spot on the sample, the minimum becomes deeper again, indicating that the change is indeed induced by radiation, rather than by, e.g., contamination over time through the imperfect vacuum. The reason why it is not as deep as at the beginning of the run is that the beam is defocused in z direction such that its standard deviation is about 1 mm, which means that even a position about 2.2 mm away is still hit by a fraction of the intensity as at the center.

In order to minimize radiation damage, we have taken the following measures: (1) The opening of some slits in the beamline optics was reduced. This reduces the intensity and reduces the signal-to-noise ratio, therefore this approach has fundamental limits, and is generally not the preferred one. (2) One can defocus the beam, in order to spread the beam intensity over a larger area. This does not lower the signal-to-noise ratio, and is therefore preferred. Here, the theoretical limit is only the sample size, 7 mm diameter in our case. Importantly, when measurements are conducted in grazing incidence under an angle of θ to the surface normal, the beam-projected width of the sample is reduced by a factor $\cos(\theta)$. In our measurements, we applied from the start settings on the mirrors that should yield a defocusing of 1 mm in vertical direction. However, no defocusing was applied in horizontal direction, because the

beam-projected dimension of the sample in this direction is smaller, such that we believed that a 1 mm defocus in horizontal direction would be too large. An intermediate value for the defocus, i.e., 0.5 mm, was not used because the necessary setting on the mirror for such a defocus was not clear. The beam size in horizontal direction should therefore have been about 100 µm.

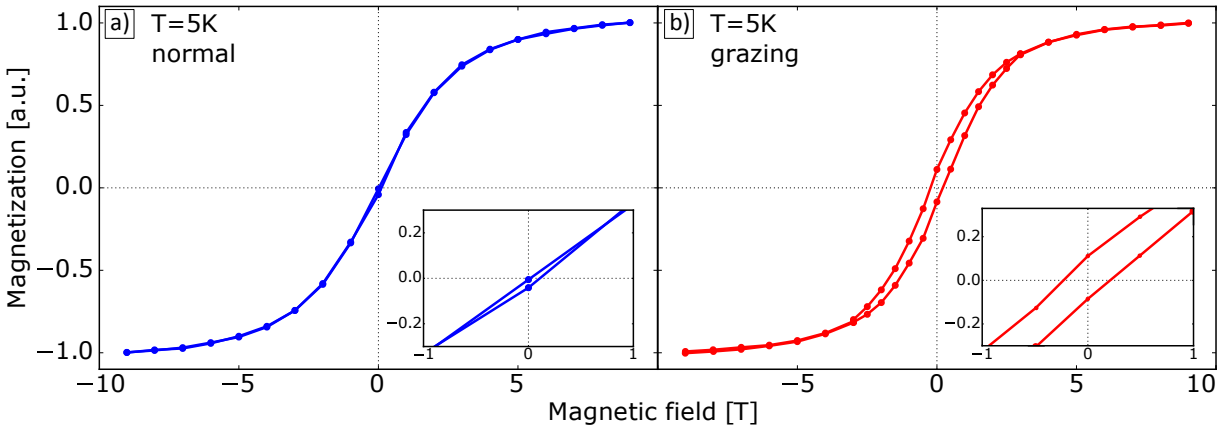

Figure 7.27: Magnetization curves for B up to ±9 T, normalized to the value at $B = 9$ T, obtained at the lowest attained temperature (indicated $T = 5$ K). (a): Normal incidence ($\theta = 0°$). (b): Grazing incidence ($\theta = 60°$). Insets: Zoom into the interval [−1 T,1 T].

Avoiding radiation damage is crucial to observe the true shape of the magnetization loop. Figure 7.27 shows the magnetization loop obtained under normal and grazing incidence for the sample with the lowest attained temperature. The loop is closed in normal incidence, but shows an opening under grazing incidence, which persists up to fields of 2.5 T. By introducing beam damage on purpose, the magnetization loop opening disappears.

During our experiments, we had difficulty reproducing the hysteresis loop opening. Specifically, a total of 7 samples with EuCot were measured with a low enough beam intensity to avoid radiation damage, but only 2 of them showed an open loop. An analysis of the loop shape by N. Rothenbach, fitting the loop to a Brillouin function using the temperature as a fit parameter, indicated that the actual temperature of the sample varied even when the indicated temperature at the sensor at the cryostat head was the same. The 2 samples that exhibited an open loop were also the ones where the actual temperature determined from fitting was lowest. We thus believe that the loop opening could not be reproducibly measured, because the lowest temperature was not reproducibly attained. This is plausible, because the lowest achievable temperature is dependent on the thermal conductance between sample and cryostat, which varies between different preparations, because every time a new sample is introduced, two thermal contacts have to be established: (1) The sample holder plate is put onto a so-called shuttle, and (2) the shuttle is put onto the cryostat. In both cases, a screwing mechanism is used to improve the thermal contact, but the quality of the contact is not consistent according to the experience of the beamline scientists. The lowest attained temperature is therefore higher for some samples than for others.

To estimate the Curie temperature, one temperature-dependent measurement was conducted. We started from a sample that showed an open loop at an indicated temperature of 5 K. Upon heating to $T = 10$ K, the loop was closed; then going to 7 K, the loop was still closed; then, going again down to 5 K, the loop was again open, but the opening was less than at the beginning of the measurements, which could be traced to the accumulated radiation damage seen in the spectral shape. Thus, the effect of temperature and radiation damage could not be entirely disentangled, but T_C is likely below 10 K, maybe even below 7 K, also for an undamaged sample.

We have considered two alternative explanations for the magnetization loop opening, but are convinced they can be excluded. Firstly, it could be that ferromagnetic europium monoxide has formed during growth or later from the background pressure, and that this gives the loop opening. But EuO is magnetically soft, with coercive field less than 100 mT [32], and thus cannot be responsible for an opening persisting up to 2.5 T. The low coercive field of EuO is in part a result of its cubic crystal structure, which suppresses anisotropy. Secondly, we considered that a layer of intercalated Eu under Gr could have accidentally formed, which is strongly ferromagnetically coupled. But the intercalated Eu is magnetically soft, too, as discussed in section 6.1.2 and Ref. [30]. The large coercive field can then only be explained by a strong in-plane uniaxial anisotropy, and Eu in EuCot islands is the only possible explanation. That the loop opening is easily destroyed by radiation is another clear sign of its origin in a molecular system.

We discuss in the following the origin of the anisotropy. N. Atodiresei et al. [43] have previously calculated the single-ion anisotropy of Eu in EuCot to be on the order of a few μeV. In contrast, the anisotropy energy resulting from the magnetic dipolar interaction is on the order of 100μeV and thus should entirely dominate; the calculation is analogous to that in section 6.1.2. The dipolar interaction should favor an arrangement where the magnetic moments are parallel to the wire axis. This nicely explains our observation that the magnetization loop is open only in grazing incidence, because the EuCot wires lie in the plane of the sample surface.

7.6 Magnetism of thulium cyclooctatetraene coffee beans

> This section is unpublished. The data was obtained during the same beamtime as that of section 7.5 with the same collaborators, see there. Previous data analysis of the magnetization loop performed by S. Kraus [117] was redone for Figs. 7.29 and 7.30. The analysis of the spectra is my own.

The TmCot coffee bean phase has been investigated by XAS/XMCD at ID32. The samples were checked by STM after the measurements to confirm the quality of the preparation; it was found to be not at all worse than as prepared in our home labs. All data were taken at an

indicated temperature of 5.2 K and in magnetic fields of $B = \pm 9$ T with left- and right-circular polarized light and for the magnetic field parallel and antiparallel to the beam. No isotropic or linearly-polarized spectra were taken.

7.6.1 Results and analysis

Lineshape

Figure 7.28 (a/b) shows the obtained spectra for the individual polarizations μ_+, μ_- for (a) normal ($\theta = 0°$) and (b) grazing ($\theta = 60°$) incidence, while (c) and (d) give the polarization-averaged (XAS) and difference (XMCD) spectra, respectively. The measured lineshape of both, the XAS and the XMCD, agree well with calculations in Ref. [266] of a $4f^{12}$ configuration, and are clearly not a $4f^{13}$.

A free Tm atom has $6s^2 4f^{13}$ configuration, and thus, a simple oxidation into the 2+ state by a single Cot ligand cannot explain the observed $4f^{12}$. However, an electron could transfer from the $4f$ into the $5d$ shell. This occurs in bulk Tm metal, where the $5d$ electron contributes to the bonding and the lineshape measured in XAS also indicates $4f^{12}$ [107]. The observed XAS lineshape is thus consistent with the coffee bean model, where each Tm atom donates its two $6s$ electrons to a Cot ring and forms a $5d$ metal-metal bond with the other Tm atoms in the trimer.

In contrast to most other XMCD spectra, that of $4f^{12}$ is of the same sign at the M_5 and M_4 edges, a result of the large orbital to spin moment ratio $m_L/m_S = 5/2$ in this configuration [178, 267]. The multiplet calculations of Refs. [266] show that the $4f^{12}$ spectra consist of only 4 lines, labeled $n = 1$ to 4 with increasing energy on the right side of Fig. 7.28 (a). Such individual identification of lines is possible only for the lightest and heaviest rare-earth elements, where the number of electrons or holes in the $4f$ shell is small. Going from a nearly empty or nearly full $4f$ shell toward the middle of the rare-earth series, the number of lines at the $M_{5,4}$ edges quickly grows such that their separation in energy becomes much smaller than the linewidth; for the half-filled $4f^7$, the number of multiplet lines is larger than 1000 [266]. The dipole-allowed $M_{5,4}$ multiplet structure on the $4f$ ion in general consists of three components, with transitions corresponding to $\Delta J = 0$, $\Delta J = +1$ and $\Delta J = -1$ [266]. In the $4f^{12}$ spectrum, the $\Delta J = -1$ transition contributes the lines 2, 3, and 4, $\Delta J = 0$ contributes the line 1, while $\Delta J = +1$ does not contribute any line [266]. In section 6.1.2, we discussed at length the problem of ambiguity in the integration of the resonances for the purpose of using the XMCD sum rules. Here, the small number of lines in the $4f^{12}$ spectrum creates the opportunity to largely avoid these problems, by fitting the lines directly. This is a great advantage, as we will see next.

Analysis via individual multiplet line intensities

The four individual spectra, i.e., for both angles of incidence and both polarizations, were fitted with the sum of four suitable line profiles and a single polynomial of degree 20 over the entire measured energy domain. For the lineprofiles, I followed Thole et al. [107] in assuming Voigt profiles at the M_5 and a Fano profile with asymmetry parameter $q_{3/2}$ at the M_4. A single Gaussian instrumental broadening constant σ was used for all lines, while for the Lorentzian lifetime broadening, the two parameters $\Gamma_{5/2}$ and $\Gamma_{3/2}$ are used for the peaks at the M_5 and M_4 edges, respectively. For the polynomial, even higher orders did not visibly improve the fit in the

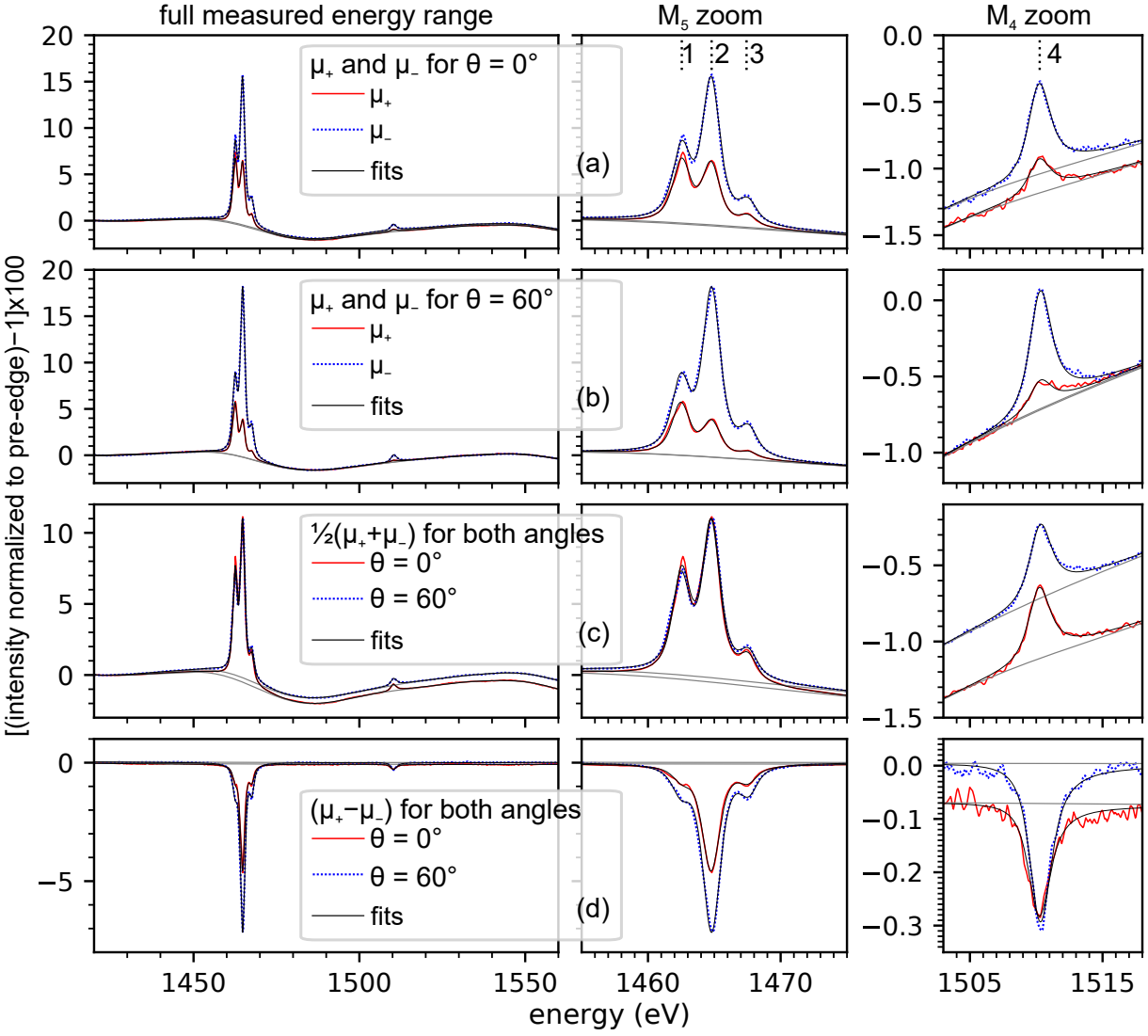

Figure 7.28: XAS and XMCD spectra obtained on the TmCot coffee beans at an indicated temperature of $T = 5\,\mathrm{K}$ and magnetic field $B = \pm 9\,\mathrm{T}$. First and second rows [(a/b)]: Spectra for the individual polarizations measured in (a) normal and (b) grazing incidence. The third row [(c)] and fourth row [(d)] show the resulting polarization-averaged (XAS) and difference (XMCD) spectra. Middle and right panels show zoom-ins onto the edges, i.e., same data as left panel. Thin lines are fits, see text.

energy region around the peaks or change the fit parameters of interest notably. In Fig. 7.28, the polynomial alone as well as the sum of polynomial and Voigt/Fano profiles is plotted as thin lines.

We are interested in the fitted intensities of the individual lines. This is because Goedkoop et al. [266] have shown that for a polarization q, the contributions $A^q_{\Delta J}$ of the $\Delta J = 0, \pm 1$ partial spectra to the total are related to the expectation values of the magnetic quantum number of the initial state $\langle M \rangle$ (where $|M| \leq J$) and its square $\langle M^2 \rangle$ (where $\langle M^2 \rangle \leq J^2$) according to the expressions given in Table 7.2. Here, $q = \pm 1$ is circular while $q = 0$ is linear polarization; the spectra $\mu_\pm$ in Fig. 7.28 were acquired for a $qB/|B| = \pm 1$. We furthermore define the helicity-polarization product $\mu = qB/|B|$. Goedkoop [178] notes that, in the case of crystal field effects, the validity of the expressions in Table 7.2 depends on neglecting crystal field effects in the final state.

	$q = 0$	$q = \pm 1$
A^q_{JJ+1}	$\frac{(J+1)^2 - \langle M^2 \rangle}{(2J+3)(J+1)(2J+1)}$	$\frac{(J+1)(J+2) \pm (2J+3)\langle M \rangle + \langle M^2 \rangle}{2(2J+3)(J+1)(2J+1)}$
A^q_{JJ}	$\frac{\langle M^2 \rangle}{J(J+1)(2J+1)}$	$\frac{J(J+1) \mp \langle M \rangle - \langle M^2 \rangle}{2J(J+1)(2J+1)}$
A^q_{JJ-1}	$\frac{J^2 - \langle M^2 \rangle}{J(2J-1)(2J+1)}$	$\frac{J(J-1) \mp (2J-1)\langle M \rangle + \langle M^2 \rangle}{2J(2J-1)(2J+1)}$

Table 7.2: The expressions for the factors $A^q_{JJ'}$ giving the intensity of $\Delta J = 0, \pm 1$ ($\Delta J = J - J'$) transitions for different values of $q = M' - M$. Reproduced with permission from Goedkoop et al. [266], © 1988 APS.

Let $I_{n,\mu,\theta}$ be the area under the n-th line in Fig. 7.28 for angle θ and helicity-polarization product μ, and let $I_{n,\Delta J}$ be the intensity of the n-th line in the ΔJ contribution. Then, the intensities are related according to

$$I_{n,\mu,\theta} = I_{n,\Delta J} A^\mu_{\Delta J}. \tag{7.1}$$

via the $A^\mu_{\Delta J}$ from Table 7.2. From the multiplet calculations of Goedkoop et al., we know that the $I_{n,\Delta J}$ vanish except for $I_{1,0}$, $I_{2,-1}$, $I_{3,-1}$, and $I_{4,-1}$ (see the spectra given in Ref. [178]). Then for each angle, equation 7.1 gives a system of four equations with four unknowns when we consider only $n = 1$ and any one of $n = 2$, 3, or 4. If we consider all the $n = 2$, 3, and 4, the system of equations is overdetermined, and allows an integrated consistency check, which it passed. For each angle, the unknowns are then $I_{1,0}$, $I_{2,-1}$, $I_{3,-1}$, $I_{4,-1}$, $\langle M \rangle$, and $\langle M^2 \rangle$, only the last two of which are of interest to us. We obtain the values in Table 7.3, which we compare to the expectation for a free, paramagnetic $4f^{12}$ ion with $J = 6$. Based on visual inspection of the quality of the fit around the maxima at the peaks, I estimate the error in the obtained $\langle M \rangle$ and $\langle M^2 \rangle$ values to be up to 10%.

θ	$\langle M \rangle$	$\langle M^2 \rangle$	$\langle M \rangle / J$	$\langle M^2 \rangle / J^2$
0°	1.74	16.8	0.29	0.47
60°	3.04	22.6	0.51	0.63
unpolarized paramagnetic $4f^{12}$	0	14	0	0.39
saturated paramagnetic $4f^{12}$	6	36	1	1

Table 7.3: Values of $\langle M \rangle$ and $\langle M^2 \rangle$ determined by using the measured line intensities $I_{n,\mu,\theta}$ and Table 7.2. Values for an unpolarized (isotropic) or saturated paramagnetic $4f^{12}$, $J = 6$ ion are given for comparison. An unpolarized paramagnetic ion corresponds to the high-temperature/low-field limit $J\mu_B B \ll k_B T$, where is $\langle M \rangle = 0$ and $\langle M^2 \rangle = \frac{1}{3}J(J+1)$ and thus for $J = 6$, $\frac{1}{3}J(J+1) = 0.39J^2$. In the saturated limit, $J\mu_B B \gg k_B T$, it is $\langle M \rangle = sJ$ and $\langle M^2 \rangle = J^2$.

Sum rules

Nistor et al. [267] have investigated Tm atoms and monolayers on a W(110) surface by XMCD and XMLD at 8 K and fields up to ±5 T, and also found the $4f^{12}$ configuration. From the XMCD sum rules, they give the relationships

$$\frac{\langle L_z \rangle}{2\langle S_z \rangle} = \frac{X_{M_5} + X_{M_4}}{X_{M_5} - \frac{3}{2}X_{M_4}} \left(1 + 3\frac{\langle T_z \rangle}{\langle S_z \rangle}\right) \tag{7.2}$$

where X_{M_5} and X_{M_4} are the integrals over the XMCD at the M_5, M_4 edges, respectively. These integrals correspond to the commonly used p and q defined in subsection 3.5.2 via $X_{M_5} = p$ and $X_{M_4} = q - p$. They use the value $\langle T_z \rangle / \langle S_z \rangle = 0.411$ from Ref. [120] to obtain $\langle L_z \rangle / (2\langle S_z \rangle) = 2.5 \pm 0.1$ in agreement with the expected value of 2.5 for the $J = 6$, $L = 5$, $S = 1$ system of $4f^{12}$. For our data, I obtain $\langle L_z \rangle / (2\langle S_z \rangle) = 2.54$ in normal and 2.49 in grazing, in excellent agreement with the theoretical free-ion value. We note that $\langle L_z \rangle / \langle S_z \rangle$ is not, in general, independent of the angle; in fact, in the $3d$ elements, $\langle L_z \rangle$ can be strongly angle-dependent, and the anisotropy of the orbital moment is directly related to the magnetocrystalline anisotropy [268–270]. However, the situation in the $3d$ elements differs from that in the $4f$ ones: For the former, the spin-orbit interaction is a small perturbation to the crystal field, while for the latter, this relationship is reversed [271]. Here, we take the very good agreement of the lineshape calculated for the free ion [178] with our measured ones as evidence that the configuration with respect to the S, L, and J quantum numbers is not substantially modified compared to the free ion. Lastly, considering a possible angular dependence of $\langle T_z \rangle / \langle S_z \rangle$, we mention that a multiplet calculation of Stepanow et al. [272] for Tb in the ligand field of a phthalocyanine double decker yielded an angle-independent value of $\langle T_z \rangle / \langle S_z \rangle$ equal to the free-ion one calculated by Teramura et al. [120]. Such multiplet calculations would be desirable also for our system, but they are complicated by the complex, low-symmetry ligand field and the presence of several inequivalent Tm atoms.

Using the $\frac{\langle T_z \rangle}{\langle S_z \rangle} = 0.411$ of Ref. [120] and the sum rules as given in equations 3.12 and 3.13, we can determine the expectation values for the orbital and spin operators and from these the

total $\langle M \rangle$ as given in Table 7.4. The $T_Z \neq 0$ influences the spin moment strongly, by more than a factor 2.

Note that the values of all integrals for sum-rule analysis in this section were obtained by summing over the fitted intensities of the individual lines, rather than performing an actual integration. This is desirable because it avoids arbitrary choices in the subtraction of the background and placement of the integration boundaries.

	$\langle L_z \rangle$	$\langle S_z \rangle$	$\langle M \rangle = \langle L_z \rangle + \langle S_z \rangle$
0°	1.16	0.23	1.38
60°	1.96	0.34	2.36
saturated $4f^{12}$ paramagnet	5	1	6

Table 7.4: Expectation values of the spin and orbital quantum numbers obtained by sum rules. The magnetic moments result by multiplication of $\langle M \rangle$ with the factors $g_L = -1$, $g_S = -2$, and $g_J = -7/6$, respectively.

Comparing the values of $\langle M \rangle$ obtained via the expressions in Table 7.2 and given in Table 7.3 with those obtained by sum rules and given in Table 7.4, we observe that the latter are systematically smaller. Because the same data and fitted line intensities went into both numbers, this error should be based on the fact that the integral r for the sum-rule evaluation was taken over the polarization-averaged spectrum, i.e., $\frac{1}{2}(\mu_+ + \mu_-)$, rather than properly over $\frac{1}{3}(\mu_+ + \mu_0 + \mu_-)$, where μ_0 is the isotropic spectrum, which we did not measure. Schillé et al. [273] discuss a measurement of an isotropic spectrum taken at 300 K for holmium. For Eu^{2+}, where the linear dichroism is tiny, it is almost $\mu_0 = \frac{1}{2}(\mu_+ + \mu_-)$, and hence this issue does not occur; yet it does for Tm. Thus, we conclude that the numbers given in Table 7.3 are the proper ones, because there, the linear dichroism was accounted for via the expressions of Table 7.2. Note again that our analysis in this section crucially relied on separating the contributions of the individual peaks 1, 2, and 3 to the M_5, which is not possible for almost all other rare earth, where the multiplet structure is too complex.

Magnetization loops

Next, we describe the magnetization loops, which were obtained by field-dependent measurement of the signal at the maximum of the XMCD at the M_5 normalized to the pre-edge signal as given in equation 3.17. The $M(B)$ curves for normal and grazing incidence are compared in Fig. 7.29 without any further scaling of the signal. They were symmetrized according to $M(B) = -M(-B)$, and also averaged over field-up and -down direction because no loop opening was found.

The curve in normal incidence appears nearly saturated at 9 T, while the grazing incidence curve is still far from saturation at this field. Remarkable is that the slope of the curves around zero in normal and grazing is equal within 5%. Generally, comparing $M(B)$ curves obtained

under different angles can be problematic, as the normalization is performed to a pre-edge background that may also be angle-dependent. However here, pre-edge and M_5 hardly change relative to each other as seen in Fig. 7.28 (c). Furthermore, that the magnetization curve at 9 T is higher in grazing compared to normal incidence is quantitatively fully supported by the values of $\langle M \rangle$ obtained from the analysis of the spectra in Tables 7.3 and 7.4.

We fitted Brillouin functions with $J = 6$ and $g_J = -\frac{7}{6}$ (as expected for $4f^{12}$) to the measured curves as shown in Fig. 7.30, with temperature and saturation value as free parameters. In normal incidence, the obtained $T_{\mathrm{fit},\,0°} = 5.7\,\mathrm{K}$ is realistic as a value for the actual sample temperature. In contrast in grazing incidence, the obtained $T_{\mathrm{fit},\,60°} = 12.5\,\mathrm{K}$ is far too high. The Brillouin fit is also better in normal than in grazing incidence: The residuals of the fit, which are plotted in Fig. 7.30 as crosses, are smaller in normal incidence and not systematically dependent on B. In contrast, in grazing incidence, the fit has a systematic deviation from the data. Note that for this plot, the symmetrization according to $M(B) = -M(-B)$ was not used, to show that the systematic deviation of the fit visible in Fig. 7.30 (b) is not an artifact of the data processing.

7.6.2 Discussion

Combining the value from the normal incidence spectral analysis of the average $\langle M \rangle / J = 0.29$ per atom with the information from the Brillouin fit that the curve is about 93% saturated would yield a value very close to $\langle M \rangle / J = 1/3$. From the coffee bean model, there are three

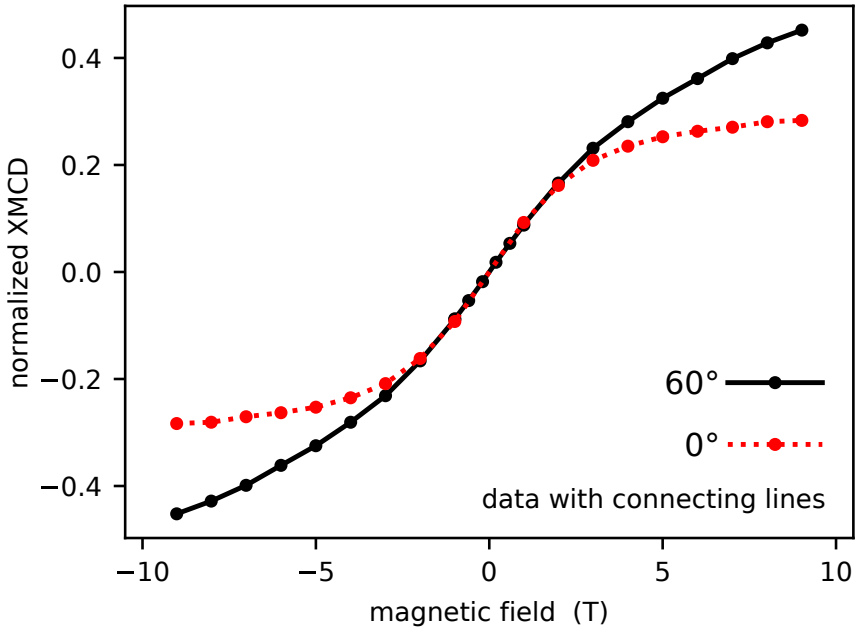

Figure 7.29: Magnetization curves for normal ($\theta = 0°$) and grazing ($\theta = 60°$), measured at an indicated $T = 5.2\,\mathrm{K}$; averaged over field-up and -down directions and symmetrized according to $M(B) = -M(-B)$.

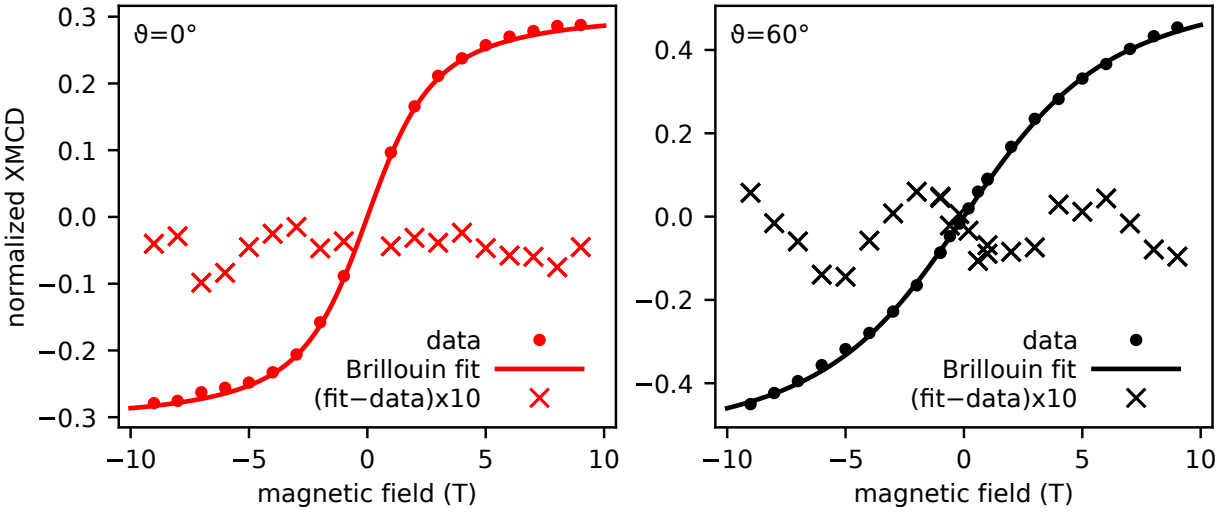

Figure 7.30: Magnetization curves (points), averaged over field-up and -down directions, but not symmetrized via $M(B) = -M(-B)$, with Brillouin function fits (solid lines) for $J = 6$ and $g_J = -\frac{7}{6}$. The residuals of the fit (crosses) are also plotted, magnified by a factor 10. (a): Normal incidence, fit result $T = 5.7\,\mathrm{K}$ and 93% saturation at $B = \pm 9\,\mathrm{T}$ (b): Grazing incidence, fit result $T = 12.5\,\mathrm{K}$ and 78% saturation at $B = \pm 9\,\mathrm{T}$.

Tm atoms in one riceball strongly bonded to each other via their $5d$ orbitals. It is therefore very tempting to assign the observed saturation at 1/3 in normal incidence to a ferrimagnetic order in the riceballs, where two Tm moments are parallel to the external field while one is antiparallel. Such an alignment could also be easily understood, simply as the result of a strong antiferromagnetic coupling, where the frustrated antiferromagnetism in the cluster of three is lifted by the external field. However, if this were true, $\langle M^2\rangle/J^2$ would be equal to one, while our analysis gives $\langle M^2\rangle/J^2 = 0.47$. Note that even without the quantitative analysis, it is immediately clear from the comparison of the polarization-averaged normal incidence spectrum in Fig. 7.28 (c) with the calculated linear dichroism spectra in Goedkoop's PhD thesis [178] or the measurements of Nistor et al. [267] that a significant part of the moment in normal incidence at 9 T is perpendicular to the beam. We can therefore exclude such a simple antiferromagnetic order with $M = (6,6,-6)$. Another idea is that the state of the atoms in saturated normal incidence is not $|M| = 6$, but rather $|M| = 2$. Then, $M = (2,2,2)$ for the three Tm atoms in a riceball would also give an observed $\langle M\rangle/J = 1/3$. Yet in this case, it would be $\langle M^2\rangle/J^2 = 2^2/6^2 = 1/9 \approx 0.11$ which is also in disagreement with the determined $\langle M^2\rangle/J^2 = 0.47$ in normal incidence. We conclude that, even neglecting the grazing incidence measurements completely, no single, pure $|M|$ for all Tm moments in the cluster can explain our measurements. I discuss in the following some literature in view of our results.

Nistor et al. [267] have simulated low-field linear dichroism spectra to investigate the ground-state of their Tm adatoms and monolayers on W(110). They find that a ground state with $M = -5$ reproduces their low-field linear x-ray dichroism measurements well for the Tm adatoms. On the other hand for the monolayer, they suggest a mixture of $M = -5$ and $M = -6$,

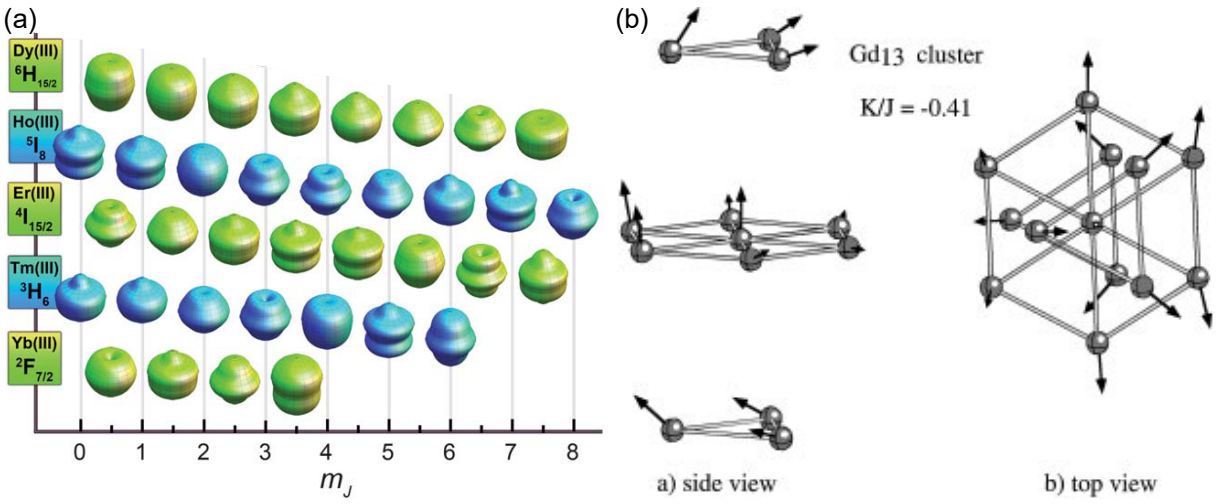

Figure 7.31: (a): Shape of the $4f$ charge distribution in some trivalent rare-earth ions for different magnetic quantum numbers, called M in this section but m_J in Ref. [274], from where this subfigure is reproduced with permission © 2011 RSC. (b): One magnetic configuration considered for hexagonal close packed, magic Gd_{13} clusters, reprinted with permission from Ref. [275] © 1996 APS.

introduced in their simulation via a 175 T strong field interpreted to be due to exchange coupling in the monolayer. They furthermore mention that a mixture of different M can occur not only via a magnetic field, but also if the crystal field has a transversal component. In contrast to their hexagonal monolayers, where the transverse component should be negligible, a transversal crystal field is certainly expected in our model of the coffee bean phase.

In normal incidence, the crystal field of an n-fold rotation-symmetric adsorption site implies that M is only a good quantum number when taken modulo n. Thus, for example, the fourfold-symmetric adsorption site of Ho on MgO (001) leads to a ground state doublet that is a mixture of $M = \pm 7$, ± 3, ∓ 1, and ∓ 5 [276]. In our case, there is no rotational symmetry axis through the Tm atoms along the direction of the external field (i.e., only 1-fold symmetry), and an arbitrary mixture of all M states is thus possible. This results in a large number of free parameters for the crystal field and the magnetic ground state of the system. The complexity is further increased by the presence of several inequivalent Tm atoms.

Rinehart and Long [274] give an intuitive picture of the origin of single-ion anisotropy of $4f$ ions based on the shape of the charge distribution in the $4f$ and its interaction with the ligand field. Due to strong spin-orbit coupling in the $4f$ shell, the charge distribution and the magnetic moment are aligned. For a particular angular momentum quantum number J ($J = 6$ for Tm^{3+}), the different possible states are denoted by the magnetic quantum number, called M in this section[5]. For each M, a different shape of the charge distribution results as shown in Fig. 7.31 (a). The M are degenerate for free ions, but their degeneracy is lifted by both, the crystal field and the external magnetic field.

[5]Ref. [267] uses J_z and Ref. [274] uses m_J, for what is called M in this section following Refs. [178, 266].

In their considerations on the design of a $4f$ single-molecule magnet, Rinehart and Long consider a quadrupolar approximation to the charge density, which can always be referred to as either prolate or oblate. While each M state is different, for Tm^{3+}, it is generally more prolate for high M, and more oblate for low M states. Even though the quadrupolar approximation is rather simplistic, we consider it in the case of our coffee beans: There, a prolate charge distribution is expected to prefer a perpendicular orientation of its high-symmetry axis to the surface, while an oblate one could prefer an in-plane orientation of the high-symmetry axis normal to the ligating Cot ring. While the prolate would thus lead to a collinear arrangement of the moments, the oblate one would prefer a noncollinear in-plane arangement, which would compete with the collinear exchange interaction.

Noncollinear order with canted spin arrangements has been found for free clusters of rare-earth atoms, prominently for the magic hexagonal close-packed Gd_{13} cluster [275, 277], but was also invoked for Tm_n clusters with $n \geq 4$ [278]. Figure 7.31 (b) shows one of the magnetic configurations considered in calculations on Gd_{13} in Ref. [275]. The complexity and broken symmetry of the configuration even for this highly symmetric, magic cluster strongly suggests that the magnetic configuration of our much less symmetric coffee beans will not be solved without input from theory. From the ab initio side, noncollinearly spin-polarized calculations within DFT will certainly provide insights. Note that DFT calculations by N. Atodiresei are already underway to confirm the structural model developed in section 7.3. For the behavior at non-zero temperature and external magnetic fields, a model Hamiltonian approach will be required. The model has to reproduce not only the observed saturated values of $\langle M \rangle$ and $\langle M^2 \rangle$ in normal incidence, but also the peculiar behavior in grazing incidence, where the response to small fields is identical to that in normal incidence, yet surpasses it at higher fields.

Lastly, I note that in our experiments, we measured only with circularly polarized x-rays, and only with the external magnetic field parallel to the beam. However, both vertical and horizontal linear polarization, as well as a magnetic field up to 4 T perpendicular to the beam, were available at ID32. Such linear dichroism measurements could have provided additional insights. They were regrettably not conducted, because we did not realize the relevance of such measurements at the time, and also were not familiar with linear dichroism.

7.7 Conclusion and outlook

EuCot forms sandwich molecular wires under all conditions where Eu and Cot can meet on the surface, while Tm and Cot could be made to form wires only under carefully tuned conditions. In contrast, VBz could not be made to grow as wires, but only as sandwich molecules with one V atom. An obvious question of interest is in how far the combinations VBz, EuCot, and TmCot define groups of similarly behaving systems.

Considering VBz_2, complexes of this composition do exist with several other d-block ele-

ments [279]. Yet whenever the sandwich molecules are rather stable with only one metal atom, this will prevent the formation of other structures, such as wires or riceballs, such that no sizable magnetic coupling could be expected. Rayane et al. [280] have investigated sandwich complexes of benzene with transition metals through measurements of their dipole moments in the free beam and DFT. They concluded a symmetric sandwich structure for the early d-block metals Sc, Ti, V, Nb, Ta and Zr, while for the late $3d$ metals Co and Ni, an asymmetric structure was found with more exposed metal atoms. In line with this, Nakajima and Kaya [96] found a preference for the formation of riceball structures with benzene rather than wires for the late $3d$ metals. Combining a benzene excess at cryogenic temperature with Co or Ni rather than V, the asymmetric structures of $NiBz_2$ and $CoBz_2$ calculated in Ref. [280] should lead to riceball-type structures also on the surface through dimerization or oligomerization. Yet likely, a mixture of different riceballs with more than one composition would form. Also, growth of long sandwich wires on graphene with benzene as a ligand appears unpromising, as the substrate and the ligand are chemically very similar and a preference for bonding to the latter is not evident.

Considering Eu and Tm with Cot, the differences in their behavior were traced to their different preference for the 3+ oxidation state. Tm already has a stronger preference for the 2+ vs. 3+ state compared to the other rare-earth metals except Sm, Eu, and Yb, of which Sm^{2+} and Yb^{2+} have $J = 0$ ground states. We can therefore not expect to be able to grow any other magnetically interesting rare-earth element into wires with Cot as easily as EuCot. Rather, the difficulties observed with TmCot are likely larger with other lanthanides, as they prefer the 3+ oxidation state even more.

I would like to propose a method to overcome this difficulty. We should reduce the electronegativity of the Cot ring, such that it is no longer able to oxidize the Tm or other rare earth to 3+. Note that the calculations by N. Atodiresei on Eu_2Cot_3 molecules [43] have already shown that the electronegativity of Cot is insufficient to oxidize Eu to 3+. The opportunities for modifying the π system's electronegativity via sidegroups or substitution in the ring are extensive. For example, replacing the hydrogens by fluorine should increase the electronegativity of Cot, by pulling the σ electrons toward the fluorine, while adding methyl sidegroups on the Cot ring should decrease it, by pushing σ electrons toward the ring. Partially methylated Cot is commercially available and might enable the fully self-limiting growth of extended nanowires also for TmCot and most other rare-earth elements. Compared to other choices for sidegroups, the methyl group has the benefit that it is most inert, and thus least likely to interfere with the desired reaction. Here, the surface scientist shall remember the low reactivity of methane under UHV conditions, which makes it one of the gases most poorly pumped by metal surface sorption pumps, such as Ti sublimation or non-evaporable getters. On the other hand, methyl sidegroups could affect the carpet structure and might lead to worse crystalline order. Substitution of carbon atoms in the Cot ring by other elements, such as boron or nitrogen, is another possibility. However, heterocyclic aromatics are generally less stable. Importantly for our syn-

thesis method, the ligand molecule must be stable not only in its reduced state but also as the neutral precursor. All candidate ligands could be investigated first by DFT in a $Tm_2(ligand)_3$ structure to confirm that their electronegativity is low enough to avoid Tm^{3+}.

Modification of the Cot ring via suitable ligands is of interest also for EuCot, as the magnetic coupling could be enhanced. Working toward this goal, also here the effects of different ligands should be examined theoretically by DFT first to screen the most promising candidates for the growth and magnetic characterization.

For the EuCot carpets on Gr/Ir(111), ferromagnetic order with hysteresis was found at temperatures somewhat above 5 K, with an anisotropy consistent with only dipolar interaction. It would have been nice to have also XMCD data of aligned EuCot on Gr/Ir(110), because in that case, a rectangle-like shape of the magnetization curve is expected when the wires are parallel to the beam. However, $T < T_C$ was not reached for the two samples with EuCot on Gr/Ir(110) investigated in the beamtime. Nevertheless, the measured magnetization loops already contain plenty of information and will be compared with model calculations presently underway in the group of our theoretical cooperation partner O. Eriksson.

We have developed Gr/Ir(110) as a substrate to align the EuCot wires. However, the concept of a low-symmetry substrate for van der Waals epitaxy is more general. The typical substrates for van der Waals heteroepitaxy all have three- or sixfold symmetry [210]. Other imaginable substrates with two-fold symmetry and without dangling bonds, such as H-terminated Si(110), are expected to be thermodynamically less stable. In contrast, Gr/Ir(110) combines the exceptional inertness and stability of graphene with the two-fold symmetry of Ir(110). It could thus enable the growth of effectively single-crystalline films of materials of any equal or higher symmetry, including cubic or hexagonal ones. One test case could be EuO, which has the cubic rocksalt structure, and can be grown on graphene on Ir(111) as a (100)-textured film but lacking a global in-plane orientation [166].

Lastly, we consider the TmCot coffee beans. In contrast to the sandwich molecular wires, we expect them from our understanding to be quite general and form also with other rare-earth elements. The highly selective formation of this structure is surprising, and that it appears not to have been described before suggests that the surface is acting as a catalyst for the reaction, a rather uncommon role for graphene. Given the interesting if even not yet fully understood magnetic structure of TmCot coffee beans, the LnCot series could result in an attractive playground for the investigation of magnetism in small rare-earth clusters. We stress here the homogeneity of the coffee bean phase, ease of preparation due to the self-limiting stoichiometry w.r.t. the Cot pressure, and high inertness by UHV standards, which all make this system very attractive for XMCD experiments. Compared to the Stern-Gerlach experiments on free rare-earth clusters [275, 277], our x-ray magnetic dichroism measurements on this surface-supported, ligand-stabilized cluster system has some unique advantages: The surface induces a common and fixed orientation, the clusters are not thermally rotating, the magnetic field may

be aligned in different directions, the minimum temperatures are lower, and x-ray magnetic dichroism has access not only to $\langle M \rangle$, but also to $\langle M^2 \rangle$.

Chapter 8

Summary

In this thesis, we used graphene on metal surfaces as a versatile system to explore a variety of topics.

Tuning the van der Waals interaction of graphene with molecules via doping

We investigated the effect of Gr doping by intercalation from the backside on the binding energy of vdW-type molecular adsorbates on the frontside of graphene. Chemical doping by intercalation allowed us to achieve particularly large shifts of the Fermi level, from p-doping by 0.6 eV to n-doping by 1.5 eV. Using STM, we directly visualized the higher binding energy on n-doped graphene, while thermal desorption measurements quantified the effect and showed that the binding energy increases by about 5% when going from p to n doping in the experimentally accessible range. DFT calculations including the van der Waals interactions via the ab-initio Langreth-Lundqvist vdW-DF method reproduced the experimental results also quantitatively. A model calculation on a freestanding Gr sheet doped by directly adding or removing charge showed that the spatial extent of the π charge density increases with n and decreases with p doping. This led to the intuitive picture of a changing polarizability of Gr due to a more or less extended π-charge density as the reason for the modified vdW binding energy. Looking back, it appears we were one among several groups demonstrating the tunability of molecular adsorption by graphene doping at around the same time [148, 160, 161]. Yet our work appears unique in the direct measurement of the adsorption energy and the use of molecules with only fluctuating electric dipoles. In future work, the van der Waals binding energy of π-conjugated molecules as adsorbates to doped graphene could serve as a benchmark for ab-initio treatments of this important type of bonding.

Eu intercalation layers under Gr on Ir, Ni, and Co

The intercalation of Eu underneath Gr grown on the dense-packed surfaces of the transition metals Co, Ni, and Ir results in atomically well-defined and monolayer-thin intercalation struc-

tures.

Eu monolayers intercalated under Gr/Ir(111) form several superstructure phases depending on the coverage. By XMCD, we found in one $(\sqrt{3}\times\sqrt{3})\mathrm{R30}^{\circ}_{\mathrm{Gr}}$ preparation ferromagnetism with quasi-spontaneous magnetization and a $T_C > 15\,\mathrm{K}$. A strong easy-plane anisotropy could be explained through the effect of dipolar interactions alone as the large moment and atomically thin structure implies a large shape anisotropy energy, while the single-ion contribution is suppressed from the lack of an orbital moment in the Eu^{2+} $4f^7$ configuration. Although the investigation of the Gr/Eu/Ir(111) system is complicated by the existence of several different phases, a monolayer of $4f^7$ magnetic moments in general appears uniquely suited to explore how dipolar interactions in a truly two-dimensional Heisenberg ferromagnet break the conditions of the Mermin-Wagner theorem.

Eu monolayers intercalated under Gr/Ni and Gr/Co exclusively form a $(\sqrt{3}\times\sqrt{3})\mathrm{R30}^{\circ}_{\mathrm{Gr}}$. The layers become magnetically ordered through an antiferromagnetic coupling to the Ni or Co substrates and display non-vanishing magnetization even at room temperature. The Eu decouples the Gr from the otherwise strongly interacting Ni and Co substrates. We have thus created a magnetic support for Gr which leaves its electronic structure largely intact. By protecting them from oxidation, the intercalation of rare-earth monolayers under Gr on metal substrates, including magnetic ones, makes such exciting low-dimensional hybrid $3d$-$4f$ systems exceptionally accessible to experiments, and in particular to x-ray magnetic dichroism and its unique capability for element- and shell-selective measurement of magnetism.

On-surface synthesis of organometallic compounds

The codeposition of metal vapors and ring-like organic molecules on the surface of graphene enables the growth of organometallic compounds in surprisingly selective ways. Sandwich molecular nanowires of cyclooctatetraene with two lanthanide elements, Tm and Eu, could be grown in high quality, revealing intriguing morphological features. The van der Waals interactions between the wires lead to bundle formation into carpets with a two-dimensional crystal structure, but isolated wires are also accessible locally, through use of a nanopatterned substrate, opening the prospect for future experiments on manipulation and scanning tunneling spectroscopy.

Using XMCD, we found ferromagnetism in EuCot nanowire carpets with a loop opening up to a magnetic field of 2.5 T, a remarkable value given the negligible single-ion anisotropy in $4f^7$. Judging the carpets as insulating from the necessity of using higher tunneling voltages for stable imaging in STM, we have thus experimentally confirmed the theoretical prediction of EuCot as an organometallic, ferromagnetic insulator.

Graphene on the surface of Ir(110) was developed as a substrate for the growth of nanowires with a single, global orientation on the sample. The concept of a low-symmetry yet highly inert substrate for van der Waals epitaxy is a general concept and could prove useful for the growth of effectively single-crystalline films of many materials that do not have six- or threefold symmetry.

Compared to Eu, the growth of wires from Tm is on the one hand more challenging, which could be traced to the accessible 3+ oxidation state of Tm ligated by Cot. Yet the trivalent state of Tm also enabled two other phases not observed for Eu, called dots and coffee beans, named according to their appearance in STM. In the dot phase, a geometry with the rare-earth ion sandwiched between graphene and Cot ring will give a strong uniaxial crystal field as desired for high anisotropy energies. For the coffee bean phase, a model is developed with Tm trimers covalently bonded via their $5d$ orbitals. Together with the surrounding Cot ligands, a riceball structure is formed, with the coffee beans finally resulting from the dimerization of riceballs. Such a molecule was previously not apparent in gas-phase experiments, and its formation could be suppressed by doping of the substrate; therefore, graphene itself must have assumed the role of a catalyst, an uncommon role for this inert material. Further speaking in the language of chemistry, the reaction to TmCot coffee beans proceeds in excellent yield.

Due to the high chemical similarity of the rare-earth elements, Eu and Tm are proposed as exemplary for those with a higher (Eu) or lower (Tm) preference for the 2+ vs. the 3+ oxidation state.

Studying the TmCot coffee beans in magnetic fields by XMCD, we find a peculiar anisotropy of the field-dependence of the magnetization, and a saturation to an average moment below the single-ion value. Due to the high spin-orbit coupling in the rare-earth elements and non-vanishing orbital moment of Tm, also sizable linear dichroism occurs, which showed that a part of the magnetic moments is perpendicular to the beam even in apparent saturation. A preliminary analysis based on the comparably simple multiplet structure particular to the $4f^{12}$ configuration of Tm^{3+} makes a noncollinear magnetic structure appear exceedingly likely. These experiments open new perspectives for studies on non-collinear magnetic clusters, which are monodisperse, well-separated by their organic ligands, and oriented by the surface.

Most generally, the degree of control and selectivity demonstrated in this work makes on-surface synthesis of organometallic compounds on an inert surface and under UHV conditions appear as a highly promising avenue toward the long-standing goal of molecular magnets with higher anisotropies and blocking temperatures.

Appendix A

Scientific appendix

This scientific appendix discusses several other results obtained during my thesis that deviated from the main thread of thoughts of the three result chapters.

A.1 Density functional theory on the trimerization transition in $LiVS_2$

This section is not yet published, but publication is planned. I conducted the work during a research stay in the group of T. Wehling, who motivated and guided the project.

Layered transition metal dichalcogenides that are reduced to a thickness down to a monolayer have attracted interest, because it has been found that the properties of monolayers can differ substantially and in useful ways from those of the bulk materials. For example, bulk MoS_2 is an indirect bandgap semiconductor, while monolayer MoS_2 has a direct bandgap [6]. And in monolayers of $NbSe_2$, the charge density wave ordering temperature is increased compared to the bulk [281].

Here, we studied the transition of bulk- to monolayer in $LiVS_2$ by means of DFT. The bulk compound $LiVS_2$ exhibits a first-order phase transition at around $T_C = 305\,\mathrm{K}$ [282]. Upon cooling below this temperature, the conductivity is reduced by an order of magnitude, the magnetic susceptibility drops, and structurally, three V atoms move closer to each other to form trimers, resulting in a $(\sqrt{3} \times \sqrt{3})\mathrm{R}30°$ superstructure in the basal plane [282]. The basic idea to explain this behavior is as follows: Above the transition temperature, the d electrons of vanadium are in partially filled bands, resulting in metallic conductivity and paramagnetism. Below the transition temperature, three V atoms form a quasi "molecular" cluster with orbital order, where the electrons on the three V atoms enter into a joint singlet state, suppressing conductivity and susceptibility [283, 284].

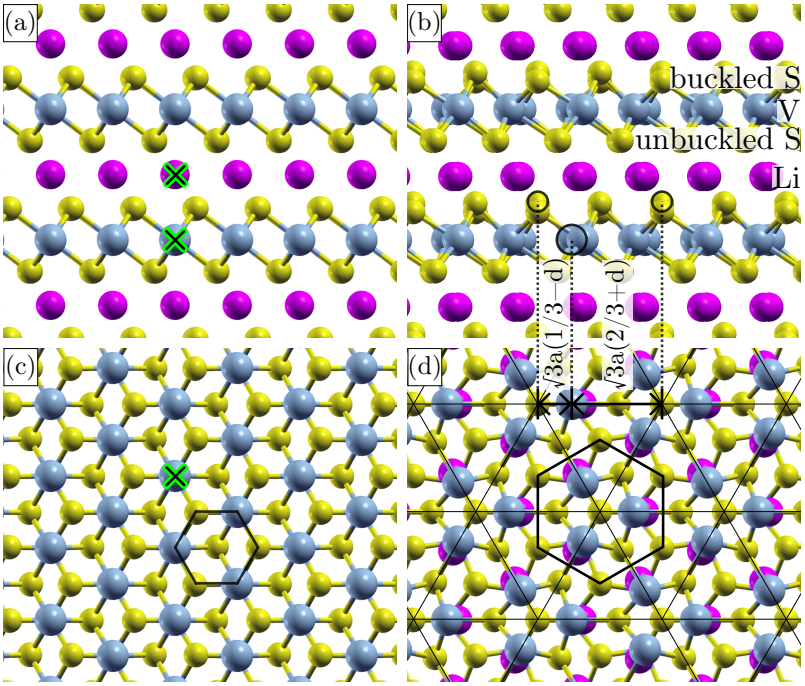

Figure A.1: Structure of $LiVS_2$ in the non-trimerized state [(a) and (c)] and in the trimerized state [(b) and (d)], corresponding to above and below the phase transition temperature, respectively. In (a) and (b), inversion centers marked with green-black cross. Wigner-Seitz cell of the (1×1) indicated in (b) and of the $(\sqrt{3} \times \sqrt{3})$R30° superstructure indicated in (d). In (d), the Wigner-Seitz cell was chosen to be centered on the center of a trimer.

How will this phase transition be affected when the material is reduced to a monolayer? Here, in anticipation of planned experiments on monolayers of VS_2 grown and doped with Li in UHV, we have conducted calculations on this question within DFT. Previous works have considered this material with DFT [284, 285], as well as using more elaborate theoretical methods [286], but the effect of the transition from bulk to monolayer has not yet been investigated.

Our DFT calculations were carried out using the VASP code [287]. We used the the PBE exchange-correlation energy functional [288], a functional based on the generalized gradient approximation (GGA). Van der Waals interactions were not included, because the bonding between the layers in $LiVS_2$ is dominated by ionic bonding, due to the lithium between the layers. A cut-off energy of 400 eV was used for the plane wave expansion.

We used a $(\sqrt{3} \times \sqrt{3})$R30° supercell as observed in the experiments [282]. A vacuum of 10 Å or more in the z direction was used in calculations on systems other than the bulk. Sampling of the Brillouin zone of the supercell with a $(6 \times 6 \times 6)$ k-point mesh for bulk calculations and a $(6 \times 6 \times 1)$ mesh for calculations that included a vacuum between the layers was found to be sufficient. The k-point mesh always included the Γ point. Values of the lattice constants were fixed at the experimental values [289].

Figure A.1 (a) and (c) show the geometry of the bulk system in the undistorted state ($T >$

T_C). The vanadium ions are in octahedral coordination with the sulfur ions; although trigonal prismatic configurations have been theoretically considered for VS_2 as well [290], vanadium is experimentally found only in octahedral coordination in both, VS_2 and $LiVS_2$. The lithium atoms are in the particular hollow sites between the sulfur atoms which are nearest to the vanadium atoms, i.e., directly above or below V, to minimize the Coulomb energy associated with the charge transfer from Li to V. This reasoning implies that $LiVS_2$ must be AA-stacked. In addition to the threefold rotation axis and three twofold mirror planes perpendicular to the basal plane, the undistorted bulk structure has inversion centers in the vanadium and lithium ions, the point group is thus D_{3d}.

If we now move three vanadium atoms closer together to form trimers, the inversion centers are lost, and the point group becomes C_{3v}. This is seen in Fig. A.1 (b) and (d), where we show the structure of the system distorted in this way, after the lithium and sulfur atoms in the supercell were structurally relaxed with the vanadium positions fixed at the experimentally observed value of the trimerizing distortion. It becomes visible that the trimerization of the vanadium atoms affects the sulfur and lithium positions: On one side of the vanadium plane [the upper side in Fig. A.1 (b)], sulfur atoms which are in the center of a trimerized triangle of vanadium ions are pushed away from the vanadium plane, while the other two sulfur atoms on the upper side of the sheet come closer to the vanadium plane. We call this the S-buckled side of the VS_2 sheet. On the other side of the VS_2 sheet [the lower side in Fig. A.1 (b)], all three sulfur atoms have the same distance from the vanadium plane. Symmetry determines which sulfur layer becomes buckled. The lithium atoms move closer to the S-buckled side. These observations imply that the trimerization of the V atoms couples to the environment.

We are now interested in a calculation of the energy gain that occurs upon trimerization. It is unclear in how far DFT can describe this transition, as this is a correlated electron system. We have therefore performed the calculation both with and without spin polarization. The magnetic moments in this system are antiferromagnetically coupled, but this results in frustration on the triangular lattice [283]. An earlier DFT calculation [285] approximated the spin configuration of the three vanadium atoms as up–down–zero. Here, we have performed noncollinear spin-polarized (SP) calculations, and found the 120°-order of the magnetic moments to be lower in energy as expected. This 120°-order should be the best approximation achievable in a mean-field theory such as DFT, and in addition provides the benefit that it is consistent with the C_{3v} symmetry of the lattice, which speeds up the computation.

In Fig. A.2 (a) we show the calculated energy per bulk supercell as the three vanadium atoms are moved closer together or further apart, described as positive or negative distortion d, respectively. For every data point in Fig. A.2 with a certain d, the vanadium ions were fixed accordingly, and the lithium and sulfur ions in the unit cell were then relaxed. The value of d is given in terms of the shift of a vanadium atom in units of the lattice constant of the supercell of $\sqrt{3} \cdot a \approx 5.85\,\text{Å}$. With this definition, the distortion as found by Katayama et al. [282]

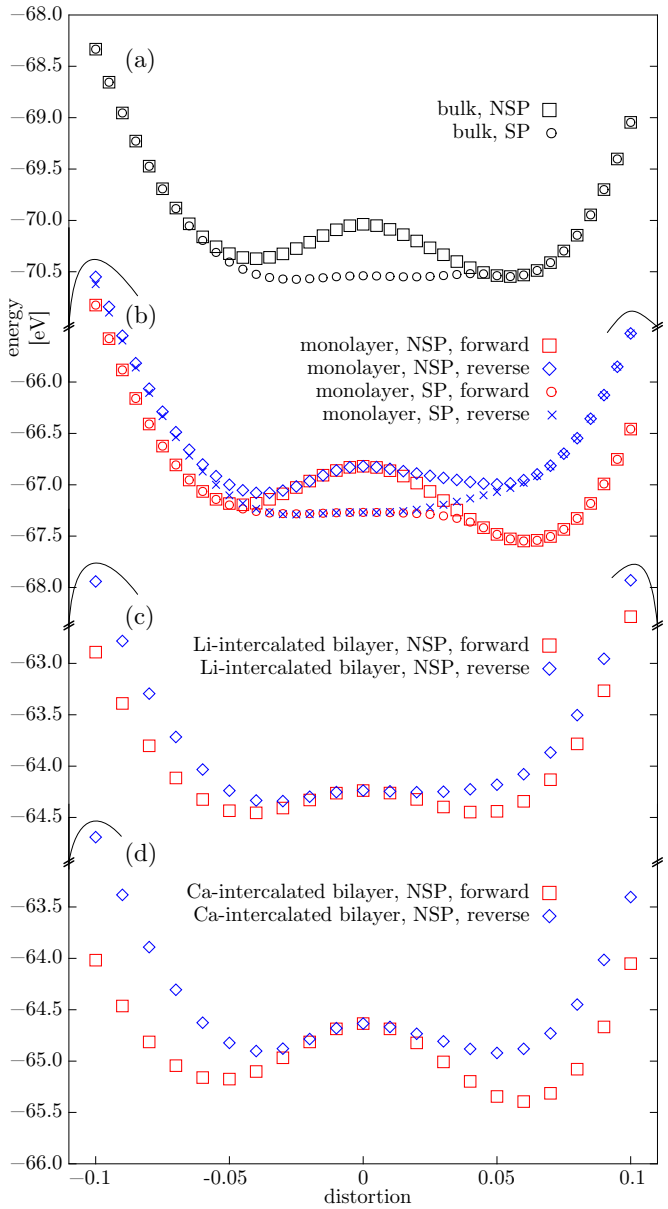

Figure A.2: Energy of the systems vs. trimerizing distortion d for (a) bulk and (b) monolayers of $LiVS_2$ as well as a (c) Li- or (d) Ca-intercalated bilayer in a $(\sqrt{3}\times\sqrt{3})$R30° superstructure, as calculated in non-spin-polarized (NSP) and noncollinear spin-polarized (SP) DFT calculations. Positive (negative) d mean V atoms moved toward (away from) a threefold rotation axis which is the center of a trimer. Energies of the bilayer systems have been halved for direct comparison to the monolayer and bulk system, such that the energy given is always per trimer. When the centers of vanadium trimers are above or below sulfur atoms which are next (opposite) to the Li or Ca layer, the distortion is termed "forward" ("reverse"). In (c) and (d), one-half of the energy per unit cell is plotted because there, each unit cell contains two VS_2 sheets.

corresponds to $d = 0.037$, while $d = 0.333$ would correspond to the extreme situation where all three vanadium atoms of a trimer are in the same place.

In the non-spin-polarized (NSP) calculation of bulk $LiVS_2$, two minima seem to appear in $E(d)$ as shown in Fig. A.2 (a). However, only the minimum for positive d is a real minimum, i.e., along all atomic coordinates. The apparent minimum for negative d is actually a saddle point, where the movement of the atomic coordinates in a direction perpendicular to what is shown as the horizontal axis here would correspond to a trimerization onto another, symmetrically equivalent centerpoint, which is shifted by one primitive lattice constant. The minimum is at about $d = 0.054$, not too far off from the experimental result of $d = 0.037$ [282]. The energy at the minimum is lower than in the undistorted state by about $\Delta E = 0.51\,\mathrm{eV}$ per supercell or $0.17\,\mathrm{eV}$ per V atom.

In contrast, the SP calculation for the bulk does not exhibit a clear minimum, but rather a broad and almost flat range between the minima of the NSP calculation. The flat region in $E(d)$ can still be interpreted as an incipient instability.

It thus appears that the NSP calculation overestimates the tendency for ordering, as seen in the overestimated d, while the SP calculation underestimates it. How can we explain this? There is a competition between the undistorted state with local magnetic moments which are antiferromagnetically ordered and the distorted, orbitally ordered, spin-singlet state without local moments. In the NSP case, magnetic moments are simply not allowed, thus the energy for the undistorted state goes up, resulting in a larger energy difference to the distorted state. The magnetic moments in the distorted state are suppressed due to the spin singlet in any case, thus here the NSP calculation is correct. As a result, the tendency toward distortion is overestimated. For the underestimation in the SP case, we believe in the following explanation: DFT for the local magnetic moments is a mean-field theory, and is therefore expected to overestimate the tendency to form magnetic moments, because fluctuations are suppressed in a mean-field approach. The SP calculation thus likely underestimates the energy in the undistorted state, where the formation of magnetic moments leads to a lower energy. In short, we believe that the truth lies in between the SP and NSP curves.

In an attempt to improve the description by DFT, we also introduced an on-site Coulomb repulsion term in the SP calculations using the DFT+U method, with some trials in the Lichtenstein approach [291] (with an exchange parameter $J = 1\,\mathrm{eV}$) and some in Dudarev's approach [292] (i.e., $J = 0$). We found that for $U = 3.6\,\mathrm{eV}$ (a value used by Ref. [285]) and down to $U = 1.0\,\mathrm{eV}$ (at the lower end of meaningful values suggested by Ref. [293] for vanadium from redox reaction enthalpies), the only minimum in the energy vs. distortion curve is at zero distortion. Even a very small $U = 0.5\,\mathrm{eV}$ already shifts the minimum of the energy to significantly lower distortion values than observed for $U = 0$.

The DFT+U approach can introduce local minima in the energy landscape, because the U term creates a barrier for continuous movement of the electrons between the orbitals. We also

observed local minima in our calculations. Therefore, we conducted trials with the occupation matrix control (OMC) method of Allen and Watson [294] using their code to artificially enforce certain occupations in the initial stages of the relaxation to find the various local minima. A trial was also conducted with the U ramping method of Meredig et al. [295]. Neither of these trials changed the conclusion that no trimerization is favored in the calculations in the range of realistic U.

As our SP-DFT calculation without U likely already overestimate the tendency to form magnetic moments, the addition of a Coulomb term U is in fact expected to worsen this problem, as the U localizes the electrons even further in specific orbitals, stabilizing magnetic moments and suppressing the spin singlet of the trimer. This issue has also been observed in calculations on some other materials, see Ref. [296] and references therein, where the authors resorted to go without U, as we will also do.

Now that we have gained from the bulk case confidence in the ability of DFT to provide us at least some description of this phase transition, we turn to discuss the calculations on the monolayer $E(d)$. Crucially, we assume our $LiVS_2$ monolayer to have the lithium adsorbed on only one side, a realistic assumption regardless whether one considers either doping by adsorption of Li onto the top side of a substrate-supported VS_2 sheet, or the other way around, i.e., doping by intercalation of Li in between its substrate and the VS_2 sheet. The calculations are conducted without substrate, i.e., the $LiVS_2$ sheet has vacuum on both sides. Then, in the monolayer, there are two different, symmetrically inequivalent ways to trimerize: The S-buckled side of the VS_2 sheet can be either on the Li-adsorbed side (henceforth called "forward" configuration), or on the side of the system without Li ("reverse"). Note that Li adsorption on one side per se only breaks the inversion symmetry; the breaking of the translation symmetry to form the larger $(\sqrt{3} \times \sqrt{3})\mathrm{R}30^\circ$ supercell must still result from the electronic instability of the frustrated system.

Our calculation of the energy of the system upon distortion shown in Fig. A.2 (b) reveal that in the forward case, the minimum of the energy per supercell curve for the NSP calculation is at $d = 0.061$ and $\Delta E = 0.73\,\mathrm{eV}$ below the undistorted configuration, compared to the bulk case values $d = 0.054$ and $\Delta E = 0.51\,\mathrm{eV}$. This implies that as a monolayer, the orbitally ordered state will be more stable than in the bulk. Assuming a linear relationship between energy gained in the phase transition and the transition temperature, we would thus expect the transition temperature to increase by about 43%, from 305 K to 437 K. Furthermore notable is that in the forward monolayer configuration, also the SP calculation, which did not yield a clear minimum at nonzero distortion for the bulk, now has a clear minimum in the same position as the NSP calculation.

In contrast, in the reverse configuration, the minimum for positive d results in $\Delta E = 0.176\,\mathrm{eV}$. Yet, an anti-trimerized, negative d minimum at $d = -0.037$, where three V atoms moved further apart rather than closer together, is in fact lower in energy with $\Delta E = 0.26\,\mathrm{eV}$

per supercell, yet still far above the forward case. The reverse configuration will thus not form. It is the entirely different behavior of the reverse and forward configurations which proves that the breaking of the inversion symmetry, rather than the reduction to a monolayer form per se, is responsible for the enhanced trimerization tendency.

For some experimental purposes, a Li-doped monolayer of VS_2 might be inconvenient: The lithium can oxidize very easily when it is adsorbed on top and exposed to the residual gas of a vacuum, even in ultra-high vacuum a sample lifetime of no more than hours is expected. On the other hand, if lithium is intercalated between VS_2 and a substrate, Li will also donate some of its charge into the substrate, complicating the situation. We have therefore conducted calculations for a bilayer of VS_2, where a Li monolayer is assumed in between the two sheets. Here, "forward" ("reverse") means the S-buckled sides of both sheets are toward (opposite) the Li layer. Thus, the V triangles point in opposite directions on the two sheets, and the symmetry of the supercell is lowered to C_{2h}.

Figure A.2 (c) shows one-half of the energy of the supercell to obtain the energy per VS_2 layer for direct comparison with the bulk and monolayer calculations. It is seen that the energy gained in the trimerized state at 0.210 eV per layer and supercell is lower than for the other systems. This is, however, expected, because only one Li layer is present for two VS_2 layers, and thus only one electron is available for two V ions. The solution could be more lithium, but intercalation of more than one monolayer of Li in between two sheets is typically not observed in experiments [297, 298]

However, if we exchange Li by a divalent electropositive metal such as calcium, a full electron is again available per V atom. We thus calculated a calcium-intercalated bilayer as well. As seen in Fig. A.2 (d), the energy gain upon trimerization of about 0.76 eV per layer and supercell is very similar and even a bit higher than in the monolayer case (0.73 eV), which shows that other effects stemming from the bulk-to-monolayer transition, such as confinement in the z direction, are clearly not decisive. Noteworthy is that both bilayer systems have an inversion center in one-third of the atoms of the central layer of Li or Ca, but this does not matter, because it is the asymmetry of the two sides of the individual VS_2 layers which is the key to the effect.

In conclusion, even though the description of the phase transition by DFT is imperfect, clear indications for the formation of the ordered trimer state and an estimate of the energy gain in the phase transition can be obtained from such calculations. We have shown that the energy gain due to orbital order in $LiVS_2$ is enhanced when the material is reduced from the bulk to a monolayer, and a 43% increase in the transition temperature upon reducing the material's thickness is thus predicted. This effect results from an interaction of two different causes of broken inversion symmetry, firstly the Li adsorption geometry and secondly the trimerization itself. This concept should be generic and transferable to any phase transition in a two-dimensional material that breaks inversion symmetry, whenever it is brought into an inversion-asymmetric environment, such as when adsorbed on a surface or itself the subject of adsorption of other species.

A.2 Polar europium oxide on Ir(111)

The XAS data presented in this section were acquired during a beamtime at the Bessy II beamline pm3 with D. Klar, A. Smekhova, C. Schmitz-Antoniak, and A. Martínez-Galera, and using the AG Wende chamber. The LEED and STM data were measured by myself.

A.2.1 X-ray absorption spectroscopy of polar bilayer EuO(111) on Ir(111)

A polar bilayer of europium monoxide (111) forms on the Ir(111) surface under slight Eu excess, and was previously characterized by S. Schumacher et al. using STM, LEED, DFT, and magneto-optical Kerr effect (MOKE) measurements in Ref. [261].

Here, I have investigated this polar bilayer by x-ray absorption spectroscopy at the Eu $M_{5,4}$ edges in total electron yield mode as shown in Fig. A.3. The spectral shape can be unambiguously attributed to a $4f^6$ electron configuration, i.e., trivalent europium, by comparing with calculated [107] or measured Eu^{3+} spectra [177]. As oxygen cannot accept more than 2 electrons, the third electron must have been transferred to the iridium substrate. This contrasts with the presumption in Ref. [261] that the Eu is divalent. Iridium is one of the most electronegative metals, its Pauling electronegativity is 2.2. This compares to 3.44 for oxygen and 1.2 for europium. The Ir(111) surface is apparently able to oxidize Eu from 2+ to 3+.

The density of states calculated by DFT in Ref. [261] also shows a certain charge transfer out of the Eu $4f$ states, but this value was not quantitatively evaluated, and seems smaller than one electron when looking at the DOS plot. However, the strong on-site Coulomb interaction of the $4f$ electrons is poorly described in DFT. Therefore, Ref. [261] used the GGA+U approach as proposed by Liechtenstein et al. [291] with $U = 7\,\mathrm{eV}$ and $J = 1\,\mathrm{eV}$. In the following, we refer only to $U_{\mathrm{eff}} = U - J$. The approach is ad-hoc and the parameter U_{eff} is empirical, i.e., it is chosen according to what leads to the best reproduction of experimental data by DFT. In a strong sign of the ad-hoc nature of the GGA+U approach, the best value for the parameter U_{eff} is not unique: Whether one tries to fit the lattice constant, certain redox reaction energies, or

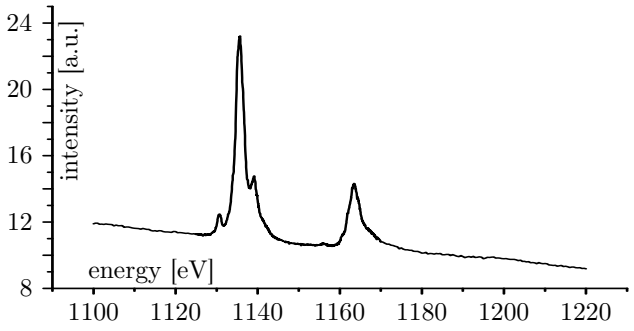

Figure A.3: X-ray absorption of the polar bilayer of EuO on Ir(111) at the Eu $M_{5,4}$ edges

the band gap, and also the oxidation state of the ion [293]. A lower value for U_{eff} would make it energetically easier to withdraw electrons from the Eu $4f$ orbital.

The 3+ oxidation state of Eu resolves a number of questions that remained open in Ref. [261]: Firstly, the high thermal stability, up to 1420 K, of the polar bilayer was previously hard to explain, because there was no mechanism for bonding of the bilayer to the Ir substrate. But if there is no bonding to the substrate, EuO should not wet the surface, but form three-dimensional cubic EuO clusters instead. The ionic bonding through charge transfer to the substrate resolves the issue.

Secondly, no magnetic signal was found in the MOKE measurements. This was not really surprising, given the monolayer thickness, the small applied field of only 100 mT and the relatively high temperature of 20 K. However, when Eu is in the trivalent state, then its total magnetic moment is zero because spin and orbital moment are oppositely equal, and a magnetization is not expected in any case.

Thirdly, the authors of Ref. [261] noted what they considered a major and unexpected discrepancy between the experimentally determined work function of the polar EuO bilayer, and the work function calculated within DFT. This too is resolved, because if a charge transfer into the substrate occurs, this will result in a contribution to the surface dipole that will lower the work function. Another effect working in the same direction is that the trivalent Eu ion has a smaller ion radius than divalent Eu. The smaller radius of the Eu ion will allow the oxygen layer to come closer toward the substrate, and this will result in another reduction of the work function through the surface dipole effect. X-ray standing wave measurements, or intensity versus energy analysis of diffracted low-energy electrons, would allow to determine the height of the oxygen ions experimentally.

I propose here the following: Density functional theory calculations should be conducted in dependence on the parameter U_{eff}. When the average height of the oxygen layer, the work function, and the charge state of Eu are then plotted in dependence of U_{eff}, a single U_{eff} should be able to reproduce all the experimental findings consistently.

A.2.2 Growth of multilayer EuO(111) on Ir(111)

That the electronegativity of the substrate favors a polar orientation of bilayer EuO with the Eu toward the substrate, and the ability of Eu to assume both the +2 and +3 oxidation states, inspired me to attempt to grow thicker EuO(111) films on Ir(111). Schumacher and Förster previously investigated growth of EuO multilayers on Ir(111) with the highest coverage of 3.4 ML. However, they tried to achieve single-phase EuO(100), because they presumed thicker EuO(111) to be unstable. They found that initially oxygen-rich conditions favored the growth of EuO(100) over EuO(111), which we can understand a bit better from the discussion below.

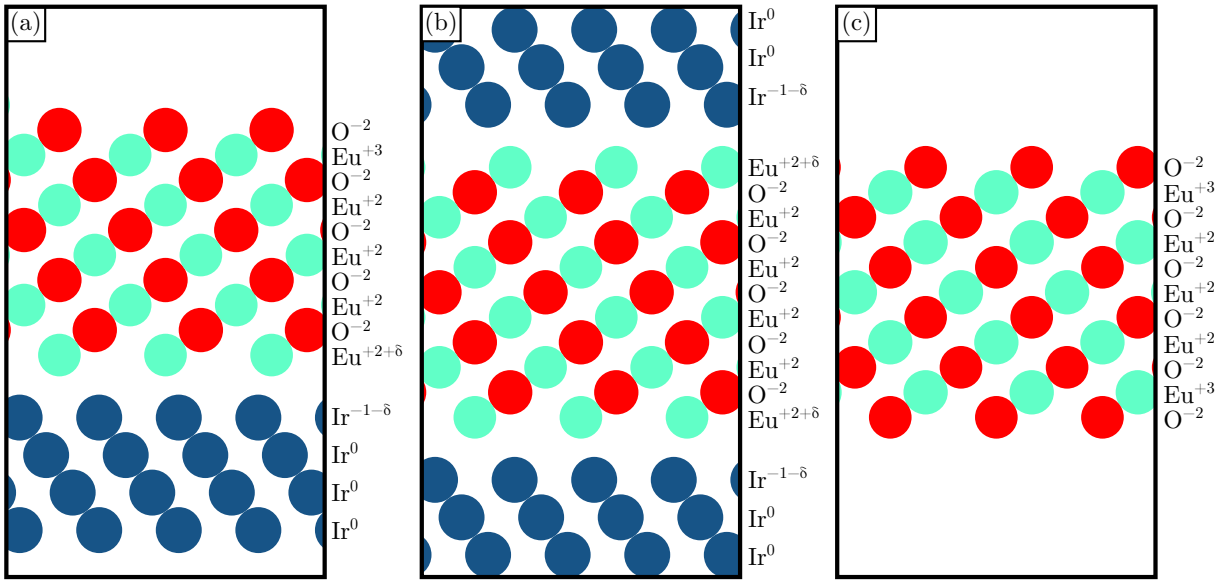

Figure A.4: Sketches of cuts through a (110) plane of slab geometries as they would be used in a DFT calcuation with periodic boundaries, with indicated oxidation states of the layers. Black boxes around the geometries indicate the periodic boundaries of the supercells. (a): Some vacuum, 4 layers of Ir(111) substrate, and 5 BL of EuO(111). The EuO(111) film is O-terminated to the vacuum, and Eu-terminated toward the Ir(111) substrate. (b): 6 layers of Ir(111) with 5 BL of EuO(111) and one additional Eu layer, such that the EuO(111) film is terminated on both of its sides with Eu to the Ir(111). No vacuum is used in this cell. (c): 5 BL of EuO(111) and one additional oxygen layer, such that the slab is O-terminated toward the vacuum on both sides.

Conceptual idea

Figure A.4 (a) sketches how the ionization states could allow a flat, unreconstructed film of EuO(111) on Ir(111) while avoiding the polarity catastrophe. Toward the substrate, the film would be Eu-terminated, while it would be O-terminated toward the vacuum. A trivalent layer of Eu below the topmost O layer would absorb the polarity at the interface to the vacuum. At the interface to the Ir substrate, charge transfer from Eu to Ir would absorb the polarity. The Eu layer at the interface with Ir could be divalent if one electron per Eu is transferred to Ir, or it could be trivalent, if two electrons were transferred; this uncertainty is indicated by the δ in Fig. A.4 (a).

This film would be stoichiometric in total. However, the EuO(111)-Ir and EuO(111)-vacuum interfaces separately would be Eu-rich and O-rich, respectively. This becomes logically most clear when a full periodic unit cell is drawn as would be used in an ab initio calculation. This is shown in Fig. A.4 (b) for the EuO(111)-Ir interface and in Fig. A.4 (c) for the EuO(111)-vacuum interface. In (b), one additional layer of Eu is needed for two EuO(111)-Ir interfaces, and in (c), one additional layer of O is needed for two EuO(111)-vacuum interfaces.

Because this EuO(111)-Ir interface is Eu-rich, its formation will be favored under conditions

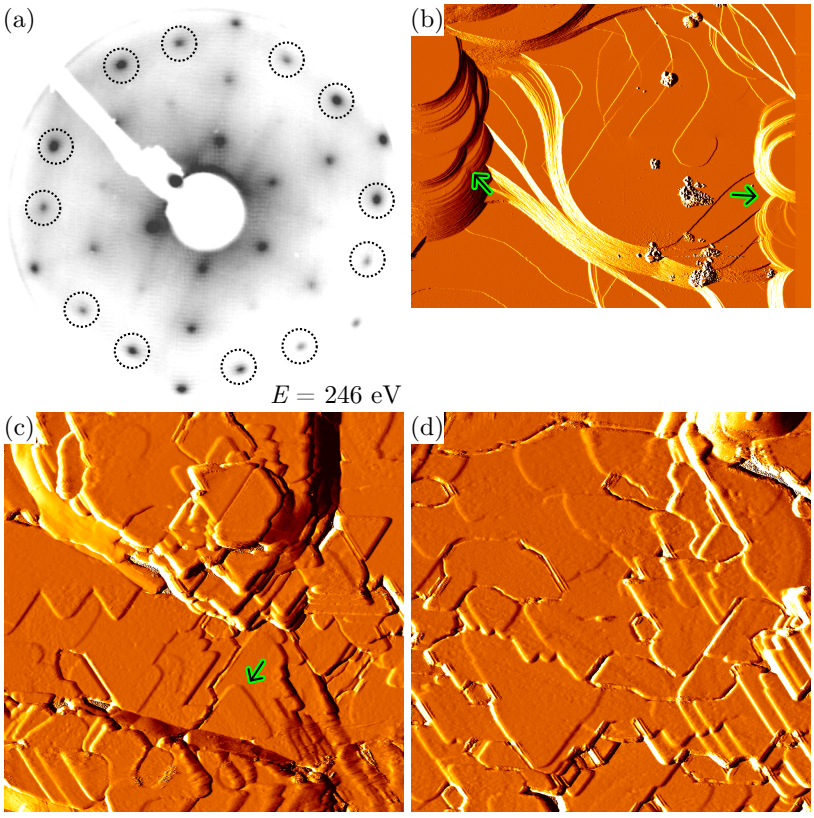

Figure A.5: (a): LEED image of a thick EuO(111) film at electron energy 246 eV. Spots are sharp, but the background intensity is high. The shown image has the background intensity cut off to improve visibility. Dashed encircled spots are those where it is most clear that the intensity of the spots has no sixfold symmetry. (b,c,d): STM topographs, image width 1.4 µm. (b): Sample with only EuO(111) bilayer, $U = +1$ V. The sample is rough with many step bundles as a result of prolonged sputtering. The annealing up to ≈ 1520 K is not sufficient to anneal the sputtering craters. Arrows indicate where a double-tip artifact is evident in this image. (c,d): Two large-scale images of thick (13 BL) EuO, $U = -2$ V. Arrows in (c) indicate a grain of the minority twin domain; twin domains are distinguished by the orientation of the triangles formed by their step edges.

of a high chemical potential of Eu. On the other hand, the O-terminated EuO(111)-vacuum interface is O-rich, thus its formation will be favored under conditions of a low chemical potential of Eu. Note that the chemical potential of Eu and O are fixed relative to each other by the enthalpy of formation of EuO. So to grow the film as sketched in Fig. A.4 (a), we have to change the chemical potential of Eu during the growth. Because the deposition rate of Eu cannot be changed over several orders of magnitude, we changed only the substrate temperature.

Experimental results

After a series of experiments trying different parameters, we were indeed able to grow a thick, non-faceted, and unreconstructed EuO(111) film on Ir(111). Figure A.5 (a) shows a LEED

image of a 13 BL film. The spots are sharp and visible up to high order. No other phase was seen at any energy, except very weak spots belonging to (100) facets of the (111)-oriented film. However, the background intensity is high; the background was removed in the shown image to enhance visibility. The symmetry of the LEED pattern is not fully sixfold symmetric, as seen in the dashed-encircled spots in Fig. A.5 (a), indicating that the two possible domains of epitaxially aligned EuO(111)/Ir(111) do not occur in equal amounts. The interface of EuO(111) with Ir(111) can be a "twin" boundary, because both EuO and Ir are fcc lattices, although they have different lattice constants and basis atoms. An energetic preference for either the stacking-faulted or unfaulted configuration is expected. Figure A.4 (a,b) show the unfaulted situation. It would be principally possible to determine whether faulted or unfaulted configuration are preferred from the LEED images, but this was not done here.

Figure A.5 (b) shows an STM topographs after growth of the polar bilayer, only to consider the morphology of the Ir(111) substrate before growth of the thicker films. Images of the latter are shown in Fig. A.5 (c/d). Throughout the EuO experiments, long sputtering time had to be used to remove the films again. This results in a roughening of the surface as seen in Fig. A.5 (b), where the formation of characteristic patterns of craters and mounds with step edge bundles is seen as described by Michely et al. for the case of Pt(111) [264]. Therefore, the roughness of the surface after the EuO film growth can be the result of the substrate roughness. Two images, (c) and (d), are shown after film growth, because the sample is not very homogenous even on a µm scale. The triangles in Fig. A.5(c) and (d) are mostly pointing downward. One exceptions is exemplarily indicated in Fig. A.5 (c) by an arrow. This agrees with the finding from the symmetry of the LEED pattern that one of the twins is preferred.

Recipe

The sample shown in Fig. A.5 (b,c,d) was grown with the recipe as follows: At a sample temperature $< 400\,\mathrm{K}$, clean Ir(111) was exposed to Eu vapor for 2 min. Then, oxygen is dosed simultaneously with Eu for 23 min 40 s. The oxygen flux is such that 13 BL EuO(111) are expected, and the Eu flux is chosen such that $f_{\mathrm{Eu}}/f_{\mathrm{O}} = 1.7$. After the oxygen valve is closed, more Eu is dosed for 30 s. The sample is then heated to 973 K for 15 min with the Eu vapor applied, then the Eu shutter is closed, and the sample held at 973 K for another 30 s, then cooled to room temperature.

The choices in the recipe are motivated as follows:

The sample was initally exposed for 2 min to Eu only, because Eu sticks to the Ir(111) surface, and there is no back-evaporation of excess Eu in the beginning. Without the initial only-Eu deposition, there is no well-defined chemical potential of Eu during the beginning of the film growth, because the sample is not in equilibrium with the vacuum vapor pressure – a dynamic equilibrium would imply back-evaporation. I believe that to obtain phase-pure samples, and to have experimental results that are relatively insensitive to the exact fluxes, a well-defined

chemical potential is most helpful. This way, I intent to transfer the idea of having a largely "self-limiting" stoichiometry by back-evaporation also to the initial growth stage. This approach constrasts with that of Förster and Schumacher, who opened the Eu shutter for the growth only slightly before the oxygen valve, and who made very high effort to be able to control the oxygen flux on the surface rapidly and precisely, with particular attention to the flux ratio during the initial growth phase.

The annealing step at 973 K was performed in Eu vapor based on experiences of D. Förster et al. [177], who found that annealing in Eu improved the mobility.

The other choices in the recipe are based on experiences from failed attempts, in particular the following problems were encountered: (1) If the sample temperature during EuO growth is 623 K instead of < 400 K, stronger facet reflexes will result, and in addition, a (2×2) superstructure with respect to Ir(111) will appear (not shown), i.e., the film will have holes where the Ir(111) substrate is still exposed. (2) If the annealing temperature is only 623 K, the spots will be blurry. (3) If the annealing temperature is only 873 K, a (2×2) superstructure with respect to EuO(111) will appear (not shown). (4) If the annealing temperature is increased much beyond 973 K, the film will break up and polar bilayer EuO on Ir(111) will appear.

The $(2 \times 2)_{\mathrm{Ir}}$ superstructure was also imaged in STM as a hexagonal lattice (not shown), which excludes that it is a $(2 \times 1)_{\mathrm{Ir}}$. Without the STM imaging, this would not have been clear because the LEED generally sees the average of all possible rotational domains on the sample. The structure of pure Eu on Ir(111) is already known to be an incommensurate aligned hexagonal Eu layer with $a_{\mathrm{Eu}}/a_{\mathrm{Ir}} \approx 10/7$ [175, 176], while the EuO polar bilayer phase has a 1:1 stoichiometry [261]. Because the $(2 \times 2)_{\mathrm{Ir}}$ appeared in response to a higher Eu exposure than previously used by Schumacher and Förster on Ir(111), I propose that this phase has the stoichiometry Eu_2O_1 and appears when the Eu excess adsorbed to Ir is larger than can be accommodated by the very dilute, repulsively interacting Eu adatom phases that were observed to coexist with the polar bilayer EuO for lower Eu excesses. A $(2 \times 2)_{\mathrm{Ir}}$ phase with Eu_2O_1 stoichiometry has nearly the same surface density of Eu, at 50% $\mathrm{ML_{Ir}}$, as the pure Eu 10/7 phase (49%) and the polar bilayer (55%). A blurred $(2 \times 2)_{\mathrm{Ir}}$ superstructure also appeared when the pure Eu 10/7 phase was annealed to 650 K after some time of exposure to the background pressure alone.

Outlook

Based on the discussed mechanism for a strongly bound interface between a polar (111) ionic crystal face and an electronegative metal, I would like to propose a different interface, where the termination of an insulator toward the vacuum can be non-polar while the interface to the substrate is polar. For this, we need a crystal face that can be polar or nonpolar, depending on the cut. An example for this is the cubic fluorite structure of CaF_2, which in the (111) direction consists of planes of calcium and flourine in the pattern F-Ca-F-F-Ca-F. This surface is polar

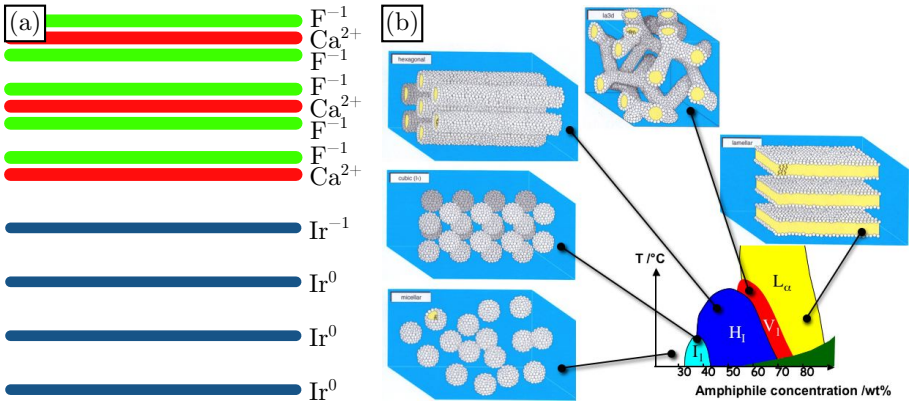

Figure A.6: (a) Sketch of an imagined interface of a CaF_2 (111) film that wets the Ir(111) surface due to interfacial charge transfer from the calcium layer. A calcium surplus would have to be applied during growth. (b) Schematic phase diagram with sketches of different phases for amphiphilic molecules in a solvent, from Ref. [299]

if it is cut between Ca and F, and it is nonpolar if cut between two F layers. CaF_2 naturally cleaves in (111) direction between two F planes. Based on the experience with EuO(111), we expect that the Ir(111) surface is wetted by CaF_2 if a calcium surplus is supplied, such that the CaF_2 film can bond to the substrate via charge transfer from Ca to Ir. A sketch is shown in Fig. A.6 (a). Experimentally, the dangerous elemental fluorine could be avoided by evaporating CaF_2 and Ca, but never F.

The surplus of the highly electropositive metal Ca (or Eu before) can be seen as a surfactant: Just like an amphiphilic molecule, i.e., a molecule that is lipophilic on one side, and hydrophilic on the other, allows to mix water and oil by reducing the interface energy, excess Ca atoms could do the same for the "mixing" of CaF_2 and Ir. Here, the word "mixing" is not really appropriate, because no liquids are involved; "mutual wetting" would be better.

I would like to draw the speculation further into more application-oriented domains. While the Pauling electronegativity of Ir (2.20) is one of the highest, the electronegativities of Fe (1.83), Co (1.88), Ni (1.91), and Cu (1.90) are still all much higher than that of Ca (1.00). By using an added electropositive metal like Ca, it could become possible to mix these metals with an ionic insulator like CaF_2. Amphiphilic molecules in solution are known to order in different phases, such as micelles, hexagonal rods, or lamella, see Fig. A.6 (b). Structures like lamella can orient under the influence of shearing flow [300, 301]. By the mixing of an insulator with a magnetic metal (Fe) or a highly-conducting metal (Cu) into a lamellar or hexagonal-rod-array phase, it could become possible to create metamaterials suitable for electric applications (note that the solid solubility of Ca in Cu or Fe is negligible [302, 303]). In a transformer, for example, it is desirable to have a magnetic material with high permeability in the direction of the magnetic field so as to achieve a high inductance, and a low electric conductivity normal to the magnetic field, to avoid eddy currents. Another example would be a high-frequency cable, where the skin

effect can be counteracted by dividing the cable into many thin strands, as in litz wire. Here, a hexagonal rod phase of Cu rods would appear ideal. Multilayers of mutually wetting Cu and insulator also appear ideally suited to make a capacitor by growth from the vapor phase, where the insulator and metal could be made thinner than usual, because the formation of pinholes in the insulator (which shortcuts the capacitor) would be energetically unfavorable.

A.3 Full set of naphthalene thermal desorption data

In chapter 5, we presented desorption of naphthalene from pristine Gr/Ir(111) and intercalated either with oxygen to saturation or Eu in a p(2 × 2) superstructure, and only two selected coverages of naphtalene for reasons of clarity. However, we also investigated two other Gr intercalation structures: (1) Cs adsorbed in a $(\sqrt{3} \times \sqrt{3})$R30° with respect to Ir, prepared by room temperature deposition of Cs from commercial dispensers [1] till saturation, and (2) Eu adsorbed in a $(\sqrt{3} \times \sqrt{3})$R30° with respect to Gr, prepared by deposition of Eu at 720 K until saturation. The full set of all our measured desorption traces for the in total five different intercalation systems and many different coverages each are shown in Fig. A.7. The coverages were determined by integrating the area under the background-substracted spectra.

A.4 Benzene, naphthalene, and hexafluorobenzene adsorbed to graphene on Ir(111)

We studied the adsorption behavior of benzene (Bz), naphthalene (Nph), and hexafluorobenzene (Hfbz) on non-intercalated Gr/Ir(111). STM was conducted on Bz, Nph, and Hfbz; TDS was conducted only on Nph and Hfbz; and LEED was conducted only on Bz and Nph.

In the case of Bz and Nph, molecular islands coexist with a phase where single molecules are located in the hcp moiré regions, shown here only for Nph in Fig. A.8. The determination of the adsorption region is based on simultaneous visibility of the moiré and the molecular overlayer. The orientation of the crystal has to be known to distinguish fcc and hcp regions. In the case of Hfbz, single molecules adsorbed in the hcp regions were also observed, but the filling factor of the moiré cells is far from unity, as shown in Fig. A.9 (a). A height profile over the Hfbz islands and the isolated molecules as shown in Fig. A.9 (c) shows that the same apparent height above Gr of about 1.5 Åis observed for both isolated molecules and the molecular islands, which strongly suggests that the isolated molecules are also Hfbz, and not some kind of contaminant. The edges of the molecular islands are kinked according to the moiré lattice in all cases.

For Bz, LEED gives a $(\sqrt{7} \times \sqrt{7})$R19° superstructure (not shown) as previously found also for Bz on graphite [89]. In contrast for Nph, at least two different phases were observed by both STM and LEED (not shown) that appeared similar to those observed for Nph on graphite by

[1] Cs dispensers obtained from SAES Getters

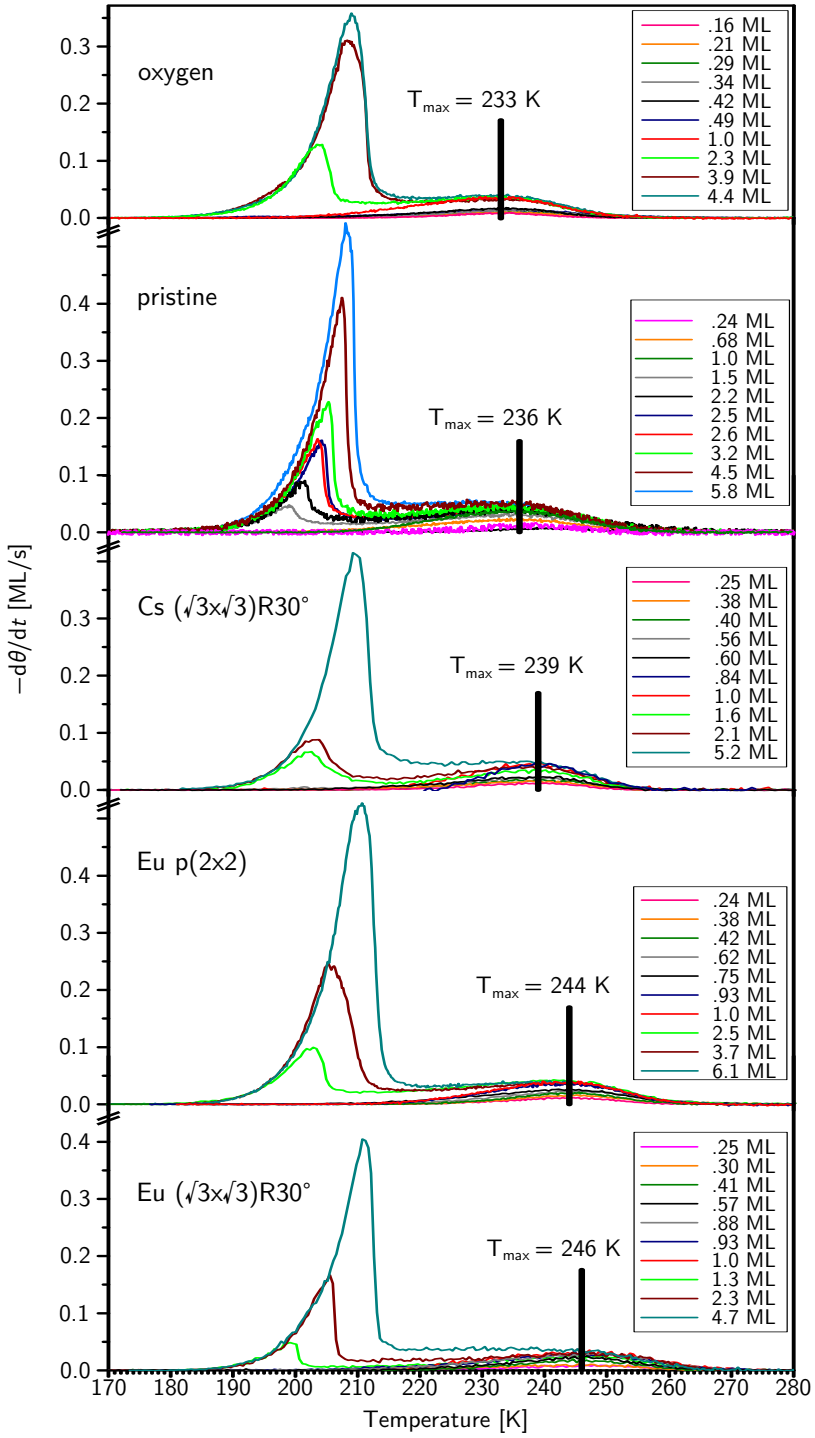

Figure A.7: Mass spectrometer signal of desorbing naphthalene ($m = 128\,\mathrm{u}$) while heating the sample with a ramp rate of $1\,\mathrm{K/s}$ for different intercalants with naphthalene coverages in the range up to a few monolayer (ML).

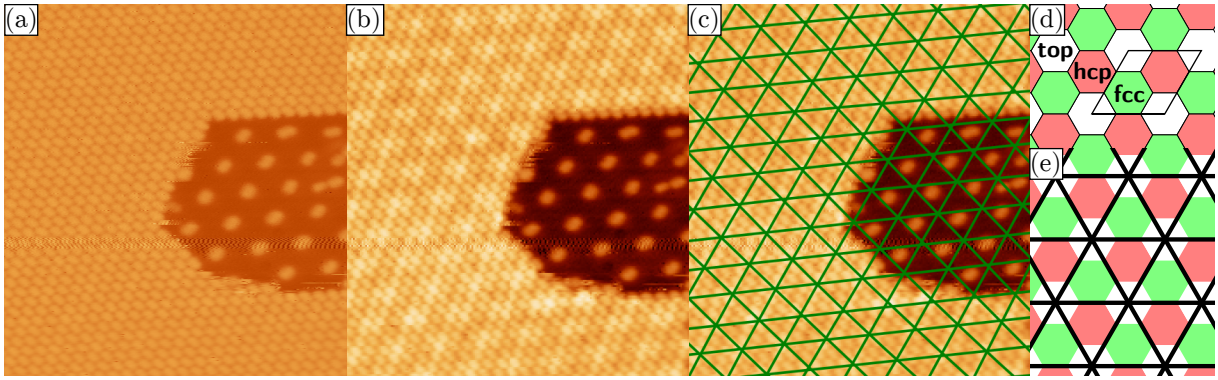

Figure A.8: (a)-(c): Naphthalene on pristine Gr by STM [$(22 \times 23)\,\mathrm{nm}^2$]. The single molecules are adsorbed in the hcp regions.

Sojka et al. [90]. For Hfbz, no LEED measurements were conducted, however, the structure could be identified by STM: The measurement of the lattice constant of the Hfbz islands gives a value of 0.77 nm, which is within 5% of a (3×3) superstructure w.r.t. the Gr lattice, within the error of the STM. In line with this, the dense-packed rows of the molecular islands are parallel to the moiré and thus to the Gr lattice. Figure A.9 (b) shows a different area on the same sample, where the coverage is locally higher. Two different widths of translational domain boundaries are seen in the layer, but there are no rotational domain boundaries, again as expected for a (3×3) superstructure.

Desorption spectra of Hfbz are shown in Fig. A.9 (d). They were obtained at $m/q = 186\,e/\mathrm{u}$ and with a heating rate of 2.5 K/s. The vertical scale is logarithmic, while the horizontal one is linear in $1/T$, such that zero-order kinetics described by the Wigner-Polanyi-equation result in straight lines in this plot. The multilayer peak is indeed well-described by a line. The deviation at the lowest intensity is more indicative of a measurement or background subtraction problem than of the desorption behavior. The submonolayer behavior is of first order, but the monolayer peak shifts to higher temperatures for diminishing coverages. The transition region between monolayer and thick layer behavior is complex, as also observed for Bz on graphite [87]. For the highest coverages, the increasing intensity at temperatures higher than the monolayer peak is attributed to desorption of multilayers from the sample holder.

Thermal desorption of naphthalene was presented in chapter 5 and section A.3. Here, we note that the background substraction for Nph was comparably difficult, as the observed intensity after the desorption event was significantly higher than before, because the Nph has a longer residence time in the chamber. In contrast, for Hfbz only a constant offset corresponding to the intensity before the desorption was subtracted.

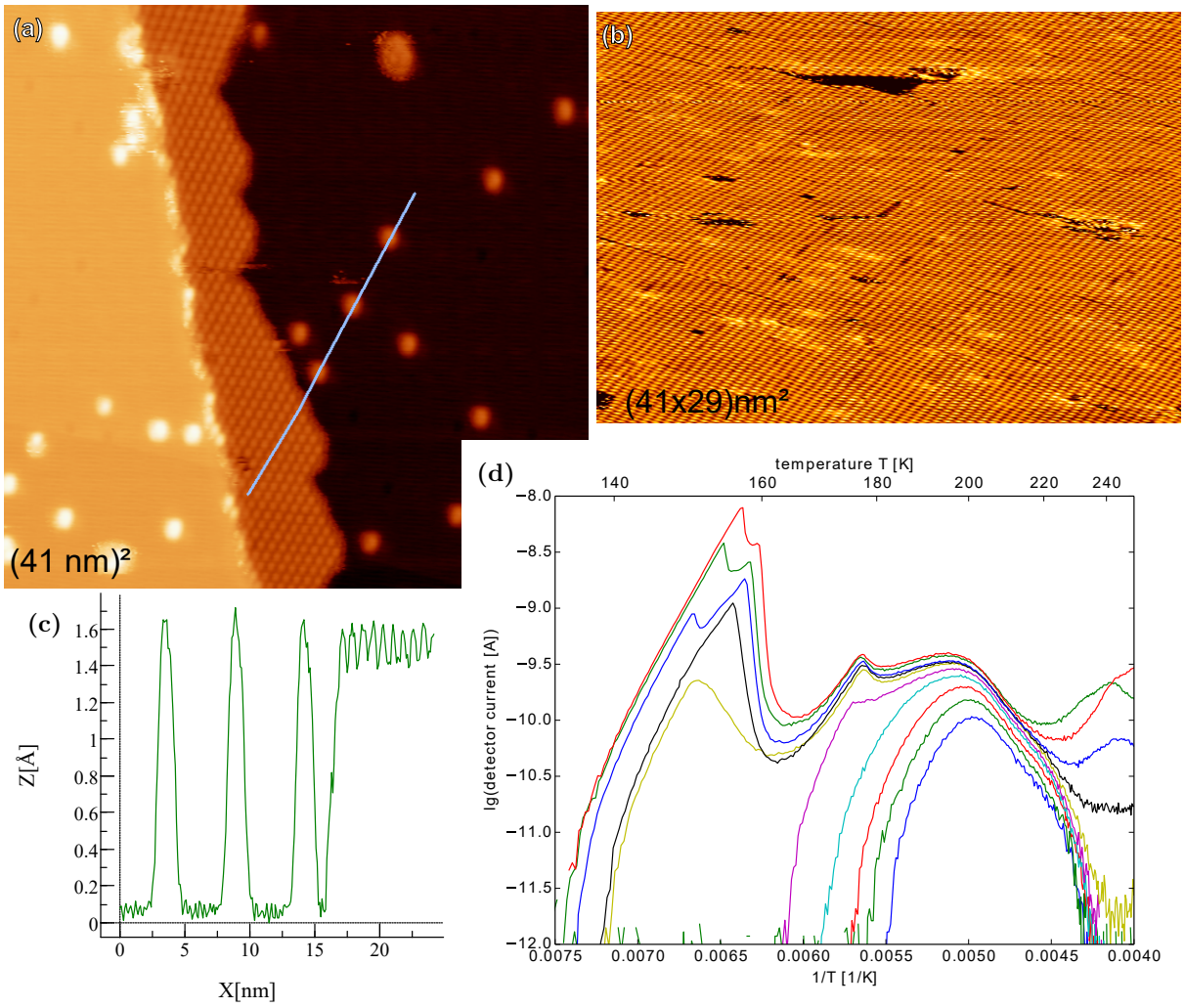

Figure A.9: STM and TDS of hexafluorobenzene on Gr/Ir(111).

Anhang B

Deutsche Kurzzusammenfassung *(German Abstract)*

Diese Arbeit nutzt epitaktisches Graphen (Gr) auf Ir in einer Vielzahl von Rollen als Ausgangspunkt von Untersuchungen zu (1) der Bindung unpolarer Moleküle an Graphen, (2) dem Magnetismus von Monolagen des Seltenerdmetalls Eu und deren Kopplung zu 3*d*-Metallfilmen, und (3) der Synthese und des Magnetismus von organometallischen Verbindungen mit aromatischen Liganden. Alle Experimente werden im Ultrahochvakuum unter Verwendung oberflächenempfindlicher Methoden durchgeführt: Beugung niederenergetischer Elektronen (LEED), Rastertunnelmikroskopie (STM), Thermodesorptionsspektroskopie (TDS), und weiche Röntgenstrahlung für magnetischen Zirkulardichroismus (XMCD). Die Experimente werden ergänzt durch Rechnungen mit Dichtefunktionaltheorie (DFT) von Kooperationspartnern.

In Projekt (1) zeigen wir bildlich mittels STM und quantitativ mit TDS, dass die Bindungsstärke von Naphthalin auf Graphen, ein Paradebeispiel für van-der-Waals-Wechselwirkung, durch n-Dotierung des Graphens gestärkt und p-Dotierung geschwächt wird. DFT-Rechnungen mit van-der-Waals-Wechselwirkung ab initio reproduzieren den beobachteten Trend der Bindungsenergien. Auf Grundlage einer Modellrechnungen wird vorgeschlagen, dass die van-der-Waals-Wechselwirkung durch die in Folge der Dotierung sich ändernde Ausdehnung der π-Orbitale moduliert wird.

In Projekt (2) schaffen wir neue Grenzflächen von Gr mit metallischen und magnetischen Unterlagen, bei denen die Gr-Bandstruktur weitgehend erhalten bleibt. Dies wird erreicht durch die Interkalation von Eu-Monolagen durch Deposition bei erhöhter Temperatur. Verschiedene Überstrukturen bilden sich in der Monolage in Abhängigkeit der Bedeckung, die hier umfassender dargestellt werden als zuvor. In einer Präparation der $(\sqrt{3} \times \sqrt{3})\mathrm{R30}^\circ_{\mathrm{Gr}}$-Überstruktur zeigt XMCD ferromagnetische Ordnung in der Eu-Monolage mit $T_C \geq 15\,\mathrm{K}$ und dominierende dipolare Anisotropie. Verwendung von Co und Ni als Gr-Substrate erlaubt höhere Ordnungtemperaturen in der Eu-Monolage. In diesem Fall bildet Eu nur eine $(\sqrt{3} \times \sqrt{3})\mathrm{R30}^\circ_{\mathrm{Gr}}$-Überstruktur. Nahkanten-Röntgenabsorption zeigt eine elektronische Entkoppelung des Gr von den sonst

stark wechselwirkenden $3d$-Metallsubstraten. XMCD wird zur elementspezifischen magnetischen Charakterisierung genutzt. Es zeigt sich eine antiferromagnetische Kopplung von Eu und Co/Ni, die stark genug ist für eine bei Raumtemperatur messbare Magnetisierung in Eu.

In Projekt (3) nutzen wir Gr als Substrat für das Wachsum organometallischer Verbindungen. Wir kodeponieren atomaren Metalldampf und ringförmige aromatischen Liganden, um Sandwich-Komplexe und molekulare Sandwich-Drähte zu erhalten. Die $4f$-Metalle Eu und Tm werden mit Cyclooctatetraene-Molekülen kombiniert, und das $3d$-Metall V mit Benzol (Bz).

Kodeposition von Eu und Cot führt immer zu EuCot-Nanodrähten solange ein Überschuss Moleküle besteht, der rückverdampfen kann. Dabei ergibt sich eine faszinierende Morphologie. Im STM erscheint EuCot isolierend, und XMCD-Messungen zeigen, dass EuCot ein Ferromagnet mit Curie-Temperatur etwas über 5 K ist. Um die Nanodrähte in der Oberflächenebene auszurichten, nutzen wir als weiteres Substrat Gr/Ir(110), eine Oberfläche mit nur zweizähliger Drehsymmetrie. Eine der Gr-Phasen ist atomar flach und erlaubt das Wachstum der EuCot-Drähte entlang der [001]-Richtung des Substrates.

Im Gegensatz zu EuCot wachsen TmCot-Nanodrähte nur auf n-dotiertem Gr, und das Wachstum reagiert empfindlich auf das Flussverhältnis Tm zu Cot. Auf undotiertem Gr führt gleichzeitige Bedampfung mit Tm und Cot hingegen zur Bildung zweier anderer Phasen: Bei niedrigen Bedeckungen mit Tm bildet sich eine Phase repulsiv wechselwirkender TmCot-Monomere, während bei höheren Tm-Bedeckungen zusätzlich eine inselbildende “Kaffeebohnen”-Phase in einem Fischgrätenmuster entsteht. Das unterschiedliche Verhalten von Eu und Tm führen wir auf den für Tm vergleichsweise vorteilhafteren +3-Oxidationszustand zurück. XMCD an der Kaffeebohnenphase zeigt eine eigenartige Anisotropie und Sättigungsverhalten.

Im Falle des VBz wurden keine Drähte erhalten, sondern nur VBz_2-Sandwichmoleküle, was auf den kovalenten Bindungscharakter zurückgeführt wird.

Appendix C

Liste der Teilpublikationen *(List of Publications)*

Teile dieser Arbeit wurden als Bestandteil der folgenden Artikel in Fachzeitschriften bereits veröffentlicht:
Parts of the results presented in this thesis can be found in the following publications:

[30] S. Schumacher, F. Huttmann, M. Petrović, C. Witt, D. F. Förster, C. Vo-Van, J. Coraux, A. J. Martínez-Galera, V. Sessi, I. Vergara, R. Rückamp, M. Grüninger, N. Schleheck, F. Meyer zu Heringdorf, P. Ohresser, M. Kralj, T. O. Wehling, and T. Michely
Europium underneath graphene on Ir(111): Intercalation mechanism, magnetism, and band structure
Phys. Rev. B **90**, 235437 (2014)

[126] F. Huttmann, A. J. Martínez-Galera, V. Caciuc, N. Atodiresei, S. Schumacher, S. Standop, I. Hamada, T. O. Wehling, S. Blügel, and T. Michely
Tuning the van der Waals Interaction of Graphene with Molecules via Doping
Phys. Rev. Lett. **115**, 236101 (2015)
selected for a viewpoint in *Physics*, selected for an Editor's suggestion, and on the cover

[162] F. Huttmann, D. Klar, N. Atodiresei, C. Schmitz-Antoniak, A. Smekhova, A. J. Martínez-Galera, V. Caciuc, G. Bihlmayer, S. Blügel, T. Michely, and H. Wende
Magnetism in a graphene-4f-3d hybrid system
Phys. Rev. B **95**, 075427 (2017)

[204] F. Huttmann, N. Schleheck, N. Atodiresei, T. Michely
On-Surface Synthesis of Sandwich Molecular Nanowires on Graphene
J. Am. Chem. Soc. **139**, 9895 (2017)

Weitere Publikationen:
Further publications:

[136] A. J. Martínez-Galera, U. A. Schröder, F. Huttmann, W. Jolie, F. Craes, C. Busse, V. Caciuc, N. Atodiresei, S. Blügel, and T. Michely
Oxygen orders differently under graphene: new superstructures on Ir(111)
Nanoscale **4**, 1932 (2016)

Konferenzbeiträge als präsentierender Autor:
Conference contributions as presenting author:

2013/11 544th W.-E.-Heraeus-Seminar, Bad Honnef (DE), Poster, *Adsorption on and Intercalation under Graphene/Ir(111): Magnetism and Binding*
2014/04 DPG Spring Meeting, Dresden (DE), Talk, *Tuning the van der Waals Interaction of Graphene with Molecules via Doping*
2014/05 Workshop of the DFG Priority Program 1459 "Graphene", Chemnitz (DE), Talk, *The Backside of Graphene: Manipulating Magnetism and Adsorption to Graphene by Intercalation*
2014/06 2nd European Workshop on Epitaxial Graphene and 2D Materials, Primošten (HR), Talk, *Tuning the van der Waals Interaction of Graphene with Molecules via Doping*
2015/03 DPG Spring Meeting, Berlin (DE), Talk, *Room-temperature Magnetic Ordering of a Eu Monolayer Under Graphene on Ni and Co Thin Films*
2015/09 31st European Conference on Surface Science (ECOSS), Barcelona (ES), Talk, *Growth of Eu-Cyclooctatetraenide Nanowires on Graphene*
2016/03 DPG Spring Meeting, Regensburg (DE), Talk, *Synthesis of Organometallic Sandwich Complexes and Nanowires on Graphene*
2016/05 3rd European Workshop on Epitaxial Graphene and 2D Materials, Bergisch Gladbach (DE), Poster, *Synthesis of Organometallic Sandwich Complexes and Nanowires on Graphene*
2016/10 European Conference on Nanofilms (ECNF), Bilbao (ES), Talk, *Synthesis of Organometallic Sandwich Complexes and Nanowires on Graphene*
2017/03 DPG Spring Meeting, Dresden (DE), Talk, *Graphene on Ir(110), a Twofold Symmetric Substrate for van der Waals Epitaxy Applied to Growth of Organometallic Nanowires*

Akademische Anerkennungen:
Academic distinctions:

- Poster Prize of the 3rd European Workshop on Epitaxial Graphene and 2D Materials, Bergisch Gladbach, 2016
- Scholarship of the Bonn-Cologne Graduate School of Physics and Astronomy 2010/10–2012/09

Appendix D

Danksagung *(Acknowledgements)*

Zum Gelingen dieser Arbeit haben viele Personen auf unterschiedliche Art und Weise beigetragen. Bei diesen möchte ich mich abschließend bedanken. *Many people have in different ways contributed to the success of this work. To those I would here like to express my gratitude.*

An erster Stelle danke ich Prof. Dr. Thomas Michely. Ich habe bei Dir als Bachelorand angefangen und werde als Doktor wohl irgendwann aufhören. Du bist dem Wort Doktorvater gerecht geworden. Ich weiß nicht, was mit einem anderem Betreuer aus mir geworden wäre. Weiterhin danke ich Prof. Dr. Heiko Wende für die Übernahme des Zweitgutachtens, die vielen Diskussionen und die produktive Kooperation; Prof. Dr. Hans-Günther Schmalz für die Bereitschaft, den Vorsitz der Prüfungskommission zu übernehmen; Prof. Dr. Tim O. Wehling für den Gastaufenthalt in seiner Gruppe, der mir das Erlernen einer neuen Methode ermöglicht hat; Dr. Oliver Breunig für die Übernahme des Beisitzes; Nicolas Schleheck, Merve Seçkin, und Stefan Kraus, deren Bachelor- und Masterarbeiten wesentliche Teile dieser Arbeit bilden; Wouter Jolie, Joshua Hall, und Stefan Kraus für das Korrekturlesen; Stefan Schumacher und Jürgen Klinkhammer, den Betreuern meiner Bachelor- und Masterarbeiten, die mich auf diesen Pfad geführt haben.

This work was in large parts done in the context of cooperations and I want to express my gratitude to all collaborators from other groups. The theory cooperation with Nicolae Atodiresei and Vasile Caciuc of the group of Stefan Blügel was most important throughout this work. Particularly without Nicolae, two out of three result chapters would not exist, as we would never have had those ideas. I acknowledge Violetta Sessi, Phillipe Ohresser, Chi Vo-Van, and Johann Coraux who worked with me during my first beamtime at ESRF ID08; David Klar, Carolin Schmitz-Antoniak, and Alevtina Smekhova, who had to do all the unrewarding work setting up the AG Wende chamber at BESSY; Kurt Kummer and Nick Brookes of ID08/32, who were the most helpful, professional and committed beamline scientists; Matthias Bernien, who showed very good leadership during the beamtime on EuCot at VEKMAG; also, Andrew Britton, Lalminthang Kipgen, and Fabian Nickel; Nico Rothenbach, Katharina Ollefs, and Lucas Arruda, who enabled Stefan and me to focus fully on the preparation at ID32; especially Nico, who did much analysis on EuCot. Lastly special thanks to Antonio Martínez-Galera. You were the best colleague at all times, but your selflessness may not always have been the best for yourself.

Doktorarbeiten sind nicht nur Wissenschaft. Mein Dank geht an Norbert Henn für das Lösen vieler technischer Probleme. Auch an meine bisher ungenannten Kollegen in der Arbeitsgruppe: Die mir widerfahrene, sehr weitgehende Gutartigkeit der mich umgebenden Menschen hoffe ich nie wieder zu verlieren. Dank unserer Sekretärin Britta Schulz für ihr Verständnis der Eigenschaften ihrer Schützlinge oder jedenfalls den immer lösungsorientierten Umgang damit; der Bonn-Cologne Graduate School of Physics and Astronomy für die finanzielle Unterstützung, dabei vor allem Petra Neubauer-Guenther, ohne deren Engagement die letzten Monate meiner Arbeit eine brotlose Zeit gewesen wären.

Ich danke meiner Familie: Barbara und Karlheinz Solbach; Jürgen Werner; Georg, Vera, und Christina Huttmann. Ihr habt mich stets nach Kräften unterstützt. Auch, wenn ich mir oft nicht helfen lassen wollte – ich hatte immer die Gewissheit haben dürfen, dass Ihr, wenn ich danach frage, sofort für mich da seid, und dafür bin ich Euch dankbar. Also to you Sabina. No other person has gained emotional significance in my life as you did. We share many memories and most of them are good ones. Thank you for being my friend during this time. Und dann danke ich Dir, McSuccess-Erfinderin, noch einmal in besonderer Weise für deine "ganzheitliche Behandlung" in der Schlussphase. Auch hier weiß man nicht, was sonst aus mir geworden wäre. Das, was du Selbstwirksamkeitserwartung nennst, hat mich wieder mehr mit Optimismus für mein weiteres Leben erfüllt.

Appendix E

Bibliography

[1] A. K. Geim and K. S. Novoselov. "The rise of graphene". *Nat. Mater.* 6 (2007), p. 183 (cit. on pp. 11, 16).

[2] K. S. Novoselov et al. "Electric Field Effect in Atomically Thin Carbon Films". *Science* 306 (2004), p. 666 (cit. on pp. 11, 16, 43).

[3] S. Z. Butler et al. "Progress, Challenges, and Opportunities in Two-Dimensional Materials Beyond Graphene". *ACS Nano* 7 (2013), p. 2898 (cit. on p. 11).

[4] K. S. Novoselov et al. "Room-Temperature Quantum Hall Effect in Graphene". *Science* 315 (2007), p. 1379 (cit. on p. 11).

[5] F. Schedin et al. "Detection of individual gas molecules adsorbed on graphene". *Nat. Mater.* 6 (2007), p. 652 (cit. on p. 11).

[6] K. F. Mak, C. Lee, J. Hone, J. Shan, and T. F. Heinz. "Atomically Thin MoS_2: A New Direct-Gap Semiconductor". *Phys. Rev. Lett.* 105 (2010), p. 136805 (cit. on pp. 11, 135).

[7] R. Larciprete et al. "Oxygen Switching of the Epitaxial Graphene-Metal Interaction". *ACS Nano* 6 (2012), p. 9551 (cit. on pp. 11, 23, 43, 47, 49, 52).

[8] D. Pacilé et al. "Artificially lattice-mismatched graphene/metal interface: Graphene/Ni/Ir(111)". *Phys. Rev. B* 87 (2013), p. 035420 (cit. on pp. 11, 23, 68).

[9] A. Bostwick et al. "Observation of Plasmarons in Quasi-Freestanding Doped Graphene". *Science* 328 (2010), p. 999 (cit. on pp. 11, 43).

[10] J. L. McChesney et al. "Extended van Hove Singularity and Superconducting Instability in Doped Graphene". *Phys. Rev. Lett.* 104 (2010), p. 136803 (cit. on p. 11).

[11] A. V. Fedorov et al. "Observation of a universal donor-dependent vibrational mode in graphene". 5 (2014), p. 3257 (cit. on p. 11).

[12] D. Marchenko et al. "Giant Rashba splitting in graphene due to hybridization with gold". *Nat. Commun.* 3 (2012), p. 1232 (cit. on p. 11).

[13] F. Calleja et al. "Spatial variation of a giant spin-orbit effect induces electron confinement in graphene on Pb islands". *Nat. Phys.* 11 (2015), p. 43 (cit. on p. 11).

[14] D. Subramaniam et al. "Wave-Function Mapping of Graphene Quantum Dots with Soft Confinement". *Phys. Rev. Lett.* 108 (2012), p. 046801 (cit. on p. 11).

[15] S. K. Hämäläinen et al. "Quantum-Confined Electronic States in Atomically Well-Defined Graphene Nanostructures". *Phys. Rev. Lett.* 107 (2011), p. 236803 (cit. on p. 11).

[16] S.-h. Phark, J. Borme, A. L. Vanegas, M. Corbetta, D. Sander, and J. Kirschner. "Direct Observation of Electron Confinement in Epitaxial Graphene Nanoislands". *ACS Nano* 5 (2011), p. 8162 (cit. on p. 11).

[17] W. Jolie et al. "Confinement of Dirac electrons in graphene quantum dots". *Phys. Rev. B* 89 (2014), p. 155435 (cit. on pp. 11, 47, 52).

[18] R. Decker, J. Brede, N. Atodiresei, V. Caciuc, S. Blügel, and R. Wiesendanger. "Atomic-scale magnetism of cobalt-intercalated graphene". *Phys. Rev. B* 87 (2013), p. 041403 (cit. on pp. 11, 23, 54, 68).

[19] M. M. Ugeda et al. "Giant bandgap renormalization and excitonic effects in a monolayer transition metal dichalcogenide semiconductor". *Nat. Mater.* 13 (2014), p. 1091 (cit. on p. 11).

[20] N. Tombros, C. Jozsa, M. Popinciuc, H. T. Jonkman, and B. J. van Wees. "Electronic spin transport and spin precession in single graphene layers at room temperature." *Nature* 448 (2007), p. 571 (cit. on pp. 12, 54).

[21] W. Han, R. K. Kawakami, M. Gmitra, and J. Fabian. "Graphene spintronics". *Nat. Nanotechnol.* 9 (2014), p. 794 (cit. on pp. 12, 54).

[22] Y. S. Dedkov and M. Fonin. "Electronic and magnetic properties of the graphene-ferromagnet interface". *N. J. Phys.* 12 (2010), p. 125004 (cit. on pp. 12, 54, 75–77).

[23] F. Mittendorfer, A. Garhofer, J. Redinger, J. Klimeš, J. Harl, and G. Kresse. "Graphene on Ni(111): Strong interaction and weak adsorption". *Phys. Rev. B* 84 (2011), p. 201401 (cit. on p. 12).

[24] F. Bianchini, L. L. Patera, M. Peressi, C. Africh, and G. Comelli. "Atomic Scale Identification of Coexisting Graphene Structures on Ni(111)". *J. Phys. Chem. Lett.* 5 (2014), p. 467 (cit. on pp. 12, 17, 18).

[25] A. Barla et al. "Complex Magnetic Exchange Coupling between Co Nanostructures and Ni(111) across Epitaxial Graphene". *ACS Nano* 10 (2016), p. 1101 (cit. on p. 12).

[26] P. Lazić, G. M. Sipahi, R. K. Kawakami, and I. Žutić. "Graphene spintronics: Spin injection and proximity effects from first principles". *Phys. Rev. B* 90 (2014), p. 085429 (cit. on p. 12).

[27] Q. Wu et al. "Efficient Spin Injection into Graphene through a Tunnel Barrier: Overcoming the Spin-Conductance Mismatch". *Phys. Rev. Applied* 2 (2014), p. 044008 (cit. on p. 12).

[28] A. Varykhalov et al. "Intact Dirac Cones at Broken Sublattice Symmetry: Photoemission Study of Graphene on Ni and Co". *Phys. Rev. X* 2 (2012), p. 041017 (cit. on p. 12).

[29] D. F. Förster, T. O. Wehling, S. Schumacher, A. Rosch, and T. Michely. "Phase coexistence of clusters and islands: europium on graphene". *N. J. Phys.* 14 (2012), p. 023022 (cit. on pp. 12, 88).

[30] S. Schumacher et al. "Europium underneath graphene on Ir(111): Intercalation mechanism, magnetism, and band structure". *Phys. Rev. B* 90 (2014), p. 235437 (cit. on pp. 12, 43, 47, 49, 52–54, 58, 62, 70, 72, 84, 88, 90, 118, 155).

[31] D. F. Förster, J. Klinkhammer, and T. Michely. "Eu oxides on Ni(100): Polar surfaces, magic clusters and structures with large lattice dilation". *Surf. Sci.* 606 (2012), p. 1019 (cit. on p. 12).

[32] J. Klinkhammer, D. F. Förster, S. Schumacher, H. P. Oepen, T. Michely, and C. Busse. "Structure and magnetic properties of ultra thin textured EuO films on graphene". *Appl. Phys. Lett.* 103 (2013), p. 131601 (cit. on pp. 12, 62, 118).

[33] R. Sutarto et al. "Epitaxial and layer-by-layer growth of EuO thin films on yttria-stabilized cubic zirconia (001) using MBE distillation". *Phys. Rev. B* 79 (2009), p. 205318 (cit. on pp. 12, 80).

[34] S. Sanvito. "Molecular spintronics". *Chem. Soc. Rev.* 40 (2011), p. 3336 (cit. on p. 12).

[35] F. T. Edelmann. "Multiple-decker sandwich complexes of f-elements". *New J. Chem.* 35 (2011), p. 517 (cit. on p. 12).

[36] N. Ishikawa, M. Sugita, T. Ishikawa, S.-y. Koshihara, and Y. Kaizu. "Lanthanide Double-Decker Complexes Functioning as Magnets at the Single-Molecular Level". *J. Am. Chem. Soc.* 125 (2003), p. 8694 (cit. on p. 12).

[37] V. V. Maslyuk et al. "Organometallic Benzene-Vanadium Wire: A One-Dimensional Half-Metallic Ferromagnet". *Phys. Rev. Lett.* 97 (2006), p. 097201 (cit. on pp. 12, 26, 93).

[38] L. Wang et al. "Novel One-Dimensional Organometallic Half Metals: Vanadium-Cyclopentadienyl, Vanadium-Cyclopentadienyl-Benzene, and Vanadium-Anthracene Wires". *Nano Lett.* 8 (2008), p. 3640 (cit. on p. 12).

[39] L. Zhou, S.-W. Yang, M.-F. Ng, M. B. Sullivan, V. B. C. Tan, and L. Shen. "One-Dimensional Iron-Cyclopentadienyl Sandwich Molecular Wire with Half Metallic, Negative Differential Resistance and High-Spin Filter Efficiency Properties". *J. Am. Chem. Soc.* 130 (2008), p. 4023 (cit. on p. 12).

[40] L. Shen, S.-W. Yang, M.-F. Ng, V. Ligatchev, L. Zhou, and Y. Feng. "Charge-Transfer-Based Mechanism for Half-Metallicity and Ferromagnetism in One-Dimensional Organometallic Sandwich Molecular Wires". *J. Am. Chem. Soc.* 130 (2008), p. 13956 (cit. on p. 12).

[41] K. Xu et al. "Efficient organometallic spin filter based on Europium-cyclooctatetraene wire". *J. Chem. Phys.* 131, 104704 (2009), p. 104704 (cit. on p. 12).

[42] C. Morari, H. Allmaier, F. Beiuşeanu, T. Jurcuţ, and L. Chioncel. "Electronic structure and magnetic properties of metallocene multiple-decker sandwich nanowires". *Phys. Rev. B* 85 (2012), p. 085413 (cit. on p. 12).

[43] N. Atodiresei, P. H. Dederichs, Y. Mokrousov, L. Bergqvist, G. Bihlmayer, and S. Blügel. "Controlling the Magnetization Direction in Molecules via Their Oxidation State". *Phys. Rev. Lett.* 100 (2008), p. 117207 (cit. on pp. 12, 65, 81, 82, 118, 128).

[44] X. Zhang, M.-F. Ng, Y. Wang, J. Wang, and S.-W. Yang. "Theoretical Studies on Structural, Magnetic, and Spintronic Characteristics of Sandwiched Eu_nCot_{n+1} ($n = 1 - 4$) Clusters". *ACS Nano* 3 (2009), p. 2515 (cit. on p. 12).

[45] X.-L. Wang, S. X. Dou, and C. Zhang. "Zero-gap materials for future spintronics, electronics and optics". *NPG Asia Mater.* 2 (2010), p. 31 (cit. on p. 15).

[46] A. H. Castro Neto, F. Guinea, N. M. R. Peres, K. S. Novoselov, and A. K. Geim. "The electronic properties of graphene". *Rev. Mod. Phys.* 81 (2009), p. 109 (cit. on p. 16).

[47] A. Al-Temimy, C. Riedl, and U. Starke. "Low temperature growth of epitaxial graphene on SiC induced by carbon evaporation". *Appl. Phys. Lett.* 95 (2009), p. 231907 (cit. on p. 16).

[48] L. Baraton et al. "On the mechanisms of precipitation of graphene on nickel thin films". *EPL (Europhysics Letters)* 96 (2011), p. 46003 (cit. on p. 16).

[49] K. V. Emtsev et al. “Towards wafer-size graphene layers by atmospheric pressure graphitization of silicon carbide”. *Nat. Mater.* 8 (2009), p. 203 (cit. on p. 16).

[50] X. Li, L. Colombo, and R. S. Ruoff. “Synthesis of Graphene Films on Copper Foils by Chemical Vapor Deposition”. *Adv. Mater.* 28 (2016), p. 6247 (cit. on p. 17).

[51] S. Bae et al. “Roll-to-roll production of 30-inch graphene films for transparent electrodes”. *Nat Nano* 5 (2010), p. 574 (cit. on p. 17).

[52] A. Dahal and M. Batzill. “Graphene-nickel interfaces: a review”. *Nanoscale* 6 (2014), p. 2548 (cit. on p. 17).

[53] Y. S. Dedkov and M. Fonin. “Electronic and magnetic properties of the graphene-ferromagnet interface”. *N. J. Phys.* 12 (2010) (cit. on p. 17).

[54] A. T. N’Diaye, J. Coraux, T. N. Plasa, C. Busse, and T. Michely. “Structure of epitaxial graphene on Ir(111)”. *N. J. Phys.* 10 (2008), p. 043033 (cit. on pp. 17, 19, 20, 58, 81, 114).

[55] E. Loginova, S. Nie, K. Thürmer, N. C. Bartelt, and K. F. McCarty. “Defects of graphene on Ir(111): Rotational domains and ridges”. *Phys. Rev. B* 80 (2009), p. 085430 (cit. on pp. 17, 20, 112).

[56] C. Busse et al. “Graphene on Ir(111): Physisorption with Chemical Modulation”. *Phys. Rev. Lett.* 107 (2011), p. 036101 (cit. on pp. 17, 20, 49, 92).

[57] J. Coraux, A. T. N‘Diaye, C. Busse, and T. Michely. “Structural Coherency of Graphene on Ir(111)”. *Nano Lett.* 8 (2008), p. 565 (cit. on p. 17).

[58] J. Coraux et al. “Growth of graphene on Ir(111)”. *N. J. Phys.* 11 (2009), p. 023006 (cit. on p. 17).

[59] L. Gao, J. R. Guest, and N. P. Guisinger. “Epitaxial Graphene on Cu(111)”. *Nano Lett.* 10 (2010), p. 3512 (cit. on p. 17).

[60] A. J. Martínez-Galera, I. Brihuega, and J. M. Gómez-Rodríguez. “Ethylene Irradiation: A New Route to Grow Graphene on Low Reactivity Metals”. *Nano Lett.* 11 (2011), p. 3576 (cit. on p. 17).

[61] J. Wintterlin and M.-L. Bocquet. “Graphene on metal surfaces”. *Surf. Sci.* 603 (2009), p. 1841 (cit. on p. 17).

[62] E. Starodub et al. “In-plane orientation effects on the electronic structure, stability, and Raman scattering of monolayer graphene on Ir(111)”. *Phys. Rev. B* 83 (2011), p. 125428 (cit. on p. 17).

[63] A. Dahal, R. Addou, P. Sutter, and M. Batzill. “Graphene monolayer rotation on Ni(111) facilitates bilayer graphene growth”. *Appl. Phys. Lett.* 100 (2012), p. 241602 (cit. on pp. 17–19, 70).

[64] J. Song, M. Bernien, C.-B. Wu, and W. Kuch. “Tuning the Electronic Properties of Rotated Graphene on Ni(111) by Nickel Carbide Intercalation”. *J. Phys. Chem. C* 120 (2016), p. 1546 (cit. on p. 17).

[65] P. Leicht et al. “In Situ Fabrication Of Quasi-Free-Standing Epitaxial Graphene Nanoflakes On Gold”. *ACS Nano* 8 (2014), p. 3735 (cit. on pp. 17, 22).

[66] J. Brede et al. “Tuning the Graphene on Ir(111) adsorption regime by Fe/Ir surface-alloying”. *2D Materials* 4 (2017), p. 015016 (cit. on pp. 17, 69).

[67] F. Mittendorfer, A. Garhofer, J. Redinger, J. Klimeš, J. Harl, and G. Kresse. "Graphene on Ni(111): Strong interaction and weak adsorption". *Phys. Rev. B* 84 (2011), p. 201401 (cit. on pp. 17, 20).

[68] P. Jacobson et al. "Nickel Carbide as a Source of Grain Rotation in Epitaxial Graphene". *ACS Nano* 6 (2012), p. 3564 (cit. on p. 18).

[69] L. L. Patera et al. "In Situ Observations of the Atomistic Mechanisms of Ni Catalyzed Low Temperature Graphene Growth". *ACS Nano* 7 (2013), p. 7901 (cit. on p. 18).

[70] R. B. McLellan. "The solubility of carbon in solid gold, copper, and silver". *Scripta Metallurgica* 3 (1969), p. 389 (cit. on p. 19).

[71] J. Knudsen et al. "Clusters binding to the graphene moiré on Ir(111): X-ray photoemission compared to density functional calculations". *Phys. Rev. B* 85 (2012), p. 035407 (cit. on pp. 19, 20).

[72] R. Van Gastel et al. "Selecting a single orientation for millimeter sized graphene sheets". *Appl. Phys. Lett.* 95 (2009), p. 121901 (cit. on p. 20).

[73] S. K. Hämäläinen et al. "Structure and local variations of the graphene moiré on Ir(111)". *Phys. Rev. B* 88 (2013), p. 201406 (cit. on pp. 20, 92).

[74] H. Hattab et al. "Interplay of Wrinkles, Strain, and Lattice Parameter in Graphene on Iridium". *Nano Lett.* 12 (2012), p. 678 (cit. on p. 21).

[75] L. Meng et al. "Silicon intercalation at the interface of graphene and Ir(111)". *Appl. Phys. Lett.* 100 (2012), p. 083101 (cit. on p. 21).

[76] M. Petrović, J. T. Sadowski, A. Šiber, and M. Kralj. "Wrinkles of graphene on Ir(111): Macroscopic network ordering and internal multi-lobed structure". *Carbon* 94 (2015), p. 856 (cit. on pp. 20, 21).

[77] S. Runte. "Atomic and Electronic Structure of Graphene and Graphene Intercalation Compounds. X-Ray Standing Wave and Scanning Tunneling Microscopy Studies". PhD thesis. Universität zu Köln, 2013 (cit. on p. 21).

[78] M. Petrović et al. "The mechanism of caesium intercalation of graphene". *Nat. Commun.* 4 (2013), p. 2772 (cit. on pp. 21, 23, 43, 52, 57).

[79] E. Voloshina and Y. Dedkov. "Graphene on metallic surfaces: problems and perspectives". *Phys. Chem. Chem. Phys.* 14 (2012), p. 13502 (cit. on p. 22).

[80] I. Pletikosić et al. "Dirac Cones and Minigaps for Graphene on Ir(111)". *Phys. Rev. Lett.* 102 (2009), p. 056808 (cit. on pp. 21, 47).

[81] U. A. Schröder et al. "Core level shifts of intercalated graphene". *2D Materials* 4 (2017), p. 015013 (cit. on pp. 22, 52).

[82] C. Herbig et al. "Mechanical exfoliation of epitaxial graphene on Ir(111) enabled by Br_2 intercalation". *J. Phys. Condens. Matter* 24 (2012), p. 314208 (cit. on p. 22).

[83] S. Schumacher, D. F. Förster, M. Rösner, T. O. Wehling, and T. Michely. "Strain in epitaxial graphene visualized by intercalation". *Phys. Rev. Lett.* 110 (2013), p. 1 (cit. on pp. 23, 44, 54, 85, 90).

[84] H. Vita, S. Böttcher, P. Leicht, K. Horn, A. B. Shick, and F. Máca. "Electronic structure and magnetic properties of cobalt intercalated in graphene on Ir(111)". *Phys. Rev. B* 90 (2014), p. 165432 (cit. on pp. 23, 54, 68, 75).

[85] R. Decker, M. Bazarnik, N. Atodiresei, V. Caciuc, S. Blügel, and R. Wiesendanger. "Local tunnel magnetoresistance of an iron intercalated graphene-based heterostructure". *J. Phys. Condens. Matter* 26 (2014), p. 394004 (cit. on pp. 23, 54).

[86] S. Schumacher et al. "The Backside of Graphene: Manipulating Adsorption by Intercalation". *Nano Lett.* 13 (2013), p. 5013 (cit. on pp. 24, 44, 88, 89).

[87] R. Zacharia, H. Ulbricht, and T. Hertel. "Interlayer cohesive energy of graphite from thermal desorption of polyaromatic hydrocarbons". *Phys. Rev. B* 69 (2004), p. 155406 (cit. on pp. 24, 43, 44, 46–48, 151).

[88] S. D. Chakarova-Käck, E. Schröder, B. I. Lundqvist, and D. C. Langreth. "Application of van der Waals Density Functional to an Extended System: Adsorption of Benzene and Naphthalene on Graphite". *Phys. Rev. Lett.* 96 (2006), p. 146107 (cit. on pp. 24, 43, 44, 51).

[89] U. Bardi, S. Magnanelli, and G. Rovida. "LEED study of benzene and naphthalene monolayers adsorbed on the basal plane of graphite". *Langmuir* 3 (1987), p. 159 (cit. on pp. 24, 45, 149).

[90] F. Sojka, M. Meissner, T. Yamada, T. Munakata, R. Forker, and T. Fritz. "Naphthalene's Six Shades on Graphite: A Detailed Study on the Polymorphism of an Apparently Simple System". *J. Phys. Chem. C* 120 (2016), p. 22972 (cit. on pp. 24, 151).

[91] T. Yamada, Y. Takano, M. Isobe, K. Miyakubo, and T. Munakata. "Growth and adsorption geometry of naphthalene overlayers on HOPG studied by low-temperature scanning tunneling microscopy". *Chem. Phys. Lett.* 546 (2012), p. 136 (cit. on pp. 24, 45).

[92] M. Dion, H. Rydberg, E. Schröder, D. C. Langreth, and B. I. Lundqvist. "Van der Waals Density Functional for General Geometries". *Phys. Rev. Lett.* 92 (2004), p. 246401 (cit. on pp. 25, 51).

[93] P. L. Pauson. "Ferrocene—how it all began". *J. Organomet. Chem.* 637 (2001), p. 3 (cit. on p. 25).

[94] F. G. N. Cloke, A. N. Dix, J. C. Green, R. N. Perutz, and E. A. Seddon. "Electron spin resonance and photoelectron studies of neutral bis(η-arene)metal compounds (metal = Ti, V, Nb, Ta, Mo, and W)". *Organometallics* 2 (1983), p. 1150 (cit. on p. 25).

[95] R. E. Dinnebier, F. Olbrich, and G. M. Bendele. "Cyclopentadienylcaesium by High-Resolution X-ray Powder Diffraction". *Acta Crystallographica Section C* 53 (1997), p. 699 (cit. on p. 26).

[96] A. Nakajima and K. Kaya. "A Novel Network Structure of Organometallic Clusters in the Gas Phase". *J. Phys. Chem. A* 104 (2000), p. 176 (cit. on pp. 26, 27, 79, 103, 108, 128).

[97] R. G. Hayes and J. L. Thomas. "Synthesis of cyclooctatetraenyleuropium and cyclooctatetraenylytterbium". *J. Am. Chem. Soc.* 91 (1969), p. 6876 (cit. on pp. 26, 79, 90).

[98] K. Miyajima, M. B. Knickelbein, and A. Nakajima. "Stern-Gerlach Study of Multidecker Lanthanide-Cyclooctatetraene Sandwich Clusters". *J. Phys. Chem. A* 112 (2008), p. 366 (cit. on pp. 27, 79).

[99] N. Hosoya et al. "Lanthanide Organometallic Sandwich Nanowires: Formation Mechanism". *J. Phys. Chem. A* 109 (2005), p. 9 (cit. on p. 27).

[100] K. Miyajima, A. Nakajima, S. Yabushita, M. B. Knickelbein, and K. Kaya. "Ferromagnetism in One-Dimensional Vanadium-Benzene Sandwich Clusters". *J. Am. Chem. Soc.* 126 (2004), p. 13202 (cit. on pp. 27, 79).

[101] M. S. R. Rao and G. Margaritondo. "Three decades of scanning tunnelling microscopy that changed the course of surface science". *Journal of Physics D: Applied Physics* 44 (2011), p. 460301 (cit. on p. 29).

[102] Y. Zhang et al. "Giant phonon-induced conductance in scanning tunnelling spectroscopy of gate-tunable graphene". *Nat. Phys.* 4 (2008), p. 627 (cit. on p. 30).

[103] S. Fahrendorf et al. "Accessing 4f-states in single-molecule spintronics". *Nat. Commun.* 4 (2013), p. 1 (cit. on pp. 30, 82).

[104] C. Davisson and L. Germer. "The scattering of electrons by a single crystal of nickel". *Nature* 119 (1927), p. 558 (cit. on p. 30).

[105] K. A. R. Mitchell. "Low-energy electron diffraction". *Contemporary Physics* 14 (1973), p. 251 (cit. on p. 30).

[106] D. A. King. "Thermal desorption from metal surfaces: A review". *Surf. Sci.* 47 (1975). Proceedings of the Third Symposium on Surface Physics University of Utrecht, The Netherlands 26-28 June 1974, p. 384 (cit. on p. 31).

[107] B. T. Thole, G. van der Laan, J. C. Fuggle, G. A. Sawatzky, R. C. Karnatak, and J.-M. Esteva. "3d x-ray-absorption lines and the $3d^9 4f^{n+1}$ multiplets of the lanthanides". *Phys. Rev. B* 32 (1985), p. 5107 (cit. on pp. 32, 58, 61, 71, 119, 120, 142).

[108] R. Nakajima, J. Stöhr, and Y. U. Idzerda. "Electron-yield saturation effects in L-edge x-ray magnetic circular dichroism spectra of Fe, Co, and Ni". *Phys. Rev. B* 59 (1999), p. 6421 (cit. on pp. 32, 61).

[109] R. A. Rosenberg, P. J. Love, and V. Rehn. "Polarization-dependent C(K) near-edge x-ray-absorption fine structure of graphite". *Phys. Rev. B* 33 (1986), p. 4034 (cit. on pp. 32, 76, 77).

[110] I. G. Rau et al. "Reaching the magnetic anisotropy limit of a 3d metal atom". *Science* 344 (2014), p. 988 (cit. on p. 32).

[111] G. van der Laan and A. I. Figueroa. "X-ray magnetic circular dichroism – A versatile tool to study magnetism". *Coordination Chemistry Reviews* 277 (2014), p. 95 (cit. on pp. 33, 34).

[112] C. Antoniak et al. "Enhanced Orbital Magnetism in $Fe_{50}Pt_{50}$ Nanoparticles". *Phys. Rev. Lett.* 97 (2006), p. 117201 (cit. on p. 33).

[113] C. De Nadai et al. "Local magnetism in rare-earth metals encapsulated in fullerenes". *Phys. Rev. B* 69 (2004), p. 184421 (cit. on pp. 34, 59, 60).

[114] J. Stöhr. "Exploring the microscopic origin of magnetic anisotropies with X-ray magnetic circular dichroism (XMCD) spectroscopy". *J. Magn. Magn. Mater* 200 (1999), p. 470 (cit. on p. 33).

[115] T. Funk, A. Deb, S. J. George, H. Wang, and S. P. Cramer. "X-ray magnetic circular dichroism—a high energy probe of magnetic properties". *Coordination Chemistry Reviews* 249 (2005), p. 3 (cit. on p. 33).

[116] G. van der Laan. "Applications of soft x-ray magnetic dichroism". *J. Phys. Conf. Ser.* 430 (2013), p. 012127 (cit. on p. 33).

[117] S. Kraus. *Nanostructures of Cyclooctatetraene with Rare Earth Metals: Growth and Magnetism*. Master thesis. Germany, 2017 (cit. on pp. 35, 36, 99, 118).

[118] B. T. Thole, P. Carra, F. Sette, and G. van der Laan. "X-ray circular dichroism as a probe of orbital magnetization". *Phys. Rev. Lett.* 68 (1992), p. 1943 (cit. on pp. 35, 59).

[119] P. Carra, B. T. Thole, M. Altarelli, and X. Wang. "X-ray circular dichroism and local magnetic fields". *Phys. Rev. Lett.* 70 (1993), p. 694 (cit. on pp. 35, 37, 59).

[120] Y. Teramura, A. Tanaka, B. T. Thole, and T. Jo. "Effect of Coulomb Interaction on the X-Ray Magnetic Circular Dichroism Spin Sum Rule in Rare Earths". *J. Phys. Soc. Jpn.* 65 (1996), p. 3056 (cit. on pp. 37, 122).

[121] D. Förster. "EuO and Eu on metal crystals and graphene: interface effects and epitaxial films". PhD thesis. Universität zu Köln, 2011 (cit. on pp. 39, 54).

[122] S. Standop. "Water Adsorption and Ion Induced Defect Formation: A Comparative Study of Graphene and Noble Metal Surfaces". PhD thesis. Universität zu Köln, 2013 (cit. on p. 39).

[123] K. Kummer et al. "The high-field magnet endstation for X-ray magnetic dichroism experiments at ESRF soft X-ray beamline ID32". *Journal of Synchrotron Radiation* 23 (2016), p. 464 (cit. on p. 40).

[124] R. van Gastel et al. "Selecting a single orientation for millimeter sized graphene sheets". *Appl. Phys. Lett.* 95, 121901 (2009), p. 121901 (cit. on pp. 41, 110).

[125] D. Appy et al. "Determining whether metals nucleate homogeneously on graphite: A case study with copper". *Phys. Rev. B* 90 (2014), p. 195406 (cit. on p. 42).

[126] F. Huttmann et al. "Tuning the van der Waals Interaction of Graphene with Molecules via Doping". *Phys. Rev. Lett.* 115 (2015), p. 236101 (cit. on pp. 43, 81, 82, 155).

[127] D. C. Langreth et al. "A density functional for sparse matter". *J. Phys. Condens. Matter* 21 (2009), p. 084203 (cit. on pp. 43, 51).

[128] E. Londero, E. K. Karlson, M. Landahl, D. Ostrovskii, J. D. Rydberg, and E. Schröder. "Desorption of n-alkanes from graphene: a van der Waals density functional study". *J. Phys. Condens. Matter* 24 (2012), p. 424212 (cit. on p. 43).

[129] S. L. Tait, Z. Dohnálek, C. T. Campbell, and B. D. Kay. "n-alkanes on Pt(111) and on C(0001)/Pt(111): Chain length dependence of kinetic desorption parameters". *J. Chem. Phys.* 125, 234308 (2006) (cit. on p. 43).

[130] H. Wang, T. Maiyalagan, and X. Wang. "Review on Recent Progress in Nitrogen-Doped Graphene: Synthesis, Characterization, and Its Potential Applications". *ACS Catal.* 2 (2012), p. 781 (cit. on p. 43).

[131] C. Coletti et al. "Charge neutrality and band-gap tuning of epitaxial graphene on SiC by molecular doping". *Phys. Rev. B* 81 (2010), p. 235401 (cit. on p. 43).

[132] C. Riedl, C. Coletti, T. Iwasaki, A. A. Zakharov, and U. Starke. "Quasi-Free-Standing Epitaxial Graphene on SiC Obtained by Hydrogen Intercalation". *Phys. Rev. Lett.* 103 (2009), p. 246804 (cit. on p. 44).

[133] V. W. Brar et al. "Gate-controlled ionization and screening of cobalt adatoms on a graphene surface". *Nature Phys.* 7 (2010), p. 43 (cit. on p. 44).

[134] T. O. Wehling, B. Grundkötter-Stock, B. Aradi, T. Frauenheim, and T. Niehaus. "Charge-doping-induced phase transitions in hydrogenated and fluorinated graphene". *Phys. Rev. B* 90 (2014), p. 085422 (cit. on p. 44).

[135] L. F. Huang et al. "Modulation of the thermodynamic, kinetic, and magnetic properties of the hydrogen monomer on graphene by charge doping". *J. Chem. Phys.* 135 (2011), p. 064705 (cit. on p. 44).

[136] A. J. Martínez-Galera et al. "Oxygen orders differently under graphene: new superstructures on Ir(111)". *Nanoscale* 8 (2016), p. 1932 (cit. on pp. 47, 155).

[137] S. Ulstrup et al. "Sequential oxygen and alkali intercalation of epitaxial graphene on Ir(111): enhanced many-body effects and formation of *p-n* interfaces". *2D Materials* 1 (2014), p. 025002 (cit. on p. 47).

[138] M. Petrović. "Synthesis and Intercalation of Epitaxial Graphene on Iridium". PhD thesis. University of Zagreb, 2014 (cit. on p. 47).

[139] J. P. Perdew, K. Burke, and M. Ernzerhof. "Generalized Gradient Approximation Made Simple". *Phys. Rev. Lett.* 77 (1996), p. 3865 (cit. on p. 48).

[140] P. E. Blöchl. "Projector augmented-wave method". *Phys. Rev. B* 50 (1994), p. 17953 (cit. on p. 48).

[141] G. Kresse and J. Hafner. "Ab initio". *Phys. Rev. B* 47 (1993), p. 558 (cit. on p. 48).

[142] G. Kresse and J. Furthmüller. "Efficient iterative schemes for ab initio total-energy calculations using a plane-wave basis set". *Phys. Rev. B* 54 (1996), p. 11169 (cit. on p. 48).

[143] K. Lee, É. D. Murray, L. Kong, B. I. Lundqvist, and D. C. Langreth. "Higher-accuracy van der Waals density functional". *Phys. Rev. B* 82 (2010), p. 081101 (cit. on pp. 48, 51).

[144] I. Hamada. "van der Waals density functional made accurate". *Phys. Rev. B* 89 (2014), p. 121103 (cit. on p. 48).

[145] A. D. Becke. "On the large gradient behavior of the density functional exchange energy". *J. Chem. Phys.* 85 (1986), p. 7184 (cit. on p. 48).

[146] R. F. W. Bader. *Atoms in Molecules – A Quantum Theory*. Oxford University Press, 1990 (cit. on p. 49).

[147] K. Berland and P. Hyldgaard. "Analysis of van der Waals density functional components: Binding and corrugation of benzene and C_{60} on boron nitride and graphene". *Phys. Rev. B* 87 (2013), p. 205421 (cit. on p. 50).

[148] M. Muruganathan, J. Sun, T. Imamura, and H. Mizuta. "Electrically Tunable van der Waals Interaction in Graphene–Molecule Complex". *Nano Lett.* 15 (2015), p. 8176 (cit. on pp. 51, 131).

[149] J. F. Dobson and T. Gould. "Calculation of dispersion energies". *J. Phys. Condens. Matter* 24 (2012), p. 073201 (cit. on p. 51).

[150] S. Grimme. "Semiempirical GGA-type density functional constructed with a long-range dispersion correction". *J. Comput. Chem.* 27 (2006), p. 1787 (cit. on p. 51).

[151] A. Tkatchenko and M. Scheffler. "Accurate Molecular Van Der Waals Interactions from Ground-State Electron Density and Free-Atom Reference Data". *Phys. Rev. Lett.* 102 (2009), p. 073005 (cit. on p. 51).

[152] E. N. Voloshina, A. Generalov, M. Weser, S. Böttcher, K. Horn, and Y. S. Dedkov. "Structural and electronic properties of the graphene/Al/Ni(111) intercalation system". *N. J. Phys.* 13 (2011), p. 113028 (cit. on pp. 52, 76).

[153] A. Varykhalov et al. "Electronic and Magnetic Properties of Quasifreestanding Graphene on Ni". *Phys. Rev. Lett.* 101 (2008), p. 157601 (cit. on p. 52).

[154] D. Haberer et al. "Tunable Band Gap in Hydrogenated Quasi-Free-Standing Graphene". *Nano Lett.* 10 (2010), p. 3360 (cit. on p. 52).

[155] P. Sutter, J. T. Sadowski, and E. Sutter. "Graphene on Pt(111): Growth and substrate interaction". *Phys. Rev. B* 80 (2009), p. 245411 (cit. on p. 52).

[156] N. A. Vinogradov et al. "Controllable p-doping of graphene on Ir(111) by chlorination with $FeCl_3$". *J. Phys. Condens. Matter* 24 (2012), p. 314202 (cit. on p. 52).

[157] J. Rafiee et al. "Wetting transparency of graphene". *Nat. Mater.* 11 (2012), p. 217 (cit. on p. 52).

[158] C.-J. Shih et al. "Breakdown in the Wetting Transparency of Graphene". *Phys. Rev. Lett.* 109 (2012), p. 176101 (cit. on p. 52).

[159] D. Kim, N. M. Pugno, M. J. Buehler, and S. Ryu. "Solving the Controversy on the Wetting Transparency of Graphene". 5 (2015), p. 15526 (cit. on p. 52).

[160] G. Hong et al. "On the Mechanism of Hydrophilicity of Graphene". *Nano Lett.* 16 (2016), p. 4447 (cit. on pp. 52, 131).

[161] A. Ashraf et al. "Doping-Induced Tunable Wettability and Adhesion of Graphene". *Nano Lett.* 16 (2016), p. 4708 (cit. on pp. 52, 131).

[162] F. Huttmann et al. "Magnetism in a graphene-$4f - 3d$ hybrid system". *Phys. Rev. B* 95 (2017), p. 075427 (cit. on pp. 53, 155).

[163] Z. Wang, C. Tang, R. Sachs, Y. Barlas, and J. Shi. "Proximity-Induced Ferromagnetism in Graphene Revealed by the Anomalous Hall Effect". *Phys. Rev. Lett.* 114 (2015), p. 016603 (cit. on p. 54).

[164] H. X. Yang, A. Hallal, D. Terrade, X. Waintal, S. Roche, and M. Chshiev. "Proximity Effects Induced in Graphene by Magnetic Insulators: First-Principles Calculations on Spin Filtering and Exchange-Splitting Gaps". *Phys. Rev. Lett.* 110 (2013), p. 046603 (cit. on p. 54).

[165] A. G. Swartz, P. M. Odenthal, Y. Hao, R. S. Ruoff, and R. K. Kawakami. "Integration of the ferromagnetic insulator EuO onto graphene". *ACS Nano* 6 (2012), p. 10063 (cit. on p. 54).

[166] J. Klinkhammer, D. F. Förster, S. Schumacher, H. P. Oepen, T. Michely, and C. Busse. "Structure and magnetic properties of ultra thin textured EuO films on graphene". *Appl. Phys. Lett.* 103 (2013), p. 131601 (cit. on pp. 54, 129).

[167] J. Brede et al. "Long-range magnetic coupling between nanoscale organic-metal hybrids mediated by a nanoskyrmion lattice". *Nat. Nanotechnol.* 9 (2014), p. 1018 (cit. on p. 54).

[168] T. Eelbo et al. "Adatoms and Clusters of $3d$ Transition Metals on Graphene: Electronic and Magnetic Configurations". *Phys. Rev. Lett.* 110 (2013), p. 136804 (cit. on p. 54).

[169] K. Nakada, M. Fujita, G. Dresselhaus, and M. S. Dresselhaus. "Edge state in graphene ribbons: Nanometer size effect and edge shape dependence". *Phys. Rev. B* 54 (1996), p. 17954 (cit. on p. 54).

[170] Y.-W. Son, M. L. Cohen, and S. G. Louie. "Half-metallic graphene nanoribbons." *Nature* 444 (2006), p. 347 (cit. on p. 54).

[171] R. Drost et al. "Synthesis of Extended Atomically Perfect Zigzag Graphene - Boron Nitride Interfaces". *Scientific Reports* 5 (2015), p. 16741 (cit. on p. 54).

[172] H. González-Herrero et al. "Atomic-scale control of graphene magnetism by using hydrogen atoms". *Science* 352 (2016), p. 437 (cit. on p. 54).

[173] J. J. Palacios, J. Fernández-Rossier, and L. Brey. "Vacancy-induced magnetism in graphene and graphene ribbons". *Phys. Rev. B* 77 (2008), p. 195428 (cit. on p. 54).

[174] H.-X. Yang, M. Chshiev, D. W. Boukhvalov, X. Waintal, and S. Roche. "Inducing and optimizing magnetism in graphene nanomeshes". *Phys. Rev. B* 84 (2011), p. 214404 (cit. on p. 54).

[175] S. Schumacher. "Structure, Magnetism, and Binding of Novel Two-Dimensional Materials: Europium-Intercalated Graphene, Cluster Lattices, and Polar Oxide Bilayers". PhD thesis. Universität zu Köln, 2014 (cit. on pp. 54, 58, 147).

[176] F. Huttmann. *Adsorption on and Intercalation under Gr/Ir(111): Magnetism and Binding.* Master thesis. 2013 (cit. on pp. 58, 147).

[177] D. F. Förster et al. "Epitaxial europium oxide on Ni(100) with single-crystal quality". *Phys. Rev. B* 83 (2011), p. 045424 (cit. on pp. 59, 71, 142, 147).

[178] J. B. Goedkoop. "X-ray dichroism of rare-earth materials". PhD thesis. Katholieke Universiteit te Nijmegen, 1989 (cit. on pp. 59, 119, 121, 122, 125, 126).

[179] V. V. Krishnamurthy et al. "Temperature dependence of Eu $4f$ and Eu $5d$ magnetizations in the filled skutterudite $EuFe_4Sb_{12}$". *Phys. Rev. B* 79 (2009), p. 014426 (cit. on p. 60).

[180] G. van der Laan. "Sum rule practice". *J. Synchrotron Radiat.* 6 (1999), p. 694 (cit. on p. 61).

[181] J. Klinkhammer, M. Schlipf, F. Craes, S. Runte, T. Michely, and C. Busse. "Spin-Polarized Surface State in EuO(100)". *Phys. Rev. Lett.* 112 (2014), p. 016803 (cit. on p. 62).

[182] N. D. Mermin and H. Wagner. "Absence of Ferromagnetism or Antiferromagnetism in One- or Two-Dimensional Isotropic Heisenberg Models". *Phys. Rev. Lett.* 17 (1966), p. 1133 (cit. on p. 63).

[183] A. Grechnev, V. Y. Irkhin, M. I. Katsnelson, and O. Eriksson. "Thermodynamics of a two-dimensional Heisenberg ferromagnet with dipolar interaction". *Phys. Rev. B* 71 (2005), p. 024427 (cit. on pp. 63, 77).

[184] "Using PPMS Superconducting Magnets at Low Fields" (2009). Quantum Design Application Note 1070-207 (cit. on p. 64).

[185] G. H. O. Daalderop, P. J. Kelly, and M. F. H. Schuurmans. "First-principles calculation of the magnetocrystalline anisotropy energy of iron, cobalt, and nickel". *Phys. Rev. B* 41 (1990), p. 11919 (cit. on p. 66).

[186] K. Barmak et al. "On the relationship of magnetocrystalline anisotropy and stoichiometry in epitaxial $L1_0$ CoPt (001) and FePt (001) thin films". *J. Appl. Phys.* 98, 033904 (2005), p. 033904 (cit. on p. 66).

[187] M. Bazarnik, R. Decker, J. Brede, and R. Wiesendanger. "Multi-layer and multi-component intercalation at the graphene/Ir(111) interface". *Surf. Sci.* 639 (2015), p. 70 (cit. on p. 69).

[188] R. W. Cahn. *Binary Alloy Phase Diagrams-Second edition. T. B. Massalski, Editor-in-Chief; H. Okamoto, P. R. Subramanian, L. Kacprzak, Editors. ASM International, Materials Park, Ohio, USA. December 1990. xxii, 3589 pp.* Vol. 2. 1991 (cit. on p. 71).

[189] C. T. Chen, F. Sette, Y. Ma, and S. Modesti. "Soft-x-ray magnetic circular dichroism at the $L_{2,3}$ edges of nickel". *Phys. Rev. B* 42 (1990), p. 7262 (cit. on p. 71).

[190] C. T. Chen et al. "Experimental Confirmation of the X-Ray Magnetic Circular Dichroism Sum Rules for Iron and Cobalt". *Phys. Rev. Lett.* 75 (1995), p. 152 (cit. on p. 71).

[191] B. Sanyal et al. "Forcing Ferromagnetic Coupling Between Rare-Earth-Metal and $3d$ Ferromagnetic Films". *Phys. Rev. Lett.* 104 (2010), p. 156402 (cit. on p. 72).

[192] C. Kittel. *Introduction to Solid State Physics*. 14th. New York: John Wiley & Sons, Inc., 2006 (cit. on p. 73).

[193] E. Ruiz, S. Alvarez, J. Cano, and V. Polo. "About the calculation of exchange coupling constants using density-functional theory: The role of the self-interaction error". *J. Chem. Phys.* 123, 164110 (2005), p. 164110 (cit. on p. 74).

[194] I. Rudra, Q. Wu, and T. Van Voorhis. "Accurate magnetic exchange couplings in transition-metal complexes from constrained density-functional theory". *J. Chem. Phys.* 124, 024103 (2006), p. 024103 (cit. on p. 74).

[195] I. A. Campbell. "Indirect exchange for rare earths in metals". *J. Phys. F: Met. Phys.* 2 (1972), p. L47 (cit. on p. 74).

[196] N. H. Duc. *Intersublattice exchange coupling in the lanthanide-transition metal intermetallics*. Ed. by K. A. Gschneidner and L. Eyring. Vol. 24. Handbook on the Physics and Chemistry of Rare Earths. Elsevier, 1997, p. 339 (cit. on p. 74).

[197] H.-S. Li, Y. P. Li, and J. M. D. Coey. "R-T and R-R exchange interactions in the rare-earth (R)-transition-metal (T) intermetallics: an evaluation from relativistic atomic calculations". *J. Phys. Condens. Matter* 3 (1991), p. 7277 (cit. on p. 74).

[198] E. N. Voloshina and Y. S. Dedkov. "Electronic and Magnetic Properties of the Graphene/Eu/Ni(111) Hybrid System". *Z. Naturforsch. A Phys. Sci.* 69 (2014), p. 297 (cit. on p. 75).

[199] C. Sorg, N. Ponpandian, M. Bernien, K. Baberschke, H. Wende, and R. Q. Wu. "Induced magnetism of oxygen in surfactant-grown Fe, Co, and Ni monolayers". *Phys. Rev. B* 73 (2006), p. 064409 (cit. on p. 76).

[200] H. Wende. "Recent advances in x-ray absorption spectroscopy". *Rep. Prog. Phys.* 67 (2004), p. 2105 (cit. on p. 76).

[201] D. Ahlers and G. Schütz. "Elastic exchange scattering amplitude studied using magnetic EXAFS". *Phys. Rev. B* 57 (1998), p. 3466 (cit. on p. 76).

[202] E. Voloshina, R. Ovcharenko, A. Shulakov, and Y. Dedkov. "Theoretical description of X-ray absorption spectroscopy of the graphene-metal interfaces". *J. Chem. Phys.* 138, 154706 (2013), p. 154706 (cit. on p. 76).

[203] P. Bruno. "Spin-wave theory of two-dimensional ferromagnets in the presence of dipolar interactions and magnetocrystalline anisotropy". *Phys. Rev. B* 43 (1991), p. 6015 (cit. on p. 77).

[204] F. Huttmann, N. Schleheck, N. Atodiresei, and T. Michely. "On-Surface Synthesis of Sandwich Molecular Nanowires on Graphene". *J. Am. Chem. Soc.* 139 (2017), p. 9895 (cit. on pp. 79, 155).

[205] K. Hoshino, T. Kurikawa, H. Takeda, A. Nakajima, and K. Kaya. "Structures and Ionization Energies of Sandwich Clusters (V_n(benzene)$_m$)". *J. Phys. Chem.* 99 (1995), p. 3053 (cit. on pp. 79, 96).

[206] T. Kurikawa et al. "Multiple-Decker Sandwich Complexes of Lanthanide-1,3,5,7-Cyclooctatetraene [$Ln_n(C_8H_8)_m$] (Ln = Ce, Nd, Eu, Ho, and Yb); Localized Ionic Bonding Structure". *J. Am. Chem. Soc.* 120 (1998), p. 11766 (cit. on pp. 79, 82).

[207] N. Hosoya et al. "Formation and Electronic Structures of Organoeuropium Sandwich Nanowires". *J. Phys. Chem. A* 118 (2014), p. 8298 (cit. on p. 79).

[208] K. Miyajima, S. Yabushita, M. B. Knickelbein, and A. Nakajima. "Stern-Gerlach Experiments of One-Dimensional Metal-Benzene Sandwich Clusters: $M_n(C_6H_6)_m$ (M = Al, Sc, Ti, and V)". *J. Am. Chem. Soc.* 129 (2007), p. 8473 (cit. on p. 79).

[209] T. Tsuji et al. "Liquid-Phase Synthesis of Multidecker Organoeuropium Sandwich Complexes and Their Physical Properties". *J. Phys. Chem. C* 118 (2014), p. 5896 (cit. on p. 79).

[210] A. Koma. "Van der Waals epitaxy for highly lattice-mismatched systems". *J. Crys. Growth* 201-202 (1999), p. 236 (cit. on pp. 80, 129).

[211] A. Koma, K. Sunouchi, and T. Miyajima. "Fabrication and characterization of heterostructures with subnanometer thickness". *Microelectron. Eng.* 2 (1984), p. 129 (cit. on p. 80).

[212] H. Haugen, D. Huertas-Hernando, and A. Brataas. "Spin transport in proximity-induced ferromagnetic graphene". *Phys. Rev. B* 77 (2008), p. 115406 (cit. on p. 80).

[213] B. Zhou, X. Chen, H. Wang, K.-H. Ding, and G. Zhou. "Magnetotransport and current-induced spin transfer torque in a ferromagnetically contacted graphene". *J. Phys. Condens. Matter* 22 (2010), p. 445302 (cit. on p. 80).

[214] A. G. Swartz, P. M. Odenthal, Y. Hao, R. S. Ruoff, and R. K. Kawakami. "Integration of the Ferromagnetic Insulator EuO onto Graphene". *ACS Nano* 6 (2012), p. 10063 (cit. on p. 80).

[215] A. Gourdon, ed. *Proceedings of the International Workshop on On-Surface Synthesis, Ecole des Houches, Les Houches 25-30 May 2014*. Springer, 2016 (cit. on p. 80).

[216] R. Lindner and A. Kühnle. "On-Surface Reactions". *Chem. Phys. Chem.* 16 (2015), p. 1582 (cit. on p. 80).

[217] L. Dong, P. N. Liu, and N. Lin. "Surface-Activated Coupling Reactions Confined on a Surface". *Acc. Chem. Res.* 48 (2015), p. 2765 (cit. on p. 80).

[218] Q. Fan, J. M. Gottfried, and J. Zhu. "Surface-Catalyzed C–C Covalent Coupling Strategies toward the Synthesis of Low-Dimensional Carbon-Based Nanostructures". *Acc. Chem. Res.* 48 (2015), p. 2484 (cit. on p. 80).

[219] F. Klappenberger, Y.-Q. Zhang, J. Björk, S. Klyatskaya, M. Ruben, and J. V. Barth. "On-Surface Synthesis of Carbon-Based Scaffolds and Nanomaterials Using Terminal Alkynes". *Acc. Chem. Res.* 48 (2015), p. 2140 (cit. on p. 80).

[220] M. Lackinger. "On-surface polymerization – a versatile synthetic route to two-dimensional polymers". *Polym. Int.* 64 (2015), p. 1073 (cit. on p. 80).

[221] L. Talirz, P. Ruffieux, and R. Fasel. "On-Surface Synthesis of Atomically Precise Graphene Nanoribbons". *Adv. Mater.* 28 (2016), p. 6222 (cit. on p. 80).

[222] E. Schmidt, K. J. Klabunde, A. Ponce, A. Smetana, and D. Heroux. *Metal Vapor Synthesis of Transition Metal Compounds.* In: *Encyclopedia of Inorganic Chemistry.* John Wiley & Sons, Ltd, 2006 (cit. on p. 80).

[223] J. M. Gottfried, K. Flechtner, A. Kretschmann, T. Lukasczyk, and H.-P. Steinrück. "Direct Synthesis of a Metalloporphyrin Complex on a Surface". *J. Am. Chem. Soc.* 128 (2006), p. 5644 (cit. on p. 80).

[224] J. M. Gottfried. "Surface chemistry of porphyrins and phthalocyanines". *Surf. Sci. Rep.* 70 (2015), p. 259 (cit. on p. 80).

[225] K. Diller, A. C. Papageorgiou, F. Klappenberger, F. Allegretti, J. V. Barth, and W. Auwärter. "In vacuo interfacial tetrapyrrole metallation". *Chem. Soc. Rev.* 45 (2016), p. 1629 (cit. on p. 80).

[226] H. Marbach. "Surface-Mediated in Situ Metalation of Porphyrins at the Solid–Vacuum Interface". *Acc. Chem. Res.* 48 (2015), p. 2649 (cit. on p. 80).

[227] D. Écija et al. "Assembly and Manipulation of Rotatable Cerium Porphyrinato Sandwich Complexes on a Surface". *Angew. Chem. Int. Ed.* 50 (2011), p. 3872 (cit. on p. 80).

[228] F. Hanke, S. Haq, R. Raval, and M. Persson. "Heat-to-Connect: Surface Commensurability Directs Organometallic One-Dimensional Self-Assembly". *ACS Nano* 5 (2011), p. 9093 (cit. on p. 80).

[229] S. Haq et al. "Clean Coupling of Unfunctionalized Porphyrins at Surfaces To Give Highly Oriented Organometallic Oligomers". *J. Am. Chem. Soc.* 133 (2011), p. 12031 (cit. on p. 80).

[230] R. Hellwig et al. "Epitaxy-Induced Assembly and Enantiomeric Switching of an On-Surface Formed Dinuclear Organocobalt Complex". *ACS Nano* 11 (2017), p. 1347 (cit. on p. 80).

[231] J. Liu et al. "Lattice-Directed Formation of Covalent and Organometallic Molecular Wires by Terminal Alkynes on Ag Surfaces". *ACS Nano* 9 (2015), p. 6305 (cit. on p. 80).

[232] P. B. Weber et al. "Surface-Guided Formation of an Organocobalt Complex". *Angew. Chem. Int. Ed.* 55 (2016), p. 5754 (cit. on p. 80).

[233] Y.-Y. Li et al. "Intrinsic Topological Insulator Bi_2Te_3 Thin Films on Si and Their Thickness Limit". *Adv. Mater.* 22 (2010), p. 4002 (cit. on p. 80).

[234] C.-L. Song et al. "Molecular-beam epitaxy and robust superconductivity of stoichiometric FeSe crystalline films on bilayer graphene". *Phys. Rev. B* 84 (2011), p. 020503 (cit. on p. 80).

[235] A. Kis et al. "Reinforcement of single-walled carbon nanotube bundles by intertube bridging". *Nat. Mater.* 3 (2004), p. 153 (cit. on p. 82).

[236] H. Dumlich, M. Gegg, F. Hennrich, and S. Reich. "Bundle and chirality influences on properties of carbon nanotubes studied with van der Waals density functional theory". *physica status solidi (b)* 248 (2011), p. 2589 (cit. on p. 82).

[237] V. Nicolosi et al. "Observation of van der Waals Driven Self-Assembly of MoSI Nanowires into a Low-Symmetry Structure Using Aberration-Corrected Electron Microscopy". *Adv. Mater.* 19 (2007), p. 543 (cit. on p. 82).

[238] F. W. Billmeyer Jr. "Lattice Energy of Crystalline Polyethylene". *J. Appl. Phys.* 28 (1957), p. 1114 (cit. on p. 83).

[239] X. Yao, S. Yuan, and J. Wang. "Theoretical Studies of Sandwich Molecular Wires with Europium and Boratacyclooctatetraene Ligand and the Structure on a H-Ge(001)-2×1 Surface". *J. Phys. Chem. C* 120 (2016), p. 7088 (cit. on p. 83).

[240] P. W. Tasker. "The stability of ionic crystal surfaces". *J. Phys. C* 12 (1979), p. 4977 (cit. on p. 83).

[241] A. K. Schmid and J. Kirschner. "In situ observation of epitaxial growth of Co thin films on Cu(100)". *Ultramicroscopy* 42-44 (1992), p. 483 (cit. on p. 88).

[242] F. Schulz, R. Drost, S. K. Hämäläinen, T. Demonchaux, A. P. Seitsonen, and P. Liljeroth. "Epitaxial hexagonal boron nitride on Ir(111): A work function template". *Phys. Rev. B* 89 (2014), p. 235429 (cit. on p. 92).

[243] F. H. Farwick zum Hagen et al. "Structure and Growth of Hexagonal Boron Nitride on Ir(111)". *ACS Nano* 10 (2016), p. 11012 (cit. on p. 93).

[244] S. Joshi et al. "Boron Nitride on Cu(111): An Electronically Corrugated Monolayer". *Nano Lett.* 12 (2012), p. 5821 (cit. on p. 92).

[245] F. Müller, S. Hüfner, H. Sachdev, R. Laskowski, P. Blaha, and K. Schwarz. "Epitaxial growth of hexagonal boron nitride on Ag(111)". *Phys. Rev. B* 82 (2010), p. 113406 (cit. on p. 92).

[246] R. Laskowski, P. Blaha, and K. Schwarz. "Bonding of hexagonal BN to transition metal surfaces: An ab initio density-functional theory study". *Phys. Rev. B* 78 (2008), p. 045409 (cit. on p. 92).

[247] S. M. Avdoshenko, I. N. Ioffe, G. Cuniberti, L. Dunsch, and A. A. Popov. "Organometallic Complexes of Graphene: Toward Atomic Spintronics Using a Graphene Web". *ACS Nano* 5 (2011), p. 9939 (cit. on pp. 92, 93).

[248] P. L. Timms. "The formation of complexes from transition-metal vapours". *J. Chem. Soc. D* (1969), 1033a (cit. on p. 93).

[249] C. Elschenbroich et al. "Metal π Complexes of Benzene Derivatives. Germanium in the Periphery of Bis(benzene)vanadium and Bis(benzene)chromium. Synthesis and Structure of New Heterametallocyclophanes". *Organometallics* 16 (1997), p. 4589 (cit. on p. 93).

[250] D. Young and M. L. H. Green. "Vapour synthesis: A new technique in synthetic chemistry". *J. Appl. Chem. Biotechnol.* 25 (1975), p. 641 (cit. on p. 94).

[251] M. Mitsui, S. Nagaoka, T. Matsumoto, and A. Nakajima. "Soft-Landing Isolation of Vanadium-Benzene Sandwich Clusters on a Room-Temperature Substrate Using n-Alkanethiolate Self-Assembled Monolayer Matrixes". *J. Phys. Chem. B* 110 (2006), p. 2968 (cit. on p. 95).

[252] M. Ormaza et al. "Assembly of Ferrocene Molecules on Metal Surfaces Revisited". *J. Phys. Chem. Lett.* 6 (2015), p. 395 (cit. on p. 95).

[253] M. P. Andrews, S. M. Mattar, and G. A. Ozin. "Bis(benzene)vanadium (η^6-$C_6H_6)_2V$: an optical, EPR spectroscopy, and Xα-MO study. 2". *J. Phys. Chem.* 90 (1986), p. 1037 (cit. on p. 96).

[254] Michael Schmid, IAP/TU Wien Surface Physics Group. *Vapor pressure calculator*. `https://www.iap.tuwien.ac.at/www/surface/vapor_pressure`. Accessed: 2017-05-19 (cit. on p. 96).

[255] J. Renard, M. B. Lundeberg, J. A. Folk, and Y. Pennec. "Real-Time Imaging of K Atoms on Graphite: Interactions and Diffusion". *Phys. Rev. Lett.* 106 (2011), p. 156101 (cit. on p. 99).

[256] N. Schleheck. *Synthesis of Organometallic Nanowires and Molecular Layers*. Master thesis. Germany, 2015 (cit. on p. 99).

[257] H. Brune, J. Wintterlin, J. Trost, G. Ertl, J. Wiechers, and R. J. Behm. "Interaction of oxygen with Al(111) studied by scanning tunneling microscopy". *J. Chem. Phys.* 99 (1993), p. 2128 (cit. on p. 105).

[258] R. Koch, M. Borbonus, O. Haase, and K. H. Rieder. "New aspects on the Ir(110) reconstruction: Surface stabilization on mesoscopic scale via (331) facets". *Phys. Rev. Lett.* 67 (1991), p. 3416 (cit. on p. 109).

[259] P. Kaghazchi and T. Jacob. "First-principles studies on clean and oxygen-adsorbed Ir(110) surfaces". *Phys. Rev. B* 76 (2007), p. 245425 (cit. on p. 110).

[260] J. J. Schulz, M. Sturmat, and R. Koch. "Illuminating structural transformation of Ir(110): A high-temperature scanning tunneling microscopy study". *Phys. Rev. B* 62 (2000), p. 15402 (cit. on p. 110).

[261] S. Schumacher, D. F. Förster, F. Hu, T. Frauenheim, T. O. Wehling, and T. Michely. "Polar EuO(111) on Ir(111): A two-dimensional oxide". *Phys. Rev. B* 89 (2014), p. 115410 (cit. on pp. 111, 142, 143, 147).

[262] H. Galloway, J. Benítez, and M. Salmeron. "The structure of monolayer films of FeO on Pt(111)". *Surf. Sci.* 298 (1993), p. 127 (cit. on p. 111).

[263] S. Runte, P. Lazić, C. Vo-Van, J. Coraux, J. Zegenhagen, and C. Busse. "Graphene buckles under stress: An x-ray standing wave and scanning tunneling microscopy study". *Phys. Rev. B* 89 (2014), p. 155427 (cit. on p. 112).

[264] T. Michely, M. Kalff, G. Comsa, M. Strobel, and K.-H. Heinig. "Step Edge Diffusion and Step Atom Detachment in Surface Evolution: Ion Erosion of Pt(111)". *Phys. Rev. Lett.* 86 (2001), p. 2589 (cit. on pp. 113, 146).

[265] I. Šrut, V. M. Trontl, P. Pervan, and M. Kralj. "Temperature dependence of graphene growth on a stepped iridium surface". *Carbon* 56 (2013), p. 193 (cit. on p. 113).

[266] J. B. Goedkoop, B. T. Thole, G. van der Laan, G. A. Sawatzky, F. M. F. de Groot, and J. C. Fuggle. "Calculations of magnetic x-ray dichroism in the 3d absorption spectra of rare-earth compounds". *Phys. Rev. B* 37 (1988), p. 2086 (cit. on pp. 119, 121, 126).

[267] C. Nistor et al. "Structure and magnetism of Tm atoms and monolayers on W(110)". *Phys. Rev. B* 90 (2014), p. 064423 (cit. on pp. 119, 122, 125, 126).

[268] P. Bruno. "Tight-binding approach to the orbital magnetic moment and magnetocrystalline anisotropy of transition-metal monolayers". *Phys. Rev. B* 39 (1989), p. 865 (cit. on p. 122).

[269] F. Wilhelm et al. "Magnetic anisotropy energy and the anisotropy of the orbital moment of Ni in Ni/Pt multilayers". *Phys. Rev. B* 61 (2000), p. 8647 (cit. on p. 122).

[270] C. Antoniak et al. "A guideline for atomistic design and understanding of ultrahard nanomagnets". *Nat. Commun.* 2 (2011), p. 528 (cit. on p. 122).

[271] R. Skomski and D. Sellmyer. "Anisotropy of rare-earth magnets". *J. Rare Earths* 27 (2009), p. 675 (cit. on p. 122).

[272] S. Stepanow et al. "Spin and Orbital Magnetic Moment Anisotropies of Monodispersed Bis(Phthalocyaninato)Terbium on a Copper Surface". *J. Am. Chem. Soc.* 132 (2010), p. 11900 (cit. on p. 122).

[273] J. P. Schillé, J. P. Kappler, P. Sainctavit, C. Cartier dit Moulin, C. Brouder, and G. Krill. "Experimental and calculated magnetic dichroism in the Ho 3d x-ray-absorption spectra of intermetallic $HoCo_2$". *Phys. Rev. B* 48 (1993), p. 9491 (cit. on p. 123).

[274] J. D. Rinehart and J. R. Long. "Exploiting single-ion anisotropy in the design of f-element single-molecule magnets". *Chem. Sci.* 2 (2011), p. 2078 (cit. on p. 126).

[275] D. P. Pappas, A. P. Popov, A. N. Anisimov, B. V. Reddy, and S. N. Khanna. "Spin Configuration of Gd_{13} Clusters". *Phys. Rev. Lett.* 76 (1996), p. 4332 (cit. on pp. 126, 127, 129).

[276] F. Donati et al. "Magnetic remanence in single atoms". *Science* 352 (2016), p. 318 (cit. on p. 126).

[277] D. Gerion, A. Hirt, and A. Châtelain. "High Curie Temperature and Possible Canted Magnetism in Free Gd Clusters". *Phys. Rev. Lett.* 83 (1999), p. 532 (cit. on pp. 127, 129).

[278] C. van Dijk, J. Bowlan, W. A. de Heer, T. Rasing, and A. Kirilyuk. "Unusual Temperature Dependence of Magnetization and Possible Magnetic Noncollinearity in Tm and Pr Clusters". *J. Phys. Chem. C* 119 (2015), p. 11153 (cit. on p. 127).

[279] J. T. Lyon and L. Andrews. "V, Nb, and Ta Complexes with Benzene in Solid Argon: An Infrared Spectroscopic and Density Functional Study". *J. Phys. Chem. A* 109 (2005), p. 431 (cit. on p. 128).

[280] D. Rayane, A.-R. Allouche, R. Antoine, M. Broyer, I. Compagnon, and P. Dugourd. "Electric dipole of metal–benzene sandwiches". *Chemical Physics Letters* 375 (2003), p. 506 (cit. on p. 128).

[281] X. Xi et al. "Strongly enhanced charge-density-wave order in monolayer NbSe2". *Nat. Nano.* 10 (2015), p. 765 (cit. on p. 135).

[282] N. Katayama et al. "Anomalous Metallic State in the Vicinity of Metal to Valence-Bond Solid Insulator Transition in $LiVS_2$". *Phys. Rev. Lett.* 103 (2009), p. 146405 (cit. on pp. 135–137, 139).

[283] H. F. Pen, J. van den Brink, D. I. Khomskii, and G. A. Sawatzky. "Orbital Ordering in a Two-Dimensional Triangular Lattice". *Phys. Rev. Lett.* 78 (1997), p. 1323 (cit. on pp. 135, 137).

[284] S. Y. Ezhov, V. I. Anisimov, H. F. Pen, D. I. Khomskii, and G. A. Sawatzky. "Orbital polarization in $LiVO_2$ and $NaTiO_2$". *Europhysics Letters* 44 (1998), p. 491 (cit. on pp. 135, 136).

[285] Y. Guo, G. Zhang, X. Zhang, T. Jia, and Z. Zeng. "Orbitally driven spin-singlet state in LiVS2". *J. Appl. Phys.* 109 (2011), 07E145 (cit. on pp. 136, 137, 139).

[286] L. Boehnke, A. I. Lichtenstein, M. I. Katsnelson, and F. Lechermann. "Hidden spin-orbital hexagonal ordering induced by strong correlations in $LiVS_2$" (2014). arxiv: 1407.4795 (cit. on p. 136).

[287] G. Kresse and J. Furthmüller. "Efficient iterative schemes for ab initio total-energy calculations using a plane-wave basis set". *Phys. Rev. B* 54 (1996), p. 11169 (cit. on p. 136).

[288] J. P. Perdew, K. Burke, and M. Ernzerhof. "Generalized Gradient Approximation Made Simple". *Phys. Rev. Lett.* 77 (1996), p. 3865 (cit. on p. 136).

[289] B. van Laar and D. Ijdo. "Preparation, crystal structure, and magnetic structure of $LiCrS_2$ and $LiVS_2$". *J. Solid State Chem.* 3 (1971), p. 590 (cit. on p. 136).

[290] Y. Jing, Z. Zhou, C. R. Cabrera, and Z. Chen. "Metallic VS_2 Monolayer: A Promising 2D Anode Material for Lithium Ion Batteries". *J. Phys. Chem. C* 117 (2013), p. 25409 (cit. on p. 137).

[291] A. I. Liechtenstein, V. I. Anisimov, and J. Zaanen. "Density-functional theory and strong interactions: Orbital ordering in Mott-Hubbard insulators". *Phys. Rev. B* 52 (1995), R5467 (cit. on pp. 139, 142).

[292] S. L. Dudarev, G. A. Botton, S. Y. Savrasov, C. J. Humphreys, and A. P. Sutton. "Electron-energy-loss spectra and the structural stability of nickel oxide: An LSDA+U study". *Phys. Rev. B* 57 (1998), p. 1505 (cit. on p. 139).

[293] S. Lutfalla, V. Shapovalov, and A. T. Bell. "Calibration of the DFT/GGA+U Method for Determination of Reduction Energies for Transition and Rare Earth Metal Oxides of Ti, V, Mo, and Ce". *J. Chem. Theory Comput.* 7 (2011), p. 2218 (cit. on pp. 139, 143).

[294] J. P. Allen and G. W. Watson. "Occupation matrix control of d- and f-electron localisations using DFT + U". *Phys. Chem. Chem. Phys.* 16 (2014), p. 21016 (cit. on p. 140).

[295] B. Meredig, A. Thompson, H. A. Hansen, C. Wolverton, and A. van de Walle. "Method for locating low-energy solutions within DFT + U". *Phys. Rev. B* 82 (2010), p. 195128 (cit. on p. 140).

[296] Y. Zhang, L. Lin, J.-J. Zhang, E. Dagotto, and S. Dong. "Pressure-driven phase transition from antiferromagnetic semiconductor to nonmagnetic metal in the two-leg ladders $A\mathrm{Fe}_2X_3$ (A = Ba,K; X = S,Se)". *Phys. Rev. B* 95 (2017), p. 115154 (cit. on p. 140).

[297] D. W. Murphy, C. Cros, F. J. D. Salvo, and J. V. Waszczak. "Preparation and properties of $\mathrm{Li}_x\mathrm{VS}_2$ ($0 \leq x \leq 1$)". *Inorganic Chemistry* 16 (1977), p. 3027 (cit. on p. 141).

[298] D. W. Murphy, F. J. Di Salvo, G. W. Hull, and J. V. Waszczak. "Convenient preparation and physical properties of lithium intercalation compounds of Group 4B and 5B layered transition metal dichalcogenides". *Inorganic Chemistry* 15 (1976), p. 17 (cit. on p. 141).

[299] Wikipedia. *Lyotropic liquid crystal — Wikipedia, The Free Encyclopedia.* [Online; accessed 9-June-2017]. 2017 (cit. on p. 148).

[300] K. Mortensen. "Structural studies of lamellar surfactant systems under shear". *Current Opinion in Colloid and Interface Science* 6 (2001), p. 140 (cit. on p. 148).

[301] A. Léon, D. Bonn, J. Meunier, A. Al-Kahwaji, O. Greffier, and H. Kellay. "Coupling between Flow and Structure for a Lamellar Surfactant Phase". *Phys. Rev. Lett.* 84 (2000), p. 1335 (cit. on p. 148).

[302] D. J. Chakrabarti and D. E. Laughlin. "The Ca-Cu (Calcium-Copper) system". *Bulletin of Alloy Phase Diagrams* 5 (1984), p. 570 (cit. on p. 148).

[303] H. Okamoto. "Ca-Fe (Calcium-Iron)". *J. Phase. Equilib. Diff.* 31 (2010), p. 88 (cit. on p. 148).

Appendix F

Erklärung gemäß Promotionsordnung

Ich versichere, dass ich die von mir vorgelegte Dissertation selbstständig angefertigt, die benutzten Quellen und Hilfsmittel vollständig angegeben und die Stellen der Arbeit - einschließlich Tabellen, Karten und Abbildungen -, die anderen Werken im Wortlaut oder dem Sinn nach entnommen sind, in jedem Einzelfall als Entlehnung kenntlich gemacht habe; dass diese Dissertation noch keiner anderen Fakultät oder Universität zur Prüfung vorgelegen hat; dass sie - abgesehen von den angegebenen Teilpublikationen - noch nicht veröffentlicht worden ist, sowie, dass ich eine solche Veröffentlichung vor Abschluss des Promotionsverfahrens nicht vornehmen werde. Die Bestimmungen der Promotionsordnung sind mir bekannt. Die von mir vorgelegte Dissertation ist von Prof. Dr. Thomas Michely betreut worden.

Köln, den 13.08.2017

Felix Huttmann